

Probing Nonlinear Dynamics in Strongly Driven Quantum Materials

Dissertation

zur Erlangung des Doktorgrades an der Fakultät für
Mathematik, Informatik und Naturwissenschaften

Fachbereich Physik
der Universität Hamburg

vorgelegt von

ALEXANDER VON HOEGEN

Hamburg

2020

Gutachter/innen der Dissertation:	Prof. Dr. Andrea Cavalleri Prof. Dr. Henning Moritz
Zusammensetzung der Prüfungskommission:	Prof. Dr. Andrea Cavalleri Prof. Dr. Henning Moritz Prof. Dr. Ludwig Mathey PD Dr. Guido Meier Prof. Dr. Michael Rübhausen
Vorsitzende/r der Prüfungskommission:	Prof. Dr. Michael Rübhausen
Datum der Disputation:	22.01.2021
Vorsitzender Fach-Promotionsausschusses PHYSIK:	Prof. Dr. Günter Hands Walter Sigl
Leiter des Fachbereichs PHYSIK	Prof. Dr. Wolfgang Hansen
Dekan der Fakultät MIN	Prof. Dr. Heinrich Graener

Eidesstattliche Versicherung / Declaration on oath

Hiermit versichere ich an Eides statt, die vorliegende Dissertationsschrift selbst verfasst und keine anderen als die angegebenen Hilfsmittel und Quellen benutzt zu haben.

Die eingereichte schriftliche Fassung entspricht der auf dem elektronischen Speichermedium.

Die Dissertation wurde in der vorgelegten oder einer ähnlichen Form nicht schon einmal in einem früheren Promotionsverfahren angenommen oder als ungenügend beurteilt.

I hereby declare, on oath, that I have written the present dissertation on my own and have not used other than the mentioned resources and aids.

The submitted written version is identical to the version on the electronic storage medium.

This work has never been presented to other persons or evaluation panels in the context of an examination.

Hamburg, den 12.10.2020

Unterschrift der Doktorandin / des Doktoranden

Abstract

The possibility to enhance desirable functional properties of correlated materials through optical excitation with intense mid-infrared pulses motivated a series of studies of their nonlinear terahertz physics. These mid-infrared light pulses are used to resonantly excite infrared-active vibrations, so that the energy of the light pulses is directly transferred into the lattice vibration. This allows for the accurate tracing of the energy flow to other nonlinearly coupled excitations of correlated materials and ultimately better understanding of their competing ground states. The balance among different low energy states, with different macroscopic properties, can be tipped by minute changes of the electron-electron interactions which in turn are sensitive to changes of the atomic arrangement. This was demonstrated in a set of experiments where the strong-field resonant excitation of the crystal lattice was observed to entail the emergence of hidden states of matter. These states are inaccessible under equilibrium conditions and show fascinating phenomena such as light-induced superconductivity and ferroelectricity, insulator-metal transitions and melting of electronic and magnetic order. To reveal these hidden states new nonlinear optical tools are required. The aim of this work is therefore to extend the well-established equilibrium technique of second harmonic generation (SHG), which is sensitive to dynamics invisible to a linear optical probing, to ultra-fast pump-probe experiment. This technique will be used to investigate how nonlinear lattice dynamics can couple to macroscopic material properties and how this can be used to manipulate them.

In many correlated materials their macroscopic properties are determined by frozen in lattice distortions. The direct control of the crystal lattice therefore would allow for the ultra-fast manipulation of these properties. First experiments achieved this type of control through nonlinear coupling between a resonantly driven infrared active mode and the lattice distortion that is responsible for the macroscopic material properties. We used this pathway to transiently reverse the polarization state of the ferroelectric LiNbO_3 and studied the ensuing dynamics with SHG, which solely is sensitive to the microscopic polarization state. The amplitude and phase sensitive detection of the lattice dynamics revealed a transient reversal of the polarization state and allowed us to reconstruct the lattice potential energy.

In high- T_c cuprates, the large amplitude excitation of the apical oxygen lattice vibration has been shown to induce transient features in the reflectivity suggestive of non-equilibrium su-

perconductivity. Yet, notwithstanding intense research efforts a microscopic mechanism for these observations is still lacking. To address this problem, we measured time- and scattering-angle-dependent second-harmonic generation in $\text{YBa}_2\text{Cu}_3\text{O}_{6+\delta}$ after exciting the apical oxygen vibration that transiently induces a superconductor-like terahertz reflectivity. Made possible by the tr-SHG technique, we observed a four-order-of-magnitude amplification of a 2.5-THz electronic mode, which displays a unique symmetry, momentum, and temperature dependence. We developed a theory involving parametric three-wave amplification of Josephson plasmons, which explains all these observations and provides a mechanism for non-equilibrium superconductivity.

Zusammenfassung

Die Möglichkeit, durch optische Anregung mit intensiven Laserpulsen im mittleren Infrarot die funktionellen Eigenschaften korrelierter Materialien zu manipulieren, motivierte die Untersuchung ihrer nichtlinearen Terahertz-Physik. In jenen Studien wurde - unter Umgehung elektronischer Anregungen - direkt Energie durch resonante Anregung infrarot-aktiver Schwingungen auf die Gitterschwingungen übertragen. So kann der Energiefluss in andere, nichtlinear gekoppelte fundamentale Anregungen der korrelierten Materialien genauestens verfolgt werden um damit letztlich ein tieferes Verständnis der konkurrierenden Grundzustände dieser Materialklasse zu gewinnen. Schon kleinste Änderungen der Elektron-Elektron-Wechselwirkung, die sehr empfindlich von der Konfiguration des Kristallgitters abhängen, rufen Übergänge zwischen den verschiedenen niederenergetischen Zuständen hervor und erzwingen makroskopische Phasenübergänge. Dies konnte in einer Reihe von Experimenten demonstriert werden, bei denen die direkte, resonante Anregung des Kristallgitters das Material in einen verborgenen Zustand beförderte, der im Gleichgewicht nicht erreichbar ist. Diese verborgenen Zustände zeigen faszinierende Eigenschaften, wie lichtinduzierte Supraleitung und Ferroelektrizität, Isolator-Metall-Übergänge und das Schmelzen elektronischer und magnetischer Ordnung. Da viele dieser verborgenen Zustände jedoch auch konventionellen linearen optischen Sonden unzugänglich sind, sind neue nichtlineare optische Werkzeuge erforderlich, um sie sichtbar zu machen. Daher ist es Ziel dieser Arbeit, die bereits etablierte Gleichgewichtstechnik der Generation der zweiten Harmonischen (SHG) eines Laserpulses auf ultraschnelle Anrege-Abfrage-Experimente zu erweitern. Mit dieser Technik soll untersucht werden, wie nichtlineare Gitterdynamik an makroskopische Materialeigenschaften koppelt und wie diese dadurch modifiziert werden können.

Die makroskopischen Eigenschaften vieler korrelierter Materialien sind durch eingefrorene Gitterverzerrungen bestimmt und die direkte Kontrolle des Kristallgitters erlaubt damit die ultraschnelle Manipulation der mit dieser Gitterverzerrung verbundenen Eigenschaften. Frühere Experimente konnten die Kontrolle des Kristallgitters durch nichtlineare Kopplung bereits demonstrieren und zeigten, dass Kopplung zwischen der resonant angetriebenen infrarotaktiven Mode und der Gitterverzerrung, die für die makroskopischen Materialeigenschaften verantwortlich ist, die kohärente Kontrolle dieser erlaubt. Dies nutzten wir, um den Polarisationszustand des Ferroelektrikums LiNbO_3 transient umzukehren, und untersuchten die sich daraus ergebende

Dynamik mit SHG, die alleinig empfindlich auf den mikroskopischen Polarisationszustand ist. Die amplituden- und phasenempfindliche Detektion der Gitterdynamik zeigte eine transiente Umkehrung des Polarisationszustandes und erlaubte, die potentielle Energie des Gitters zu rekonstruieren.

Vergleichbare Experimente in Hochtemperatur-Kuprat-Supraleitern wie $\text{YBa}_2\text{Cu}_3\text{O}_{6+\delta}$ zeigten, dass die Anregung der apikalen Sauerstoffgitterschwingung transiente Merkmale in der Reflektivität bewirken, die auf induzierte Nicht-Gleichgewichts-Supraleitung hindeuten. Trotz intensiver Forschungsbemühungen fehlt jedoch bisher ein mikroskopischer Mechanismus, der diese Beobachtungen erklärt. Wir nutzten dieselbe Anregung, die transient eine supraleiterähnliche Terahertz-Reflektivität induziert, und messen die zeit- und streuwinkelabhängige Generation der zweiten Harmonischen in $\text{YBa}_2\text{Cu}_3\text{O}_{6+\delta}$. Ermöglicht durch die tr-SHG-Methode, beobachten wir eine Verstärkung einer elektronischen 2.5-THz-Mode, die eine einzigartige Symmetrie-, Impuls- und Temperaturabhängigkeit aufweist, um vier Größenordnungen. Diese Beobachtungen motivierten eine Theorie der parametrischen Drei-Wellen-Verstärkung von Josephson-Plasmonen, die eine Erklärung für die Nicht-Gleichgewichts-Supraleitung liefert.

Contents

Introduction	1
1 Linear and Nonlinear Optical Properties of Solids	9
1.1 Linear Optical Properties	10
1.1.1 Dielectric Function	10
1.1.2 Phonons	14
1.1.3 Plasmons	15
1.1.4 Polaritons	16
1.2 Nonlinear Optics	18
1.2.1 Raman-Scattering	18
1.2.2 Second Order Optical Susceptibility	19
1.2.3 Second Harmonic Generation	22
1.2.4 Symmetry of Second Harmonic Generation	24
1.2.5 Hyper-Raman Scattering	26
1.2.6 Third Order Optical Susceptibility	28
1.3 Nonlinear Optics using Femtosecond Pulses	29
1.3.1 Basic Concepts of Short Laser Pulses	30
1.3.2 Homogeneous and Inhomogeneous solution in Second Harmonic Generation	31
1.4 Time-resolved Optical Experiments	33
1.4.1 Time-resolved Raman and Hyper-Raman scattering	33
1.4.2 Measuring Polaritons with Short Laser Pulses	38

2	Nonlinear Phononics in LiNbO₃	41
2.1	Introduction	41
2.2	Theory of Nonlinear Phononics	42
2.2.1	Nonlinearities of a Strongly Driven Lattice Vibration	43
2.2.2	Nonlinear Coupling of a Strongly Driven Lattice Vibration	48
2.2.3	Cubic Coupling $Q_i^2 Q_j$	48
2.2.4	Quartic Coupling $Q_i^2 Q_j^2$ and $Q_i^3 Q_j$	49
2.3	Nonlinear Phononics in LiNbO ₃ : Experimental demonstration	55
2.3.1	Reconstruction fo the Interatomic Potential of LiNbO ₃	55
2.3.1.1	Properties of insulating ferroelectric LiNbO ₃	55
2.3.1.2	Time-Resolved Second Harmonic Detection Setup	58
2.3.1.3	High-Order Nonlinear Phononics: Experimental Results	59
2.3.1.4	FDTD-Simulations of Anharmonic Phonon-Polariton Propagation	64
2.3.1.5	Reconstruction of the Interatomic Potential	64
2.3.2	Nonlinear Phonon Coupling: Experimental Results	67
2.4	Summary	74
3	Theory of Cuprate Superconductors and Josephson Physics	75
3.1	Introduction	75
3.2	Superconductivity	76
3.3	Dynamics of a Superconductor: London Equations	78
3.4	Josephson Effect	81
3.4.1	Equivalent Circuit of Josephson Junctions	83
3.4.2	Stack of Josephson Junctions	85
3.5	Cuprates	89
3.5.1	Optical Properties of Cuprates	91
4	Parametrically Amplified Phase-Incoherent Superconductivity in YBa₂Cu₃O_{6+δ}	101
4.1	Introduction	101

4.2	Properties of $\text{YBa}_2\text{Cu}_3\text{O}_{6+\delta}$	104
4.2.1	Phase diagram of $\text{YBa}_2\text{Cu}_3\text{O}_{6+\delta}$ and Precursor Superconductivity	106
4.3	Coherent Josephson Plasmon Dynamics in $\text{YBa}_2\text{Cu}_3\text{O}_{6+\delta}$	109
4.3.1	Time-Resolved Second Harmonic Detection Setup	109
4.3.2	Time-Resolved Second Harmonic Measurements	109
4.3.3	Doping-dependence	113
4.3.4	Time-resolved SH-polarimetry	116
4.3.5	Momentum-resolved SH measurement	120
4.4	Coherent Phonon Dynamics in $\text{YBa}_2\text{Cu}_3\text{O}_{6+\delta}$	121
4.4.1	Characteristics of the Resonantly Driven Phonons	122
4.4.2	Cubic-order Phonon Coupling	124
4.4.3	Quartic-order Phonon Coupling	124
4.5	Temperature Dependence of Josephson Plasmons and Phonons	128
4.6	Theoretical Model of Phonon-Josephson Plasmon Coupling	131
4.6.1	THz-optical Response of Parametrically Amplified Josephson Plasmons	136
4.7	Discussion	139
4.8	Summary	139
	Conclusion and Outlook	143
	Author Contributions	147
	List of Publications	149
	Appendix A Nonlinear Optics and Pump-Probe Experiments	151
A.1	Basics of Pump probe Experiments and Experimental Practice	151
A.2	Optical Parametric Amplification	153
A.3	Difference Frequency Generation	154
A.4	Generation of Broadband Mid-Infrared Radiation	155
A.5	Time-Resolved Detection of Strong Mid-Infrared Fields	156
A.6	Phase-Matching Type-I and Type-II	157

Appendix B Time-resolved SH experiments on LiNbO₃	159
B.1 Scaling the Reconstructed Potential	159
B.2 Phase-matching between the Probe Light and the Phonon-Polariton	160
B.3 Effect of Inter-Phonon Coupling of the Type $g_j Q_{\text{IR}}^2 Q_j$	160
B.4 Nonlinear Eigenfrequency Renormalization	161
B.5 Solution of Mathieu Equation and Exponential Scaling	163
B.6 Interaction Length in LiNbO ₃ SH Experiments	164
B.7 Finite-Differences Time Domain Simulations	166
B.8 Modelling Resonant Phonon Excitation	168
B.9 Interference Signal LiNbO ₃	170
B.10 DFT Calculations LiNbO ₃	170
Appendix C Time-resolved SH experiments on YBa₂Cu₃O_{6+δ}	173
C.1 Signal Dissection of the Time-Resolved SH Signal from YBa ₂ Cu ₃ O _{6+δ}	173
C.2 Momentum-Resolved Detection of the Josephson Plasmon Polariton	173
C.3 SH-Polarimetry Measurements for p-Analyzer	176
C.4 Excitation Frequency Dependence of the Josephson Plasmon Amplification . . .	176
C.5 Theoretical Analysis of the Josephson Plasmons and Plasmon-Phonon coupling .	179
C.5.1 Analysis of the Collective Modes	179
C.5.2 Phonon-Plasmon Interaction	183
C.6 DFT Calculations YBa ₂ Cu ₃ O _{6.5}	184

Introduction

Strongly Correlated Materials and Hidden Order

The electrical properties of semiconductors and metals, routinely used in technological devices of our daily lives, are well understood within classical band theory, neglecting the ubiquitous Coulomb repulsion between electrons [1]. This behavior arises from the fact that the electrons are delocalized and their kinetic energy is far larger than the electron-electron interaction.

However, in the recent decades a new class of solid state systems dubbed *strongly correlated materials* has gained a lot of attention, potentially paving the way for future electric devices. Fascinating phenomena found in these materials are insulator-metal transitions [2, 3], colossal magnetoresistance [4, 5] and high temperature superconductivity [6, 7]. Here, the electronic and magnetic properties are derived from the strong repulsive interaction among electrons which competes with their kinetic energy, magnetic degrees of freedom and constraints by the lattice structure [8, 9]. These interactions differ from uncorrelated materials in that they exhibit comparable energy scales and therefore give rise to competing low energy states. The energy differences between these states are often vanishingly small so that local quantum degrees of freedom associated with individual lattice site and even large scale fluctuations become relevant [1, 8, 9]. As a result, these materials react strongly to changes of external parameters which tip the fine energy balance of the competing states in favor of one competitor. In most cases, these transitions are accompanied by a breaking of local symmetries and the ordering of quantum degrees of freedom, which is essential for the emergence of macroscopic functional properties. Commonly used control knobs are chemical doping, pressure, temperature, magnetic fields or electrostatic gating in a field-effect geometry, for example turning an insulator into a metal [1–3, 10]. These types of material control were successfully employed to study the properties of different classes of strongly correlated materials and address the microscopic physics that determine their macroscopic properties [11, 12].

Transition metal oxides are a prominent example of strongly correlated materials. In these systems, oxygen ligands ionize the transition metal atoms, resulting in partially filled d-orbitals in the outermost shell. Their occupation and overlap with adjacent oxygen p-orbitals determine the electronic and magnetic properties of the material. For example, the competition between electron delocalization, determined by the orbital overlap, and the onsite Coulomb repulsion, cast within the Pauli principle for the orbital occupation, sets the electronic transport and the magnetic properties [13, 14].

The development of sources of ultrashort laser pulses, with typical pulse durations on the femtosecond scale [15, 16] made it possible to control the functional properties of strongly correlated materials on extremely short timescales. Time-resolved experiments revealed insulator-to-metal [8, 17], superconductor-to-normal state [18, 19], non-thermal melting [20–22] as well as magnetic transitions [23–25]. Importantly, these ultrafast phase transitions are different from any adiabatic counterpart and explore regions of the potential energy surface hidden to any equilibrium experiment [23, 26, 27].

These seminal experiments relied on femtosecond light pulses in the visible (\sim eV photon energy), which excite the electronic system and do not directly couple to the characteristic low-energy excitations (\sim 100 meV), the fundamental modes of the relevant structural (phonon), electronic (plasmon) and magnetic (magnon) degrees of freedom. The high-energy optical excitation, however, inadvertently heats up the electronic system, melting any preexisting broken symmetry and drives a transitions into a disordered state. Therefore, this type of excitation is inadequate to induce transitions between two low-energy broken-symmetry states and it remained an open question which type of excitation allows for the stabilization of a new long-range order without quenching the pre-existing one, i.e., the possibility to break symmetries by light.

The recent availability of ultra-short laser pulses in the relevant mid-infrared and THz region (1 meV to 100 meV) [29] allowed researchers to overcome this limitation through direct excitation of the characteristic low-energy degrees of freedom of strongly correlated materials. For example, resonant excitation of lattice vibrations was used to transiently manipulate the materials properties, exploiting the strong correlation between the electronic properties and the lattice structure. In contrast to optical excitation in the visible, the energy of the optical drive is directly transferred into a collective structural motion. This direct energy pathway, reducing dissipation through the electronic system, allows for the emergence of new low-energy collec-

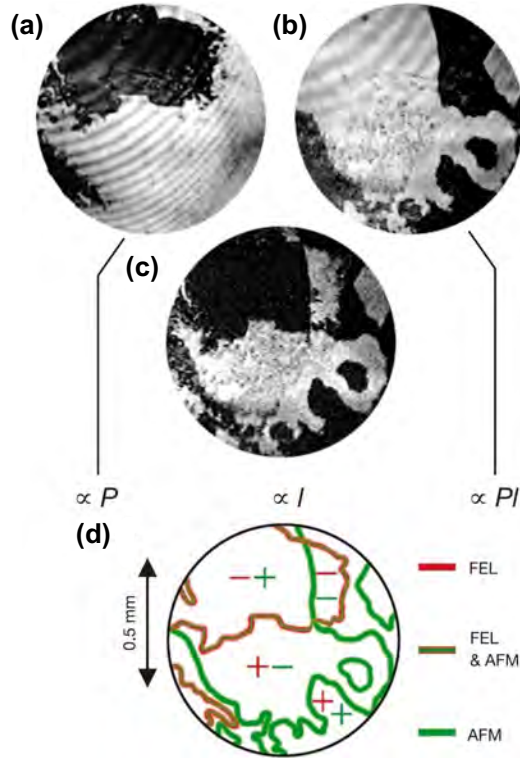


Figure 1: SH topography of hidden order. (a) Energy sensitive second harmonic topography can reveal hidden, coexisting electric and magnetic domains in materials like YMnO₃. Dark and bright areas correspond to opposite ferroelectric domains P and $-P$. (b) SH light with an energy sensitive to the magneto-electric ordering shows bright and dark regions which have an opposite sign of the product $M \times P$. (c) Interference of these two second harmonic contributions from P and $M \times P$ unveils the antiferromagnetic domains. (d) All this together prints a map of the topology of the ferroelectric (red) and AFM (green) domain walls, which would remain hidden with linear optical topography. Figure taken from Ref. [28]

tive properties. This approach proved to be successful, showing light-induced superconductivity [30–32], insulator-metal transitions [33, 34], melting of magnetic order [35, 36] and para-to-ferroelectric transitions [37, 38]. These experiments hold the promise of a deeper understanding of the microscopic mechanism relevant in strongly correlated system, by establishing a causal bridge between the direct resonant excitation of low energy collective modes and the emergence of unconventional material properties.

Most of these experiments relied on probing a linear optical response and have only just recently been augmented into the nonlinear regime, by not only ever stronger excitation pulses but also increasingly powerful and diverse optical probe pulses. These nonlinear optical probing schemes

reveal complementary information to their linear counterpart and have already been successfully established for the characterization of equilibrium states of matter [39–41]. Especially, optically silent collective excitations, such as pair-density waves and Higgs modes [41–44], remain hidden in linear spectroscopy but become optically active at higher probe-field strength. The generation of higher harmonics of the fundamental laser field can reveal the fundamental symmetry of an ordered phase as well as discern different types of broken symmetry. An impressive demonstration of the capabilities of nonlinear spectroscopy is the phase-sensitive topographic imaging of ferroic domains [28, 39, 45]. These areas of distinct values of the order parameter would be indiscernible in linear optical topography (see Fig. 1).

The aim of this thesis is to apply nonlinear optical probes in the time domain, extending the capabilities of the established linear time-resolved optical spectroscopy. Second harmonic generation of near-infrared femtosecond pulses in the probed materials was used to combine the exceptional time resolution of optical pump-probe experiments with the capability of measuring the dynamics of odd- and silent modes.

Two key experiments were conceived. The first experiment on the prototypical ferroelectric material LiNbO_3 attempted to reverse the ferroelectric polarization by resonant optical excitation of crystal lattice vibrations. Here, the ensuing lattice and polarization dynamics were traced by measuring the generated second harmonic intensity as a function of time after the excitation. The second experiment revisited earlier experiments on the high-temperature superconductor $\text{YBa}_2\text{Cu}_3\text{O}_{6+\delta}$, where to date light-induced superconductivity was probed by time-resolved linear THz spectroscopy. Here, time-resolved second harmonic generation was used to measure the coherent dynamics following the same excitation that was observed to induce transient superconductivity.

Reversal of the ferroelectric polarization

Their robust polarization states qualified ferroelectrics as promising materials for data storage applications in the form of FeRAM [46]. However, the switching speed between the two digital states '0' and '1', which are the two oppositely poled states, are limited by the nucleation and growth of ferroelectric domains as sketched in Figure 2 (a) [47, 48], posing a fundamental limitation to the development of future non-volatile storage devices and novel hetero-materials.

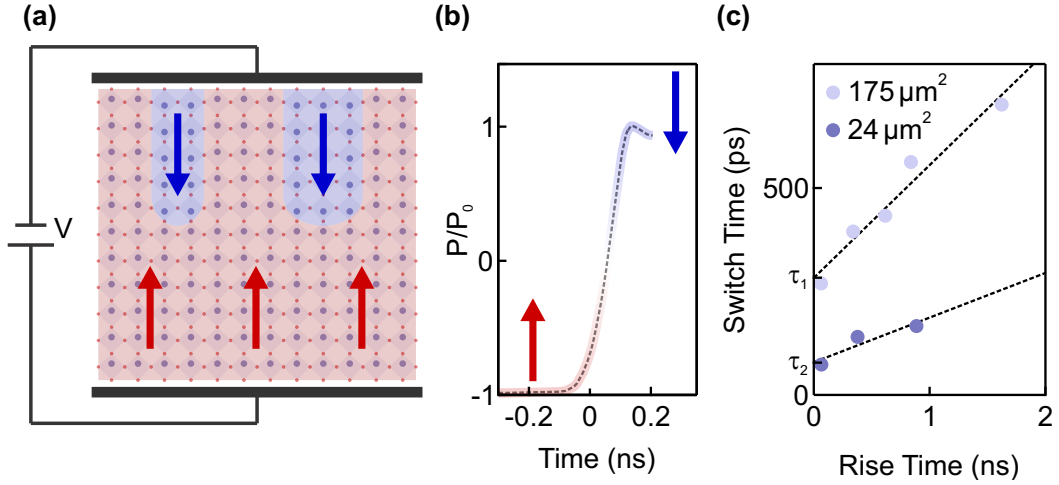


Figure 2: Switching of ferroelectric domains. (a) Ferroelectric switching typically involves the application of a voltage V between to electrodes. Depending on the polarity, ferroelectric domains of the opposite polarization (blue arrows) will start growing from one of the electrodes towards the other. (b) The switching time between two fully polarized states (red and blue) depends on the magnitude and rise time of the electric fields. The data shown was taken from Ref. [48]. (c) However, even in the limit of a vanishing rise time of the voltage pulse the switching time remains finite (τ_i). This fundamental limit is dependent on the geometry and size of the ferroelectric domain, as evidence for two different device sizes. The data shown was taken from Ref. [48].

One potential approach to overcome this fundamental limit is the direct excitation of the lattice modes responsible for the ferroelectric distortion. This would allow switching speeds, which are limited only by the intrinsic microscopic time scales of the crystalline lattice, typically in the picosecond range. Attempts to directly couple to ferroelectric distortion with picosecond THz pulses, however, were not successful [49–51].

An alternative route to ultrafast lattice control was demonstrated recently and involves the nonlinear coupling of individual phonon modes [52–54]. These *nonlinear phononics* were induced by the resonant excitation of an infrared active lattice mode through intense laser pulses in the mid-infrared. Theorized more than 40 years ago [55–57] as *ionic Raman scattering*, this type of control not only allows one to induce coherent oscillations, but also a directional displacement of the atoms along the coupled phonon modes. Thus, these nonlinear phononics rectify the oscillatory atomic motions of the driven mode and transiently change the crystal structure on average. Recent ultrafast x-ray diffraction experiments [54, 58] measured this rectification of the atomic motion directly in the time domain.

This powerful new toolset allows for the fs-control of the lattice structure and was just recently complemented with tools for their theoretical understanding (nonequilibrium Dynamical Mean Field Theory, time-dependent Density Matrix Renormalization Group or quantum Boltzmann equations) [59–61]. Ab-initio calculations of this type predicted that this nonlinear coupling allows for the control of the polarization state in ferroelectric materials and thus the ultra-fast reversal of the polarization [62, 63]. Here, a high frequency vibration is coupled to the ferroelectric distortion and exerts a unidirectional force towards the oppositely poled state, potentially leading to the ultrafast reversal of the ferroelectric polarization. This motivated the first experiment presented in this thesis, in which the atomic motions induced by strong (30 MV/cm) mid-infrared pulses in LiNbO₃ were measured with fs-time resolution second harmonic generation [64, 65]. In this experiment, we observed the strongly anharmonic motion of the driven mode itself and the cohering ultra-fast reversal of the ferroelectric polarization.

Light-induced superconductivity

Since their discovery in 1911, superconducting materials [66] have sparked significant research efforts towards a room-temperature lossless conductor. The discovery of high-temperature superconductivity in strongly correlated CuO₂-materials [6, 7] represented a big leap forward. Yet, unlike superconductors which can be described with the BCS theory [67], a microscopic understanding of these materials still eludes us and they remain puzzling not only in their superconducting state but also in their normal state. Especially, the understanding of the so-called *pseudogap phase*, which directly transforms into the superconducting phase at the critical temperature T_c , remains a challenge. This phase was suggested to arise from competing orders in the form of pair density waves, but could also be precursor state of superconductivity, where the CuO₂-planes are hypothesized to host preformed pairs above the critical temperature T_c [68–72].

In recent years, time-resolved optical experiments sought to control superconductivity on ultrafast timescales [30–32, 41, 73–75]. An intriguing approach to achieve this type of control is the resonant optical excitation of vibrations of the apical oxygen ions, which revealed transient behavior in compounds like YBa₂Cu₃O_{6+ δ} [30, 32] and La_{1.8– x} Eu_{0.2}Sr _{x} CuO₄ [31] compatible with that of a superconductor above the equilibrium T_c .

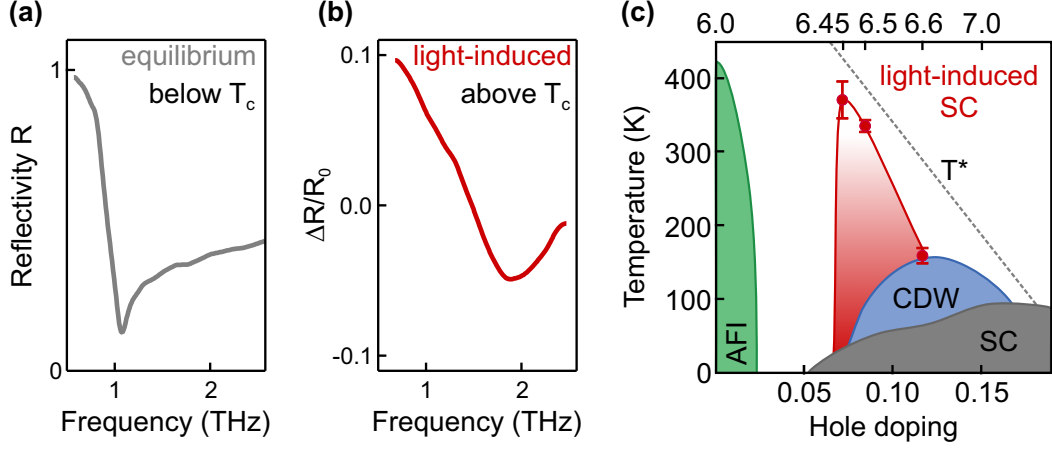


Figure 3: Light-induced superconductivity. (a) Equilibrium Josephson plasma edge in the THz-reflectivity R of the high- T_c superconductor $\text{YBa}_2\text{Cu}_3\text{O}_{6.5}$ below the critical temperature. (b) Light-induced plasma edge of the same compound after excitation of the apical oxygen vibration above the critical temperature. The plot shows the normalized reflectivity $\Delta R/R_0$. (c) Phase-diagram of the $\text{YBa}_2\text{Cu}_3\text{O}_{6+\delta}$ compounds displaying the equilibrium phases; antiferromagnetic Insulator (AFI, green), charge-density wave (CDW, blue), superconductor (grey) and the pseudogap transition temperature T^* . The red symbols denote the maximum temperature up to which the light induced superconductivity could be observed. The data was taken from Ref. [32] and panel (c) is adapted from Ref. [76].

In equilibrium, cuprate superconductors like $\text{YBa}_2\text{Cu}_3\text{O}_{6+\delta}$, superconductivity manifests as characteristic reflectivity edges as shown exemplary in Fig. 3 (a) for the case of $\text{YBa}_2\text{Cu}_3\text{O}_{6.5}$. These edges disappear above the critical temperature T_c . In the aforementioned experiments, optical driving of the apical oxygen vibration induced reappearance of this characteristic edge far above T_c (see Fig. 3 (b)). This light-induced superconductivity survived up to the transition temperature T^* of the enigmatic pseudogap-phase as is shown in the phase diagram of $\text{YBa}_2\text{Cu}_3\text{O}_{6+\delta}$ in Fig. 3 (c).

The experimental observation of light induced coherence in underdoped $\text{YBa}_2\text{Cu}_3\text{O}_{6+\delta}$ compounds above the transition temperature T_c suggests that a redistribution of interlayer Josephson coupling [30] may be the origin of the superconductor-like optical features in the transient THz reflectivity. In contrast, the single layer Cuprate $\text{La}_{1.8-x}\text{Eu}_{0.2}\text{Sr}_x\text{CuO}_4$, experiences a more direct competition between the superconducting phase and a stripe ordered phase that suppresses equilibrium superconductivity. It has been suggested that the direct lattice excitation melts and removes the striped order restoring the superconducting state [31]. More recently these experiments have been corroborated by strong-field THz third harmonic generation, which

enabled the detection of optically silent pair density waves, Higgs oscillations and a precursor superconducting state in $\text{YBa}_2\text{Cu}_3\text{O}_{6+\delta}$ [32, 41, 42].

In this thesis work, the above experiments on underdoped $\text{YBa}_2\text{Cu}_3\text{O}_{6+\delta}$ were revisited by time-resolved second harmonic generation experiments, with the goal of a deeper understanding of the origin of this light induced coherence. In this experiment we observed a 2.5-THz electronic mode, which exhibits a unique symmetry, momentum, and temperature dependence.

Thesis Structure

This thesis is structured as follows. An introduction to linear and nonlinear optics and their application to time-resolved optical experiments is presented in Chapter 1. The experiments on LiNbO_3 , in which the ultra-fast reversal of the ferroelectric polarization and the reconstruction of the interatomic potential lattice response are demonstrated, are covered in Chapter 2. Chapter 3 introduces the physics of high temperature superconductors of the cuprate family. The measurements of the nonlinear phonon-Josephson-plasmon coupling are covered in Chapter 4, followed by a conclusion of this thesis.

Chapter 1

Linear and Nonlinear Optical Properties of Solids

The propagation of electromagnetic waves in a medium is described by the inhomogeneous wave equation,

$$\left(c^2 \nabla^2 - \frac{\partial^2}{\partial t^2}\right) \mathbf{E} = \frac{1}{\epsilon_0} \frac{\partial^2 \mathbf{P}}{\partial t^2}. \quad (1.1)$$

Here, c is the vacuum speed of light, ϵ_0 the permittivity of vacuum and \mathbf{E} is the electric field component of the electromagnetic wave [77]. As opposed to propagation in vacuum, the interaction of the electric field \mathbf{E} with the medium creates a polarization \mathbf{P} which is due to the presence of the electric field \mathbf{E} itself along with the polar excitations \mathbf{Q}_i of the material. The motion of these polar excitations creates a dipole which can conversely directly couple to the electric field of light and influence its propagation. Therefore, the total polarization inside the material can be expanded in powers of these fields

$$\mathbf{P}(t) = \epsilon_0 \left[\chi^{(1)} \mathbf{E} + Z^* \mathbf{Q}_{\text{IR}} + \chi^{(2)} \mathbf{E}^2 + \frac{\partial \chi^{(1)}}{\partial Q_{\text{R}}} \mathbf{Q}_{\text{R}} \mathbf{E} + \chi^{(3)} \mathbf{E}^3 + \frac{\partial \chi^{(2)}}{\partial Q_{\text{IR}}} \mathbf{Q}_{\text{IR}} \mathbf{E}^2 + \dots \right] \quad (1.2)$$

The susceptibilities $\chi^{(i)}$ are generally due to the electronic system under the assumption that the light frequency is significantly below the electronic transitions. These terms are responsible for the nonlinear optical effects [78]. The additional terms describe the interaction of the light field with the polar excitations of the solid [79–82]. Z^* is the effective charge of the polar vibration \mathbf{Q}_{IR} , $\partial \chi^{(1)} / \partial Q_{\text{R}}$ is the change of the first order susceptibility induced by vibrations of Q_j , responsible for Raman scattering and $\partial \chi^{(2)} / \partial Q_{\text{IR}}$ is the modulation of the hyper-polarizability $\chi^{(2)}$ by an infrared-active vibration. The following paragraphs will discuss the analytical solutions of the linear and nonlinear optical response of a solid. This lays the foundation for

implementing an ultra-fast nonlinear probe to reveal coherent dynamics of polar excitations, such as infrared-active phonons and plasmons. The discussion will focus on the topic of second harmonic generation and presents the equations which are necessary for analyzing time-resolved optical experiments.

1.1 Linear Optical Properties

1.1.1 Dielectric Function

The first order optical response of a solid concerns terms in the polarization \mathbf{P} which are linear with the electric field. In the following text, the basics of a linear light-matter interaction will be summarized for the case of one spatial dimension.

The linear propagation of light at frequencies below the electronic transitions but still above those of the low energy polar excitations is determined by the linear susceptibility $\chi^{(1)} = 1 + \varepsilon_\infty$ [77, 78, 83]. Here ε_∞ is the material-specific dielectric response of the high-energy electronic transitions and 1 is the dielectric response of the vacuum. When the frequency of the light approaches the energy of the polar excitations Q_{IR} , additional features appear in the reflectivity spectrum. Under this resonant condition, the electric field E directly couples to the dipole moment of the excitation and its dynamic response is described by a driven damped harmonic oscillator,

$$\ddot{Q}_{\text{IR}} + 2\gamma_{\text{IR}}\dot{Q}_{\text{IR}} + \omega_{\text{IR}}^2 Q_{\text{IR}} = \frac{Z_{\text{IR}}^*}{\mu} E \quad (1.3)$$

Here Z_{IR}^* is the effective charge and μ the effective mass of the atoms involved in the polar vibration [78, 83]. The term γ_{IR} accounts for dissipative energy flow into other degrees of freedom. This results from anharmonic coupling between individual elementary excitations, as discussed in Chapter 2. $\omega_{\text{IR}} = 2\pi\nu_{\text{IR}}$ is the angular frequency of the excitation, the energy of which is given $E_{\text{IR}} = h\nu_{\text{IR}}$, where h is Planck's constant. Usually, for excitation such as lattice vibrations and plasmons, E_{IR} is on the order of 1 meV to 100 meV which corresponds to the mid-infrared spectral region [9, 84]. Mid-infrared wavelengths are four orders of magnitude larger than the lattice constant a_0 , and the corresponding wave vectors given by $|\mathbf{k}| = 2\pi/\lambda$ are thus negligible compared to the wave vectors of lattice vibrations ($0 \leq |\mathbf{k}| \leq \pi/a_0$). As a result, momentum conservation allows only polar optical modes at $|\mathbf{k}| \approx 0$ to be directly excited by

light.

The solution of the equation of motion (eq. 1.3), when subject to a monochromatic drive field $E(t) = E_0 e^{i\omega t}$, reveals the frequency dependent optical response. As an Ansatz, the solution takes the form $Q_{\text{IR}}(t) = Q_{\text{IR},0} e^{i\omega t}$ [77, 78] and when substituted into eq. 1.3 it yields the steady-state amplitude of the polar vibration as a function of excitation frequency ω ,

$$Q_{\text{IR}}(\omega) = \frac{Z_{\text{IR}}^*/\mu}{\omega_{\text{IR}}^2 - \omega^2 - i\gamma_{\text{IR}}\omega} E_0. \quad (1.4)$$

The polar vibrations driven by the electric field E then creates a polarization $P = NZ^*Q_{\text{IR}}$, where N is the number of oscillators per unit volume. Inserting eq. 1.4 into this expression yields the frequency dependent complex polarization of the material:

$$P_{\text{IR}}(\omega) = NZ_{\text{IR}}^*Q_{\text{IR}} = \frac{NZ_{\text{IR}}^{*2}}{\mu} \frac{1}{\omega_{\text{IR}}^2 - \omega^2 - i\gamma_{\text{IR}}\omega} E, \quad (1.5)$$

which can be incorporated into the wave equation eq. 1.1. Here, NZ_{IR}^{*2}/μ is commonly referred to as the oscillator strength. The resonant denominator in the expression for $P_{\text{IR}}(\omega)$ indicates that when the oscillator is driven at Ω_{TO} , the so-called *transverse optical frequency*, it will reach the highest amplitude for a given electric field strength E . The auxiliary *electric displacement field* $D = \epsilon_0 E + P$ is given by,

$$D = \epsilon_0 E + P = \epsilon_0 \epsilon_r(\omega) E \quad (1.6)$$

where ϵ_r is the frequency-dependent relative permittivity. At frequencies near ω_{IR} the complex refractive index

$$\tilde{n}(\omega) = \sqrt{\epsilon_r(\omega)} = n(\omega) + i\kappa(\omega). \quad (1.7)$$

disperses significantly (see Fig. 1.1). The real part of the refractive index determines the phase velocity $v_{ph}(\omega) = c/n(\omega)$ of a propagating light field, where c is the speed of light in vacuum, while the imaginary part determines the attenuation of the light field inside the material. These resulting optical features can be understood by considering the frequency dependence of the reflectivity (see Fig. 1.1 (c)), which is given by

$$R = \left| \frac{1 - \tilde{n}(\omega)}{1 + \tilde{n}(\omega)} \right|^2. \quad (1.8)$$

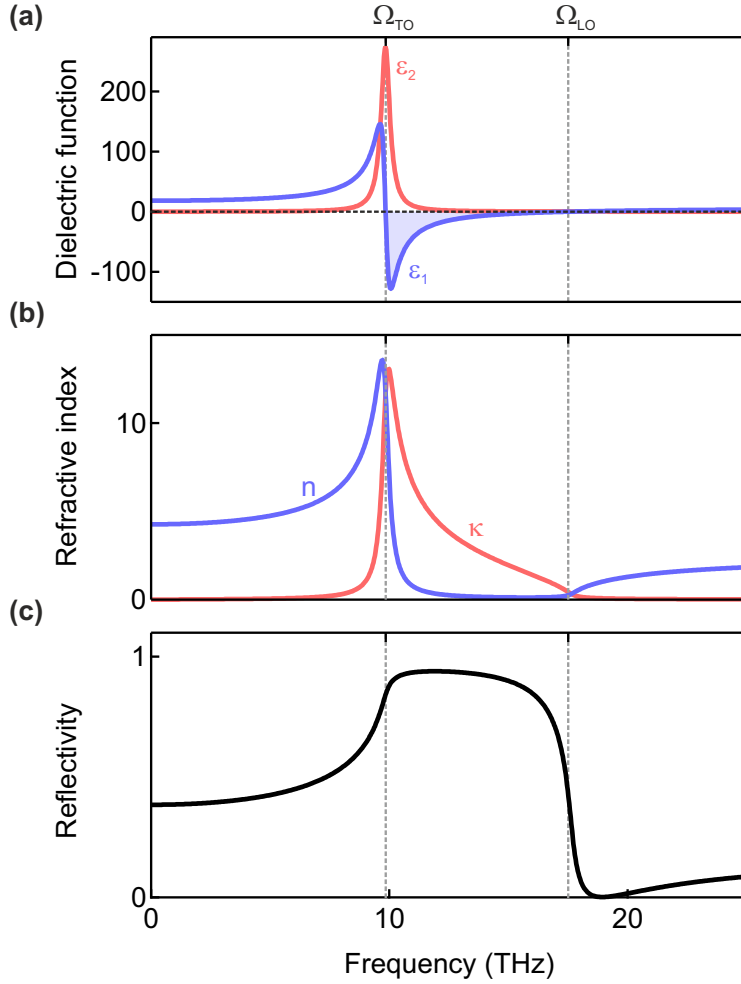


Figure 1.1: Optical properties of a charged oscillator. (a) Dielectric function of a charged oscillator. At the transverse optical frequency Ω_{TO} the real (blue) and imaginary (red) part of the dielectric function of a charged oscillator strongly disperse and peak, respectively. The real part crosses zero at the longitudinal frequency Ω_{LO} . (b) Refractive index of a charged oscillator. The real (blue) and imaginary (red) part of the refractive index strongly disperse close to Ω_{TO} . Above Ω_{TO} and below Ω_{LO} the real part of the refractive index is almost zero, whereas the imaginary part takes a large positive value, signifying strong attenuation. (c) Reflectivity profile of a charged oscillator. The reflectivity profile (black) of a single charged oscillator shows a region of almost perfect reflectivity ($R \approx 1$), the *Reststrahlenband* [85], between Ω_{TO} and Ω_{LO} .

Above the resonance frequency Ω_{TO} the real part of the complex permittivity $\varepsilon_r(\omega)$ becomes negative (see Fig. 1.1 (b)), which leads to a π phase shift between the driving field E and the polarization induced by the oscillator. The resulting destructive interference screens the electric field and prevents further propagation inside the solid. This manifests itself in the reflectivity spectrum as a band of high reflectance (see Fig. 1.1 (c)) together with an almost vanishing real part of the refractive index. The real part of $\varepsilon_r(\omega)$ crosses zero at the so called *longitudinal frequency* $\varepsilon_r(\Omega_{\text{LO}}) = 0$, above which light can again propagate in the solid, corresponding to a reduction in the reflectivity. The precise point of the zero crossing is determined by the oscillator strength $\Omega_{\text{LO}}^2 - \Omega_{\text{TO}}^2 = NZ_{\text{IR}}^{*2}/\mu$. Additionally, the wavelength of light inside the medium diverges at Ω_{LO}

$$\lambda_{\text{medium}} = \lambda_{\text{vac}}/n(\omega). \quad (1.9)$$

This results in a spatial profile of the excitation which corresponds to a longitudinal wave at zero momentum (see Fig. 1.2), hence longitudinal frequency.

The imaginary part of the permittivity is associated with the attenuation of the propagating light field. If $\varepsilon_2 = \text{Im}(\varepsilon_r)$ is non-zero, the light field will transfer energy into the solid by exciting persistent oscillations of the polar-mode. In the absence of damping, the excitation will continue to oscillate even after the electric field is gone. If $\varepsilon_2(\omega) = 0$, the light will displace the polar oscillation only as long as the electric field is present and no energy loss takes place. The imaginary part $\varepsilon_2(\omega)$ takes the shape of a Lorentzian with peak frequency of Ω_{TO} and a width determined by the phenomenological damping constant γ_{IR} from eq. 1.3 (see Fig. 1.1 (a)).

Reflectivity spectra, such as the one shown in Fig. 1.1 (c), are usually measured with a broadband light source in combination with a Fourier-transform infrared spectrometer (FT-IR)[86]. The resulting curve can be fit using the model presented above, and quantitative information such as the complex frequency-dependent refractive index $\tilde{n}(\omega) = \sqrt{\varepsilon_r(\omega)}$ can be extracted. The following paragraphs give an introductory description of two prominent infrared-active excitations in solids will be introduced, namely, oscillations of the crystal lattice, which are known as phonons, and oscillations of the free electron density, known as plasmons.

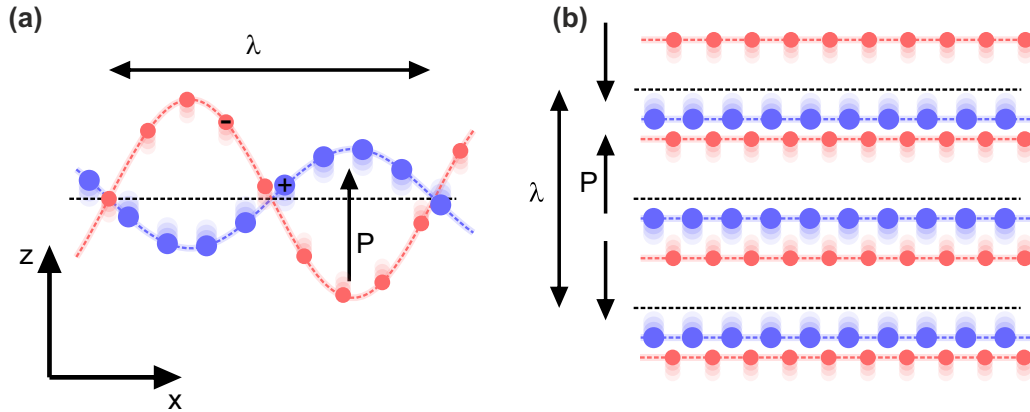


Figure 1.2: Charged transverse and longitudinal oscillations. (a) Schematic of a transverse optical vibration. An optical phonon is the relative motion of two charged atoms (blue and red). When this vibration carries an electric dipole moment P (black arrow) it is known to be 'infrared-active'. For infrared active phonons, the wavelength λ is given by the wavelength of the light pulse which excites the oscillation. (b) Schematic of a longitudinal optical vibration. A longitudinal oscillation is characterized by a propagation direction parallel to the polarization vector P . The motion can be understood as the relative motion of charged plates like a capacitor.

1.1.2 Phonons

Vibrations of the crystal lattice result in low energy excitations that can have energies up to 240 meV (60 THz) [9, 84]. The elementary quanta of these excitations are called *phonons*, and the classical normal modes of the lattice vibrations are often also called by the same name. Optically active phonons involve out-of-phase motion of the ions of the crystal. This is depicted in Fig. 1.2 for the relative motion of positively and negatively charged ions. If this vibration carries an electric dipole it can directly couple to the electric field of light, as expressed in eq. 1.3. Hence, these *infrared-active* lattice vibrations are visible in linear optical infrared spectroscopy, like FT-IR spectroscopy. Each ion carries a certain mass and charge, which determine the resonance frequency Ω_{TO} and the effective charge Z^* associated with the vibration. If the atomic vibration does not carry a dipole moment it is considered to be *Raman* active [79]. These modes do not directly couple to light and are only visible through nonlinear light scattering (see below).

The lattice vibrations of a solid can be divided into a set of eigenmodes which are precisely determined by the point group symmetry of the crystal. Each eigenmode can be categorized as one of the following irreducible representations [86–88],

A,B: 1D representation, symmetric and anti-symmetric under rotation, respectively

E: 2D representation

T: 3D representation

These irreducible representations can each be divided into sub-groups using a set of indices, of which the following are the most important

1 and 2: symmetric or anti-symmetric to mirroring along the principle axis of the pointgroup

g and u: symmetric or anti-symmetric to inversion

In a centrosymmetric point group, the distinction between g (gerade, even) and u (ungerade, odd) modes, under the operation of inversion, generally distinguishes between infrared active (ungerade) and Raman active (gerade) modes. A total list of the symmetry operations of each irreducible representation can be found in the character tables of the corresponding point group [89].

1.1.3 Plasmons

The collective excitation of the free electrons in a solid by an electric field results in plasma oscillations, which are modulations of the free electron density [90]. In contrast to lattice vibrations, plasma oscillations are longitudinal waves, i.e., their propagation direction is parallel to the polarization (see Fig. 1.2 (b)) and they resonate at the plasma frequency Ω_p . The corresponding quantum is called a *plasmon*. Similar to lattice vibrations, the dynamics of the plasma can be described by eq.1.3 by neglecting the term $\omega_{IR}^2 Q_{IR}$ due to the lack of a restoring force for the free electrons.

$$\ddot{Q}_p + 2\gamma_p \dot{Q}_p = \frac{e}{m_e} E \quad (1.10)$$

Consequently, the amplitude response as a function of excitation frequency becomes

$$Q_p(\omega) = \frac{-e/m_e}{\omega^2 + i\gamma_{IR}\omega} E_0 \quad (1.11)$$

resulting in the same optical properties as discussed above, but with $\Omega_{TO} = 0$ and $\Omega_{LO} = \Omega_p$. The oscillatory motion of the plasma does not directly become apparent from eq.1.10, but it can be rewritten to

$$\ddot{Q}_p + 2\gamma_p \dot{Q}_p + \omega_p^2 Q_p = 0, \quad (1.12)$$

by considering Fig. 1.2 (b) and the relation between the electric field and the accumulated charges $E = -e\rho/\epsilon_0 Q_p$ and $\omega_p^2 = e^2\rho/m_e\epsilon_0$. Here, ρ is the electron density. Therefore, an electric field induces a self-sustained longitudinal plasma oscillation with resonance frequency Ω_p . At frequencies away from the plasma resonance at Ω_p , the plasma oscillations will mostly have transverse character because the electrons will follow the electric field of the light, as explained in the following paragraph.

1.1.4 Polaritons

The interaction of the polar excitations, described in the preceding paragraphs, with light gives rise to hybrid states called polaritons. A descriptive way of thinking about this hybridization is to imagine a propagating electric field in a medium. At every point during its propagation this field will couple to the polar resonance and excite oscillations. In turn, this polar oscillation will re-emit light, which also propagates into the material, re-exciting polar oscillations. Such strong coupling appears when the dispersion relations of the light and the excitation intersect, i.e., their energies and momenta match (see Fig. 1.3, dashed lines). The corresponding polariton dispersion can then be inferred from the dispersion of light

$$\omega^2 = c^2 k^2 / \epsilon_r(\omega) \quad (1.13)$$

together with the dielectric function $\epsilon_r(\omega)$ derived above [91, 92]. For a simple harmonic oscillator model discussed above, it becomes

$$\omega^2(k) = \frac{\Omega_{\text{TO}}^2 \epsilon_0 + c^2 k^2}{2\epsilon_\infty} \pm \frac{1}{\epsilon_\infty} \sqrt{\left(\frac{\Omega_{\text{TO}}^2 \epsilon_0 + c^2 k^2}{2}\right)^2 - c^2 k^2 \Omega_{\text{TO}}^2 \epsilon_\infty}, \quad (1.14)$$

with $\epsilon_0 = \epsilon_\infty + NZ_{\text{TO}}^{*2}/\epsilon_0\mu\Omega_{\text{TO}}^2$, the low frequency ($\omega \rightarrow 0$) limit of the dielectric function. The real part of this expression is shown in Figure 1.3 (solid line). Below the TO frequency, the polariton propagates with a velocity defined by the slope of the dispersion curve $\partial\omega/\partial k$, but it becomes a stationary solution with a flat dispersion close to Ω_{TO} . At the longitudinal frequency Ω_{LO} , the momentum of the polariton wave is zero and the wave resembles a longitudinal excitation. No solution exists in the Reststrahlenband between Ω_{TO} and Ω_{LO} . Above the LO frequency the polariton dispersion rapidly approaches the dispersion of light given by $\omega = ck/\sqrt{\epsilon_\infty}$. Here, the solutions are again ‘photon-like’ and purely transverse.

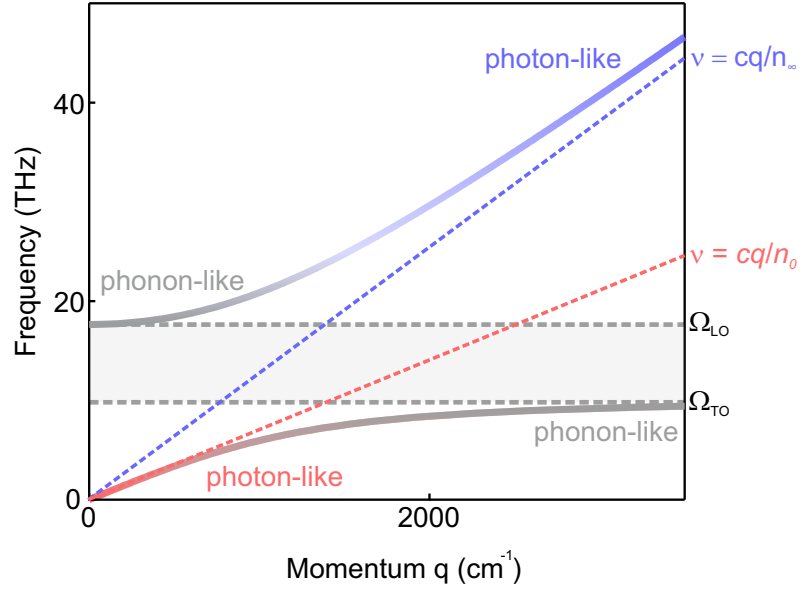


Figure 1.3: Dispersion of a phonon-polariton. The interaction of light with a charged oscillator in a material gives rise to hybrid states, so-called *polaritons*. The dispersion is a result of an avoided crossing between the phonon (dashed grey line) and light (dashed blue and red lines) dispersion. Below Ω_{TO} the polariton is mostly photon-like and the dispersion is equal to that of light (dashed red line). Close to Ω_{TO} the polariton becomes phonon-like and the dispersion asymptotically approaches Ω_{TO} , leading to a vanishing group velocity and a stationary lattice vibration. At Ω_{LO} the phonon polariton has zero momentum and therefore infinite wavelength giving rise to a longitudinal lattice vibration. Above Ω_{LO} the dispersion again approaches the dispersion of light (dashed blue line) and the polariton is again photon-like.

This discussion can be extended to plasmons by considering the case discussed above the the limit of $\Omega_{\text{TO}} \rightarrow 0$ and $\Omega_{\text{LO}} = \Omega_{\text{p}}$. Away from the plasma-resonance plasmon-polaritons rapidly become ‘photon-like’ and the plasmon loses its longitudinal character.

1.2 Nonlinear Optics

The linear interaction of light with matter as summarized in the preceding paragraphs is only one part of the optical toolbox. Higher order terms of the nonlinear polarization in eq. 1.2, which include the product of two or more electric fields, can reveal fundamental excitations and dynamics in solids invisible to linear optics. The most relevant nonlinear interactions for the scope of this thesis will be defined in the following paragraphs.

1.2.1 Raman-Scattering

The first non-linear term involving more than one field in the polarization P is the modulation of the $\chi^{(1)}$ by Raman active excitations Q_R . As noted, these modes do not carry an electric dipole and thus cannot couple to light directly, making them they are invisible to linear infrared spectroscopy [79]. However, the motion of these Raman modes modulates the electronic polarizability α of the material and therefore the electronic susceptibility ($\chi_e^{(1)} = \varepsilon_\infty - 1$). To first order the change of the electronic susceptibility can be approximated as

$$\chi_e^{(1)}(t) = \chi_{e,0}^{(1)} + \left(\frac{\partial \chi_e^{(1)}}{\partial Q_R} \right) Q_R(t) + \dots \quad (1.15)$$

which yields the contribution

$$P_R(t) = \left(\frac{\partial \chi_e^{(1)}}{\partial Q_R} \right) Q_R(t) E(t) \quad (1.16)$$

to the polarization inside the material [79, 93]. If the motion of the Raman mode $Q_R(t)$ is considered to be harmonic with frequency Ω_R (see eq. 1.3), then the term $P_R(t)$ acts as a source of radiation at frequencies $\nu_{in} \pm \Omega_R$,

$$Q_R(t) E(t) \propto \sin(2\pi\Omega_R t) \sin(2\pi\nu_{in} t) = \frac{1}{2} (\cos(2\pi(\Omega_R - \nu_{in})t) - \cos(2\pi(\Omega_R + \nu_{in})t)) \quad (1.17)$$

Hence, a Raman mode leads to an inelastic frequency shift of the incoming light field. These processes are sketched in Fig. 1.4 (a) in an energy diagram as *Stokes-scattering* ($\nu_{in} - \Omega_R$) and *Anti-Stokes scattering* ($\nu_{in} + \Omega_R$). In continuous-wave Raman-scattering experiments, a monochromatic laser is used to obtain a spectrum sketched in Fig. 1.4 (b), which identifies

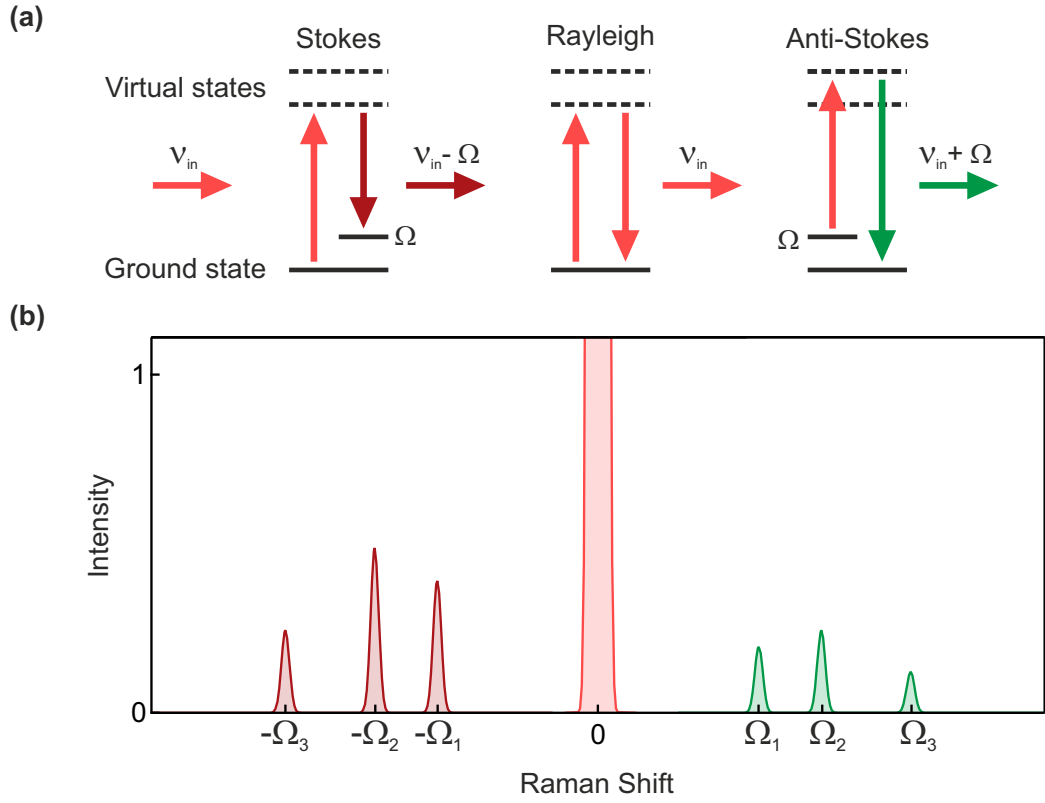


Figure 1.4: Raman scattering. (a) An incident light field of frequency ν_{in} (light red) excites the system from the ground state into a virtual electronic state. Upon relaxation, the system emits a photon at frequency $\nu_{in} - \Omega$ (dark red) and remains in a vibrationally excited state. This scattering process is called Stokes-Raman scattering. The inverse-process in which an incident photon absorbs a phonon and the system emits a photon at $\nu_{in} + \Omega$ (green) is called Anti-Stokes-Raman scattering. Additionally, the incident light will also cause an elastic scattering process, which does not involve scattering from vibrational modes. This is known as Rayleigh scattering. (b) An example of a light scattering spectrum resulting from Stokes, Anti-Stokes and Rayleigh scattering.

Raman active modes as frequency shifted peaks. The polarization dependent detection of the inelastically scattered light allows one to assign each Raman mode to a certain symmetry determined by the point group of the crystal [94].

1.2.2 Second Order Optical Susceptibility

The second expansion term of the electronic susceptibility, $\chi^{(2)}$, involves the interaction of two electric fields E_{ω_1} and E_{ω_2} . This type of nonlinear interaction (and any other quadratic expansion term) is only allowed in materials which have broken *inversion symmetry* [78]. This becomes obvious when considering the potential energy of the electrons in the solid. If a material

possesses inversion symmetry the motion of the electrons for positive and negative deflection x must be symmetric $U(x) = U(-x)$. This excludes odd order terms from the potential energy surface and consequently leads to only odd harmonics in the spectrum of the motion (see chapter 2 for more details). If two light fields E_{ω_1} and E_{ω_2} interact in a solid material which exhibits a second order nonlinearity $\chi^{(2)}$ they will generate a light field E_{ω_3} at a third, different, frequency ω_3 . For two monochromatic plane waves

$$E_{\omega_i}(x, t) = E_{\omega_i,0} e^{i(k_i x - \omega_i t)} + c.c. \quad (1.18)$$

and if dissipation can be neglected, the second order polarization $P^{(2)}$ becomes

$$P_{\omega_3}^{(2)}(x, t) = \chi^{(2)}(\omega_3, \omega_1, \omega_2) E_{\omega_1}(x, t) E_{\omega_2}(x, t). \quad (1.19)$$

which represents a source for radiation at frequencies $\omega_3 = \omega_1 \pm \omega_2$ (see Fig. 1.5). This becomes apparent from inserting the expression for the fields E_{ω_i} into $P^{(2)}$

$$P_{\omega_3}^{(2)}(x, t) = \chi^{(2)}(\omega_3, \omega_1, \omega_2) \left(E_{\omega_1,0} e^{i(k_1 x - \omega_1 t)} + c.c. \right) \left(E_{\omega_2,0} e^{i(k_2 x - \omega_2 t)} + c.c. \right) \quad (1.20)$$

$$\begin{aligned} P_{\omega_3}^{(2)}(x, t) = \chi^{(2)}(\omega_3, \omega_1, \omega_2) & \left(E_{\omega_1,0} E_{\omega_2,0} e^{i((k_1+k_2)x - (\omega_1+\omega_2)t)} + c.c. \right) \\ & + \left(E_{\omega_1,0} E_{\omega_2,0}^* e^{i((k_1-k_2)x - (\omega_1-\omega_2)t)} + c.c. \right) \end{aligned} \quad (1.21)$$

$$P_{\omega_3}^{(2)}(x, t) = P_{\omega_1+\omega_2}^{(2)}(x, t) + P_{\omega_1-\omega_2}^{(2)}(x, t) \quad (1.22)$$

This nonlinear polarization leads to the emission of an electric field of the form,

$$E_{\omega_3}(x, t) = E_{\omega_3,0} e^{i(k_3 x - \omega_3 t)} + c.c.. \quad (1.23)$$

Also, the momentum k_i of each wave in the solid is determined by the corresponding refractive index $n(\omega_i)$,

$$k_i = \frac{n(\omega_i) \omega_i}{c} \quad (1.24)$$

and thus, generally different for each light field. If eq.1.23 and the sum frequency component

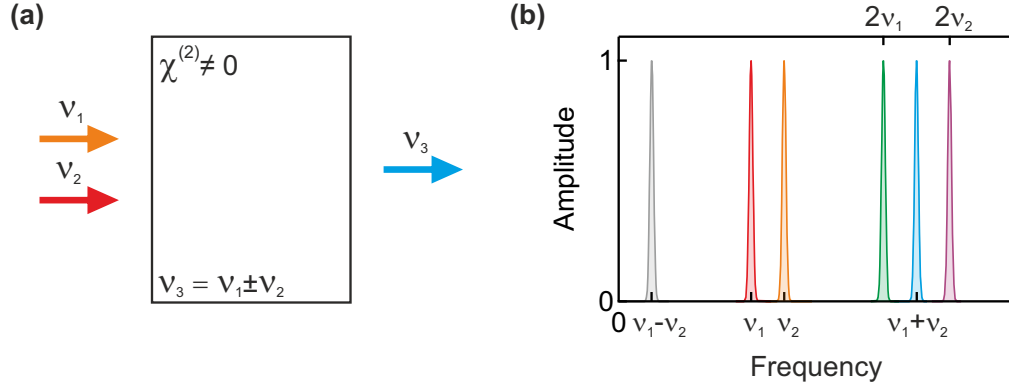


Figure 1.5: Second order nonlinear processes. (a) Two laser fields of frequency ν_1 and ν_2 (orange and red) interact in a material with a non-zero second order optical susceptibility $\chi^{(2)}$ and generate a new light field at frequency $\nu_3 = \nu_1 + \nu_2$ (blue). (b) Schematic spectrum of light produced by a second order non-linearity. The interaction leads to the processes of difference (grey peak) and sum (blue peak) frequency generation. When the two fields are degenerate, second harmonic generation (violet and green peaks) is produced.

of eq.1.22 are now inserted into the wave equation eq.1.1, they describe the spatial evolution of the field $E_{\omega_3}(x, t)$. After some simplification [78] the spatial evolution of E_{ω_3} is described by,

$$\left(\frac{d^2 E_{\omega_3}}{dx^2} + 2ik_3 \frac{dE_{\omega_3}}{dx} \right) = \frac{\chi^{(2)} \omega_3^2}{c^2} E_{\omega_1} E_{\omega_2} e^{i(k_1 + k_2 - k_3)x}. \quad (1.25)$$

Here, the first term on the left-hand side ($d^2 E_{\omega_3}/dx^2$) is significantly smaller than the second ($\sim dE_{\omega_3}/dx$) and can be neglected, which is known as the *slowly varying amplitude approximation* [78]. The spatial evolution is then finally given by,

$$\frac{dE_{\omega_3}}{dx} = i \frac{\chi^{(2)} \omega_3^2}{2c^2 k_3} E_{\omega_1} E_{\omega_2} e^{i\Delta k x}. \quad (1.26)$$

Here $\Delta k = k_1 + k_2 - k_3$ is often referred to as *momentum mismatch* [78, 95] between the two source fields E_{ω_1} and E_{ω_2} and the nonlinearly generated field E_{ω_3} . It relates the phase of the nonlinear polarization and the generated field E_{ω_3} and within the distance $l_{coh} = 1/\Delta k$ the radiation emitted by the nonlinear dipoles add up constructively in the forward direction. The conversion efficiency will drastically decrease for propagation distances $z > l_{coh}$, due to destructive interference of the nonlinear dipoles (see Fig. 1.6) [78, 95].

In the case of phase matching, $\Delta k = 0$, the coherence lengths becomes infinite and maximum conversion efficiency is obtained. This is routinely possible in birefringent crystals where the

refractive index depends on the polarization of the incident light field (see Fig. 1.6 (d)). Careful adjustment of the crystal angles and light polarization can allow for $\Delta k = 0$ (see Appendix A.6). Phase matching is of high importance for efficient light conversion in processes such as *optical parametric amplification*, *difference frequency generation* (see Appendix A.3) and *second harmonic generation*, which will be discussed next.

1.2.3 Second Harmonic Generation

Second harmonic generation is a special case of the nonlinear interaction of two fields discussed above. Here, a single light field E_{ω_1} interacts with itself, which creates a nonlinear polarization

$$P_{2\omega_1}^{(2)}(t) = \chi^{(2)}(2\omega_1, \omega_1, \omega_1) E_1^2(\omega_1) \quad (1.27)$$

at twice the frequency of the incident field. This interaction is equivalently explained by eq.1.26 but instead of three fields, the derivation is limited to only two fields E_{ω} and $E_{2\omega}$. The spatial evolution of the fundamental and second harmonic field amplitudes is then described by:

$$\frac{dE_{\omega}}{dx} = i \frac{\chi^{(2)} \omega^2}{2c^2 k_{\omega}} E_{2\omega} E_{\omega}^* e^{-i\Delta k x} \quad (1.28)$$

$$\frac{dE_{2\omega}}{dx} = i \frac{\chi^{(2)} 2\omega^2}{2c^2 k_{2\omega}} E_{\omega}^2 e^{i\Delta k x}. \quad (1.29)$$

where $\Delta k = 2k_{\omega} - k_{2\omega}$. Neglecting depletion of the pump field E_{ω} and dissipation, the solution of $E_{2\omega}$ is given by the integral of eq. 1.29 from 0 to depth L ,

$$E_{2\omega} = i \chi^{(2)} (2\omega)^2 / (2c^2 k_{2\omega}) E_{\omega}^2 \int_0^L e^{i\Delta k x} dx. \quad (1.30)$$

The intensity of the second harmonic field at the end of the nonlinear crystal is then given by the time-averaged Poynting vector $I = 2n\epsilon_0 c |E_{\omega}|^2$ [77],

$$I_{2\omega} = \frac{\chi^{(2)^2} (2\omega)^2}{n_{\omega}^2 n_{2\omega} c^2} L^2 I_{\omega}^2 \text{sinc}^2(\Delta k L / 2), \quad (1.31)$$

which is an oscillatory function with period $1/\Delta k = l_{\text{coh}} = \lambda_{\omega} / (2(n_{2\omega} - n_{\omega}))$. This is again due to the phase mismatch of the waves at ω and 2ω . Importantly, at each point L in the crystal two

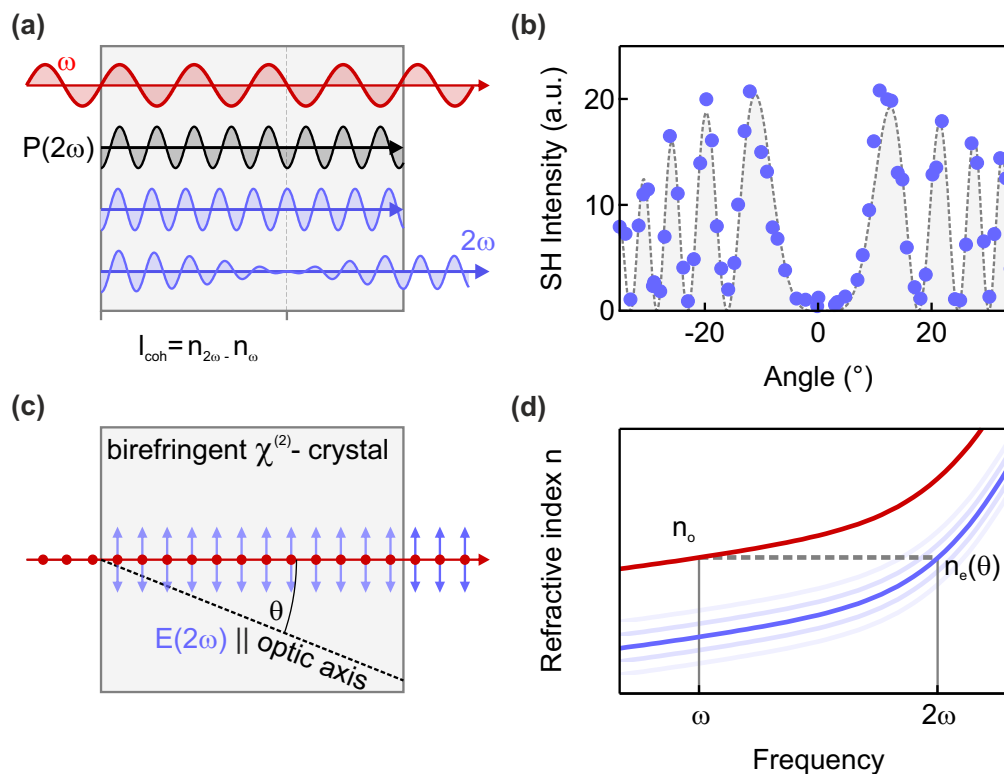


Figure 1.6: Second harmonic generation and phase-matching. (a) Sketch of the second harmonic generation process. A field at frequency ω (red) generates a polarization at 2ω (black). The phase of this polarization propagates at the phase velocity of the fundamental field, $v(\omega) = c/n_\omega$. The polarization radiates and generates a field at the second harmonic frequency (blue), which propagates with its own phase velocity, $v(2\omega) = c/n_{2\omega}$. After one coherence length $l_{\text{coh}} = \lambda_\omega/2(n_{2\omega} - n_\omega)$, the second harmonic polarization and the generated SH field are exactly π out-of-phase and interfere destructively. (b) Visualization of the concept explained in (a) using data measured in Ref. [96]. The propagation distance inside the crystal was controlled by rotating the crystal, which leads to an oscillating SH intensity. (c) Sketch of angle-phase-matching in a uniaxial birefringent crystal. Phase-matching between the second order polarization and the SH field can be achieved by using a birefringent crystal. The second harmonic field is polarized along the plane containing the optic axis. Phase-matching can be achieved by angle tuning the relative orientation of $E_{2\omega}$ to the optic axis. (d) Typical ordinary n_o and extraordinary n_e refractive indices for a birefringent material. Usually, the refractive index of the fundamental beam $n_{o,\omega}$ can be matched to the angle dependent extraordinary refractive index of the second harmonic light $n_{o,\omega}(\theta)$ (effect of angle tuning depicted in shaded blue) (see Appendix A.6).

second harmonic waves exist: One that is generated by the fundamental wave at this position and will travel with speed c/n_ω , and one that is the superposition of SH fields generated at positions $x < L$ traveling with speed $c/n_{2\omega}$. These two waves are called the *inhomogeneous* and *homogenous* solutions, respectively [39, 97–101]. After one coherence length of propagation, these two waves are 180° out of phase leading to destructive interference and conversion of $E(2\omega)$ back to $E(\omega)$. This results in the oscillatory behavior of $I_{2\omega}(z)$ sketched in Fig. 1.6 (a) and (b). In reflection geometry, when the generated SH field is propagating backwards, the SH field primarily originates from a thin layer within a coherence length behind the sample surface. This coherence length is significantly shorter compared to transmission geometry due to the backward momentum transfer $\Delta k = 2k_\omega + k_{2\omega}$. This makes reflection-geometry SHG sensitive to the first few hundred nanometers behind the surface [39, 102–104].

1.2.4 Symmetry of Second Harmonic Generation

So far, the second order nonlinearity $\chi^{(2)}$ was assumed to be scalar, but in reality it is a third-rank tensor $\chi_{ijk}^{(2)}$, which links all components of the 3-dimensional field vectors.

$$P_{i,\omega_3} = 2\epsilon_0 \sum_{jk} \chi_{ijk}^{(2)}(\omega_3, \omega_1, \omega_2) E_{j,\omega_1} E_{k,\omega_2} \quad (1.32)$$

Hence, the nonlinear response of a material depends on the polarization of the interacting light fields with respect to the crystal axis. The structure of the tensor $\chi_{ijk}^{(2)}$ is determined by the point group of the crystal and would allow 324 independent constants. However, symmetry considerations, such as reality and permutation symmetry of the fields [105, 106] and specifically the Kleinmann symmetry consideration [107], reduce the number of independent coefficients to 18. These independent coefficients are the entries of a 3×6 matrix where permutation symmetry simplifies the notation to

$$\mathbf{P} = \begin{pmatrix} d_{11} & d_{12} & d_{13} & d_{14} & d_{15} & d_{16} \\ d_{21} & d_{22} & d_{23} & d_{24} & d_{25} & d_{26} \\ d_{31} & d_{32} & d_{33} & d_{34} & d_{35} & d_{36} \end{pmatrix} \mathbf{E}, \quad (1.33)$$

where the coefficient $d_{i,j} = 1/2 \chi_{ij}^{(2)}$ is used as an abbreviation. The tensor \mathbf{E} contains the

relevant permutations of the three electric field components E_i and takes the form

$$\mathbf{E} = \begin{pmatrix} E_1^2 \\ E_2^2 \\ E_3^2 \\ 2E_2E_3 \\ 2E_1E_3 \\ 2E_1E_2 \end{pmatrix}. \quad (1.34)$$

The number of these coefficients can be further reduced by considering the point group symmetry of the given material. Neumann's principle dictates that the tensors which describe macroscopic properties must have a symmetry that is identical to that of the point group of the material [107]. Thus, any such tensor must be left invariant under the symmetry operations of the material's point group. Conversely, this implies that one can determine the point group of an unknown material from the knowledge of the tensor's symmetry. The tensor elements in eq.1.33 are experimentally accessible by *SHG polarimetry* measurements. Here, the polarization of the incident light field is rotated with respect to the crystal axis (see Fig. 1.7) while an analyzer in front of the detector ensures detection of the individual SH field components $E_{i,2\omega}$. By choosing appropriate parameters for the incident polarization, analyzer, and sample orientation, one can selectively probe the different elements of the nonlinear susceptibility tensor $\chi_{ijk}^{(2)}$. Two typical polarimetry measurements, in which the polarization angle of the incident light is varied between 0 and 360°, is shown in Fig. 1.7.

In the past decades second harmonic generation has become a powerful tool to reveal hidden features in complex materials that are invisible to linear optical techniques. Examples include ferroelectric [39], magnetic [108–110], and multiferroic [28, 45, 111, 112] ordering in certain quantum materials. In these experiments, the SHG process reflects microscopic properties of the material on the unit cell length scale, and then $\chi_{ijk}^{(2)}$ is proportional to the respective order parameter, like the static polarization in a ferroelectric [39, 113]. In addition, macroscopic electrical currents break inversion symmetry and act as a source for SHG [114].

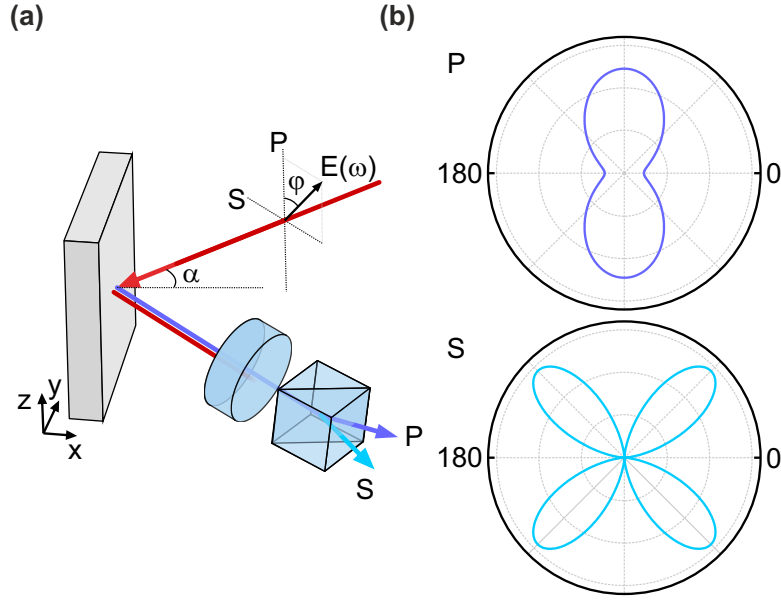


Figure 1.7: Second harmonic polarimetry. (a) In a SH polarimetry measurement the polarization angle ϕ of the fundamental field E_ω is controlled by a waveplate before it interacts with the sample. The generated SH light is then analyzed and divided into the two orthogonal polarization directions (S and P) before being detected. (a) This allows for the detection two orthogonal components of the second order nonlinear polarization, P_z and $P_{x,y}$ for the geometry in panel (a). The SH intensity can then be plotted against the polarization angle and fitted by eq. 1.31. Typically, these plots use polar coordinates and show between 2 and 8 lobes depending on the point-group symmetry of the nonlinear crystal. The polar graphs show simulations of a SH polarimetry signal for a Pmm2 pointgroup.

1.2.5 Hyper-Raman Scattering

Vibrations of the crystal lattice can modulate the second order nonlinear tensor $\chi_{ijk}^{(2)}$ leading to a process called *Hyper-Raman scattering* [115]. In this case, the symmetry selection rules are complementary to those of conventional Raman scattering and rather comparable to those of infrared spectroscopy. Generally, all infrared-active (odd) modes of a solid are Hyper-Raman-active and in extension also optically silent modes, which are neither observable in Raman-scattering or infrared spectroscopy, become Hyper-Raman-active [116–119]. Modes with amplitude $Q_{\text{IR}}(t)$ modulate $\chi_{ijk}^{(2)}$ according to,

$$\chi_{ijk}^{(2)}(t) = \chi_{ijk,0}^{(2)} + \left(\frac{\partial \chi_{ijk}^{(2)}}{\partial Q_{\text{IR}}} \right) Q_{\text{IR}}(t) + \dots \quad (1.35)$$

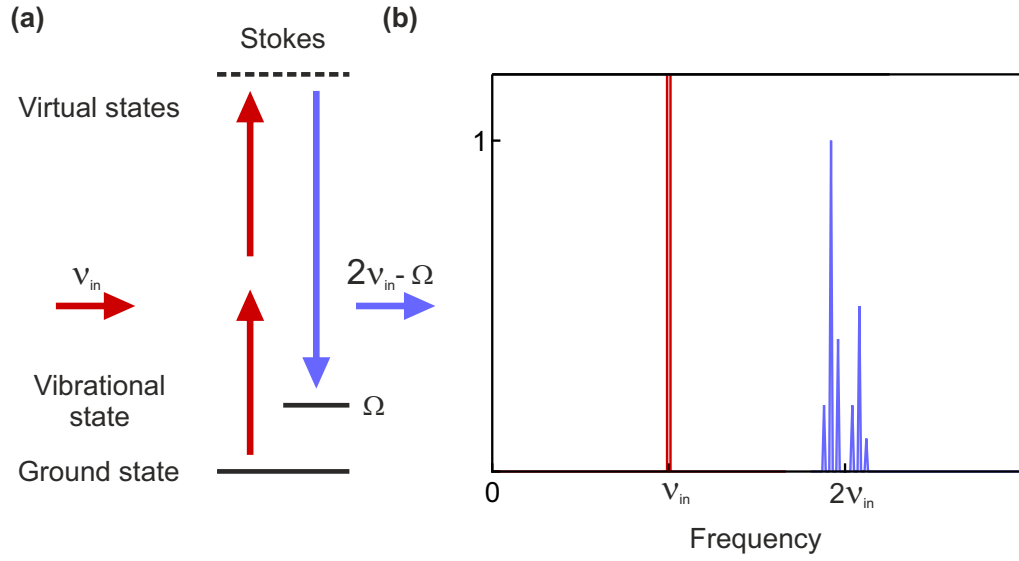


Figure 1.8: Hyper-Raman scattering. (a) Energy diagram of Stokes-Hyper-Raman scattering. An incoming light-field with frequency ν_{in} (red) promotes the system from the ground state into a virtual electronic excited state. Contrary to Raman scattering, Hyper-Raman scattering involves the absorption of two photons (two vertical red arrows). Upon relaxation to a vibrationally excited state, the system emits a photon with frequency $2\nu_{\text{in}} - \Omega$ (vertical blue arrow). The inverse process of transferring energy from an existing phonon to the light field involves the emission of a photon with frequency $2\nu_{\text{in}} + \Omega$. (b) The respective processes in (a) lead to the characteristic Hyper-Stokes and Hyper-Anti-Stokes peaks in the spectral region near the second harmonic frequency $2\nu_{\text{in}}$ (blue peaks). If the material does not have a static second order nonlinearity $\chi^{(2)}$, one does not observe emission at $2\nu_{\text{in}}$.

Crucially, even in centrosymmetric materials with $\chi_{\text{ijk}}^{(2)} = 0$, the Hyper-Raman tensor elements $\frac{\partial \chi_{\text{ijk}}^{(2)}}{\partial Q_{\text{IR}}}$ do not necessarily vanish, because the odd parity of $\chi_{\text{ijk}}^{(2)}$ is compensated for by the odd parity of Q_{IR} [116]. In other words, even when dipole SHG is not allowed by the symmetry of the crystal, Hyper-Raman scattering is still possible. In a centrosymmetric material the second order nonlinear polarization is therefore,

$$P_{\text{HR}}(t) = \left(\frac{\partial \chi_{\text{ijk}}^{(2)}}{\partial Q_{\text{IR}}} \right) Q_{\text{IR}}(t) E^2(t) \quad (1.36)$$

and, following the arguments presented above, a source of radiation at frequencies $2\nu \pm \Omega$, close to the second harmonic frequency. Fig. 1.8 shows a schematic HRS spectrum, where the sidebands due to the light-lattice interaction appear close to the second harmonic frequency 2ν [116, 120]. Different polarization directions of incident and detected light are individually

sensitive to phonon modes of different symmetries and dipole orientations. Thus, the polarization sensitive detection of the light generated by a hyper Raman process reveals information about the point group symmetry of a certain dipolar vibration.

1.2.6 Third Order Optical Susceptibility

If the amplitude E of the electric fields involved in the interaction are large enough, nonlinear processes due to the third-order nonlinear susceptibility $\chi_{ijkl}^{(3)}$ also become important. In this case, three electric fields E_{ω_i} create a polarization,

$$P_{i,\omega_4}^{(3)} = \epsilon_0/4 \sum_{jkl} \chi_{ijkl}^{(3)}(\omega_4, \omega_1, \omega_2, \omega_3) E_{j,\omega_1} E_{k,\omega_2} E_{l,\omega_3}. \quad (1.37)$$

Similar to second harmonic generation caused by $\chi^{(2)}$, the third-order nonlinear susceptibility $\chi^{(3)}$ can lead to *third harmonic generation*. The corresponding nonlinear polarization is given by,

$$P_{i,3\omega}^{(3)} = \epsilon_0 \chi_{ijkl}^{(3)}(3\omega, \omega, \omega, \omega) E_{j,\omega} E_{k,\omega} E_{l,\omega}. \quad (1.38)$$

The equations describing this process are obtained in a manner similar to those derived for SHG in section 1.2.3.

Most importantly, the third order nonlinearity can lead to a process called *electric-field induced second harmonic generation*. In this case two light fields at frequency Ω and ω interact and generate a polarization close to the second harmonic frequency 2ω ,

$$P_{i,2\omega+\Omega}^{(3)} = \epsilon_0 \chi_{ijkl}^{(3)}(2\omega + \Omega, \omega, \omega, \Omega) E_{j,\omega} E_{k,\omega} E_{l,\Omega}. \quad (1.39)$$

Like Hyper-Raman scattering this leads to two peaks in the optical spectrum at $2\omega \pm \Omega$, and only for a static electric field, $\Omega = 0$, true second harmonic light at frequency 2ω is emitted from the sample.

Further, in contrast to eq. 1.22 the third-order polarization $P^{(3)}$ also allows components at the initial frequencies of the incident fields. For example, in the case of the incident field with frequency ω_3 :

$$P_{i,\omega_3}^{(3)} = \epsilon_0 \chi_{ijkl}^{(3)}(\omega_3, \omega_1, \omega_1, \omega_3) E_{j,\omega_1}^* E_{k,\omega_1} E_{l,\omega_3}. \quad (1.40)$$

Together with the linear polarization $\chi_{ij}^{(1)} E_{j,\omega_3}$, the total polarization P_{i,ω_3} at frequency ω_3 can

be written as,

$$P_{i,\omega_3} = \chi_{ij}^{(1)} E_{j,\omega_3} + \chi_{ijkl}^{(3)}(\omega_3, \omega_1, \omega_1, \omega_3) E_{j,\omega_1}^* E_{k,\omega_1} E_{l,\omega_3}, \quad (1.41)$$

and therefore, the refractive index of the field $E_{j,\omega_3}(t)$ changes as a function of the intensity $I = |\mathbf{E}(t)|^2$,

$$n(E(t)) = n_{0,\omega_3} + \delta n |\mathbf{E}(t)|^2 \quad (1.42)$$

This nonlinear process is called *cross-phase modulation* or *Kerr effect* [78, 121]. Consequently, this time varying refractive index $n(E(t))$ introduces a time varying spectral phase and with it a time dependent instantaneous frequency

$$\omega(t) = \frac{d\varphi}{dt} = 2\pi z/\lambda_0 \frac{dn}{dt} \quad (1.43)$$

which leads to a significant change of the frequency content of the light field $E(t)$. If the three fields of eq. 1.40 are degenerate this process is called *self-phase modulation* and it becomes significant for strong electric fields compressed to short pulses.

1.3 Nonlinear Optics using Femtosecond Pulses

The second harmonic generation described in the previous paragraphs was originally discovered in 1961 [122] with the development of the first optical laser just a year before. Nonlinear optical techniques became increasingly popular with the advent of pulsed lasers, which output electric fields which are temporally confined to pulses of picosecond (ps) to femtoseconds (fs) duration. This can lead to extremely high peak electric fields on the order of ~ 100 MV/cm [ref23inchap0], which are comparable to the intrinsic interatomic fields $E_{at} = \frac{e}{4\pi\epsilon_0 a_0^2} \sim$ GV/cm, resulting in large nonlinear optical effects. Femtosecond light pulses were first achieved by *mode-locking* techniques in laser oscillators. This was followed by the development of *Chirped Pulse Amplification*, by Gerard Albert Mourou, Donna Strickland and Arthur Ashkin, in which the laser pulses supplied by the oscillators are amplified to peak powers on the order of petawatts [16]. The pioneers of this technique were later awarded the 2018 Nobel prize in physics. The time-resolved optical experiments presented in this thesis employ femtosecond laser pulses. Therefore, the following paragraphs will explain some fundamentals of ultra-short laser pulse propagation and how the resulting nonlinear optical processes introduced above can be used to unravel the dynamics of electronic and lattice excitations on their intrinsic time scales.

1.3.1 Basic Concepts of Short Laser Pulses

Due to the uncertainty principle for frequency and time, optical fields of a few ps to fs durations require certain energy bandwidth of the optical spectrum, different to the monochromatic continuous wave fields discussed in the previous paragraphs. For a *transform-limited* pulse of Gaussian shape, the FWHM-pulse duration Δt is related to the inverse of the spectral width $\Delta\nu$ through the relation [123]:

$$\Delta t \Delta\nu = 0.44. \quad (1.44)$$

This is only valid if the spectral phase is constant throughout the whole spectrum. However, if the pulse experiences a frequency dependent phase $\Delta\varphi(\nu)$, it will be stretched in time to a duration longer than the one predicted by eq.1.44. This effect is called *chirp*, and it is usually accounted for by adding a quadratic temporal phase to the frequency of a laser field with envelope $E_0(t) = E_0 e^{(-t^2 4\ln(2)/\Delta t^2)}$,

$$E(t) = E_0(t) \sin(2\pi\nu t + \Delta\varphi t^2), \quad (1.45)$$

which is equivalent to introducing a frequency of the electric field that changes linearly with time. This chirp can be positive ($d\nu/dt > 0$) or negative ($d\nu/dt < 0$) and is acquired when a pulse propagates through a dispersive medium with frequency dependent refractive index $n(\nu)$. This acquired chirp can be reduced by using an oppositely chirped medium or a compressor built from prisms or gratings [16, 124].

The temporal profile $E_0(t)$ and phase $\varphi(t)$ of a laser pulse can be accurately measured by different techniques. Two of the most commonly-used techniques in the near-infrared and visible wavelength range are frequency resolved *auto-* and *cross-correlations*, where the pulse is sampled with itself or a gate pulse [125–127]. These techniques involves overlapping the two pulses inside a nonlinear crystal. If both fields are also temporally overlapped, the two electric fields interact through the non-zero second order nonlinearity $\chi^{(2)}$ of the crystal. Information concerning the spectral content of the pulses is contained in the resulting nonlinear emission of light. Examples of auto-correlation [126] and cross-correlation [127] are sketched in Fig. 1.9 (b) and a description of these processes is detailed in Appendix A.5.

The short duration of fs-laser pulses has very important implications for nonlinear optical processes [128]. For example, the frequency dependent refractive index $n(\omega)$ of the material leads temporal *walk-off* of two nonlinearly interacting laser pulses [123]. In second harmonic genera-

tion, walk-off happens when the second harmonic emission and the incident laser pulse spatially separate due the difference in their *group velocities*. This drastically limits the interaction length and the phase matching bandwidth of the nonlinear process [129]. The group velocity v_g , given by

$$v_g(\omega_0) = \left(\frac{\partial \omega}{\partial k} \right)_{\omega_0} \quad (1.46)$$

defines the speed of a pulse with center frequency ω_0 inside a medium and is thus crucial in describing propagation of short pulses.

1.3.2 Homogeneous and Inhomogeneous solution in Second Harmonic Generation

In the case of second harmonic generation using femtosecond light pulses, the light conversion efficiency in phase-matched conditions is drastically reduced when the homogeneous and inhomogeneous solutions of the wave equation are both considered. This results from the different propagation velocities of the two SH fields, which leads to their temporal separation. The homogenous solution of the SH field is generated in the first coherence length l_{coh} below the crystal surface and will propagate at the group velocity of the SH frequency, $v_g(2\omega)$. The inhomogeneous solution of the SH field, however, is constantly generated and reabsorbed by the propagating fundamental light pulse and thus propagates at the group velocity $v_g(\omega)$ [97, 101]. Hence, the two SH pulses will separate while propagating through the crystal. As a result, the two pulses that leave a crystal of length L will be separated by the difference of the two group velocities $\Delta t = \Delta v_g/L$ [100, 101]. If the walk-off distance $l_{\text{wo}} = v_g \Delta t$ is large compared to the crystal size L , an oscillatory behavior of the output intensity, as seen for monochromatic light, is observed (see Fig. 1.9 (b) and Fig. 1.6 (b)) [97, 101].

If the two SH pulses can be measured separately one obtains spatial information of the nonlinear coefficient in the material. The homogeneous solution is sensitive to the magnitude of $\chi^{(2)}$ within one coherence length below the surface, whereas the inhomogeneous solution is constantly generated in the bulk [64, 97, 101]. Therefore, if $\chi^{(2)}$ is zero in the first coherence length behind the surface and non-zero in the bulk, then only one pulse (the inhomogeneous solution) will exit the sample [64, 101] (see Appendix B.6).

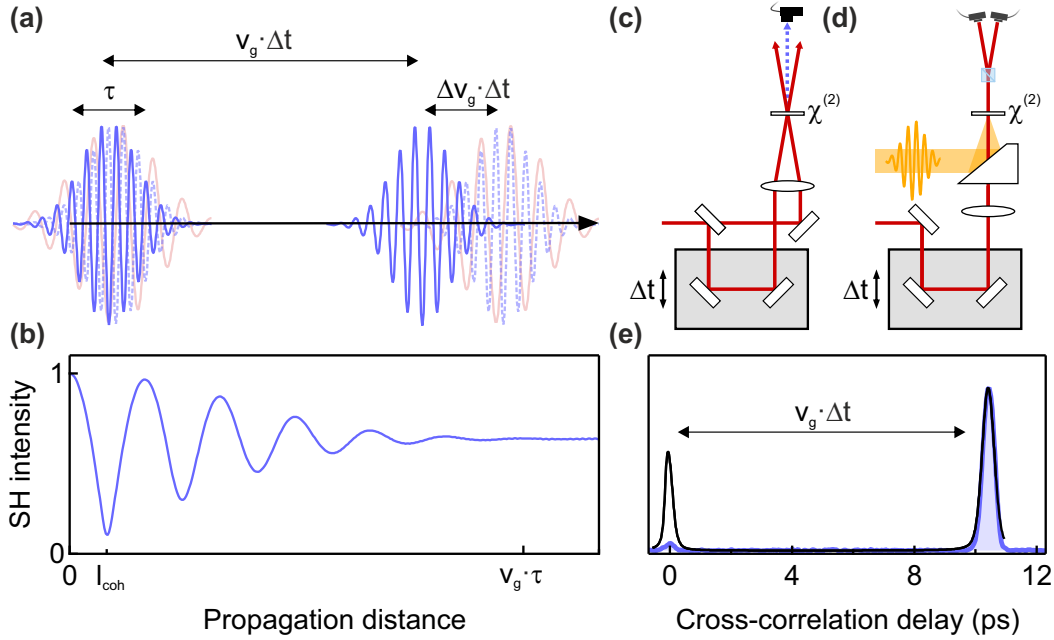


Figure 1.9: Homogenous and inhomogeneous solutions of SH generation. (a) Sketch of the walk-off of homogeneous and inhomogeneous solution of SHG. At the surface of the crystal, the homogeneous solution (blue) and the inhomogeneous (dashed blue) solution of the nonlinear wave equation temporally overlap, which leads to oscillatory behavior of the total SH intensity shown in panel (b). (b) Oscillatory behavior of the SH intensity that exits the crystal. Due to the difference in group velocity between the inhomogeneous solution, which is phase locked to the fundamental pulse (red), and the homogeneous solution, they separate after $\Delta t = \Delta v_g/L$, and the output SH becomes constant. (c) and (d) Ultra-short laser pulses can be characterized by frequency resolved optical gating (FROG) (c) and electro-optic sampling (EOS) (d). Both techniques rely on nonlinear mixing in a $\chi^{(2)}$ -medium. In a FROG measurement one pulse is split into two pulses of equal intensity which are then non-collinearly overlapped in nonlinear crystal. In EOS a low frequency (MIR or THz, yellow) pulse is collinearly overlapped with a NIR gate pulse in a $\chi^{(2)}$ -medium. (e) Homogeneous and inhomogeneous solution of SHG from LiNbO₃. The homogeneous and inhomogeneous solution of SHG can be detected by the scheme in (c). The intensity cross-correlation of an 800-nm wavelength pulse with the SH light generated by a similar 800 nm pulse in LiNbO₃, shows the temporally separated inhomogeneous ($\Delta t = 0$ ps) and homogeneous ($\Delta t = 10.5$ ps) solution (Data taken from [64]). This measurement agrees well with a simulation (black line) done with software package SNLO [130]. Part of the figure are adapted from Ref. [64].

1.4 Time-resolved Optical Experiments

Femtosecond laser pulses allow for the exploration of the optical properties of solids with a time resolution determined by the pulse duration. Hence, it is possible to follow non-equilibrium evolutions of correlated materials on the relevant timescales of charge carrier and crystal lattice dynamics. In a pump-probe experiment, a laser pulse, called the *pump*, creates an excited state in the material, and a second, time-delayed laser pulse, called the *probe*, samples the induced changes of the optical properties (see Fig. 1.10) [131]. By varying the relative arrival time Δt between the pump and probe pulses, it is possible to obtain information of the optical properties of the material at times before, after and throughout the course of the excitation.

The wavelengths of the pump and probe pulses can range from the THz and mid-infrared [64, 65], to excite and probe low energy excitations, up to x-rays, to sample the structural properties [54, 58]. The pump-pulses lead to coherent collective modulations of the material properties which appear as coherent oscillations of the optical properties. In the experiments presented in this thesis mid-infrared pulses, generated by difference frequency generation from the output of two optical parametric amplifiers, are used to resonantly drive infrared active excitations in complex materials. The resulting time-dependent modulation of the optical properties are then mapped using probe pulses with a carrier wavelength of 800 nm.

1.4.1 Time-resolved Raman and Hyper-Raman scattering

The time-resolved detection of Raman and Hyper-Raman modes in solids, either structural or electronic in origin, relies on the nonlinear light conversion presented in the preceding paragraphs. In general, the interaction of the probe light field E_{probe} with the solid is described by the wave-equation,

$$\left(\frac{\partial^2}{\partial z^2} - \frac{n^2}{c^2} \frac{\partial^2}{\partial t^2} \right) E = \frac{1}{c^2} \frac{\partial^2 P(E_{\text{probe}}, Q_1, Q_2, \dots)}{\partial t^2} \quad (1.47)$$

where Q_i denotes any excitation of the sample. Here, it will be assumed that the incident probe electric field E_{probe} remains undepleted throughout the interaction, and the spectral changes to the field E resulting from the nonlinear interaction are small perturbations [93, 116, 132]. Under this approximation, the following nonlinear polarization can be written as:

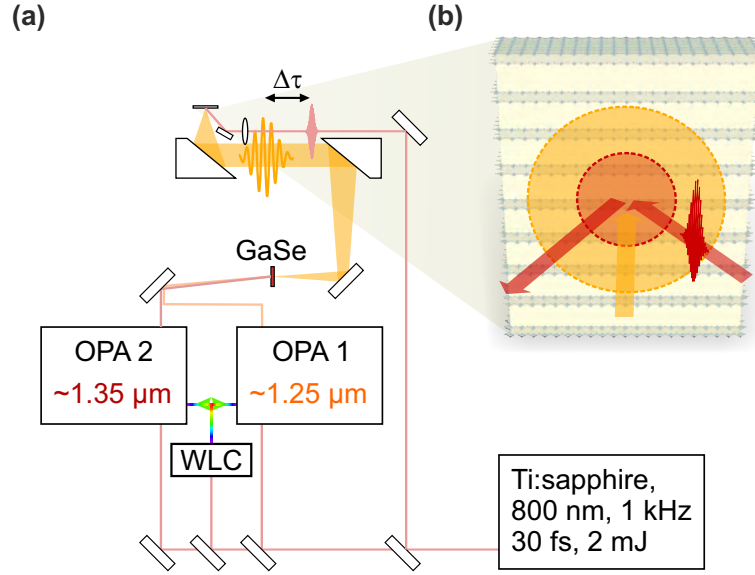


Figure 1.10: Schematic of a typical MIR-pump NIR-probe setup. (a) Femtosecond laser pulses from a Ti:sapphire amplifier pump two optical parametric amplifiers (OPA), which are seeded by the same white light continuum (WLC). These OPAs output two signal beams usually output at 1.235 μm and 1.335 μm which are overlapped in a 330 μm thick GaSe crystal to produce MIR radiation through difference frequency generation. This results in carrier envelope phase-stable pulses with energies of 3 μJ , durations of 150 fs, and carrier wavelengths of 17- μm (see Appendix A.4). These mid-infrared pulses (yellow) are focused to a spot size of approximately 65 μm onto the sample by using a telescope composed of two off-axis parabolic mirrors. The NIR probe pulses are derived from the same amplifier system and are spatially overlapped with the MIR light on the sample (80 nJ energy, 35 μm spotsize). (b) To ensure the detection from a homogeneously excited volume, the probe pulses (red) are focused to a significantly smaller size compared to the pump pulses (yellow).

$$\text{Raman Scattering: } P_{\text{R}}(t) = \left(\frac{\partial \chi_e^{(1)}}{\partial Q_{\text{R}}} \right) Q_{\text{R}}(t) E_{\text{probe}}(t)$$

$$\text{Hyper Raman Scattering: } P_{\text{HR}}(t) = \left(\frac{\partial \chi_e^{(2)}}{\partial Q_{\text{IR}}} \right) Q_{\text{IR}}(t) E_{\text{probe}}^2(t)$$

$$\text{Electro Optic Effect: } P_{\text{EO}}(t) = \chi^{(2)} E_{\text{THz}}(t) E_{\text{probe}}(t)$$

$$\text{Electric Field Induced SHG: } P_{\text{EFISH}}(t) = \chi^{(3)} E_{\text{THz}}(t) E_{\text{probe}}^2(t)$$

In the following, the spectral changes to the probe field will be derived for the simplest case of Raman scattering, the other cases can be inferred from that result [120, 133]. The wave-equation for the case of Raman scattering becomes:

$$\left(\frac{\partial^2}{\partial z^2} - \frac{n^2}{c^2} \frac{\partial^2}{\partial t^2}\right) E = \frac{\rho}{c^2} \left(\frac{\partial \chi_e^{(1)}}{\partial Q_R}\right) Q_R(t) E_{\text{probe}}(t). \quad (1.48)$$

The general solution obeying the relevant boundary condition ($E(z=0) = E_{\text{probe}}(z=0)$) is [132]:

$$E(z, t) = E_{\text{probe}}(z, t) - \frac{1}{cn} \frac{\partial \chi_e^{(1)}}{\partial Q_R} z \frac{\partial}{\partial t} Q_R(z, t + \Delta t) E_{\text{probe}}(z, t) \quad (1.49)$$

Here, Δt denotes the time delay between pump and probe pulse and

$$Q_R(z, t + \Delta t) = Q_R(z) \sin(2\pi\Omega_R(t + \Delta t)) \quad (1.50)$$

is the amplitude of a coherent Raman-active vibration with frequency Ω_R . In the following $Q_R(z, t + \Delta t)$ is assumed to be stationary, i.e., $Q_R(z) = Q_{R,0}$. The Fourier transform of $E(z, t)$ yields the time-delay dependent spectral content of the emerging probe pulse

$$E(\omega, \tau) e^{-in\omega z/c} = E_{\text{probe}}(\omega) + \beta\omega \left[E_{\text{probe}}(\omega + \Omega) e^{i\Omega\Delta t} - E_{\text{probe}}(\omega - \Omega) e^{-i\Omega\Delta t} \right] \quad (1.51)$$

where $\beta = l/cn \partial \chi_e^{(1)} / \partial Q_R$, with l being the interaction length of the excitation and probe pulses [132]. After the interaction, the probe pulse spectrum consist of three distinct spectral components: The unperturbed probe spectrum $E_{\text{probe}}(\omega)$ and two frequency shifted sidebands at $\omega \pm \Omega_R$ with time-delay dependent spectral phases $\pm\Omega_R\Delta t$ (see Fig. 1.11). The phase sensitive detection of these sidebands $\Delta E(\omega, \Delta t) = \beta\omega E_{\text{probe}}(\omega \pm \Omega) e^{i\pm\Omega\Delta t}$, for example achieved by spectral interference with the local oscillator $E_{\text{probe}}(\omega)$ on the detector, carries information about the phase and amplitude of the excitation Q_R . Consider now the spectrum of the intensity:

$$I(\omega, \Delta t) = \left| E_{\text{probe}}^2(\omega) + 2\Delta E(\omega, \Delta t) E_{\text{probe}}(\omega) + \Delta E^2(\omega, \Delta t) \right| \quad (1.52)$$

Here, the second term, $\sim \Delta E(\omega, \Delta t) E_{\text{probe}}^2(\omega)$, denotes interference of the sidebands with the unperturbed probe spectrum (see Fig. 1.11 (b)). This *heterodyned* component of the intensity, is linearly proportional to the amplitude of the excitation field Q_R . The third term $\sim \Delta E^2(\omega, \Delta t)$ is called the *homodyned* component. It is proportional to Q_R^2 and oscillates at twice the frequency of the excitation Q_R ($2\Omega_R$). Generally, the heterodyned component is significantly larger than the homodyned and the latter can be neglected. A spectrally integrating photo detector, like a

photodiode, yields the total intensity change

$$I(\Delta t) = \int I(\omega, \Delta t) d\omega \quad (1.53)$$

$$= I_{\text{probe}} + \alpha\Omega_R \cos(2\pi\Omega_R\Delta t) + \gamma\Omega_R^2 \cos(2\pi(2\Omega_R)\Delta t) \quad (1.54)$$

of the probe pulse that can be measured in a pump-probe experiment [93, 132, 134]. Crucially, this time-delay dependent signal has a $\pi/2$ phase shift relative to the launched coherent vibration Q_R and an amplitude that is proportional to the vibrational frequency Ω . Hence, it is proportional to the velocity $\dot{Q}_R(\Delta t)$ of the coherent vibration. Fig. 1.11 (c) shows a sketch of a typical time-resolved signal, in which the heterodyned sidebands appear as coherent oscillations of frequency Ω_R on top of a slowly varying background, which results from incoherent dynamics. The Fourier-transform of this signal, shown in Fig. 1.11 (d), reveals these oscillations as a Lorentzian peak centered at frequency Ω_R .

To obtain the spectral changes for the cases of Hyper-Raman scattering, electro-optic sampling and field-induced second harmonic generation (eq. 1.4.1-1.4.1) one needs to replace $\partial\chi_e^{(1)}/\partial Q_R$ by $(\partial\chi_{ijk}^{(2)}/\partial Q_{iR}) Q_{iR}(t) E_{\text{probe}}(t)$, $\chi^{(2)} E_{\text{THz}}(t)$ and $\chi^{(3)} E_{\text{THz}} E_{\text{probe}}(t)$, respectively. The resulting spectral changes of the four different cases are sketched in Fig. 1.11 (a).

Contrary to Raman scattering and the electro-optic effect, hyper-Raman scattering and EFISH generate sidebands close to the second harmonic frequency of the probe electric field. Usually, $E_{\text{probe}}(t)$ does not contain any spectral component at second harmonic frequencies and thus effectively reduces the detection to the homodyned part. In order to still obtain the heterodyned component a local oscillator at these second harmonic frequencies has to be spatially and temporally overlapped with the probe pulse on the detector [64]. This either happens naturally due to a non-zero $\chi^{(2)}$ in the sample material or by a second reference beam generated in a second non-linear crystal.

The temporal resolution for this type of detection scheme crucially depends on the spectral width of the probe pulse. A rough estimate of the time resolution is given by the Nyquist theorem [135], which states that a pulse of bandwidth $\Delta\nu$ can sample a signal up to $\Delta\nu/2$ without distortions. This arises from the necessity of spectral overlap between sidebands and probe spectrum to allow interference. This is more qualitatively captured by considering the sampling efficiency $S(\Omega)$ which is given by [136],

$$S(\Omega) = \int_{\Omega}^{\infty} d\omega R(\omega) |E(\omega)| |E(\omega - \Omega)| e^{i[\phi(\omega) - \phi(\omega - \Omega)]}. \quad (1.55)$$

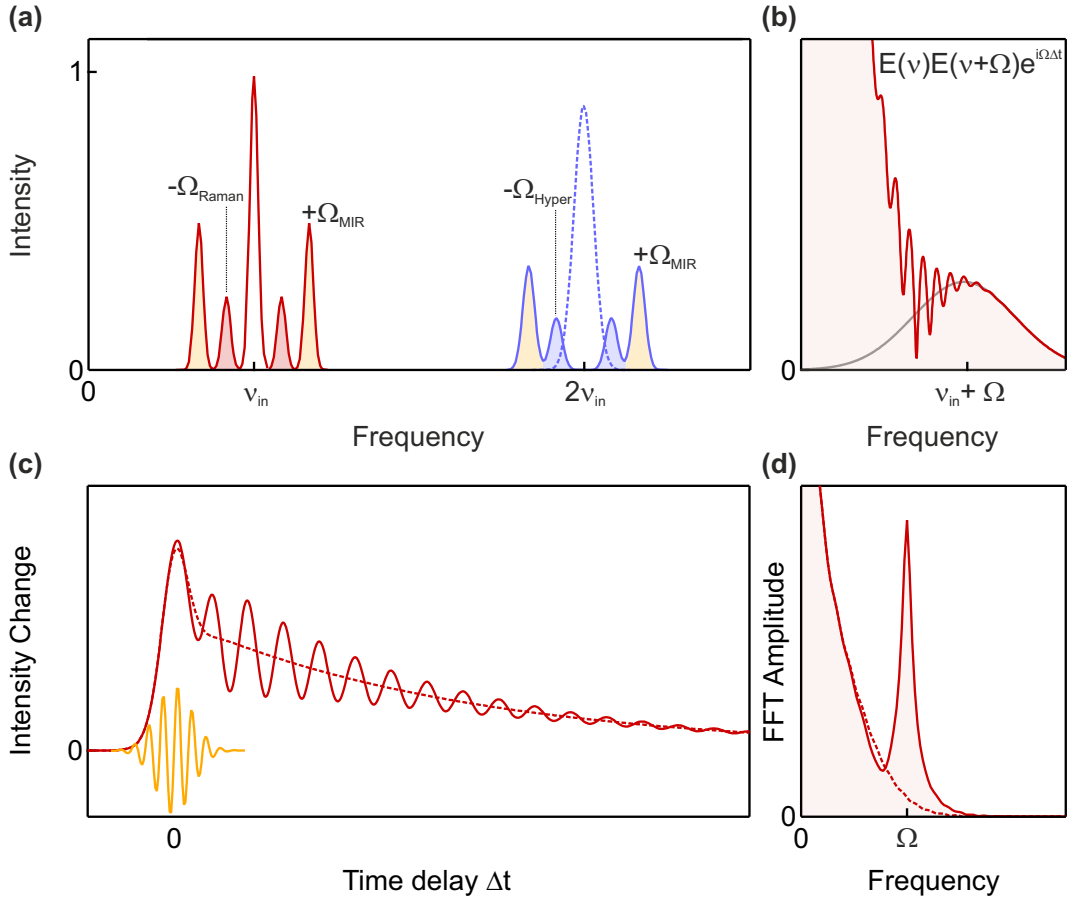


Figure 1.11: Spectral changes in time-resolved optical experiments. (a) Sketch of the spectral changes due to ultra-fast nonlinear light scattering. Generally, nonlinear optical interaction with coherent dynamics in solids lead to side bands imparted onto to the fundamental ν_{in} (unfilled red peak) or second harmonic $2\nu_{in}$ (dashed blue peak) frequency. The direct interaction of the MIR/THz pump field with the optical probe pulse through the electro-optic effect or electric field-induced SHG leads to sidebands of Ω_{MIR} imparted onto the frequencies ν_{in} and $2\nu_{in}$ (yellow shaded peaks). Raman- and Hyper-Raman scattering also lead to sidebands offset by Ω_{Raman} and Ω_{Hyper} (red and blue shaded peaks). (b) Sketch of the interference between sidebands and unaltered probespectrum. The sidebands have a time-delay Δt phase and interfere with the unperturbed probe spectrum (unfilled red and dashed blue peak) which leads to periodic modulation of probe intensity on the detector as shown in panel (c). (c) Simulation of a typical pump-probe time trace. When the pump and probe pulses overlap at time delay $\Delta t = 0$, the Kerr effect leads to a slowly varying background which follows the intensity envelope of the pump-pulse. This excitation is usually followed by coherent oscillations on top of a slowly varying background. (d) Fourier transform of the signal in panel (c), revealing the amplitude and frequency of the oscillations. The slowly varying background in the time-resolved signal leads to background in the FFT (dashed line).

Here, $R(\omega)$ is the frequency response of the detection system, $|E(\omega)| e^{i\phi(\omega)}$ the complex amplitude of the sampling pulse on the detector. In short, the sampling efficiency is given by the convolution of the probe spectrum with the local oscillator. If there is not sufficient bandwidth in $E(\omega)$, then the sampling efficiency is poor. Further discussion of time resolution is done in Chapter 2.

1.4.2 Measuring Polaritons with Short Laser Pulses

In the special case where the material is transparent for the probe pulse the assumption of a stationary excitation $(z, t) = Q(t)$ is not valid anymore. This is due to both, the propagation of the probe pulse itself and of the polaritons generated by the mid-infrared pump. Similar to the nonlinear mixing of two electric fields, phase-matching becomes important when considering the propagation of polaritons [92, 137]. This makes it necessary to also consider the conservation of the total momentum of all involved waves in the scattering process explained above. The momentum of the excitation q has to be equal to the difference of the momentum of probe field k_i and the scattered probe field k_s ,

$$q = n_i k_i - n_s k_s \quad (1.56)$$

which can be approximated with [92, 137],

$$\Omega(q) = v_g q. \quad (1.57)$$

This relation implies that a pulse with group velocity v_g phase-matches to a polariton of frequency $\Omega(q)$ when the two dispersion relations intersect, as shown in Fig. 1.12 (a). Accordingly, the frequency Ω at which the time delay dependent signal oscillates, depends on the group velocity and consequently on the center wavelength of the probe pulse [65, 92, 137, 138] [65, 92, 137, 138]. This is illustrated in a depth vs. time map of a phonon polariton simulation shown in Fig. 1.12 (b). Here, for every point in time a full 1D cut along the crystal length is plotted and the phonon-polariton amplitude is shaded in red (positive) and blue (negative). The dashed red line indicates the propagation of a probe pulse with a group velocity that is almost perfectly phase-matched to a phonon-polariton that propagates deep inside the material. The result is a long interaction length and therefore the selective detection of this particular phonon-polariton frequency.

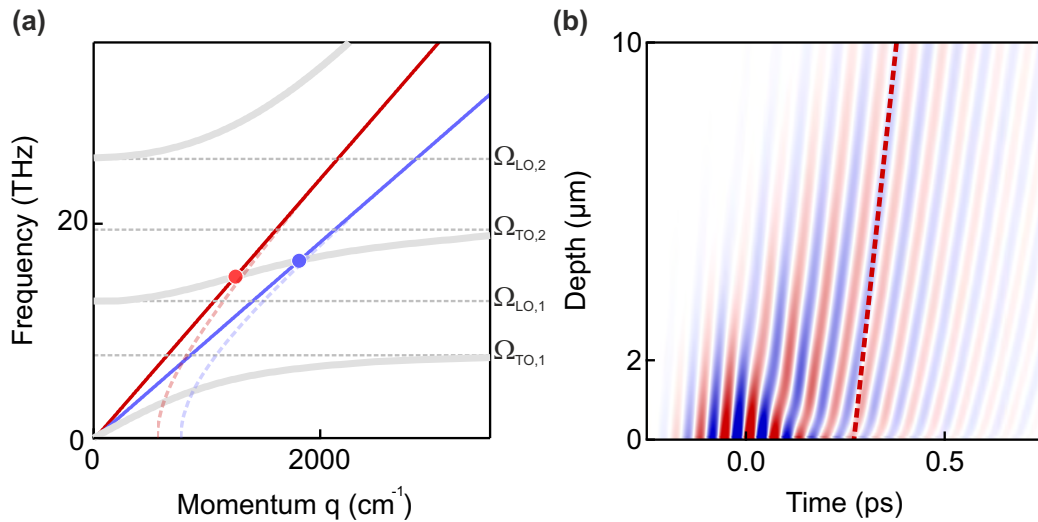


Figure 1.12: Phase-matching of phonon-polaritons. (a) Phonon-polariton dispersion of two phonons and phase-matching of optical probe pulses. Phase-matching takes place between a polariton and an optical when $\Omega(q) = v_g q$ is fulfilled. For the case when polariton and probe pulse propagate collinearly, phase-matching takes place when the dispersion of the optical pulse $v_g q$ (red and blue lines) intersects the phonon-polariton dispersion (red and blue dots). When the probe pulse and the polariton do not propagate collinearly phase-matching is described by the dashed lines. (b) This phase-matching can be understood as a matching of the velocity of the laser pulse with the phase velocity of the phonon-polariton. The laser pulse will always interact with the same part of the phonon-polariton wave as can be seen by the simulations in panel (b). The depth vs. time plot shows the phonon-polariton amplitude shaded in blue (negative) and red (positive). The propagating probe pulse (dashed red line) is phase-matched to a phonon-polariton that propagates deep inside the bulk and is always overlapped with the same oscillation cycle (blue).

Chapter 2

Nonlinear Phononics in LiNbO_3

2.1 Introduction

The nonlinearities of the crystal lattice become apparent at temperatures close to the Debye temperature, when the amplitude of the atomic thermal vibrations becomes significant ($> 1\%$) compared to the lattice spacing. These large amplitude stochastic vibrations lead to non-linear phonon-phonon scattering (Umklapp scattering) and manifest as thermal expansion and a finite thermal conductance [139–141]. A sufficiently small light field interacting with a polar vibration of the lattice adds a small coherent component on the stochastic thermal vibration, which makes the harmonic approximation appropriate to describe the linear light-lattice interaction and hence justifies the model of a driven harmonic oscillator for crystal lattice vibrations, discussed in Chapter 1. However, at larger driving fields the harmonic approximation breaks down for these coherent vibrations. For an adequate description of the resulting atomic trajectories the knowledge of the full lattice potential, including anharmonicity, is required.

This chapter will focus on the description of coherent nonlinear lattice vibrations and the non-linear coupling between the individual eigenmodes of the crystal. First, the theoretical basis of this so called *nonlinear phononics* will be introduced. Subsequently, these ideas will be demonstrated by a set of experiments involving time-resolved second harmonic generation to measure the real-time dynamics of infrared active lattice vibrations. Parts of this chapter are taken from Ref. [64, 65].

2.2 Theory of Nonlinear Phononics

The polarization induced in a solid by light can be expanded in powers of the incident electric field E and leads to the nonlinear optical phenomena described in Chapter 1. In a similar way, the potential energy of the crystal lattice can be expanded in powers of the individual eigenmodes with amplitudes Q_i and additional coupling terms allow energy transfer between two or more modes,

$$V_{\text{lattice}}(Q_1, Q_2, \dots, E) = \sum_i \Omega_i^2 Q_i^2 + \sum_{i,n} a_{i,n} Q_i^n + \sum_{i,j,k,l} g_{ijk} Q_i Q_j Q_k + h_{ijkl} Q_i Q_j Q_k Q_l + \dots \quad (2.1)$$

These nonlinear expansion terms become accessible at large atomic displacements far away from the equilibrium positions, for example achieved by strong external driving with a laser pulse [52]. In eq. 2.1, the first two terms describes the harmonic potential energy and higher order expansions of each individual lattice mode Q_i with harmonic eigenfrequency Ω_i , as a polynomial expansion with coefficients $a_{i,n}$ (see Fig. 2.1). The third sum contains the coupling of different lattice modes written up to the quartic order.

The existence of certain combinations $g_{IRjk} Q_{IR} Q_j Q_k$ or $h_{IRjkl} Q_{IR} Q_j Q_k Q_l$ is strictly tied to the symmetries of the crystal and the eigenmodes involved in the nonlinear interaction. In a centrosymmetric crystal a coupling constant is nonzero, if the tensor product of the involved modes is part of the A_g totally symmetric irreducible representation. In the special case of one (optically) driven infrared mode Q_{IR} the only symmetry allowed cubic term is $\Delta V = g Q_{IR}^2 Q_R$, where Q_R denotes the amplitude of a Raman active vibration. The irreducible representation of the Raman mode Q_R has to be contained in the irreducible representation of the product group of the infrared mode Q_{IR} with itself, $I(Q_R) = I(Q_{IR}) \times I(Q_{IR})$ [52, 58, 62].

This complex notion can be broken down to a simple rule: a coupling term is allowed when the product of all the involved phononic fields is even. For example, with $Q_{IR}^2 \equiv \text{even}$ and $Q_R \equiv \text{even}$, their product is even, too. Generally, infrared-active modes are odd (break inversion symmetry) and Raman modes are even (conserve inversion symmetry). The direct products between irreducible representations can be found in the product table of the point group for a given crystal structure [142]. Generally, if the excited infrared mode is of A_u or B_u symmetry, the cubic coupling terms in eq. 2.1 are only allowed when the coupled (Raman) modes are of A_g symmetry. The same symmetry considerations are also true for the quartic terms h_{ijkl} , however

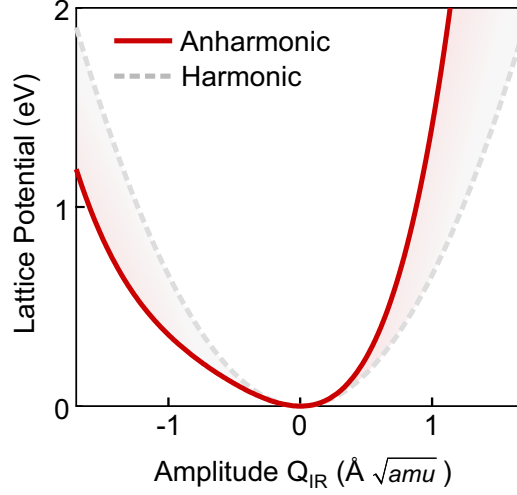


Figure 2.1: Anharmonic lattice potential. Anharmonic and harmonic lattice potential energy as a function of the phonon Amplitude Q_{IR} . The harmonic approximation (dashed grey line) of the lattice potential energy is only valid for small displacements from the equilibrium position $Q_{\text{IR}} = 0$. At large vibrational amplitudes the full lattice potential energy (red line) strongly deviates from the harmonic approximation and has to be taken into account to properly describe the lattice dynamics.

here coupling between different infrared active modes is possible because the product group $I(Q_{\text{IR},1}) \times I(Q_{\text{IR},2}) \times I(Q_{\text{IR},3}) \times I(Q_{\text{IR},4})$ can contain the totally symmetric A_g -symmetry. Similar to optical fourth order processes (Hyper-Raman scattering and Third-Harmonic generation), this type of coupling allows the interaction between polar infrared vibrations and optically silent modes.

2.2.1 Nonlinearities of a Strongly Driven Lattice Vibration

The following paragraph deals with the direct excitation of polar lattice vibrations by resonantly tuned laser pulses. In the harmonic approximation, the potential energy is given by

$$V_{\text{lattice}}(Q_1, Q_2, \dots, E) = \sum_i \Omega_i^2 Q_i^2 + \sum_i Z_i Q_i E \quad (2.2)$$

The last term describes the coupling of infrared active modes with effective charge Z_i to an external electric field E [62, 83, 143]. When only one lattice mode $Q_i = Q_{\text{IR}}$ with resonance frequency Ω_{IR} is driven by a weak external electric field $E_0 \sim 0.1 \text{ MV/cm}$, the equation of motion

reduces to that of a single harmonic oscillator,

$$\ddot{Q}_{\text{IR}} + 2\gamma_{\text{IR}}\dot{Q}_{\text{IR}} + \Omega_{\text{IR}}^2 Q_{\text{IR}} = Z_{\text{IR}}^* E. \quad (2.3)$$

As discussed in Chapter 1, this equation of motion has steady state solutions of the form $Q_{\text{IR}}(t) = Q_{\text{IR},0}\sin(2\pi\Omega_{\text{IR}}t + \varphi)$. Figure 2.2 (a) shows a solution of eq. 2.3 for a driving field $E(t)$ which is in resonance with the infrared mode and of finite temporal width T ,

$$E(t) = E_0\sin(2\pi\Omega_{\text{IR}}t)e^{-t^2 4\ln(2)/T^2}. \quad (2.4)$$

For this low excitation field strength E_0 the vibration exhibits only a single harmonic frequency component and oscillations around the equilibrium position $Q_{\text{IR}} = 0$, as revealed by the Fourier transform of the simulated time trace in Fig. 2.2 (b). The amplitude of the oscillations decreases exponentially due to a finite damping coefficient γ_{IR} .

At larger electric field strength, neglecting nonlinear coupling to other modes, the immediate nonlinear response of the system is due to the self-anharmonicity $\Delta V(Q_{\text{IR}}) = a_{\text{IR},n}Q_{\text{IR}}^n$ where $n = 1, 2, \dots$, of the individual mode Q_{IR} (see Fig. 2.2) [65]. The magnitude of the coefficients $a_{\text{IR},n}$ are determined by the symmetry of the ionic environment and, like in second harmonic generation, all even coefficients ($n = 2, 4, \dots$) vanish if the crystal shows inversion symmetry. The $\Delta V(Q_{\text{IR}})$ term immediately contributes to the equation of motion of the driven mode through the force acting on the eigenmode $F = -\nabla_{Q_{\text{IR}}} \Delta V(Q_{\text{IR}})$,

$$\ddot{Q}_{\text{IR}} + 2\gamma_{\text{IR}}\dot{Q}_{\text{IR}} + \nabla_{Q_{\text{IR}}} \Delta V(Q_{\text{IR}}) = Z_{\text{IR}}^* E \quad (2.5)$$

$$\Rightarrow \ddot{Q}_{\text{IR}} + 2\gamma_{\text{IR}}\dot{Q}_{\text{IR}} + \Omega_{\text{IR}}^2 Q_{\text{IR}} + a_{\text{IR},2}Q_{\text{IR}}^2 + a_{\text{IR},3}Q_{\text{IR}}^3 + a_{\text{IR},4}Q_{\text{IR}}^4 + \dots = Z_{\text{IR}}^* E(t). \quad (2.6)$$

Substituting the steady state solution of the harmonic oscillator into this equation the higher order terms Q_{IR}^n , will oscillate at multiples of the fundamental frequency $n\Omega_{\text{IR}}$, giving rise to higher harmonics of Ω_{IR} in the spectrum of the motion. Figure 2.2 (b) shows a solution of eq. 2.6 for a driving field strength of $E_0 \sim 10 \text{ MV/cm}$. The coefficients $a_{\text{IR},n}$ for this simulation have been determined by first-principles density functional theory (DFT) methods for the ferroelectric material LiNbO₃ [65] (see Appendix B.10). At this stronger driving field, corresponding to

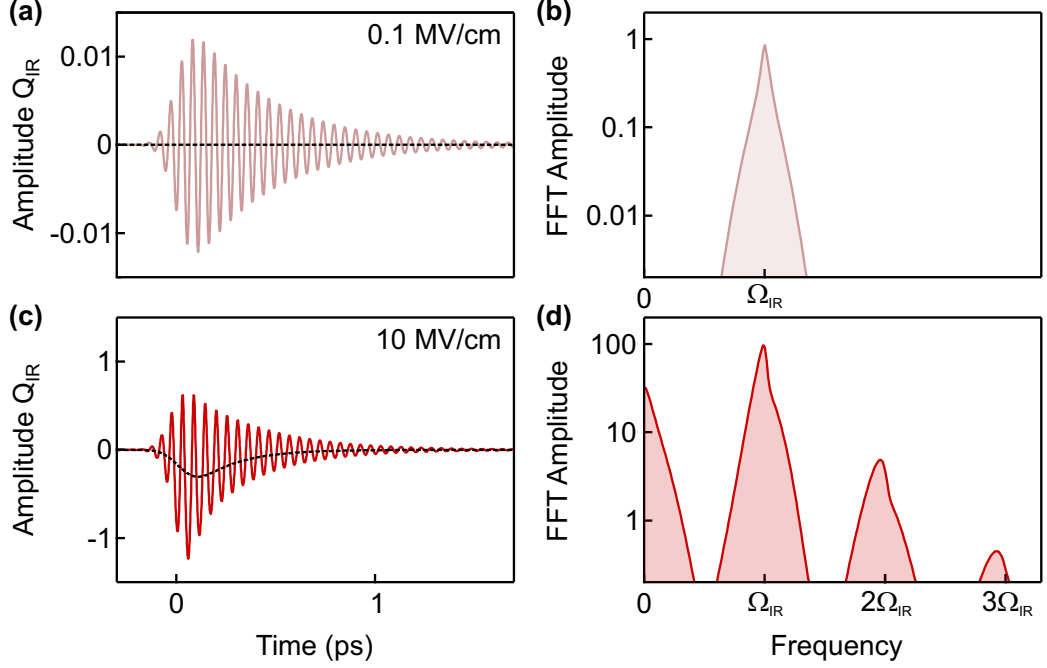


Figure 2.2: Simulations of harmonic and anharmonic lattice dynamics. (a) Simulated phonon amplitude Q_{IR} for a low field resonant excitation. At low driving fields ($E = 0.1 \text{ MV/cm}$) the lattice performs harmonic oscillations around the equilibrium position $Q_{\text{IR}} = 0$. (b) The corresponding FFT of the time-trace shows a single Lorentzian peak at the resonance frequency Ω_{IR} . (c) Simulated phonon amplitude Q_{IR} for a strong field ($E = 10 \text{ MV/cm}$). The high field oscillation involve motions at higher harmonics of Ω_{IR} and a rectified component (solid black line in panel (c)). (d) The corresponding FFT of the strong field response shows multiple peaks at high harmonics. The Lorentzian shape observed in the low field response in panel (b) becomes slightly distorted due to a renormalization of the resonance frequency at large amplitudes of Q_{IR} (see Appendix B.4).

an excitation at $E_0 \sim 10 \text{ MV/cm}$ peakfield, the oscillations are rectified to negative amplitudes, indicated by the black line in Fig 2.2 (c), and show the predicted additional spectral components at higher harmonics of the fundamental frequency Ω_{IR} (see Fig. 2.2 (d)). The nonlinear response is reminiscent of the high harmonic generation in nonlinear optics and indeed also contributes to the effective nonlinear coefficients $\chi^{(n)}$, though significantly less than its electronic counterpart [144]. Additionally, the instantaneous oscillation frequency $\Omega_{\text{IR}}(Q_{\text{IR}}(t))$ depends on the amplitude of the lattice vibration. This becomes obvious when rewriting the equation of motion,

$$\ddot{Q}_{\text{IR}} + 2\gamma\dot{Q}_{\text{IR}} + (\omega_{\text{IR}}^2 + a_3Q_{\text{IR}} + a_4Q_{\text{IR}}^2 + \dots)Q_{\text{IR}} = Z^*E(t), \quad (2.7)$$

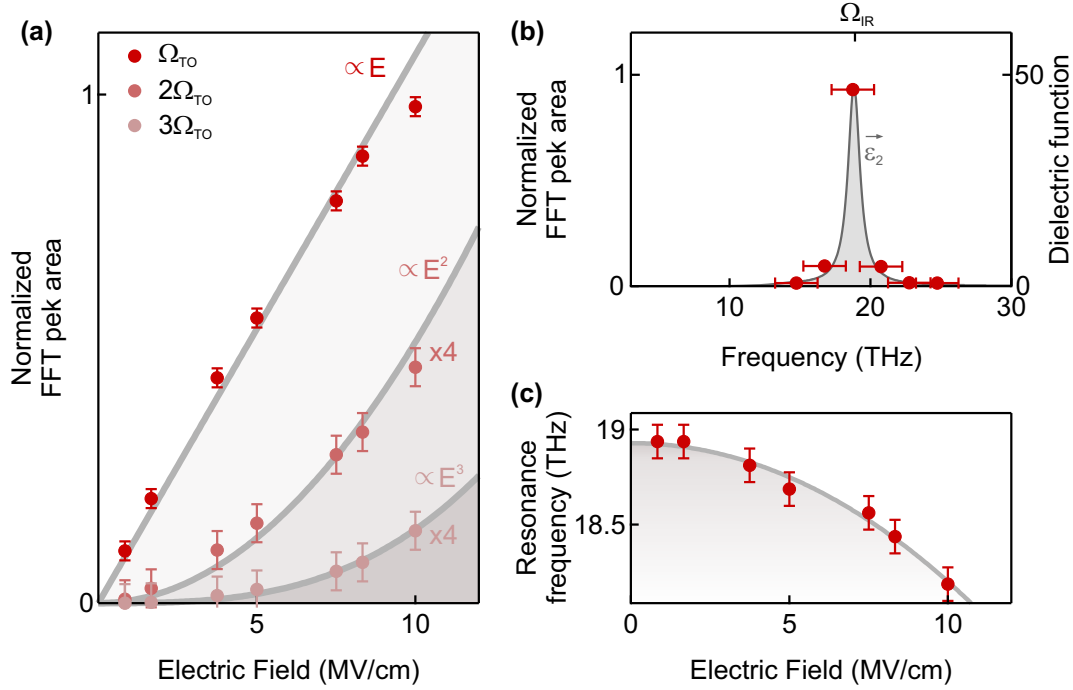


Figure 2.3: Simulated response characteristic of lattice vibrations at strong driving. (a) Simulated excitation field dependence of the first three harmonic components of the vibrational phonon amplitude. The higher harmonics (see Fig. 2.2 (d)) increase as a function of electric field and each harmonics follows a polynomial law (grey lines). The points were extracted by integrating over the individual harmonic peaks shown in Fig. 2.2 and for the second and third harmonic amplitudes are multiplied by four for clarity. (b) Simulated excitation frequency dependence of the vibrational phonon amplitude. For a fixed driving field strength ($E = 4$ MV/cm from panel (a)), the amplitude of the vibration Q_{IR} (red dots) peaks when the electric field frequency is in resonance with Ω_{IR} . The shape of the amplitude response follows the imaginary part of the dielectric function (grey). (c) Simulated electric field dependence of the frequency re-normalization of the phonon vibration. The resonance frequency renormalizes Ω_{IR} and becomes electric field dependent. The grey line is a fit of the form $\Omega_{IR}(E) = \Omega_{IR,0} - aE^2$ (see Appendix B.4).

yielding the instantaneous frequency of the oscillator:

$$\omega(Q_{IR}) = \sqrt{\omega_{IR}^2 + a_3 Q_{IR} + a_4 Q_{IR}^2 + \dots} \quad (2.8)$$

This leads to a temporal chirp of the oscillatory motion due to the exponential decay of the vibrational amplitude and an on average frequency re-normalization as is further discussed in Appendix B.4. This time-averaged frequency re-normalization results in a shift of the higher

harmonics away from integer multiples of Ω_{IR} . This is shown in Fig. 2.3 (c). The red points are determined by a fit to the peak of the fundamental oscillation (see Fig. 2.2 (b) and (d)).

The dependence of the different harmonic orders on the incident electric field can be determined by perturbation theory [78]. In this approach, the electric field is considered to be a small perturbation $\delta E = \lambda E$ to the equation of motion eq. 2.6. Also the total displacement $Q_{IR}(t)$ is expanded into orders of λ^n : $Q_{IR} = \lambda Q_1 + \lambda^2 Q_2 + \dots$. Then, in order to obtain a solution for an arbitrary value of λ every term proportional to λ , λ^2 etc. must satisfy the equation individually. This procedure yields

$$\lambda : \Rightarrow \ddot{Q}_1 + 2\gamma_{IR}\dot{Q}_1 + \omega_{IR}^2 Q_1 = Z_{IR}^* E \quad (2.9)$$

$$\lambda^2 : \Rightarrow \ddot{Q}_2 + 2\gamma_{IR}\dot{Q}_2 + \omega_{IR}^2 Q_2 + a_{IR,2} Q_1^2 = 0 \quad (2.10)$$

The lowest order equation is simply the harmonic equation of motion, for which the steady state amplitude $Q_{IR,0}$ is given by

$$Q_{IR,0}(\omega) = Q_1(\omega) = \frac{Z_{IR}^*/\mu}{\omega_{IR}^2 - \omega^2 - i\gamma_{IR}\omega} E_0 = \frac{Z_{IR}^*/\mu}{D(\omega)} E_0. \quad (2.11)$$

and therefore, the amplitude Q_1 grows linearly with the strength of the external electric field. Substitution of this expression into the second equation for Q_2 , eliminates Q_1 and allows one to determine the field dependence of Q_2 . As the term Q_1 enters quadratically into this equation the corresponding solution Q_2 will oscillate at twice the frequency as well as being rectified ($\Omega = 0$). Repeating the procedure from section 1.1.1 yields

$$Q_2(2\omega) = \frac{-a_{IR,2} Z_{IR}^{*2} / \mu^2}{D(2\omega) D(\omega)} E_0^2, \quad (2.12)$$

and shows that the second harmonic of the lattice vibration will grow as the square of the driving field strength. The scaling of the even higher harmonics can be predicted in an equal manner and yields that the amplitude of every harmonic scales with the driving electric field like a polynomial of the respective order i.e. $Q_{IR}(n\omega) = E_0^n$, as is shown in Figure 2.3 (a). The field dependence of the individual harmonics is determined by integrating over the individual peaks in Fig. 2.2 (d). However, at sufficiently strong driving fields the change of the instantaneous frequency due to renormalization becomes so dramatic, that the excitation can not be considered

as resonant anymore and the maximum amplitude saturates. This behavior is similar to that of the Duffing oscillator model [145, 146]. However, at moderately low fields ($E_0 \sim 4$ MV/cm) the amplitude of Q_{IR} peaks when driven at Ω_{IR} , and the amplitude response follows the imaginary part of eq. 2.11, as shown in Fig. 2.3 (b). Here, the red dots are determined by integrating over the harmonic peaks in Fig. 2.2.

2.2.2 Nonlinear Coupling of a Strongly Driven Lattice Vibration

If the driven mode is excited to amplitudes, at which the nonlinear effects discussed above become significant, it can also couple nonlinearly to other vibrational modes of the solid. This nonlinear coupling between two and up to four lattice modes is described by terms signified in eq. 2.1,

$$V_{\text{lattice}}(Q_{\text{IR}}, Q_{2\dots}, E) = \sum_{\text{IR}, j, k, l} g_{\text{IR}jk} Q_{\text{IR}} Q_j Q_k + h_{\text{IR}ijkl} Q_{\text{IR}} Q_j Q_k Q_l + \dots \quad (2.13)$$

according to the symmetry restrictions discussed above. It is these coupling terms, that are responsible for the macroscopic thermal conductance and thermal expansion [141, 147]. Their coherent control through ultra-short laser pulses allows for the manipulation of the crystal structure on fs-timescales [52, 58, 62]. These *nonlinear phononics* were first observed experimentally in 2011, in which coherent oscillations of a Raman mode coordinate were induced by resonant excitation of an infrared-active phonon [52, 53]. Since then other aspects of this nonlinear phonon-phonon interaction were demonstrated, involving ultra-fast x-ray diffraction techniques for the detection of the ensuing lattice dynamics [54, 58]. The next paragraphs will focus on a theoretical description of nonlinear phononic coupling in centrosymmetric materials.

2.2.3 Cubic Coupling $Q_i^2 Q_j$

The lowest order cubic term that involves coupling between two lattice modes was first considered theoretically already in the 1970s as *Ionic Raman scattering* [55–57]. These early works predicted that the excitation of an infrared-active lattice vibration replaces the intermediate electronic state in conventional Raman scattering. Hence, this process solely relies on the lattice anharmonicities, instead of electron-phonon scattering. In conventional Raman scattering, where the driving force acting onto the Raman mode is proportional to the square of the electric field E^2 and therefore is a unidirectional force within the duration of the excitation pulses

[93, 132]. Similarly, ionic Raman scattering exerts a unidirectional force onto a coupled Raman mode Q_R and rectifies the Raman mode coordinate as long as the optically excited phonon Q_{IR} has a finite amplitude. This becomes clear when substituting the term $gQ_{IR}^2 Q_R$ into the equation of motion of the two lattice modes,

$$\ddot{Q}_{IR} + 2\gamma_{IR}\dot{Q}_{IR} + (\omega_{IR}^2 + \mathbf{g}Q_R)Q_{IR} + \nabla_{Q_{IR}}\Delta V(Q_{IR}) = Z_{IR}^*E(t) \quad (2.14)$$

$$\ddot{Q}_R + 2\gamma_R\dot{Q}_R + \omega_R^2 Q_R + \mathbf{g}Q_{IR}^2 = 0. \quad (2.15)$$

The driven mode Q_{IR} exerts a force proportional to Q_{IR}^2 onto the mode Q_R which is, $\sim \sin^2(\omega_{IR}t) \sim 1 - \cos(2\omega_{IR}t)$, and therefore follows the envelope of the vibrational motion of Q_{IR} . This rectified component leads to a time averaged displacement and a quasi-static change of the crystal structure along the Q_R coordinates. Further, if the driving pulse $E(t)$ is short compared to the Raman oscillatory period $1/\Omega_R$, then Q_R is impulsively excited to an oscillatory motion around the transiently displaced coordinate $Q_{R,disp}$ (see Fig. 2.4 (c) and (d)). Conversely, the displaced Raman mode acts back onto the driven mode and linearly renormalizes its frequency as $\omega_{IR}^2(Q_R) = \omega_{IR,0}^2 + gQ_R$ (see Fig. 2.4 (b) and (f) and Appendix B.3). Figure 2.4 shows the solutions of the equations of motion of Q_R and Q_{IR} for a driving pulse tuned into resonance with the infrared-active mode (see eq. 2.4) and effective peak field strength $E_0 \sim 10$ MV/cm. The steep rise of the envelope of Q_{IR} leads to coherent oscillations and quasi-static displacement of Q_R . The latter can be understood as a displacement of the potential energy of the coupled mode to a new ‘equilibrium’ position as displayed in Fig. 2.4 (d). Finally, this nonlinear coupling must conserve the total momentum and since the infrared mode is driven at $k = 0$, only Raman modes at wave vector $q = 2k = 0$ can be excited.

2.2.4 Quartic Coupling $Q_i^2 Q_j^2$ and $Q_i^3 Q_j$

Higher order nonlinear phononics involving the interaction of three or more modes as predicted by eq. 2.1 has eluded experimental verification until recently [65, 148]. This type of coupling not only allows for the interaction of infrared and Raman modes through $Q_{IR}^2 Q_R^2$ but also coupling of odd (infrared) modes. However, for Raman-modes the nonlinear coupling effects are dominated by cubic coupling and eq. 2.15. For infrared-active modes in an inversion-symmetric material, these cubic terms are forbidden by symmetry and the lowest-order nonlinear-phononic coupling

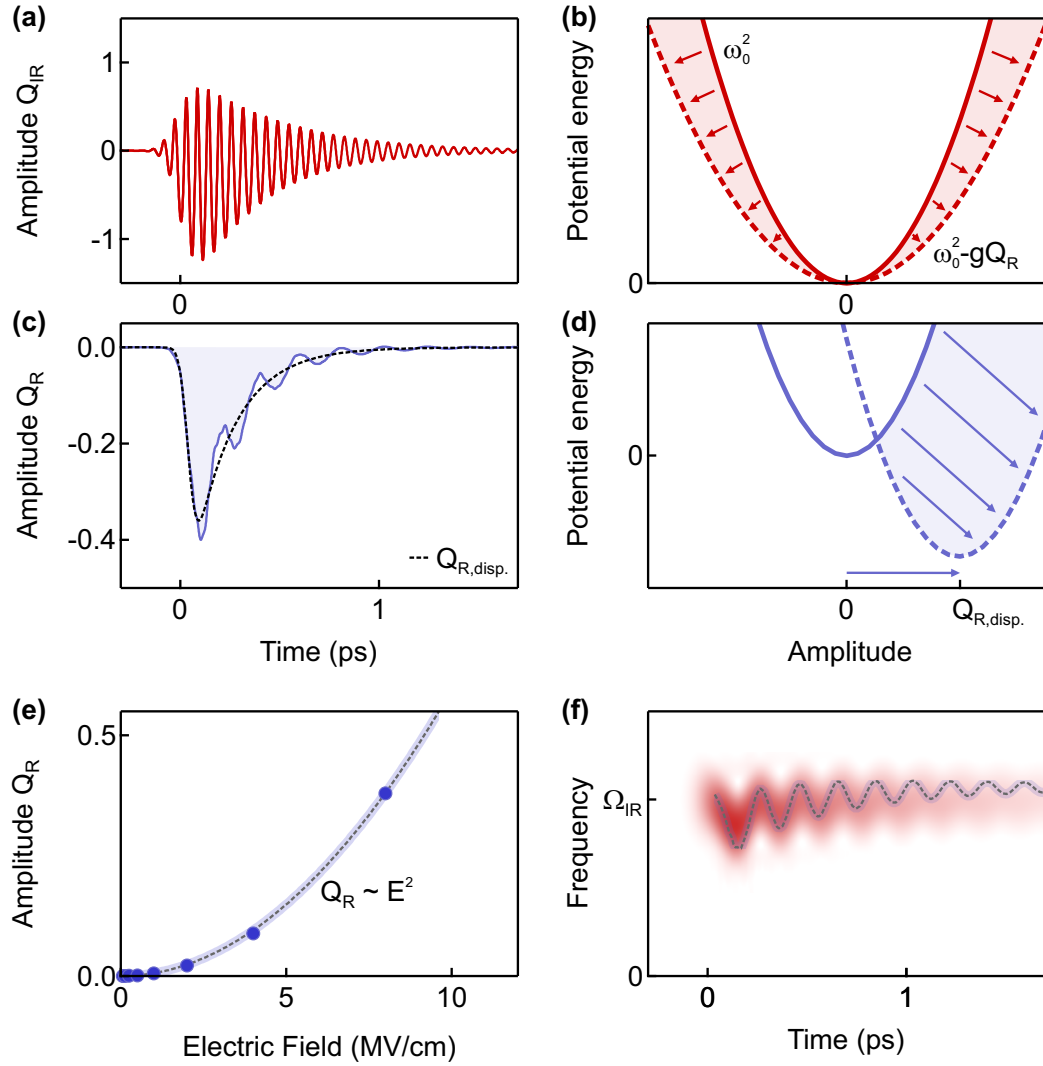


Figure 2.4: Simulations of $Q_{\text{IR}}^2 Q_{\text{R}}$ phonon coupling. (a) Simulated phonon amplitude Q_{IR} for strong resonant excitation. The strongly driven infrared mode Q_{IR} can couple to a Raman mode Q_{R} which leads to its quasi-static displacement (dashed line in panel (c)). (b) Changes of the potential energy of the driven mode due to the back-action of the Raman mode. The coupling renormalizes the frequency $\omega_{\text{IR}}^2(Q_{\text{R}}) = \omega_{\text{IR},0}^2 + gQ_{\text{R}}$ (see panel (f)), which is visualized as a periodic modulation of the potential energy of the driven mode. (c) Simulated phonon amplitude Q_{R} of a coupled mode for the strong resonant excitation of panel (a). A short excitation pulse ($\Delta t < 1/\Omega_{\text{R}}$) impulsively excites the Raman mode to oscillations at its eigenfrequency Ω_{R} , around the displaced equilibrium position. (d) Changes of the potential energy of the coupled mode. The quasi-static displacement can be understood as a shift of the potential energy, which results in a unidirectional force $F = gQ_{\text{IR}}^2$ acting on Q_{R} so long as $Q_{\text{IR}} \neq 0$. (e) Simulated excitation field dependence of the coupled mode amplitude Q_{R} . The displacement and the amplitude of the coherent oscillations of Q_{R} scale with the square of the excitation field E . (f) Simulated temporal modulation of the infrared mode frequency $\Omega_{\text{IR}}(t)$ extracted by a windowed FFT. The displacement and oscillatory motion of Q_{R} (dashed line) change the instantaneous frequency of Q_{IR} (shaded red).

term is $h_{ijkl}Q_iQ_jQ_kQ_l$. Again, for the coupling coefficient h_{ijkl} to be non-zero the product of the irreducible representation $I(Q_{\text{IR},1}) \times I(Q_{\text{IR},2}) \times I(Q_{\text{IR},3}) \times I(Q_{\text{IR},4})$ has to contain the totally symmetric A_g -symmetry. A combination of infrared modes that always fulfill these symmetry restrictions is

$$\Delta V(Q_{\text{IR}}, Q_{\text{P}}) = hQ_{\text{IR}}^2Q_{\text{P}}^2 \quad (2.16)$$

because the totally symmetric irreducible representation A_g is part of the product of any irreducible representation with itself, $A_g \subset I(Q_{\text{IR}}) \times I(Q_{\text{IR}})$. Importantly, coupling of this type (distinct from cubic coupling) can lead to the creation of pairs of phonons with opposite wavevectors $\mathbf{q}_1 = -\mathbf{q}_2$, even when the excited phonon is at zero momentum $\mathbf{q}_{\text{IR}} = 0$. A consequence of the bi-quadratic coupling of the type $Q_{\text{IR}}^2Q_{\text{P}}^2$ is a mutual modulation of the frequencies of both vibrations,

$$\ddot{Q}_{\text{IR}} + 2\gamma_{\text{IR}}\dot{Q}_{\text{IR}} + (\omega_{\text{IR}}^2 + hQ_{\text{P}}^2)Q_{\text{IR}} + \nabla_{Q_{\text{IR}}}\Delta V(Q_{\text{IR}}) = Z_{\text{IR}}^*E(t) \quad (2.17)$$

$$\ddot{Q}_{\text{P}} + 2\gamma_{\text{P}}\dot{Q}_{\text{P}} + (\omega_{\text{P}}^2 + hQ_{\text{IR}}^2)Q_{\text{P}} = 0. \quad (2.18)$$

As a result, the force acting on Q_{P} ,

$$F(Q_{\text{P}}) = hQ_{\text{IR}}^2Q_{\text{P}}, \quad (2.19)$$

remains zero if its initial amplitude before excitation $Q_{\text{P}}(t < 0)$, is equal to zero. Consequently, even though the resonance frequency Ω_{P} and the potential energy of Q_{P} are modulated, the mode remains motionless (see Fig. 2.5 (a) and (b)). However, if $Q_{\text{P}}(t < 0) \neq 0$, Q_{P} will experience exponential gain (and Appendix B.5) as long as Q_{IR} is oscillating (see Fig. 2.5 (c), (d), (e)). This behavior is a parametric amplification and is reminiscent to the optical light conversion in second-order nonlinear optical ($\chi^{(2)}$) media discussed in Chapter 1 and Appendix A.2. Key characteristics of parametric amplification is always the time dependence of the oscillator's parameters, i.e., its frequency $\Omega_{\text{P}}(t)$ in the case of bi-quadratic coupling (see Fig. 2.5 (f))[146]. Even though the bi-quadratic term $Q_{\text{IR}}^2Q_{\text{P}}^2$ can lead to parametric amplification the cubic-linear coupling $Q_{\text{IR}}^3Q_{\text{P}}$ typically dominates the quartic order nonlinear response among infrared active modes at early times. However, due its cubic-linear form the symmetry selections rules for $Q_{\text{IR}}^3Q_{\text{P}}$ significantly restricts this process, because not every product group of coupled modes

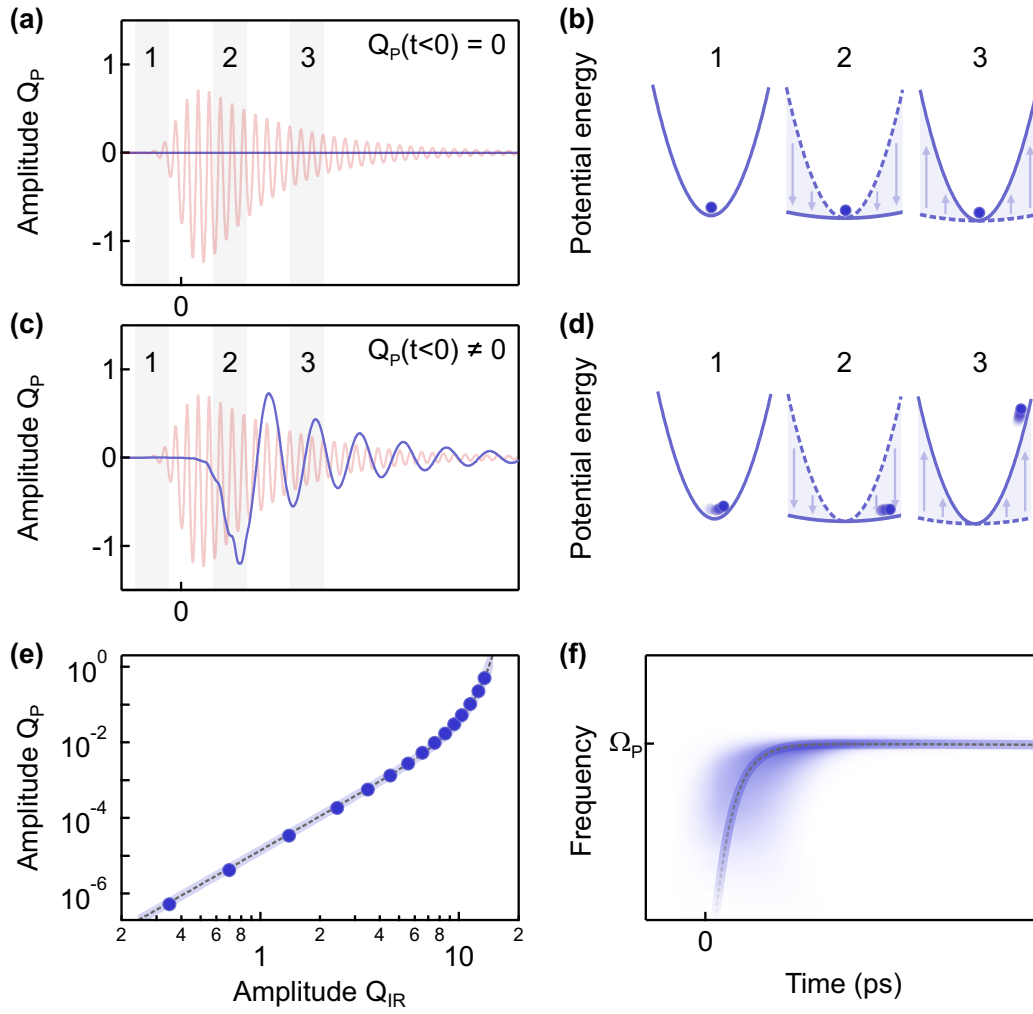


Figure 2.5: Simulations of $Q_i^2 Q_j^2$ phonon coupling. (a) Simulated phonon amplitude Q_P for a strong field resonant excitation as in Fig. 2.2. If the amplitude of the coupled mode Q_P is zero for times before the excitation pulse drives the infrared mode Q_{IR} ($Q_P(t < 0) = 0$) then the force acting on Q_P due to the quartic coupling term $Q_{\text{IR}}^2 Q_P^2$ is zero and Q_P remains motionless. (b) This situation is captured by considering the potential energy of the coupled mode which is periodically modulated by Q_{IR}^2 only at $Q_P \neq 0$. (c) If $Q_P(t < 0) \neq 0$, Q_P is excited to finite amplitude and will experience exponential gain as long as Q_{IR} is excited (see panel (e)). (d) Potential energy of Q_P when $Q_P(t < 0) \neq 0$. A small, but finite initial potential/kinetic energy of Q_P is amplified to a large excursion. (e) Simulated excitation strength dependence of the coupled mode amplitude Q_P as function of the driven mode amplitude Q_{IR} . The cumulative energy gain (depicted in (d)) leads to an exponential increase (dashed line) of the vibrational amplitude of Q_P . (f) Simulated softening of the coupled mode mode frequency $\Omega_P(t)$. For large enough driving amplitude Q_{IR} the instantaneous frequency $\Omega_P(Q_{\text{IR}})$ (shaded blue) almost reaches zero and relaxes back to the equilibrium frequency as Q_{IR}^2 . At longer times, the energy transfer from Q_{IR} to Q_P stops and Q_P performs oscillations at its equilibrium resonance frequency Ω_P .

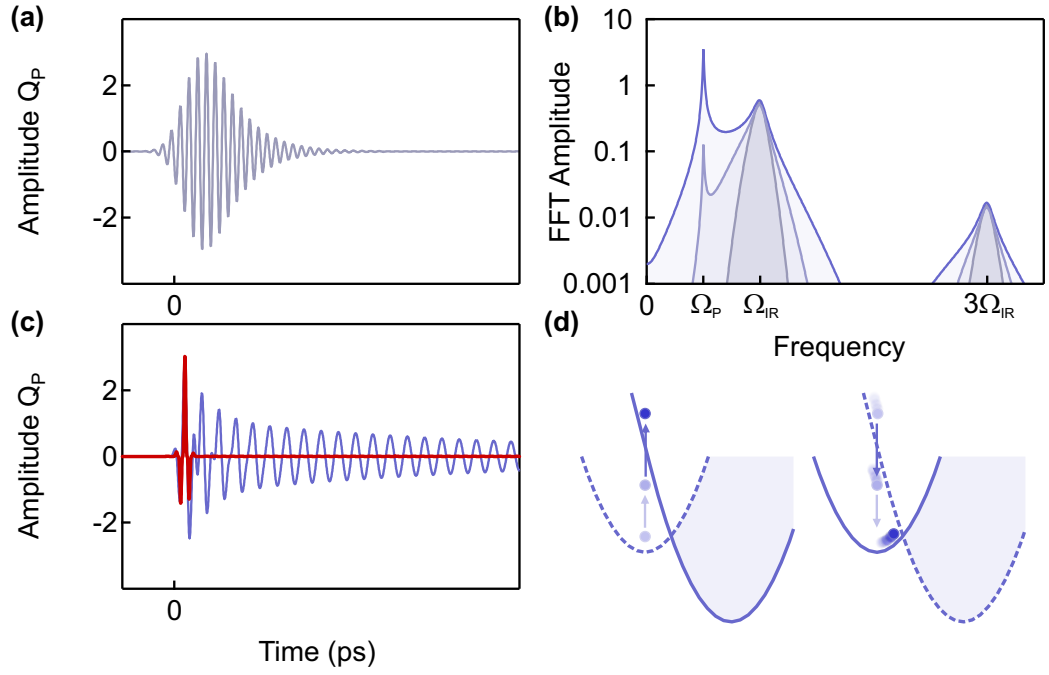


Figure 2.6: Simulations of $Q_i^3 Q_j$ phonon coupling. (a) Simulated phonon amplitude Q_P for a strong field resonant excitation as in Fig. 2.2. A long driving pulse ($1/\Delta t < \Omega_{IR} - \Omega_P$), excites Q_P to oscillations at Ω_{IR} and $3\Omega_{IR}$ but not at its eigenfrequency Ω_P (grey peaks in panel (b)). (b) Simulated FFT Amplitude spectra for three different excitation durations of the coupled mode similar to panel (a). If the pulse duration of the excitation pulse and consequently the rise time of Q_{IR} becomes shorter than $\Delta t < 1/(\Omega_{IR} - \Omega_P)$, Q_P starts oscillating at its resonance frequency Ω_P (sharp peak). (c) The imbalance of the oscillations of Q_{IR} on the rising flank lead to an impulsive force onto Q_P (red curve) and as a result to sustained oscillations at Ω_P . (d) Sketch of the evolution of the potential energy of the coupled mode during the optical excitation. Sketch of the potential energy of Q_P at two times. The short impulse shifts the potential energy of Q_P to the lower right/left (solid blue line) and instantaneously increases the potential energy of the motion (blue dot). The sudden gain of potential energy is partially converted into kinetic energy (blurred dots) while the potential energy is shifted back to its equilibrium position (solid blue line).

contains the totally symmetric representation. In practice, the term leads to a force proportional to Q_{IR}^3 which acts onto the coupled mode,

$$\ddot{Q}_{IR} + 2\gamma_{IR}\dot{Q}_{IR} + \omega_{IR}^2 Q_{IR} + \mathbf{3h}Q_{IR}^2 Q_P + \nabla_{Q_{IR}} \Delta V(Q_{IR}) = Z_{IR}^* E(t) \quad (2.20)$$

$$\ddot{Q}_P + 2\gamma_P \dot{Q}_P + \omega_P^2 Q_P + \mathbf{h}Q_{IR}^3 = 0. \quad (2.21)$$

Figure 2.6 shows solutions of the equation of motion for the coupled phonon amplitude Q_P . For a comparably long excitation pulse ($T > 1/\Omega_P$), Q_P oscillates at Ω_{IR} and $3\Omega_{IR}$ but not at its own resonance frequency Ω_P (see Fig. 2.6 (a) and (b)). This is a result of the odd force term which, different to the quadratic force term Q_{IR}^2 for cubic coupling, on average does not lead to a net energy transfer between Q_{IR} and Q_P . However, for short excitation pulses $E(t)$ the imbalance of the oscillations of Q_{IR} on the rising edge leads to an impulsive force onto Q_P . This short impuls is drawn as a red line in Fig. 2.6 (c) and excites sustained oscillations at the resonance frequency Ω_P shown by the blue curve in Fig. 2.6 (c) and by the amplitude FFT spectrum in panel Fig. 2.6 (b) (sharp peak).

This becomes more apparent when considering the frequency domain. The impulsive force exhibits a broad spectrum, which covers the resonance frequency of the coupled mode, i.e., $1/T < \Omega_P - \Omega_{IR}$. This can be seen in Fig. 2.6 (b), which shows the FFTs of three simulated time traces for different excitation pulse duration. Only when the width of the excitation pulse spectrum (shaded Lorentzian), centered around Ω_{IR} , covers Ω_P a net energy transfer from the driven mode to the coupled mode is possible and Q_P performs sustained oscillations at its resonance frequency (sharp peak in Fig. 2.6 (b)). For increasingly shorter excitation pulse durations T the amplitude of these sustained oscillations increases as shows for three different values of T in Fig. 2.6 (b). These impulsively excited oscillations are then further amplified by the bi-quadratic term $Q_{IR}^2 Q_P^2$.

All these considerations can equally be applied to materials with broken inversion symmetry. However, the distinction between even and odd modes (A_g vs A_u etc.) breaks down (see Chapter 1) and (almost) every product of two irreducible representations includes the totally symmetric group A . This implies that in materials with broken inversion symmetry coupling of the type $g_{ijk} Q_i Q_j Q_k$ is also possible between infrared active modes. This becomes important in materials where the macroscopic material properties are entangled with the displacement of an infrared active mode Q_P , such as ferroelectrics.

2.3 Nonlinear Phononics in LiNbO₃: Experimental demonstration

These theoretical predictions of nonlinear phononic effects have already been demonstrated in several experiments. An infrared active lattice mode, resonantly excited by a strong field mid-infrared pulse, was shown to excite oscillations of Raman active modes probed by Raman scattering of near-infrared pulses in bulk crystals of La_{0.7}Sr_{0.3}MnO₄ [52] and YBa₂Cu₃O_{6.5} [53]. These experiments were corroborated by ultra-fast x-ray diffraction experiments that revealed the transient deformation of the crystal lattice along the coupled Raman mode coordinates through cubic coupling $gQ_{\text{IR}}^2 Q_{\text{R}}$ [58]. A set of experiments on SiC involving both excitation and detection resonant with an infrared-active mode revealed nonlinearities in the excitation process itself and of the driven phonons, in the time-domain [149]. However, these experiments were missing an amplitude and phase sensitive probe of infrared active lattice vibrations to reveal coherent oscillations of the driven mode infrared active mode. The following paragraphs will present work done in the scope of the thesis project and introduce ultra-fast second harmonic generation as a quantitative tool to measure the amplitude and phase of polar lattice dynamics directly in the time domain. At the same time new insights into ultra-fast materials control and the measurement of interatomic forces will be presented.

2.3.1 Reconstruction fo the Interatomic Potential of LiNbO₃

2.3.1.1 Properties of insulating ferroelectric LiNbO₃

The experiments presented in the next paragraphs were conducted on LiNbO₃, which crystallizes in a non-centrosymmetric trigonal unit cell with $3m$ symmetry (see Fig. 2.7 (a)). Below $T_c = 1200^\circ\text{C}$ [113], the Li and Nb sublattices are displaced against the oxygen octahedra. Hence, the material develops a static ferroelectric polarization P_s along the rhombohedral (111) direction that corresponds to the hexagonal z -axis. The existence of a static polarization implies a broken symmetry concomitant with a finite second order nonlinearity $\chi^{(2)}$. The corresponding $\chi^{(2)}$ -tensor of the $3m$ pointgroup is given by

$$\chi^{(2)} = \begin{pmatrix} 0 & 0 & 0 & 0 & d_{15} & -d_{22} \\ -d_{22} & d_{22} & 0 & d_{15} & 0 & 0 \\ d_{31} & d_{31} & d_{33} & 0 & 0 & 0 \end{pmatrix} \quad (2.22)$$

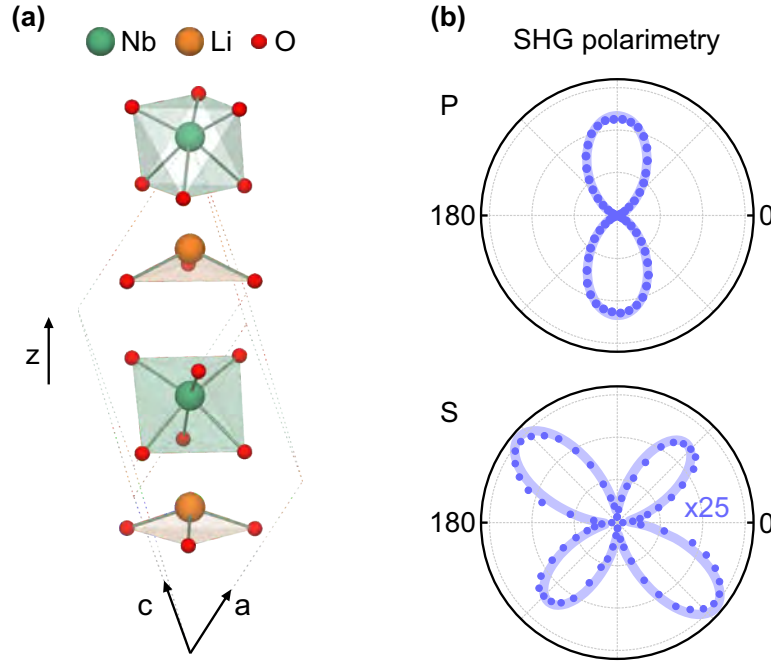


Figure 2.7: Structure of ferroelectric LiNbO₃. (a) LiNbO₃ crystallizes into a non-centrosymmetric trigonal unit cell with $3m$ point group symmetry. Below $T_c \approx 1200^\circ\text{C}$, the Li and Nb sublattices are displaced against the oxygen octahedra and the material develops a static ferroelectric polarization P_s along the hexagonal z -axis. (b) SH-polarimetry measurements on LiNbO₃. The analyzer was oriented along the z -axis (P analyzer) and xy -axis (S analyzer).

which results in a static SH-polarimetric response as shown in Figure 2.7 (b). Here, P and S denote the analyzer orientation along the crystal c -axis and a - b -axis, respectively. The SH light polarized along the c -axis is significantly more intense than the in-plane component. The values of the tensor elements $\chi_{ij}^{(2)}$ are linearly proportional to P_s , making the SH intensity a good measure of the static polarization [113, 150].

The low-frequency optical properties for light polarized along the LiNbO₃ c -axis are dominated by two optical phonon modes at 7.8 and 18.9 THz. It also includes a weak mode at 8.2 THz and a feature at 21 THz, which has been attributed to two-phonon absorption [151]. All these modes appear as peaks in the imaginary part of the dielectric function shown in Fig. 2.8 (a). The mode that was excited in the experiment is denoted with $\Omega_{TO} = 18.9\text{ THz}$ and the respective longitudinal optical frequency is at $\Omega_{LO} = 26\text{ THz}$. Figure 2.8 shows the THz reflectivity spectrum of the investigated sample (grey line), measured via Fourier transform infrared spectroscopy (FT-IR), together with fits of the four (dashed line) Lorentzian oscillators.

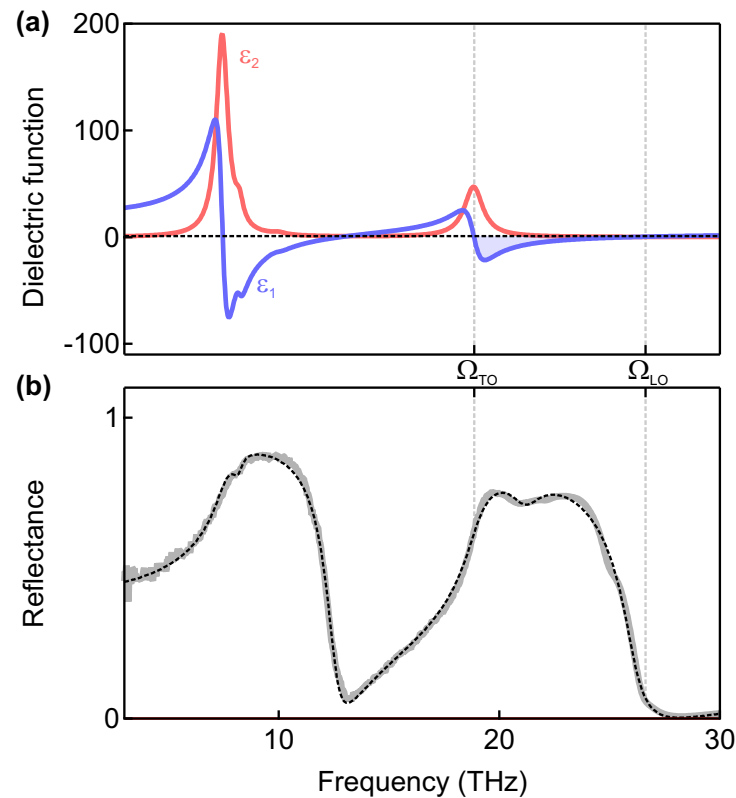


Figure 2.8: Optical properties of ferroelectric LiNbO₃. (a) Dielectric function of LiNbO₃ along the c-axis. The real part is drawn in red and the imaginary component of the dielectric functions is drawn in blue. The low-frequency linear optical properties in LiNbO₃ are dominated by two optical phonon modes at 7.9 and 18.9 THz together with weaker modes at 8.2 THz and a feature at 21 THz. (b) Reflectivity spectrum of LiNbO₃ along the c-axis. The driven oxygen vibration has a resonance frequency of $\Omega_{TO} = 18.9$ THz and corresponding longitudinal frequency of $\Omega_{LO} = 26$ THz.

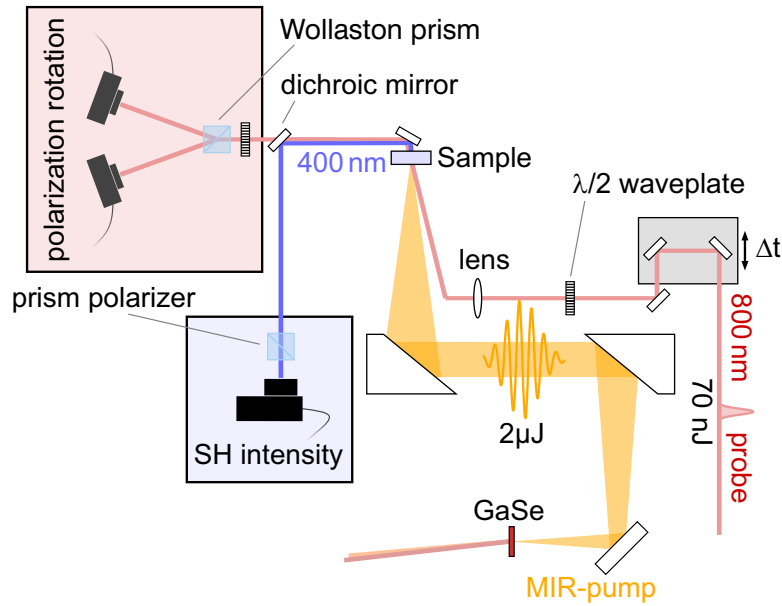


Figure 2.9: Schematic of the time-resolved second harmonic and polarization rotation detection setup. 30-fs, 800-nm pulses with 70 nJ pulse energy are used for second harmonic generation in single domain LiNbO₃ crystals. The polarization of these probe-pulses are controlled by a $\lambda/2$ waveplate. After interaction with the sample the SH beam is separated from the fundamental 800-nm light by a dichroic mirror. Polarization sensitive detection is achieved by using a prism polarizer in the SH beam before detection with a photomultiplier tube (PMT). The polarization of the 800-nm light is analyzed by balancing the intensity on two photodiodes by a $\lambda/2$ waveplate and a Wollaston prism. The pump-pulses for the experiment are generated by difference frequency generation in GaSe (see Appendix A.3). CEP stable mid-infrared pump pulses of 2 nJ to 3 nJ pulse energy and frequencies tunable from 15 THz to 30 THz are focused by a telescope to a spotsize of 60 μm to achieve peak-field strength of up to 30 MV/cm [29].

2.3.1.2 Time-Resolved Second Harmonic Detection Setup

Figure 2.9 depicts a schematic of the optical setup developed to simultaneously measure the time-resolved SH intensity emitted from the sample and the linear polarization rotation of the 800-nm probe light (both in transmission). For the pump-probe experiment, a telescope delivers CEP stable mid-infrared pump pulses (2 μJ to 3 μJ pulse energy) to the sample and focuses the beam to a lateral spot size of 60 μm [29]. The center frequency and temporal profile of these pulses were determined by electro-optic sampling (see Appendix A.5). Figure 2.10 shows the real-space motions of the highest frequency infrared-active vibration of LiNbO₃, which was excited by mid-infrared pulses tuned to a center frequency $\nu_{\text{MIR}} = 17.5$ THz, slightly red-shifted

compared to the TO phonon frequency ($\Omega_{\text{TO}} = 18.9 \text{ THz}$) [151, 152] (see Fig. 2.10 (c)). The spectrum of this pulses (shaded yellow in Fig. 2.10 (b)) still covered the phonon frequency, plotted as a red peak in Fig. 2.10 (c), within its bandwidth ($\Delta\nu \approx 6 \text{ THz}$). The corresponding electric field transient is shown in the inset of Fig. 2.10 (b).

The resultant dynamics were measured by 30 fs, 800 nm pulses with 70 nJ pulse energy which impinge the sample at a 1 kHz repetition rate. These pulses pass through a $\lambda/2$ -waveplate, to control their linear polarization, and a lens to focus the beam to a 25 μm spot size on the sample. After passing through the sample the SH beam is separated from the fundamental 800-nm light by a dichroic mirror. An analyzer (prism polarizer) in the SH beam selects a specific polarization of the SH light which is detected with a highly sensitive photomultiplier tube (PMT). The polarization of the 800-nm light is analyzed by balancing the intensity on two photodiodes by a $\lambda/2$ -waveplate and a Wollaston prism.

The time-resolved dynamics are measured by changing the relative time of arrival of pump and probe-pulses on the sample. This is done by using a translation stage in the beam path of the 800 nm probe-pulses. The time-delay Δt is controlled by moving the stage incremental from time delays $\Delta t < 0$ (probe arrives before pump) to time delays $\Delta t > 0$ (pump arrives before probe). The changes of the SH intensity and the 800-nm polarization rotation (PR) induced by optical pumping with respect to pump-probe time delay are electronically read-out by lock-in amplifiers which lock into the rotation frequency of a mechanical chopper that modulates the mid-infrared pump beam at half the laser repetition rate.

2.3.1.3 High-Order Nonlinear Phononics: Experimental Results

In the linear response regime, the real space distortions of the excited TO-phonon mode involve rotations of the oxygen octahedra around the c-axis, accompanied by c-axis motions against the Nb and Li sublattices (see Fig. 2.10 (a)). Due to the broken inversion symmetry of the crystal, the A_1 mode is both Raman and infrared active with an electric dipole moment along the c axis. Crucially, a stable absolute carrier-envelope-phase of the MIR pump field made it possible to directly follow the atomic trajectories in both amplitude and phase. An electro optic sampling measurement of the electric field transient is shown in the inset of Fig. 2.10 (b). Without the CEP stability the phase-linked atomic motions would average to zero due to the inherent multi-shot nature of these pump-probe experiments. Spectral interferometry between the PR

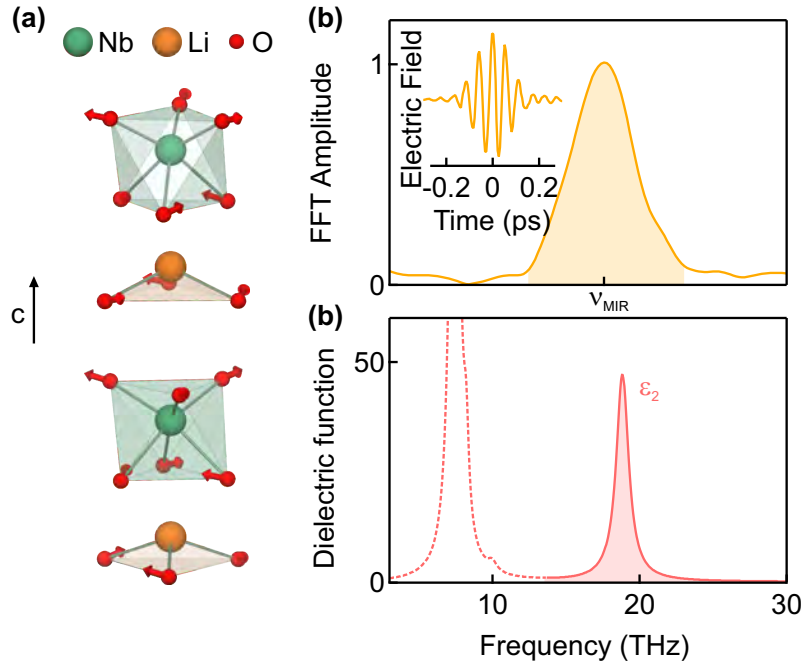


Figure 2.10: Resonantly driven A₁ lattice vibration in LiNbO₃. (a) Real space motions of the highest frequency A₁ mode of LiNbO₃. These involve rotations of the oxygen octahedra, accompanied by c-axis motions against the Nb and Li sublattices. (b) Spectrum and electric field transient (inset) of the generated MIR pulses, measured by EOS. In the experiment the A₁ mode was excited with mid-infrared femtosecond pulses, tuned to $\nu_{\text{MIR}} = 17.5$ THz, slightly red-shifted compared to the TO phonon frequency ($\Omega_{\text{TO}} = 18.9$ THz). The center frequency and temporal profile of these pulses was determined by electro-optic sampling (see Appendix A.5). (c) Imaginary part of the dielectric function of LiNbO₃ and the spectral width of the MIR pulses used (shaded in yellow) to excite the highest frequency mode (red).

and SH signal and a local oscillator derived from the same probe pulse yielded both phase and amplitude of the phonon dynamics [132, 134, 136]. The time resolution of these experiments was dictated by the bandwidths of the local oscillators on the detector, plotted in Fig. 2.11, and calculated using eq. 1.55 (see Chapter 1) to be 16 and 12 fs for the SH and PR, respectively [136, 153]. Hence, these measurements are able to resolve coherent oscillations up to 60 and 80 THz in SH and PR, respectively, and are thus sensitive to the phase of oscillations up to the fifth overtone of the excited TO phonon mode.

For small amplitude excitation (0.1 MV/cm peak electric field), both PR and SH measurements yielded harmonic oscillations (see Fig. 2.12 (a) and (c) dashed lines), which were readily attributed to a combination of harmonic oscillations of a 15-THz phonon-polariton and the 19-

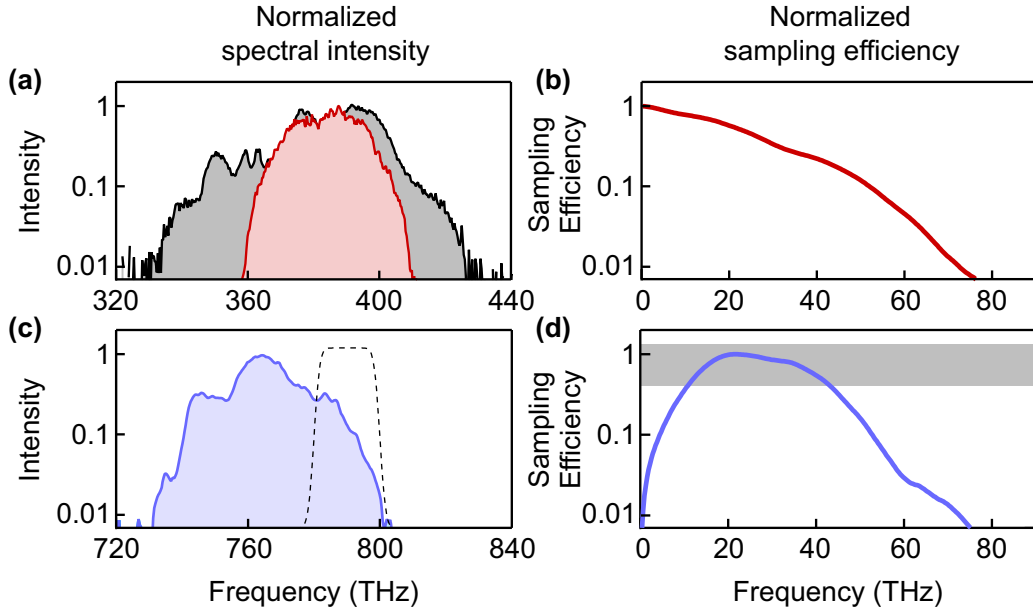


Figure 2.11: Sampling efficiency of the time-resolved SH experiment. (a) Spectrum of the 800-nm probe pulse before (red) and after (grey) propagation through the unpumped LiNbO₃ crystal in units of THz. (b) The sampling efficiency of the 800-nm light was calculated with the spectrum shown in panel (a). (c) The spectrum of the generated SH light (blue curve) is a factor of $\sqrt{2}$ broader than the incident spectrum of the 800-nm probe and is plotted together with the normalized transmission of the bandpass filter placed in front of the photo-multiplier tube (dashed curve). (d) The sampling efficiency of the SH light with the spectrum shown in panel (c) is almost constant in the 15 THz to 45 THz region. The figure and caption are adapted from [65].

THz TO phonon of the A₁ mode [154]. The pump-probe spectrum of this small-field response is well understood by considering the phase-matching between the probe pulses and the phonon-polariton propagating inside the crystal [92, 155] as explained in Chapter 1 and Appendix B.2. At high a pump field (20 MV/cm electric field), a strongly anharmonic response was observed in both PR and SH signals, shown as solid lines in Fig. 2.12 (a) and (c). Figure 2.12 (b) and (d) display the corresponding amplitude spectra. In addition to the fundamental frequency components of the harmonic oscillator, a number of high harmonics appeared. The most pronounced peaks were found at multiples of the 15-THz phonon-polariton mode, visible up to $n = 5$ (75 THz). The amplitudes of the first three harmonics, obtained by integrating over the respective peaks at $\nu = 15, 30$ and 45 THz in Fig. 2.12 (c), display a linear, quadratic and cubic dependence respectively on the excitation field as predicted by eq. 2.4 and 2.12 and shown in Figure 2.13(a). The PR spectrum also exhibits peaks at the sum and difference frequencies of

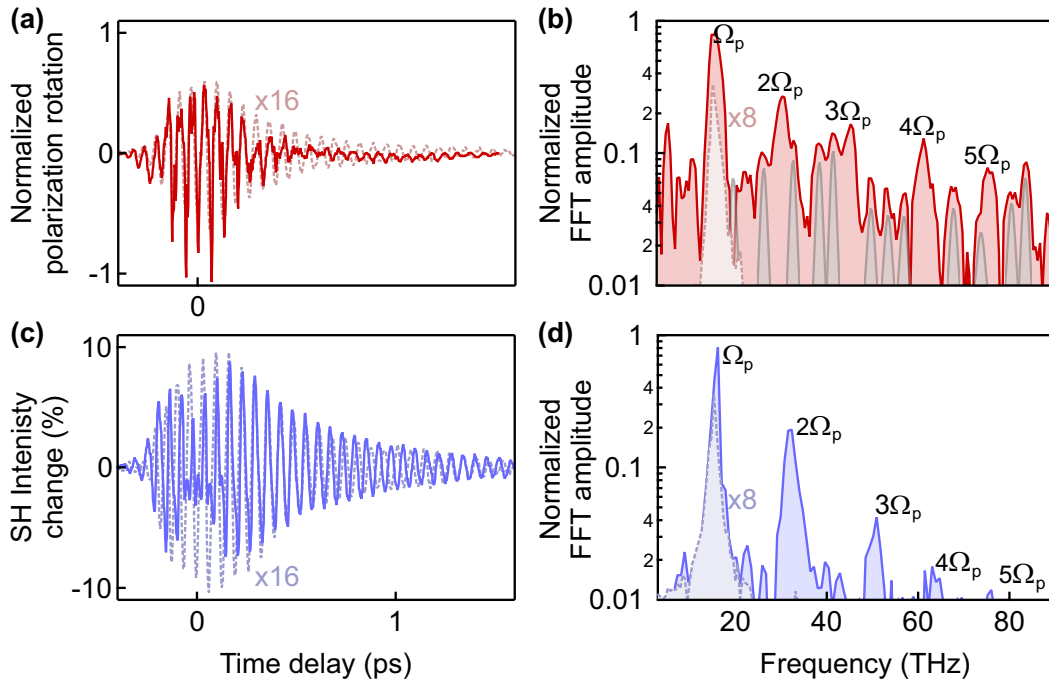


Figure 2.12: Time-resolved SH intensity and polarization rotation signals. (a) The time-resolved polarization rotation of the 800-nm probe for a low excitation field ($E = 0.1$ MV/cm, dashed light red) showed harmonic oscillations with a single frequency component (dashed peak in panel (b)). At a higher excitation field ($E = 20$ MV/cm, full red curve) the oscillations become highly anharmonic and asymmetric. The corresponding FFT in panel (b) shows peaks at higher harmonic of the phonon-polariton frequency Ω_p and sum- and difference frequencies with Ω_{TO} . (c) The time-resolved SHG measurements also showed harmonic oscillations (dashed light blue) with a single frequency component (dashed peak in panel (d)) for the low excitation field ($E = 0.1$ MV/cm). At the higher excitation field ($E = 20$ MV/cm, full red blue) the oscillations become highly anharmonic and the corresponding FFT in panel (d) shows peaks at higher harmonic of the phonon-polariton frequency Ω_p . No peaks at sum and difference frequencies appeared in the SH measurements.

these harmonics. Of note, the harmonics appear slightly red-shifted with respect to the integer multiples, as expected from a nonlinearly driven lattice vibration. This red-shift was predicted by eq. 2.8 and is due to the frequency renormalization at large vibrational amplitudes (see Appendix B.4). A pump frequency dependence of the amplitude response at ν_p is shown in Figure 2.13 (b). The red data points were determined by integrating over the peak centered around ν_p for an excitation field of 5 MV/cm. To obtain comparable results for the different excitations fields the responses were normalized by the penetrations depth (grey line) which changes from 400 nm close to Ω_{TO} to about 3 μm below Ω_{TO} and above Ω_{LO} . As predicted by eq. 2.11 the

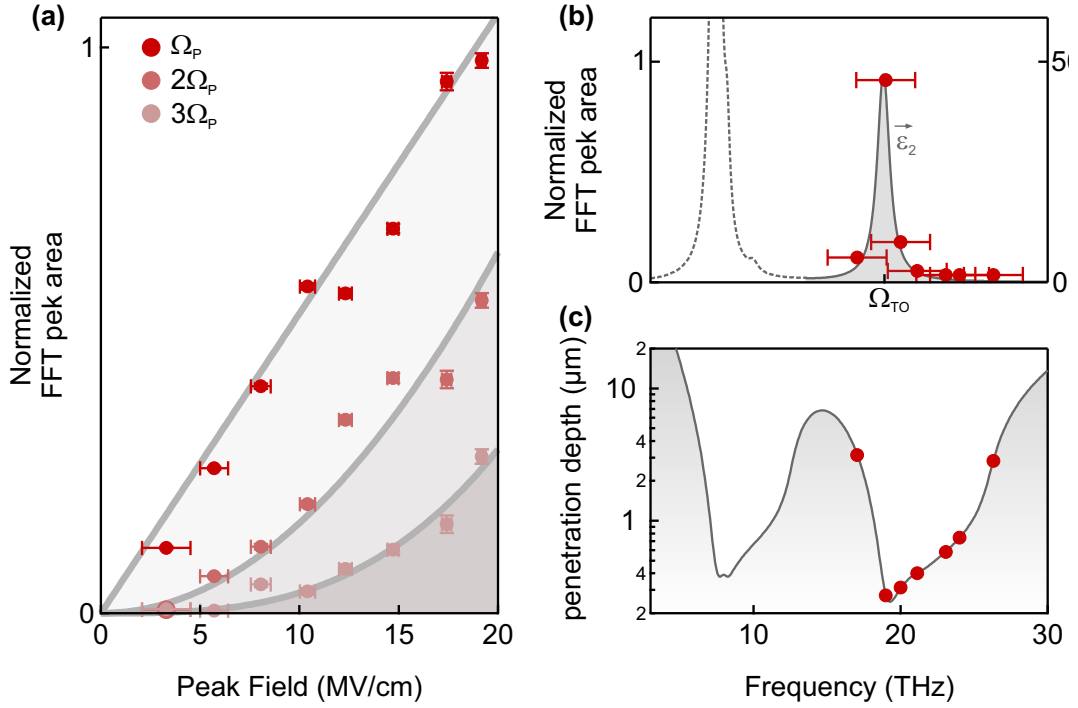


Figure 2.13: Experimental response characteristic of lattice vibrations at strong driving. (a) Experimental excitation field dependence of the first three harmonic components of the time-resolved SH-signal. The higher harmonics (see Fig. 2.12) increase as a function of electric field and each harmonics follows a polynomial law (grey lines). The fundamental oscillation amplitude at Ω_p scales linear with the excitation field, the second harmonics at $2\Omega_p$ quadratically and the third harmonic at $3\Omega_p$ cubically. (b) Experimental excitation frequency dependence of the vibration amplitude of the time-resolved SH-signal. For a given driving field strength, the amplitude of the coherent oscillations peak when the driving field frequency is in resonance with Ω_{TO} . The shape of the amplitude response follows the imaginary part of the dielectric function (grey) as predicted by Fig. 2.3. (c) Frequency-dependent penetration depth of LiNbO₃. To obtain comparable results for the different excitations fields the responses were normalized by the penetrations depth (grey line) which changes from 400 nm close to Ω_{TO} to about 3 μm below Ω_{TO} and above Ω_{LO} . The red points denote the center frequencies of the MIR pulses.

total amplitude response peaks in resonance with the TO phonon frequency and follows the imaginary part of the dielectric function $Im(\epsilon)$, which is associated with the energy transfer from the light field to the solid. From the presented data alone, the amplitudes of the atomic velocities can only be quantified up to a constant B as the absolute values of the second order nonlinearity $\partial\chi_{ijk}^{(2)}/\partial Q_{IR}$ are not unknown. Still, the nonlinear theory discussed in the previous paragraph adequately explains these observations.

2.3.1.4 FDTD-Simulations of Anharmonic Phonon-Polariton Propagation

An even more comprehensive description of our experimental observations can be obtained by considering the propagation of the excited phonon-polaritons. To this end finite difference time-domain simulation combining Maxwell's equations with the nonlinear lattice eq. 2.1, were carried out. Figure 2.14 (a) displays the amplitude of the propagating total electric field as a function of sample depth d and time t . Both the phonon-polaritons and the broadband radiation emitted from the anharmonic motions propagate from the surface into the bulk, following the dispersion imposed by the material. By integrating the simulated total electric field along the 800-nm light line $d_{800} = v_g t$ for each pump-probe time delay Δt , exemplarily sketched by the red line for a delay of 0.3 ps in Fig. 2.14 (a), we can calculate the response measured in the time-resolved PR experiments. Figure 2.14 (c) shows the simulated time trace which yields qualitative agreement with the polarization-rotation measurement that are shown in Fig. 2.12. Figure 2.14 (e) displays the corresponding amplitude spectrum, which comprises peaks at all sum and difference frequencies of the polariton and the TO mode, also in agreement with the experiment (see Fig. 2.12 (b)).

As introduced in Chapter 1, a coherent vibration at frequency Ω generates radiation frequency-shifted from the second harmonic field E_{SH} due to hyper-Raman scattering. This implies that the detected spectral interferometry signal from the second harmonic intensity I_{SH} is proportional to the velocity of the lattice oscillation $I_{\text{SH}}(\Delta t) = B\dot{Q}_{\text{IR}}(\Delta t)$. Therefore, we can compare the simulations of Fig. 2.14 with experiments of Figs. 2.12 (b) and (d) by spatially integrating the time derivative of the simulated lattice coordinate $Q(t, z)$ along the 400-nm light line, shown as a dashed blue line in Fig. 2.14 (b). This integral was taken over the first 2 μm beneath the surface, where the SH light is generated in the experiment [64]. The simulated signal $I_{\text{SH}}(\Delta t)$ is plotted in Fig. 2.14 (d) and contains frequency components at multiples of 16 and 19 THz, evidenced in the corresponding Fourier transform in Fig. 2.14 (f), in agreement with the measured data of Figs 2.12 (d).

2.3.1.5 Reconstruction of the Interatomic Potential

Ultimately, the knowledge of $\dot{Q}_{\text{IR}}(\Delta t)$, enables the reconstruction of the microscopic lattice potential $U(Q)$ explored during each oscillation cycle. This can be done by considering the coherent vibration of the lattice mode at times after the pump pulse, that is when no external

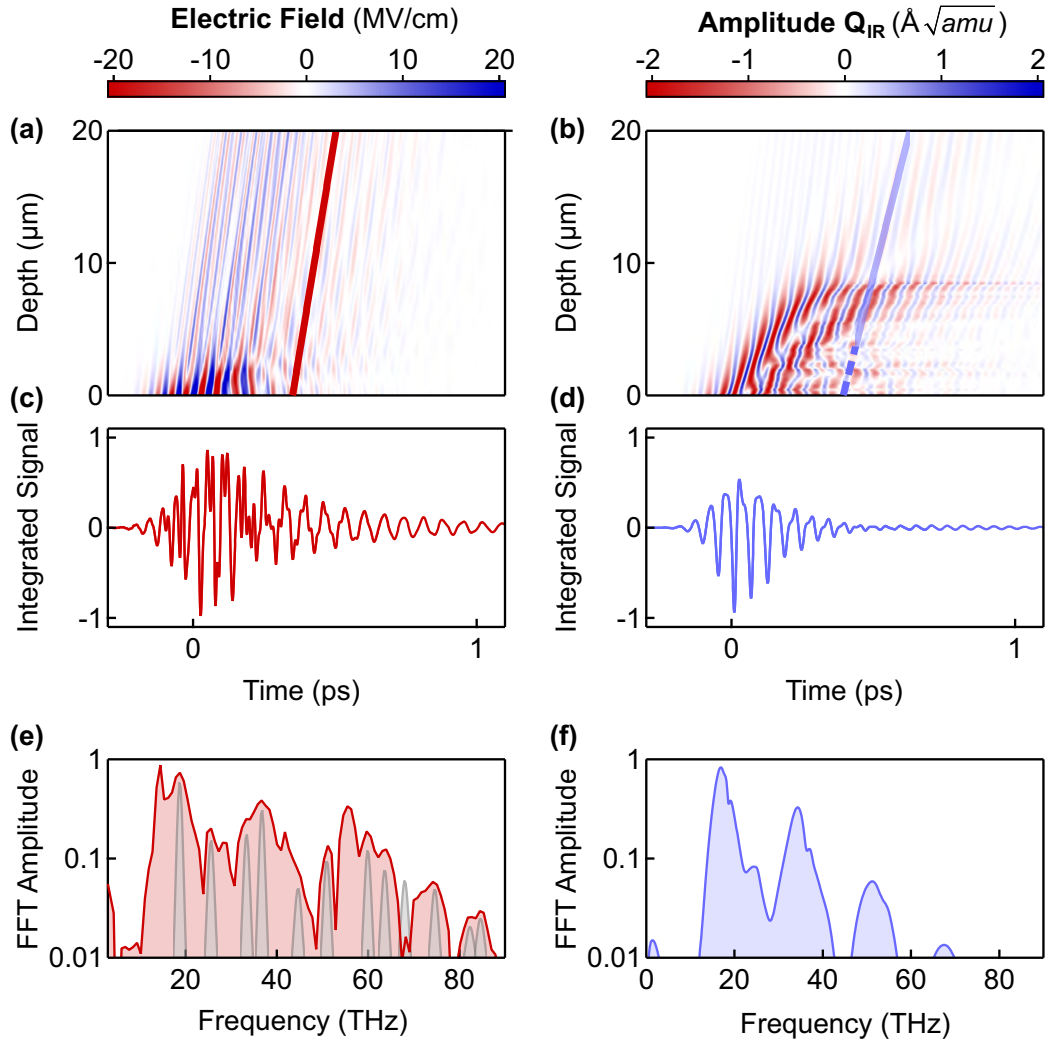


Figure 2.14: FDTD phonon-polariton propagation simulations. (a) The FDTD-simulations allow us to plot the electric field as a function of depth d and time t inside LiNbO₃ after mid-infrared excitation. The red solid line shows the propagation of the 800-nm probe pulse for one pump-probe time delay Δt , following the relation $d_{800} = v_{g,800}t$ with $v_{g,800}$ the group velocity at 800-nm waveneght. (c) The time trace derived by integrating along the dashed red line in panel (a) for all pump-probe delays and the corresponding amplitude spectrum shows a similar qualitative response as the experimental PR time-trace. (e) The spectrum shows harmonics of Ω_p and Ω_{TO} as well as mixed frequencies. (b) The results of the FDTD-simulations of the vibrational amplitude Q_{IR} after the same mid-infrared excitation as in panel (a) allow for the comparison with the SH experiment. The partly dashed blue line shows the propagation of the SH light at 400 nm, also for a single time delay Δt . (d) Through spatially integrating the time derivative of Q_{IR} along the dashed blue line within the first $2\mu\text{m}$ for all pump probe delays one obtains a response like the experimental SH time trace. (f) The FFT Amplitude spectrum of panel (e) shows broad peaks at the harmonics of Ω_p like in the experiment. Part of the figure and caption are adapted from Ref. [65].

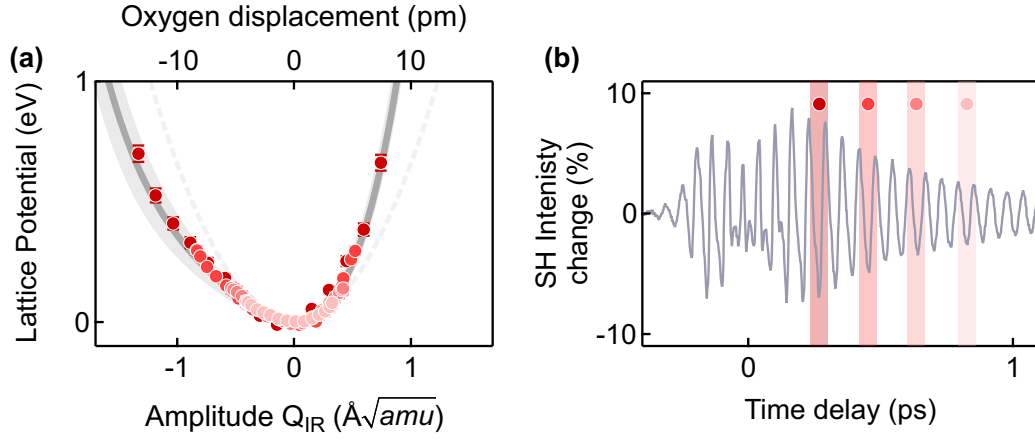


Figure 2.15: Reconstructed A_1 mode potential energy. (a) Reconstructed potential energy of the driven lattice mode. The potential energy of the A_1 mode (dark grey line) could be reconstructed from different cycles (red colored circles) of the time-resolved SH measurement shown in panel (b). The grey solid line is the mode potential obtained by DFT calculations and the grey shaded area is an estimate of its systematic uncertainties. The experimental potential is scaled to the calculated potential using a single scaling factor (see Appendix B.1). From this comparison, one can estimate a maximum mode excursion of $1.4 \text{ \AA}\sqrt{amu}$, corresponding to ~ 14 pm displacements of the oxygen atoms from their equilibrium positions. The dashed curve is the potential in the harmonic approximation. Part of the figure and caption are adapted from Ref. [65]

force is being applied. For weak phonon damping ($\gamma \ll \Omega$) the total energy ε of the free oscillations can be approximated as being constant over each cycle $V(\Delta t) + E_{\text{kin}}(\Delta t) = \varepsilon$. Then, the instantaneous potential energy $V(\tau) = \varepsilon - E_{\text{kin}}(\Delta t)$ can be retrieved from the knowledge of the kinetic energy, which is in turn proportional to the square of the measured second harmonic signal $E_{\text{kin}}(\tau) = 1/2\dot{Q}(\Delta t)^2 = 1/2I_{\text{SH}}(\Delta t)^2/B^2$. The instantaneous potential energy $V(\Delta t)$, which is now known bar the proportionality term $1/B^2$, can then be converted into $V(Q)$ by integrating the second harmonic signal $I_{\text{SH}}(\Delta t) = B\dot{Q}(\Delta t)$ over time, which yielded $Q(\Delta t)$. Hence, this procedure allowed us to extract the shape of the lattice potential with only a single proportionality constant remaining unknown. To obtain an estimate for the proportionality constant B and compare the validity of the reconstruction, Figure 2.15 compares the potential energy of the A_1 -mode calculated from DFT (grey line) to the reconstructed potential (filled circles). The two curves were matched by adjusting the single free parameter B by a fit (see Appendix B.1). Within the systematic uncertainties of the DFT calculations illustrated by the

grey shaded area, both curves agree up to the highest amplitudes reached experimentally. The comparison allows for an estimate of the maximum amplitude of the total displacement of the oxygen atoms to be 14 pm, which is about 7% of the next nearest neighbor distance!

2.3.2 Nonlinear Phonon Coupling: Experimental Results

At these extreme atomic displacements, close to the Lindemann criterion for the melting of a crystal lattice [156], the coupling to other lattice modes was predicted to be significant. Density functional theory calculations predicted that this coupling is dominated by the interaction of high-frequency infrared modes and the infrared mode which is responsible for the ferroelectric polarization Q_P , mediated cubic order coupling $Q_{IR}^2 Q_P$ [63]. In ferroelectric materials, this type of coupling between two infrared active modes is allowed due to the less strict symmetry selection rules of the broken inversion symmetry pointgroup. The essential physics of the theoretical model presented Ref. [63] can be demonstrated on a minimum model, which is illustrated in Fig. 2.16. The potential energy of the ferroelectric mode Q_P is modeled as a double well potential, as shown in Figure 2.16 (a),

$$V(Q_P) = -\frac{1}{4}\Omega_P^2 Q_P^2 + \frac{1}{4}c_P Q_P^4 \quad (2.23)$$

where potential minima correspond to the two oppositely poled states of the ferroelectric. Ω_P is the resonance frequency of ferroelectric mode for a certain temperature below the Curie temperature [64]. The dominant coupling between the driven infrared mode Q_{IR} and the ferroelectric mode Q_P was predicted to be of the type $gQ_{IR}^2 Q_P$ [63] and the two resulting equations of motion for the driven and coupled mode are,

$$\ddot{Q}_{IR} + 2\gamma_{IR}\dot{Q}_{IR} + (\omega_{IR}^2 + \mathbf{g}Q_P)Q_{IR} + \nabla_{Q_{IR}}\Delta V(Q_{IR}) = Z_{IR}^* E(t) \quad (2.24)$$

$$\ddot{Q}_P + 2\gamma_P\dot{Q}_P - \frac{1}{2}\omega_P^2 Q_P + c_P Q_P^3 + \mathbf{g}Q_{IR}^2 = 0. \quad (2.25)$$

Upon driving the high frequency mode, the double well potential deforms, and raises and lowers the occupied and unoccupied potential minimum, respectively. This is shown in Fig. 2.16 (a) in a frozen phonon picture for three amplitudes Q_{IR} . For a small driven phonon amplitude Q_{IR} , the occupied minimum remains a stable local minimum protected by energy barrier and the ferroelectric mode Q_P will adiabatically follow the dynamic potential minimum. This is shown Fig. 2.16 (b) (light blue curve) by solving the equations of motion eq. 2.24 and eq. 2.25 below

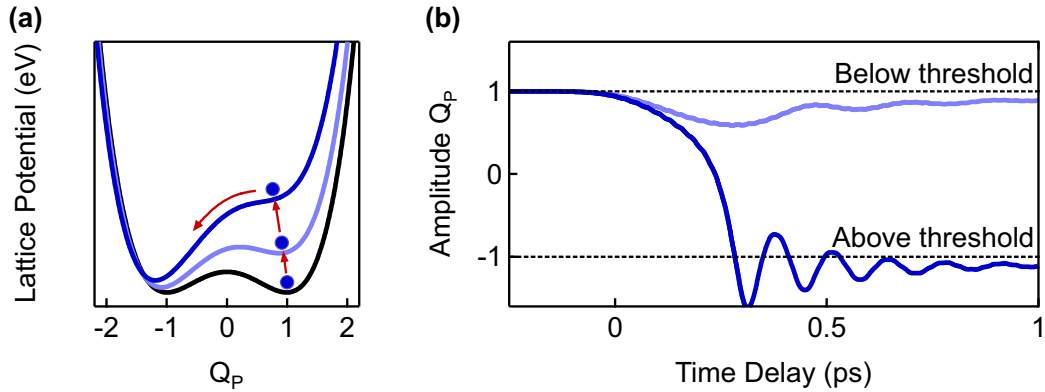


Figure 2.16: Minimal Model of nonlinear phononic ferroelectric switching. (a) Lattice potential energy of the ferroelectric mode as a function of the amplitude Q_P . The lattice potential energy in equilibrium (black line) exhibits two minima at $Q_P \pm 1$ which correspond to the two oppositely poled states of the ferroelectric. In a frozen phonon picture, for finite amplitudes of the driven mode Q_{IR} the potential will be distorted (light and dark blue lines) and Q_P will be displaced along the red arrows. (b) Simulated phonon amplitude Q_P for two excitation strengths. For an excitation strength below the switching threshold (light blue) the solutions of the equations of motion predict a small displacement of Q_P away from its equilibrium position $Q_P = 1$. Above the switching threshold (dark blue) Q_P rapidly displaces and moves into the oppositely poled state. Part of the figure and caption are adapted from Ref. [64]

the switching threshold. After excitation, Q_P is displaced from its equilibrium position (dashed line, $Q_P = 1$) but quickly relaxes back to its initial state. For a larger driven amplitude Q_{IR} , the occupied potential minimum is destabilized, and the system is forced into the oppositely poled state (blue curve in Fig. 2.16 (a)).

The solution for this above threshold excitation is shown in Fig. 2.16 (b) (dark blue curve). After excitation, Q_P is rapidly displaced into the oppositely poled state ($Q_P = -1$) and performs highly damped oscillations around its new equilibrium position. This model is highly simplified but captures the key predictions of the theory published in Ref. [63]. These are the excitation threshold, a resonant effect at the Ω_{IR} and polarization reversal independent of the initial state, i.e., polarization reversal should always be observed starting from both equilibrium states without changing the pump pulse characteristics [64].

This type of nonlinear phonon coupling leads to the idea of ultra-fast reversal of the ferroelectric polarization P_s by light. As mentioned in the introductory paragraph to LiNbO₃, the static values of the tensor elements $\chi^{(2)}$ are linearly proportional to P_s . The changes of the second

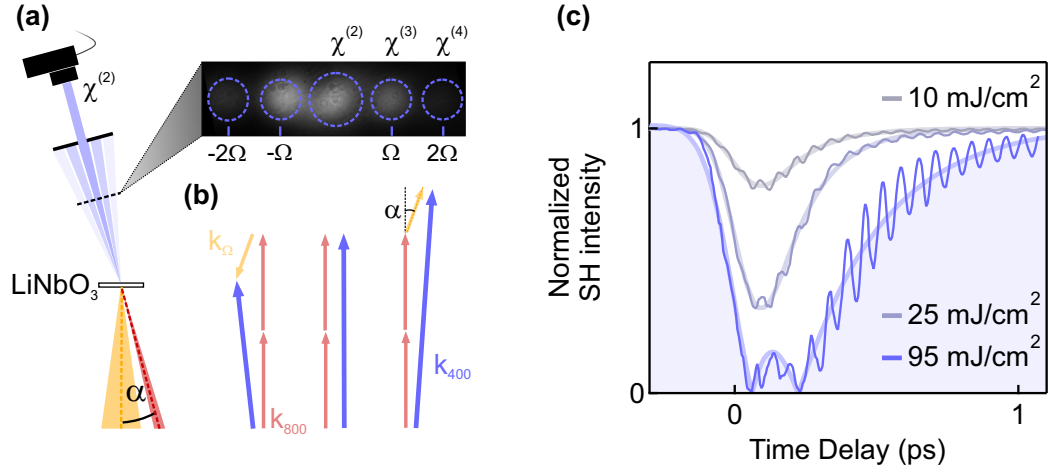


Figure 2.17: Spatial-filtering of different nonlinear processes in time-resolved SHG. (a) Schematic of a non-collinear SH pump-probe geometry. Conservation of momentum leads to a deflection of the SH when higher order $\chi^{(3)}$ or $\chi^{(4)}$ processes involve interaction with more than two fields. The deflection angle is given by the angle between pump and probe α and the amplitude of the wavevector of the fields involved in the scattering (k_{Ω} , k_{800} , k_{400}). The SH light generated by the second order process $\chi^{(2)}$ does not get deflected and spatial filtering allows for its selective detection. (b) Schematic of the conservation of momentum in the non-linear scattering process. The arrows denote the wavevector of the 800 nm (red), 400 nm (blue) and the MIR light (yellow). (c) Measured time-resolved $\chi^{(2)}$ -component of the SH-light. The time-resolved second harmonic intensity is normalized to its value before excitation. After resonant excitation of the highest A_1 in LiNbO₃, the SH intensity decreases (grey curves). This drop increases with pump fluence. For fluences above the threshold value, 60 mJ/cm², the second harmonic signal vanishes completely, followed by a transient recovery before relaxing back to its equilibrium value. Part of the figure and caption are adapted from Ref. [64].

order nonlinearity due to an infrared active phonon mode $\partial\chi^{(2)}/\partial Q_{\text{IR}}$ discussed so far act as a modulation around this static value of $\chi^{(2)} \propto P_s$. Therefore, the measurement of only the $\chi^{(2)}$ of the second harmonic intensity generated by the 800-nm wavelength pulses would allow one to follow the time-dependent dynamics of P_s .

To isolate the $\chi^{(2)}$ response, higher order contributions near the second-harmonic frequency $2\nu_{\text{Probe}}$, most notably those descending from cubic $\chi^{(3)}$ nonlinearities at frequencies $2\nu_{\text{Probe}} \pm \nu_{\text{MIR}}$, were filtered spatially by making use of the momentum transfer in the nonlinear scattering process. By choosing an oblique incidence with angle α between pump and probe, as can be seen in Figure 2.17 (a), the SH light descending from higher orders ($\chi^{(3)}, \chi^{(4)}, \dots$) will be deflected from the $\chi^{(2)}$ -component due to conservation of momentum. This is exemplarily depicted in Fig. 2.17

for the nonlinear mixing between pump and probe due to the $\chi^{(3)}$ -nonlinearity (electric field induced second harmonic generation). The resulting wavevector of the 400 nm light k_{400} is the sum of the wavevectors of the MIR light k_{Ω} and two times the wavevector of the 800 nm light k_{Ω} , either in forward scattering (right) or backward scattering (left). The deflection angle can be determined from the angle α and the wavelength of the MIR light inside the material. Therefore, the signal contribution descending from $\chi^{(2)}$ can be isolated by filtering out the deflected beams using a pinhole.

Figure 2.17 (b) displays the isolated $\chi^{(2)}$ response measured for three excitation fluences. For the lowest fluence fluence (10 mJ/cm², grey curve), the SH intensity reduces by 20% from its equilibrium value, which was normalized to 1. This depletion of the $\chi^{(2)}$ -component increases when increasing the fluence to 25 mJ/cm² (light blue curve). At the maximum fluence possible in our setup (95 mJ/cm²), the second-harmonic intensity was observed to completely disappear, recover to a finite value, and then go to zero again, before relaxing back to the equilibrium intensity. To confirm that this behavior at the highest fluence is related to an overshoot of the ferroelectric distortion into the oppositely poled state, i.e., a transient reversal of the polarization, it is necessary to determine the absolute sign of $\chi^{(2)}$. This is because, in the case which of a transient reversal the sign of $\chi^{(2)}$ would change. However, from the measurement of the SH intensity $I_{\text{SH}} \propto |\chi^{(2)}|^2$ alone it is impossible to determine this sign of $\chi^{(2)}$.

To derive whether the ferroelectric polarization was indeed reversed during these dynamics, the time-dependent phase of the SH electric field was measured by interfering it with a reference SH field, generated in a second LiNbO₃ crystal that was not excited by a mid-infrared pulse, as sketched in Fig. 2.18 (a). The resulting pattern, which consisted of pronounced fringes on top of a Gaussian background (see Appendix B.9), was detected with a charge coupled device (CCD) camera,

$$I_{\text{total,SH}}(\varphi(\Delta t)) = \left| |E_{\text{SH}(\Delta t)}| e^{i\varphi(\Delta t, x)} + |E_{\text{SH,ref}}| e^{i\varphi_{\text{ref}}} \right|^2 \quad (2.26)$$

$$= |E_{\text{SH}(\Delta t)}|^2 + |E_{\text{SH,ref}}|^2 + 2 |E_{\text{SH,ref}}| |E_{\text{SH}(\Delta t)}| \cos(\varphi(\Delta t)) \quad (2.27)$$

Changes in the phase of the second-harmonic signal generated in the driven LiNbO₃ crystal appeared as changes in the spatial position of these fringes on the camera. Figure 2.18 (b) displays the time dependent interference signal after subtracting the Gaussian background, for the maximum pump fluence of 95 mJ/cm². Constructive and destructive interference between the SH

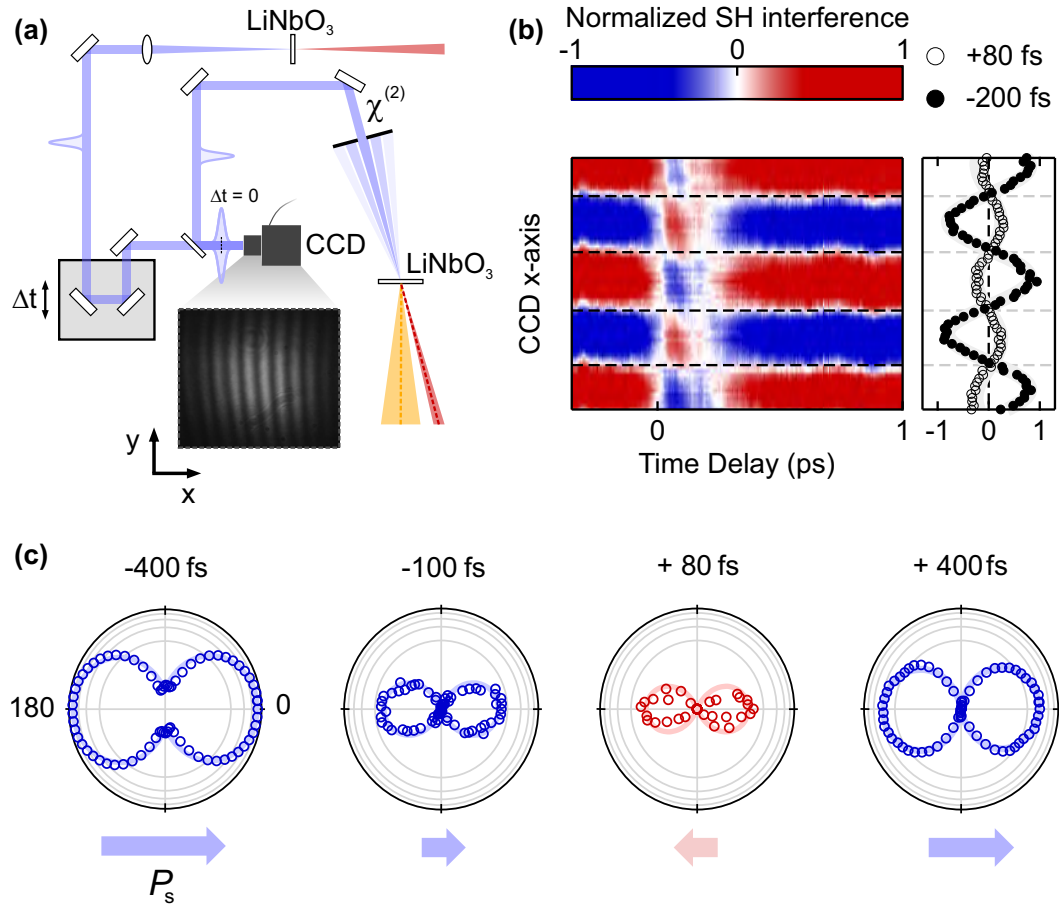


Figure 2.18: Phase sensitive detection of the second harmonic light. (a) Schematic of the SH-interferometric setup. To determine the phase of the second harmonic light from the excited sample it is interfered with a reference second harmonic field from an unexcited sample on the sensor of a CCD camera. The interference pattern shows fringes on top of a Gaussian background, which encode the relative phase of the SH light from the sample with the reference beam. (b) Time-dependent interference fringes on the CCD. A time-delay scan (between pump and probe) revealed the phase of the emitted SH light from the sample through the time delay dependent position of the interference fringes, shaded in blue and red. For better statistics the interference pattern was integrated along the y-axis of the camera and normalized. (c) Normalized interference fringes at -200 fs and in the reversed polarization state at 80 fs. (d) SH-polarimetry measurements at four time-delays. The arrows indicate the time dependent amplitude and sign of the ferroelectric polarization for each time delay, determined from panel (b). The solid lines are fits to the data using the $\chi^{(2)}$ tensor of LiNbO₃. Part of the figure and caption are adapted from Ref. [64].

light from the sample and the reference beam are shaded in red and blue, respectively. Before, the excitation the both beams have constant phase and the interference pattern is unchanging. After excitation, the SH intensity first reduced with a constant phase. As the intensity reached zero at 0 fs time delay (compare to Fig. 2.17 (b)), the phase of the second-harmonic field flipped by 180°, revealed by a sudden sign change of the interference fringes (red to blue and vice versa). This sign change is clearly visible in Fig. 2.18 (c), in which the interference fringes are shown for a negative delay at -200 fs and in the reversed state at 80 fs. The phase then remained constant until the SH intensity vanished again at 200 fs time delay (compare to Fig. 2.17 (b)), when the phase switched back to the initial value. Thus, for time delays between 0 and 200 fs, the polarization was transiently reversed.

Time-resolved SH polarimetry measurements allowed us to monitor the point group symmetry of the transient reversal. For these measurements, the analyzer was set to transmit SH light polarized parallel to the crystals c-axis (P polarization) and the incoming polarization of the probe pulses was rotated at various constant time delays. As shown in Figure 2.18 (d), for four time delays, the polarization dependence of the second harmonic retained the same symmetry and shape of that observed at equilibrium for all time delays (also compare to Fig. 2.7 (b)). Hence, the dynamical reversal occurs only along the hexagonal c-axis with no rotations in the plane, which would appear as a rotation of the major lobes of the polarimetry signal by 180°.

This transient reversal of the ferroelectric polarization was only possible for a pump-pulse frequencies tuned close to the phonon resonance $\Omega_{\text{TO}} = 18.9 \text{ THz}$. Figure 2.19 (a) shows the excitation fluence dependence of the peak polarization change at three different pump frequencies. Accordingly, the plotted peak change of P_s scales as the square of the excitation field E^2 . Also, the comprehensive pump frequency dependence (see Fig. 2.19 (b)) closely follows a similar dependence as observed for the driven lattice vibration in Figure 2.13. The individual data points were determined by fitting the slope of the fluence dependence in panel (a) of Fig. 2.19 and normalizing by the penetration depth. Correspondingly, due to the resonant excitation of Q_{IR} , the largest displacement of the ferroelectric mode Q_{P} ($Q_{\text{P}} \propto P_s$) can be concluded to scale as the square of the driven mode Q_{IR} , as predicted by eq. 2.25 and Fig. 2.4 (e) for coupling of the type $gQ_{\text{IR}}^2Q_{\text{P}}$.

The last important prediction of the underlying nonlinear phononics theory, published in of Ref. [63], is the bi-directionality of the reversal process, foretelling that the sign of the force

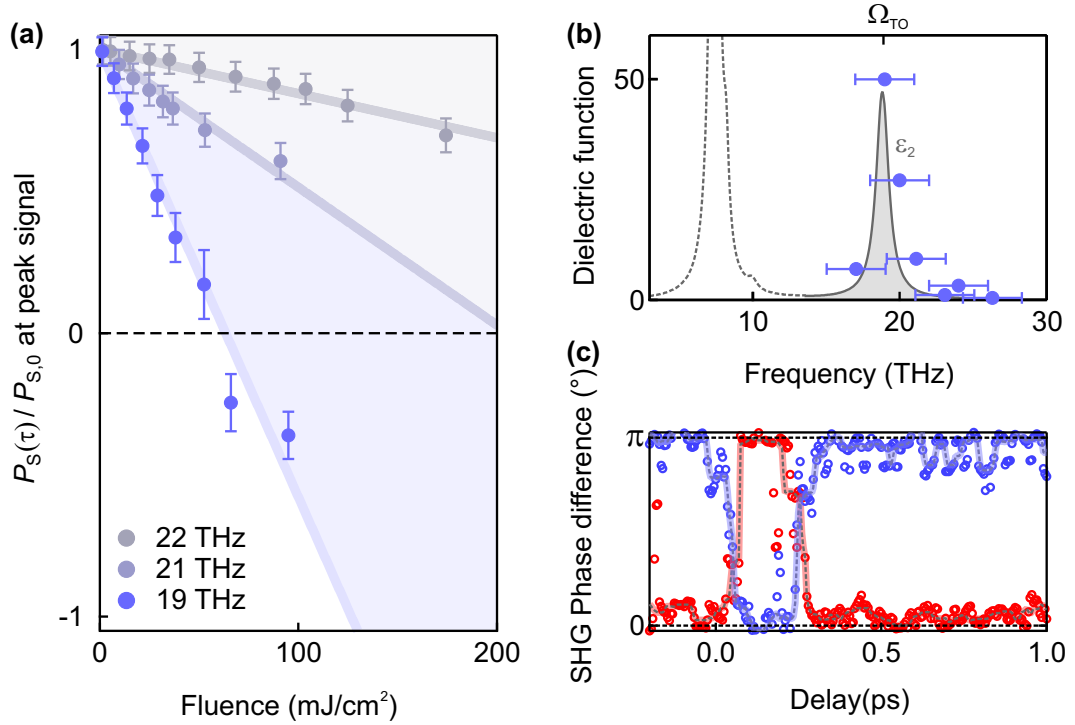


Figure 2.19: Experimental response characteristic of the transient polarization reversal. (a) The normalized polarization at the peak of the time dependent signal $P_S(\Delta t)/P_{S,0}$ scales linearly with the pump fluence. The three curves correspond to excitation with pulses at different frequencies. The polarization only reverses for excitation above 60 mJ/cm^2 with 19-THz pulses. (b) Experimental excitation frequency dependence normalized polarization change. The full frequency dependence (blue dots) reveals a resonant response at the mode transverse optical frequency Ω_{TO} . The individual points are determined from the slope of linear fits to the fluence dependence in panel (a). The solid grey line shows the imaginary part of the dielectric function of LiNbO₃ for comparison. (c) Phase of the SH-field for two oppositely poled initial conditions. The polarization reversal could be achieved starting from both initial polarization states (blue and red circles). In both cases, the phase of the SH light shows a jump of $\pm\pi$ at the peak of the signal before relaxing back to the initial phase. Part of the figure are adapted from Ref. [64].

acting on Q_P depends on the initial equilibrium polarization state. Polarization reversal should therefore be possible starting from both equilibrium states without changing the pump pulse characteristics. This is reported in Fig. 2.19 (c), where the phase of the SH-light is plotted as a function of time delay Δt , starting from an oppositely poled equilibrium polarization states, obtained by simply rotating the single domain crystal by 180°. In Fig. 2.19 (c), the two oppositely poled states of the crystal are denoted with the phase emitted SH light of either 0 or π . The blue circles were obtained after repeating the experiment on the rotated sample. In

both configurations, the characteristic sudden change of the phase by 180° can be observed. Hence, the reversal without rotation, the bidirectional nature of the effect and the resonance with the frequency of the infrared mode, all indicate that the essence of this phenomenon is well understood in terms of anharmonic phonon coupling of the type $gQ_{\text{IR}}^2Q_{\text{P}}$ and a directional displacement of the ferroelectric mode [63].

2.4 Summary

The theory of high-order nonlinear phononics was experimentally demonstrated by exciting the highest frequency A₁ mode in the model system LiNbO₃. After strong-field mid-infrared excitation, time-resolved second harmonic generation revealed harmonics of the driven mode up to the fifth order. Phase and amplitude sensitive detection of these large amplitude atomic vibrations allowed for the reconstruction of the mode lattice potential up to displacements which correspond to 7% of the interatomic distances. Furthermore, nonlinear phononic coupling of these large amplitude vibrations, resolved by frequency filtered SH detection, revealed the transient short-lived reversal of the ferroelectric polarization at the peak of the excitation. This effect was theoretically predicted by an earlier published set of DFT calculations, was driven through the nonlinear coupling of the type $gQ_{\text{IR}}^2Q_{\text{P}}$. The phononic nature of these effects was confirmed by changing the frequency of the excitation pulse, which revealed a peaked response when the excitation pulse was tuned into resonance with the highest frequency A₁ mode. This nonlinear control of the crystal lattice is of interest for functional heterostructure design, its control, and might find immediate use to employ complex functionalities in materials that exhibit more than ferroic order. Ultimately, these experiments demonstrate the capabilities of femtosecond time-resolved SH detection as a quantitative tool to measure ultra-fast symmetry breaking dynamics in solids in the time-domain. Importantly, the phase, amplitude, and polarization sensitive detection of the second harmonic light revealed dynamics and symmetries invisible to a linear probe. This technique can naturally be extended to other materials, especially to those that exhibit equilibrium centrosymmetry without a static $\chi^{(2)}$ nonlinearity.

Chapter 3

Theory of Cuprate Superconductors and Josephson Physics

3.1 Introduction

Depending on how well a material conducts an electrical current it is categorized as either a metal, semiconductor, insulator, or superconductor. The control of the current flow through these types of materials, by external parameters, allowed the implementation of micro fabricated devices, such as transistors [157], that strongly influence our daily life. In the past decades the ultra-fast control of the electronic properties through light became increasingly popular with the prospect of femtosecond electronic switches [158]. These devices rely on the collective oscillatory excitation of the free electron density, i.e., *plasmons* [159, 160]. Plasmons are a direct manifestation of light-electron interaction and they can be used to shape [161] and amplify light [162, 163]. A particular example of these electronic excitations is the *Josephson plasmon* in high- T_c cuprate superconductors, which is formed by the tunneling of Cooper Pairs between adjacent CuO_2 -layers in the superconducting state below the critical temperature T_c [164, 165]. The frequency ω_p of the plasma modes is related to the superfluid density ρ_s as $\omega_p^2 \propto \rho_s$, typically in the THz frequency range.

The study of Josephson plasmons with resonant THz radiation allows for the exploration of the microscopic coherent dynamics of the superconducting charge carriers and their interaction with other degrees of freedom. The following chapter will first introduce the fundamentals of the superconducting state and then focus on the mathematical description of Josephson plasma modes, by introducing the Josephson relations that describe the interaction of the supercon-

ducting phase with electromagnetic fields. In this context, earlier experiments which observed precursor states of superconductivity above T_c will be revisited. They serve as a motivation for time-resolved optical second harmonic generation experiments carried out in underdoped cuprates $\text{YBa}_2\text{Cu}_3\text{O}_{6+\delta}$ within this thesis. The results of these experiments allowed us to develop a microscopic theory, which explains a series of earlier time-resolved THz spectroscopy studies on non-equilibrium superconductivity induced by optical excitation. Parts of this chapter are taken from [166].

3.2 Superconductivity

Superconductivity is a unique material property, where a solid loses its electrical resistivity below a critical temperature T_c . This phenomenon was first discovered in 1911 by Heike Kamerlingh Onnes, when cryogenically cooling mercury to liquid helium temperatures (see Fig. 3.1 (a)) [66]. At these low temperatures the electrons close to the Fermi energy, responsible for the electrical transport, form into pairs. Pairing of these otherwise repelling charged particles is mediated by an arbitrarily small [67, 167] attractive force which creates a bound state of two electrons with opposite spin and momentum to lower their energy to below the Fermi energy and therefore (see Fig. 3.1 (b) and (c)). In contrast to the individual fermionic free electrons these pairs of electrons act similar to Bosons and, accordingly, can condense into a single, zero-momentum ground state with macroscopic occupation ($\sim 10^{20}$). Similarly to a Bose-Einstein condensate of Bosons, this ground state can be expressed as one coherent state of electron pairs with undetermined particle number N but fixed phase θ . This macroscopic coherent ground state is protected by an energy gap Δ around the Fermi energy (see Fig. 3.1 (b)) separating it from the Fermionic single electron states. This energy gap corresponds to the energy necessary to break the pairing of two electrons and it closes at T_c (see Fig. 3.1 (e)). To describe the electron pair ground state one can thus define a *macroscopic wave function* [168]

$$\psi(r) = \langle \psi | \hat{\alpha} | \psi \rangle = \sqrt{\rho_s(\mathbf{r}, t)} e^{i\theta(\mathbf{r}, t)} \quad (3.1)$$

Here $\sqrt{\rho_s(\mathbf{r}, t)} = \sqrt{\hat{n}(\mathbf{r}, t)}$ is given by the density of pairs and $\theta(r, t)$ is the phase of the superconducting condensate [168, 170, 171]. Bardeen, Cooper and Schrieffer demonstrated in their seminal work that indeed a many-particle two- electron pair state can be described as a co-

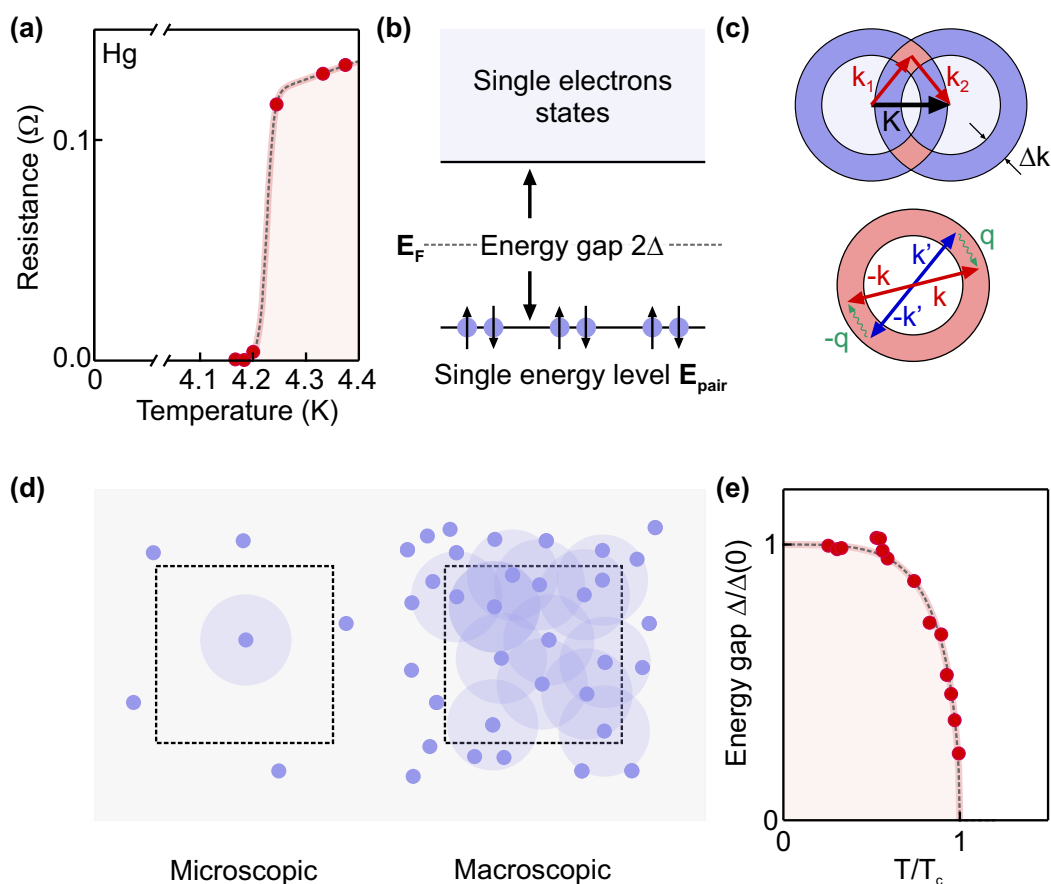


Figure 3.1: Zero resistance and the macroscopic wavefunction. (a) Electrical resistance of mercury at low temperature. At 4.2 K the metal shows a transition into a state with zero resistance (data taken from Ref. [66]). (b) Energy level diagram close to the Fermi energy. Electron pairs with opposite spin and momentum (blue dots and arrows) are condensed into a single ground state (E_{pair}) which is protected by an energy gap ΔE from the single electron states. (c) Scattering cross section for two momenta K of the electron pairs. The pairs are bound by exchange bosons with momentum q (green arrows). The conservation of momentum dictates that the total momentum K of the electron pair must be conserved in the interaction. For $K \neq 0$ this is only possible for the red shaded phase-space volume when considering a small momentum interval Δk around the Fermi energy. This phase-space volume becomes largest when $K = 0$, i.e., the pairing electrons have opposite momentum. (d) Phase space volume for low and high particle number. If the particle number is large (macroscopic) the average number of particle as well as the particle number fluctuation inside a given volume (dashed box) will be large. The particle number is fluctuating but the fluctuations around the average are relatively small. (e) Energy gap of superconducting ground state as a function of temperature (data taken from Ref. [169] for Sn).

herent state [67]. For *conventional superconductors*, like mercury, they propose, the electron pairing to be due to an attractive interaction mediated by the crystal lattice. A passing electron locally distorts the lattice to create a concentration of positive charge, which relaxes back on the time scale τ_{lattice} of a lattice vibration, much slower than the electrons speed (v_F). Thus, a second electron can feel the attractive Coulomb force, which lowers its energy below the Fermi energy and conversely creates a bound state. The timescale of the attractive interaction τ_{lattice} determines the effective size of such a Cooper pair,

$$\xi = v_F \tau_{\text{lattice}}. \quad (3.2)$$

Each pair thus stretches over $\xi = 10 \text{ nm}$ to 1000 nm and consequently, a large number of pairs occupy the same space, momentum and energy state leading to the macroscopic occupation of the ground state (see Fig. 3.1 (c)) [168, 170–173]. This BCS-theory of superconductivity first allowed for the justification of the phenomenological theories by Fritz and Heinz London (London equations) as well as the Ginzburg-Landau theory and gave the microscopic explanation outlined above. Conventional superconductors are typically elemental metals (Hg $T_c = 4 \text{ K}$ [66], Pb $T_c = 7.2 \text{ K}$ [174]) with large Fermi surfaces.

3.3 Dynamics of a Superconductor: London Equations

The dynamics of the condensate are determined by the Schrödinger equation. For a charged particle with charge q_s and mass m and the cinematic momentum $mv = \hbar/i\nabla - q_s\mathbf{A}$ reads,

$$\frac{1}{2m} \left(\frac{\hbar}{i} \nabla - q_s \mathbf{A} \right)^2 \psi + [q\phi + \mu] \psi = i\hbar \frac{\partial \psi}{\partial t}. \quad (3.3)$$

Here ϕ is the electrostatic, μ the chemical and vector potential \mathbf{A} . As know from quantum mechanics [173], the Schrödinger equation is equivalent to continuity equation of the condensate density $\partial \rho_0(\mathbf{r})/\partial t + \nabla \cdot \mathbf{J}_p = 0$, where \mathbf{J}_p is the probability-current density,

$$\mathbf{J}_p = \frac{i\hbar}{m} (\psi \nabla \psi^* - \psi^* \nabla \psi) - \frac{q_s}{m} \psi \psi^* \mathbf{A}. \quad (3.4)$$

Combining this with the expression for macroscopic wave function in eq. 3.1 yields the current

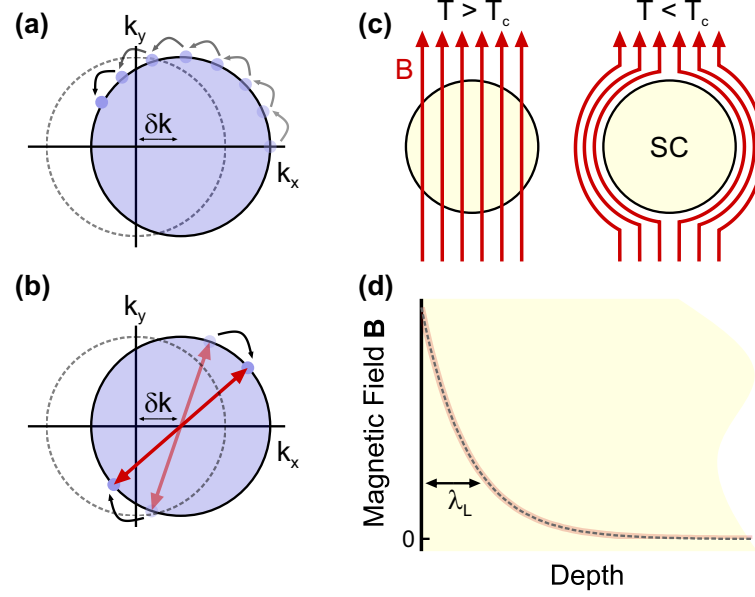


Figure 3.2: Scattering of paired electrons and London equations. (a) Displaced Fermi surface in momentum space and schematic scattering processes. Individual scattering processes (black arrows) bring electrons (blue dot) from the front of the Fermi sphere to the back and reduce the shift δk of the Fermi sphere and thus the current. In a superconductor with paired electrons, the same scattering processes (arrows) involves two electrons and therefore maintains the shift δk of the Fermi sphere. (b) Schematic of the Meissner effect. The Meissner effect leads to the full expulsion of a magnetic field (red arrows) from a superconducting material below the transition temperature T_c (shaded beige). (c) Schematic of a magnetic field penetrating into a superconductor. The external magnetic field leads to persistent loop-currents in the material which results in its exponential screening on the length scale λ_L .

density carried by the paired electrons,

$$\mathbf{J}_p = q_s \rho_s(\mathbf{r}, t) \left(\frac{\hbar}{m} \nabla \theta(\mathbf{r}, t) - \frac{q}{m} \mathbf{A} \right) = q_s \rho_s(\mathbf{r}, t) \mathbf{v}_s, \quad (3.5)$$

which is determined by the phase gradient $\nabla \theta(\mathbf{r}, t)$. This important relation connects the quantum phase $\theta(\mathbf{r}, t)$ of the macroscopic state to the velocity \mathbf{v}_s , a classical concept [172, 175]. The energy-phase relation can be obtained by substituting eq. 3.1 into the Schrödinger equation

$$\hbar \frac{\partial}{\partial t} \theta(\mathbf{r}, t) = \frac{1}{2\rho_s} \Lambda \mathbf{J}_p^2 + q_s \phi + \mu \quad (3.6)$$

where the first term on the right-hand side is the kinetic energy ($\Lambda = m/\rho_s q_s^2$). Importantly,

the super current density in eq. 3.5, which is a measurable observable, only depends on the phase gradient $\nabla\theta$ and the vector potential \mathbf{A} , which both are no physical observables. This requires making the expression for \mathbf{J}_p gauge invariant, which can be done by introducing the gauge-invariant phase gradient [168, 173]

$$\gamma = \nabla\theta(\mathbf{r}, t) - \frac{q_s}{\hbar}\mathbf{A}. \quad (3.7)$$

Together, these equations describe the two principal properties of a superconductor, that is zero resistance and perfect diamagnetism (Meißner effect) that are cast in form of the London equations [176]. Similar to Ohm's law in a metal, they relate the current to the electromagnetic fields in a superconductor.

1. **London-equation:** $\partial_t \mathbf{j} = \frac{1}{\Lambda} \mathbf{E}$

2. **London-equation:** $\nabla \times \mathbf{j} = -\frac{1}{\Lambda} \mathbf{B}$

The first London equation states that the electric field is zero for a stationary current \mathbf{j} . In turn, this means that a current can persistently flow through a superconductor without an applied electric field, i.e., the electric resistance is zero. According to the second London equation, a magnetic field induces persistent loop currents that in turn expel this magnetic field, explaining the Meißner effect. This is sketched in Figure 3.2 (c). The magnetic field lines are depicted as red arrows, which above T_c penetrate the material but are fully expelled below T_c . However the extrusion is not complete as can be seen rewriting the second London equation using Maxwells equations

$$\nabla^2 \mathbf{B} - \frac{1}{\lambda_L^2} \mathbf{B} = 0, \quad (3.8)$$

where $\lambda_L^2 = c\Lambda/4\pi$ is the London penetration depth of the magnetic field [173]. This equation shows that magnetic fields indeed penetrate a superconductor up to London penetration depth. This is depicted in Figure 3.2 (d) which shows a sketch of the spatial profile of a magnetic field penetrating a superconductor. The magnetic field decays exponentially towards the interior of the superconductor. Microscopically, the perfect conductance can be explained by considering possible scattering events for the electrons. Figure 3.2 (a) shows how in momentum space a current flow equals a rigid shift of the Fermi sphere by $\langle \delta k \rangle = m/\rho q \hbar \langle j \rangle$. In a metal, current flow is limited by the scattering of electrons from the front of the Fermi sphere to the back, and

consequently a momentum loss of $2k_F$. This can happen in one or multiple scattering events as sketched as black arrows in Figure 3.2 (a). In a superconductor, the same scattering process has to involve the second electron of the pair, which is necessarily scattered to the front of the Fermi sphere to preserve the pairing. This situation is depicted in Figure 3.2 (b), the scattering of the individual electrons is again shown as black arrows, which point towards the opposite direction. As a result, no momentum is lost and the displacement of the Fermi sphere does not change, i.e., the current flows without resistance (see Fig. 3.2 (b)). Of course, this assumes that the energy scale of the scattering process is below the superconducting energy gap and thus too low to break the pairing [173].

3.4 Josephson Effect

The Josephson effect is an immediate consequence of the long-range quantum coherence of superconductors. It describes the quantum-mechanical coherent tunneling of Cooper pairs between two superconductors separated by a non-superconducting barrier as sketched in Fig. 3.3 (a). This structure is called a Josephson junction. Each of the superconductors hosts a density of Cooper pairs which can both be described with a macroscopic wave function

$$\psi_i = \sqrt{\rho_{s,i}} e^{i\theta_i} \quad (3.9)$$

In 1962, Brian Josephson analyzed the tunneling process of the Cooper pairs across the junction and predicted that, unexpectedly, a zero-voltage current will flow, according to

$$I = I_c \sin(\theta_1 - \theta_2). \quad (3.10)$$

Thus the current is only determined by the phase difference $\varphi = \theta_1 - \theta_2$ of the two condensates on either side of the junction [164, 177, 178]. Here, $I_c = 2K\sqrt{\rho_1\rho_2}/\hbar$ is the critical current which the Josephson junction can support without losing its superconducting properties. For $I \leq I_c$, the current is dissipationless, i.e., it is a supercurrent. For $I \geq I_c$, a finite voltage V will develop across the junction and the two condensate wave functions will become time-dependent according to

$$\frac{\partial\varphi}{\partial t} = \frac{2\pi}{\Phi_0} V, \quad (3.11)$$

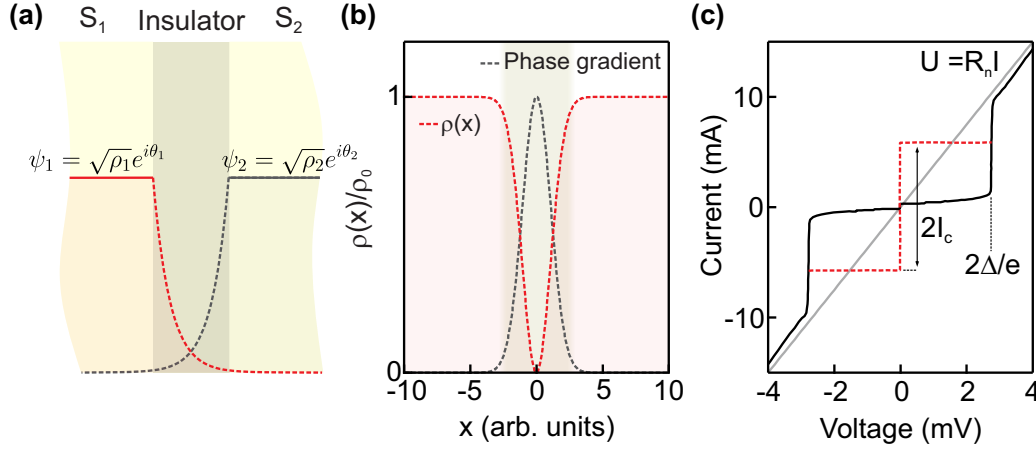


Figure 3.3: Josephson junction. (a) Schematic of a Josephson junction, which is a superconductor (S_i)-insulator-superconductor junction. The two superconductors each host a condensate, which can be described by a macroscopic wavefunction ψ_i , with density ρ_i and phase θ_i . The wavefunction of the superconductors (dashed lines) extend into the thin insulating layer and further into the respective other superconductor. (b) Superfluid density and phase gradient across the Josephson junction. The superfluid density (dashed red line) inside the insulating layer is diminished but finite and a strong phase gradient (dashed grey line) inside the insulator develops. (c) I-V characteristic of a Josephson junction. Currents through junction smaller than the critical current I_c flow dissipation less and no voltage drop occurs across the junction. For currents larger than I_c , a finite voltage drop develops across the junction which leads to an alternating current with amplitude I_c (dashed red line). When the voltage drop is equal to the twice the gap size 2Δ , the pairs are broken up and the junction I-V-characteristic follows Ohm's law $U = R_n I$.

with $\Phi_0 = h/2e$ the magnetic flux quantum. This results in an alternating current with amplitude I_c and frequency $\nu = 2eV/h$, the so called *a.c. Josephson effect*,

$$I(t) = I_c \sin(\varphi + 2eV/ht) \quad (3.12)$$

and the special I-V characteristic of a Josephson junction shown in Fig. 3.3 (b). The two equations eq. 3.10 and 3.11 are known as the first and second Josephson equations. Their experimental confirmation in 1963 confirmed the existence of a macroscopic quantum coherent state below T_c [179].

In analogy to the temporal oscillations of the Josephson current caused by a voltage drop across the junction, a magnetic field leads to spatial oscillations of the supercurrent. If a magnetic field is aligned along the junction the phase-difference φ between the Josephson coupled super-

conductors will change along the x -direction (perpendicular to B) (see Fig. 3.4 (b)). This is due to the gauge invariance of the phase-gradient $\nabla\theta$ of the individual superconductors and the gauge invariance of the phase-difference φ across the junction. It is found that the gradient of phase-difference is proportional to the normalized magnetic flux through the junction [173],

$$\nabla\varphi = \frac{2\pi}{\Phi_0} 2\lambda_L [\mathbf{B} \times \mathbf{z}]. \quad (3.13)$$

where λ_L is the London penetration depth and z the direction normal to the junction. This leads to a periodic modulation of the current across the junction (see Fig. 3.4 (b)) according to

$$I(x) = I_c \sin\left(\varphi + \frac{2\pi}{\Phi_0} 2\lambda_L B_y x\right). \quad (3.14)$$

In total eq. 3.10, 3.11 and 3.13 describe the interaction of Josephson junctions with electromagnetic waves.

3.4.1 Equivalent Circuit of Josephson Junctions

Josephson's equations succeed to accurately describe the situation in the zero-voltage limit. However, they fail to model dissipation effects of quasiparticles which become important in the finite voltage regime ($I > I_c$). One approach to combine the Josephson physics with quasiparticle dissipation is the Resistively and Capacitively Shunted Junction (RCSJ) model [180, 181]. In the RCSJ-model the Josephson junction is described as an inductance shunted in parallel by a voltage independent resistance R and a capacitance C (see Fig. 3.4). Here, the capacitance and resistor account for charging and dissipation effects and the Josephson junction is modelled as an inductance.

The analogy of the Josephson junction to an inductance becomes obvious from the transient change of the current through the junction

$$\frac{\partial I}{\partial t} = \frac{\partial I}{\partial(\varphi)} \frac{\partial(\varphi)}{\partial t}. \quad (3.15)$$

This relation is similar to the voltage-current relation across a conventional non-superconducting inductance

$$\frac{\partial I}{\partial t} = \frac{\partial I}{\partial(\varphi)} \frac{2\pi}{\Phi_0} V. \quad (3.16)$$

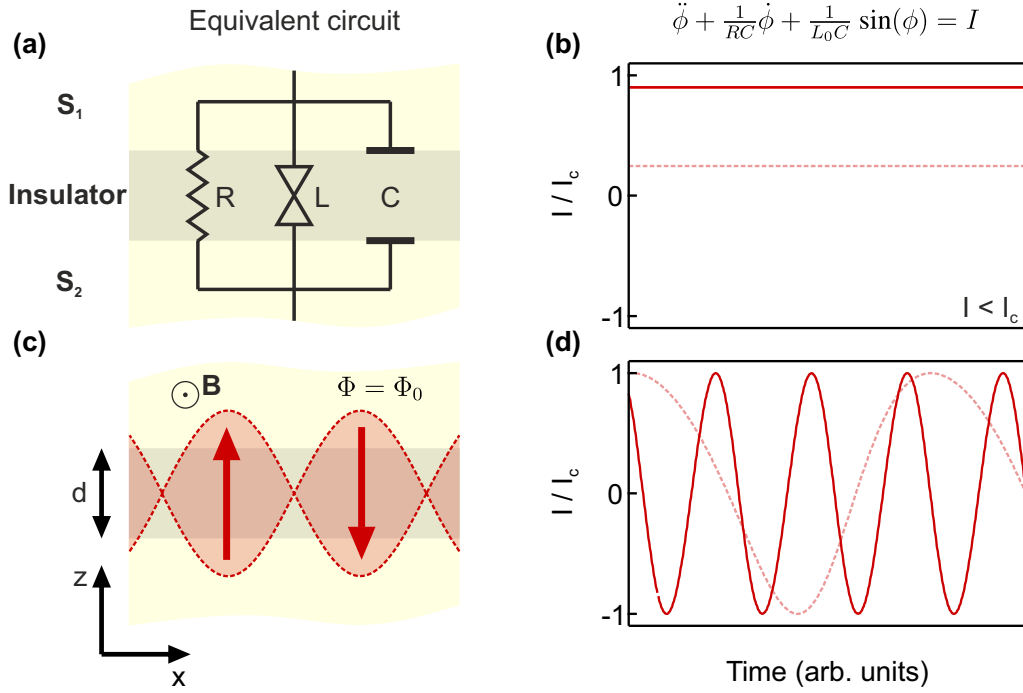


Figure 3.4: Equivalent circuit of a Josephson junction. (a) Equivalent circuit of a Josephson junction. A Josephson junction can be modeled by an equivalent circuit of an inductor L in parallel with a capacitor C and resistor R . (b) Solutions of the differential equation of the circuit for low (dashed) and high (solid) current. The solutions yield a constant current flow for $I < I_c$ and an oscillating current flow with frequency $\Omega = 2eV/h$ for $I > I_c$. The frequency increases for a higher voltage drop across the junction (red and dashed red line in panel (d)). (c) Spatial modulation of the Josephson current due to a perpendicular magnetic field. A constant magnetic field \mathbf{B} perpendicular to the junction leads to a spatial modulation of the Josephson current across the junction (red arrows). The oscillation period is given by the magnetic flux through the junction, $\lambda_x \approx \Phi_0/Bd$. In the situation shown the flux through the junction Φ is equal to the magnetic flux quantum Φ_0 . (d) Solutions of the differential equation of the circuit for low (dashed) and high (solid) voltage.

Therefore, a Josephson junction can be thought of as an ideal inductance,

$$L_J = \frac{\Phi_0}{2\pi I_c} \cos(\varphi), \quad (3.17)$$

without resistance. Together with the dissipative and capacitive currents, the total current through the Josephson junctions is equal to the sum of the contributions from each parallel element (see Fig. 3.4). Therefore, the corresponding differential equation which describes the equivalent circuit is

$$I_c \sin(\varphi) + \frac{V}{R} + C \frac{\partial V}{\partial t} = I_{\text{ext}}, \quad (3.18)$$

with I_{ext} the external current bias. The Josephson relations help two rewrite eq. 3.18 to the equation of motion of the phase difference φ ,

$$\frac{\partial^2 \varphi}{\partial t^2} + \frac{1}{RC} \frac{\partial \varphi}{\partial t} + \omega_J^2 \sin(\varphi) = I_{\text{ext}}, \quad (3.19)$$

where $\omega_J = \sqrt{2eI_c/\hbar C} = 1/\sqrt{L_0 C}$ is the characteristic frequency of the Josephson junction. As addressed in Chapter 1, in the limit of small amplitudes, when $\sin(\varphi) \approx \varphi$, eq. 3.19 corresponds to the equation of motion of a damped, driven harmonic oscillator. Again, $1/\gamma = RC$ determines the damping due to dissipative quasiparticles tunneling across the junction ($I > I_c$). The solution to this equation are plasma oscillations of the superconducting charge carriers as plotted exemplary in Fig. 3.4 (c) and (d) for below threshold ($I < I_c$) and above threshold ($I > I_c$) excitation. They lead to an electric current and field normal to the insulating barrier and correspond to longitudinal excitations of the Cooper pair density (see Chapter 1). These are the fundamental low-energy excitations of high-temperature cuprate superconductors and are called *Josephson-plasma resonances* (see Chapter 3.5).

3.4.2 Stack of Josephson Junctions

A stack of Josephson junctions is formed by connecting a number of laterally extended weak links (of dimension larger than the Josephson penetration depth λ_J) in series (see Fig. 3.5 (a)). In such a system the strong coupling between adjacent junctions has to be considered to accurately describe their collective response to electromagnetic radiation. If all junctions are equivalent, as in Figure 3.5 (a), the electric and magnetic field in each junction are related through the Maxwell equation and the 1st Josephson equation. Figure 3.5 (b) summarizes the relevant fields and currents in a sketch of a stack of Josephson junctions with number l . For the case of an electric field polarized along the z-axis and the magnetic field polarized along the y-axis, the combination of the two sets of equations yields,

$$\frac{\partial H^1}{\partial x} = \frac{4\pi}{c} \left[I_c \sin(\varphi^1) + \sigma E_z^1 \right] + \frac{\varepsilon}{c} \frac{\partial E_z^1}{\partial t} \quad (3.20)$$

where ε is the dielectric constant of the insulating layer [182]. The phase difference between

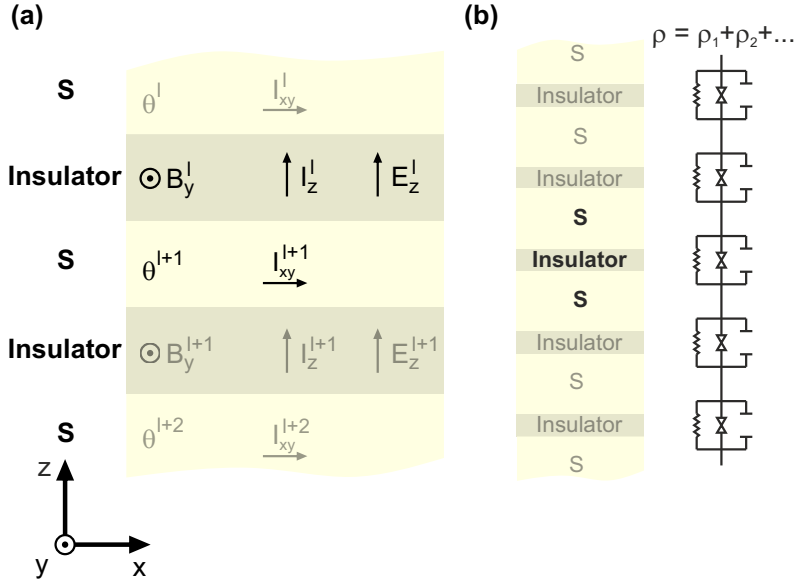


Figure 3.5: Stack of Josephson junctions. (a) Schematic of a stack of equivalent Josephson junction and the relevant fields to describe its electrodynamics. The electric E_z^l and magnetic B_y^l fields act in the insulating layers. Every superconducting layer host a condensate with phase θ^l and carries a current in the x-y plane I_{xy} . (b) Schematic of a stack of equivalent Josephson junction and the corresponding equivalent circuit. A stack of equivalent Josephson junctions can be modeled by connecting several junctions of impedance ρ_i in series.

adjacent layers evolves according to

$$\nabla_{xy}\varphi^l = \frac{8\pi^2\lambda_{xy}^2}{c\Phi_0 d} (\mathbf{I}_{xy}^l - \mathbf{I}_{xy}^{l+1}) + \frac{2\pi d}{\Phi_0} [\mathbf{B}^l \times \mathbf{z}], \quad (3.21)$$

where \mathbf{I}_{xy}^l is the in-plane supercurrent in the l-th superconducting layer and the Nabla operator $\nabla_{xy} = (\partial_x, \partial_y)$ only acts on the in-plane direction [183, 184]. Additionally, the total current in each layer must be conserved thus the continuity equation,

$$\nabla_{xy} (\mathbf{I}_{xy}^l) = -\frac{1}{d} (I_z^{l+1} - I_z^l) - \frac{1}{d} \left(\frac{\varepsilon_z}{4\pi} \frac{\partial}{\partial t} + \sigma_z \right) (E_z^{l+1} - E_z^l). \quad (3.22)$$

This equation states that an in-plane gradient must be compensated by an out-of-plane current to prevent accumulation of charges. Here, the first term of the right hand side accounts for the Josephson supercurrent between adjacent layers, whereas the second term accounts for dissipative charge transport in the insulating layer with dielectric constant ε_z and conductivity σ_{xy} [184]. This continuity equation can be substituted into eq. 3.21 and the difference $\nabla_{xy} (\mathbf{I}_{xy}^l - \mathbf{I}_{xy}^{l-1})$ is commonly written using the discrete differential operator $\Delta^l I_z^l = I_z^{l+1} + I_z^{l-1} - 2I_z^l$ [184]. Together

with eq. 3.20 and the first and second Josephson equation this yields

$$\nabla_{xy}^2 \varphi^1 = \frac{1}{\lambda_J^2} \left(1 - \frac{\lambda_{xy}^2}{d^2} \Delta^1 \right) \left(\sin(\varphi^1) + \frac{4\pi\sigma_z \lambda_J^2}{c^2} \frac{\partial \varphi^1}{\partial t} + \frac{\varepsilon_z \lambda_J^2}{c^2} \frac{\partial^2 \varphi^1}{\partial t^2} \right), \quad (3.23)$$

the so-called discrete *sine-Gordon equation*, where $\lambda_J^2 = \frac{c\Phi_0}{8\pi^2 I_c d}$ is the Josephson penetration depth [182]. The Josephson penetration depth corresponds to the London penetration depth of the weak coupling region with reduced super fluid density ($\lambda_J^2 \propto 1/\rho_s^*$) [182, 185]. Typical values are $\lambda_J \sim 10 \mu\text{m}$ to $100 \mu\text{m} \gg \lambda_L$ [185].

In the limit of small amplitudes ($\sin(\varphi^1) \approx \varphi^1$), like the RCSJ-model, the system shows collective oscillations of the Cooper pairs across the junctions. These oscillations resonate with the Josephson plasma frequency $\Omega_J^2 = \frac{c^2}{\varepsilon_z \lambda_J^2}$ and the electric field is orientated along the z -direction. Depending on the propagation direction, the sine-Gordon equation gives rise to transverse (in-plane propagation, see Fig. 3.6 (a)) and longitudinal (out-off-plane propagation, see Fig. 3.6 (b)) plasma oscillations. For small amplitudes the solutions take the form of plane waves $\varphi(\mathbf{r}, t) = \varphi_0(\mathbf{r}, t) e^{i(\mathbf{q}\mathbf{r} - i\omega t)}$ and the dispersion along the in-plane direction $q_{x,y}$ is given by [182],

$$\Omega^2(q_{x,y}) = \Omega_J^2 + c/\sqrt{\varepsilon_z} q_{x,y}^2. \quad (3.24)$$

Therefore the Josephson plasma oscillations in-plane show an equally rapid dispersion as electromagnetic waves (see Fig. 3.6 (a)). For propagation along the z -direction, the dispersion of the longitudinal plasma waves can be determined by incorporating charging effects of the superconducting electrodes as is carried out in Ref. [183]. With the Debye length μ , defining the distance over which mobile charge carriers can screen an electric field, the longitudinal plasma dispersion

$$\Omega^2(q_z) = \Omega_J^2 + c^2 \mu^2 q_z^2 / \lambda_z^2 \quad (3.25)$$

is substantially weaker (see Fig. 3.6 (b)). For small charging effects $\mu \rightarrow 0$, the dispersion reduces to $\Omega(q_z) = \Omega_J$ [183]. The sine-Gordon equation (eq. 3.23) can be brought into an easier form by introducing the dimensionless variables $x \rightarrow x/\lambda_z$, $y \rightarrow y/\lambda_z$ and $t \rightarrow \omega_J t$. Furthermore, the discrete differential operator Δ^1 transforms into the continuum operator $\partial^2/\partial z^2$ if the wavelength of the electromagnetic radiation is much larger than the layer spacing d [182],

$$\nabla_{xy}^2 \varphi = \left(1 - \frac{\partial^2}{\partial z^2} \right) \left(\sin(\varphi) + \gamma \frac{\partial \varphi}{\partial t} + \frac{\partial^2 \varphi}{\partial t^2} \right). \quad (3.26)$$

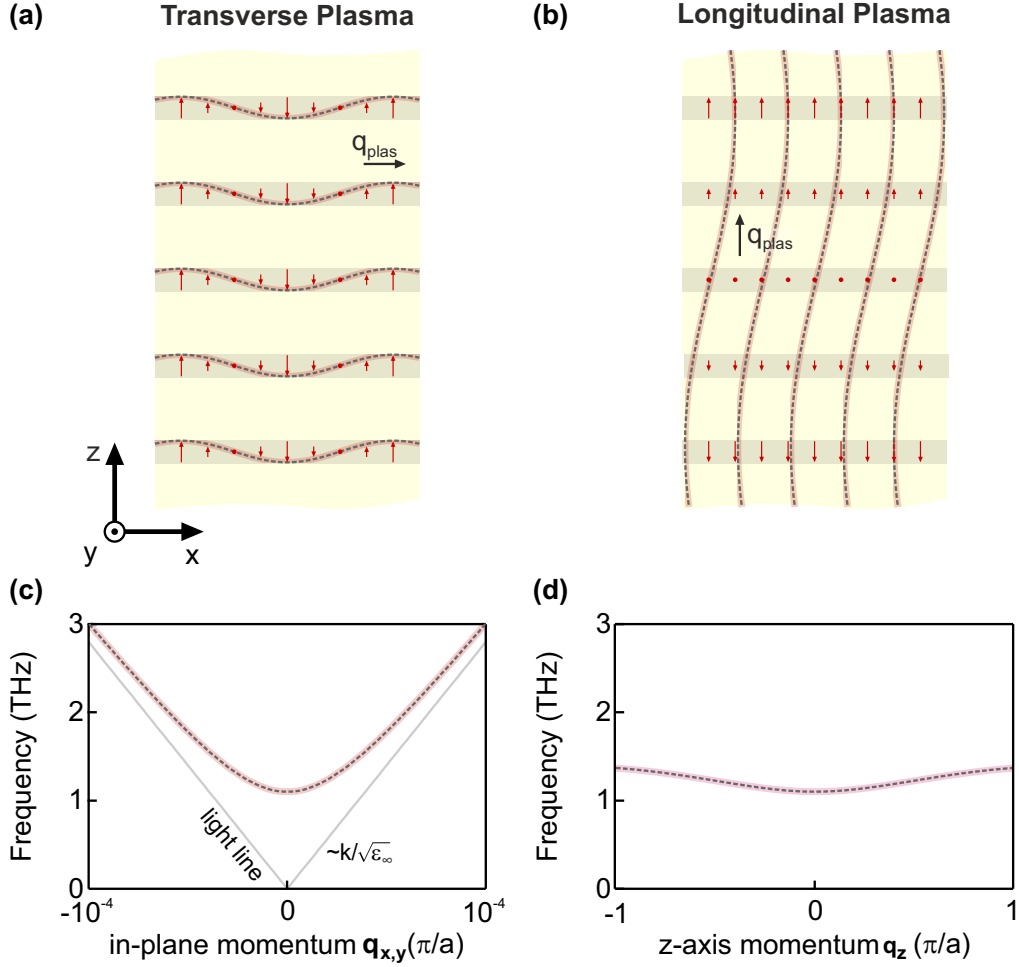


Figure 3.6: Transverse and longitudinal Josephson plasma modes and their dispersion relation of the Josephson plasma mode. (a) Schematic of transverse and longitudinal Josephson plasma modes. The electrodynamics of such a stack gives rise to Josephson plasma modes, which can either propagate perpendicular to the stacking direction and form transverse modes (shown in panel (b)) or along the stacking direction to form a longitudinal excitation of the Josephson plasma. In both cases the tunneling currents (red arrows) are parallel to the stacking direction. (c) Dispersion relation of a transverse Josephson plasma mode. The dispersion of a transverse mode (dashed line), which propagates along the junctions, shows a parabolic dispersion close to $q_{\text{plas.}} = 0$, which approaches the linear dispersion of light $\nu = k/\sqrt{\epsilon_{\infty}}$ already at a fraction of 10^{-4} of the Brillouin zone. The transverse Josephson plasma mode resembles the dispersion of a longitudinal phonon (see Chapter 1). (d) Dispersion relation of a longitudinal Josephson plasma mode. The longitudinal plasma mode only shows a weak dispersion up to the Brillouin zone boundary.

As outlined in the next section, this long-wavelength limit becomes important for the special case of cuprate superconductors which represent stacks of intrinsic Josephson junctions [186]. In these materials the typical frequencies ω_J of the Josephson junctions are on the order of THz with wavelength of $\sim 300 \mu\text{m}$. Every Josephson junction in these materials has microscopic dimensions on the order of the crystal unit cell (few Å) (see Fig. 3.7 a), which are therefore much smaller than the relevant THz-wavelength.

3.5 Cuprates

Cuprate superconductors attracted great attention since their discovery by Bednorz and Müller in 1986 [6, 7], with critical temperatures T_c that exceed the boiling temperature of liquid nitrogen (see Fig. 3.7 (a)) [187]. The high critical temperatures of cuprates significantly exceed the putative limit of $T_c = 30 \text{ K}$ derived from Fermi-liquid-like metals described by the BCS theory [188] and hold broader potential for applications.

The cuprate superconductors are generally considered to be quasi two-dimensional systems in which mobile charge carriers primarily reside within weakly coupled copper oxygen (CuO_2) planes as sketched in Fig. 3.7 (b) and (c). The superconducting layers are separated by neighbouring dielectric planes giving rise to a layered crystal structure. Furthermore, the dielectric layers function as charge reservoir layers that control the carrier concentration in the CuO_2 plane(s) [189, 190]. In the special case of Y-Ba-Cu-O based superconductors the doping is controlled through the amount of oxygen inside the reservoir layers $\text{YBa}_2\text{Cu}_3\text{O}_{6+\delta}$. More generally, doping can be controlled by elemental substitution of the parent compound ($\text{La}_{2-x}\text{Ba}_x\text{CuO}_4$). All cuprate compounds have in common that superconductivity emerges from an antiferromagnetic Mott insulating phase of the parent compounds, shaded green in Figure 3.7 (c) [165, 192]. This is because the CuO_2 -planes define the electric and magnetic properties of the cuprate materials. Due to their orbital order (see Fig. 4.7 (b)), super exchange interaction between the Cu^{2+} and O^{2-} ions within the layers leads to an antiferromagnetic ordering of the spins. This spin ordering results is the reason why the undoped parent compounds are anti-ferromagnetic insulators (AFI). At higher doping, the critical temperature T_c of the superconducting state follows a dome-like shape as a function of doping, with a maximum T_c around 16% doped holes per CuO_2 unit (optimally doped). A similar phase diagram is seen when electrons are doped

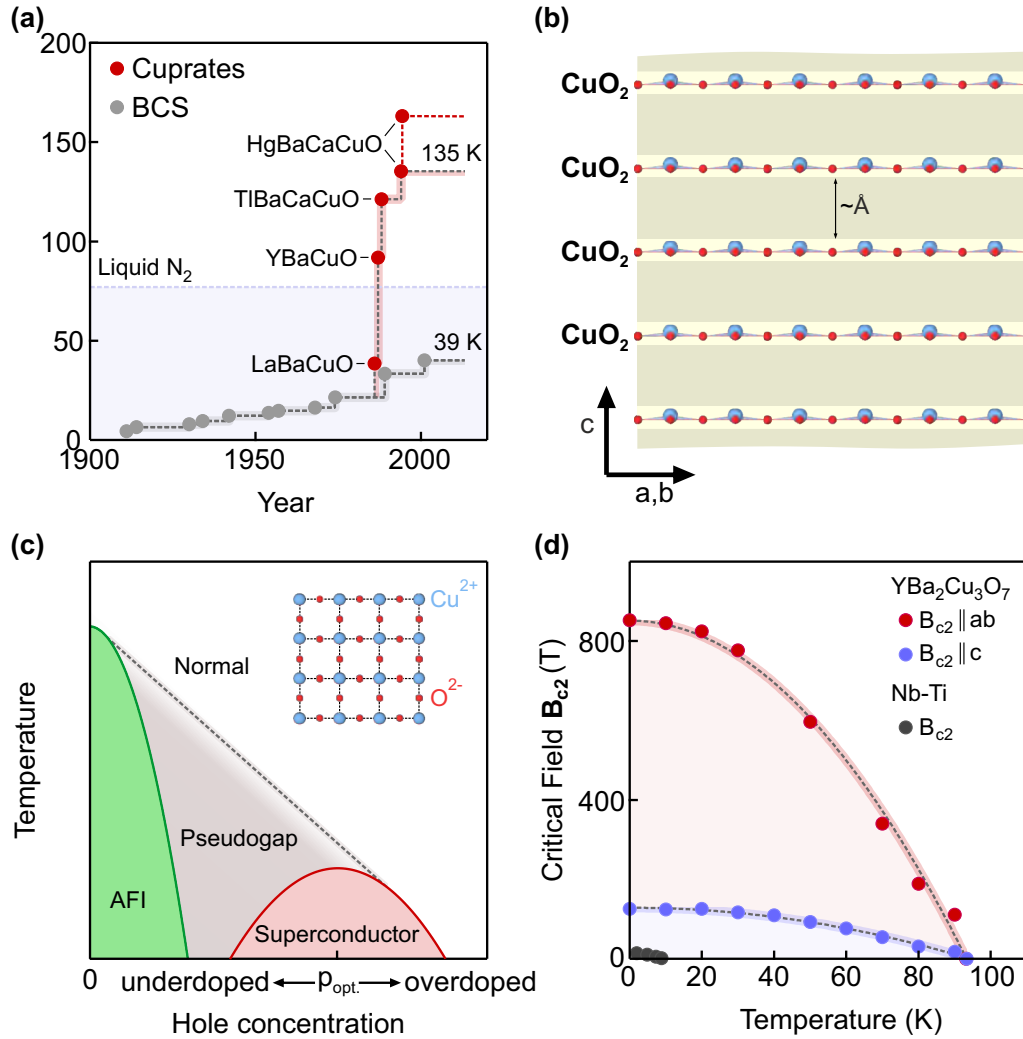


Figure 3.7: Cuprate superconductors. (a) Maximum T_c of cuprate and BCS superconductors. The discovery of cuprate superconductors (red dots) in 1961 increased the maximum critical temperature significantly above the boiling temperature of liquid nitrogen (dashed line) and the T_c of conventional BCS-type (grey dots) superconductors. (b) Schematic structure of a cuprate superconductor. All cuprate materials exhibit a layered structure, where CuO_2 planes are separated by insulating layers. (c) Generic phase diagram of the cuprates. Orbital ordering of the order of CuO_2 layers, with Cu^{2+} (blue) and O^{2-} (red) ions, leads to superexchange interaction of these localized charges and to an antiferromagnetic ordering of the spins. The undoped parent compound of the cuprate materials are antiferromagnetic insulators (AFI) at low doping plotted in green. At finite doping level, a superconducting dome emerges (red) around optimal doping p_{opt} . Between the AFI and superconducting phase, an exotic *normal* state exists which is called pseudogap phase (shaded in grey). (d) Upper critical field as a function of temperature. The pair-breaking field $B_{c,2}$ along the planes (red dots) is usually an order magnitude larger compared to the out-of-plane direction (blue dots). The anomalous low charge carrier density of cuprates further leads to significantly higher critical fields compared to conventional superconductors (grey dots). Part of this figure are adapted from Ref. [191]

into the parent compound, however with a more robust antiferromagnetic phase and a lower T_c [193]. Above T_c , the materials transition into an exotic 'normal' state phase which is called the pseudogap phase, which will be further discussed below. Below T_c , due to their layered structure, 3D superconducting transport is mediated by tunneling of paired electrons between adjacent CuO_2 -planes [194]. However, the origin of the pairing is still subject to controversial debate [194, 195].

The c -axis electrodynamics of cuprates are governed by the physics described by the sine-Gordon equation (eq. 3.23). This leads to a strong anisotropy of the superconducting properties most notably the Ginzburg-Landau coherence ξ length and the London penetration depth λ_L [185]. The weak coupling between superconducting layers leads to a significantly higher effective mass of the charge carriers along the c -axis ($m_c \gg m_{ab}$) and therefore $\xi_c \ll \xi_{ab}$ ($\xi \propto 1/m$) and $\lambda_{L,c} \gg \lambda_{L,ab}$. The significantly longer London penetration λ_L depth for $B \parallel c$ becomes immediately apparent from the small supercurrent along the c -axis associated with the Josephson tunneling. The anisotropy of the Ginzburg-Landau coherence length ξ on the other hand leads to a strong anisotropy of the upper critical fields $B_{c,2}$, above which Cooper pairs are broken ($B_{c,2} \propto 1/\xi^2$). Due to $\xi_{\text{cuprates}} \ll \xi_{\text{BCS}}$, cuprates show much higher critical fields compared to conventional superconductors (see Fig. 3.7 (c)) [185]. The latter is a consequence of the anomalous low charge carrier density and thus low Fermi velocity in cuprates [192, 196]. Typical values of ξ_{cuprates} and $\lambda_{L,\text{cuprates}}$ are ~ 1 nm and 100 nm to 1000 nm respectively.

3.5.1 Optical Properties of Cuprates

In typical cuprate materials the Josephson frequency $\Omega_J = \sqrt{c^2/\varepsilon_z \lambda_J^2}$ in the sine-Gordon equation takes a value on the order of \sim THz. This results in characteristic features in the infrared optical properties of these materials. As discussed in Chapter 1 a Josephson plasma wave (JPW), like any other (normal) plasma wave, screens electromagnetic radiation below the plasma frequency. In the case of a JPW this plasma frequency corresponds to the Josephson frequency ω_J at which the real part of the dielectric function ε_1 crosses zero. Above ω_J transverse solutions of the sine-Gordon equation exist in the form of Josephson-plasma-polaritons and thus, light can propagate into the material (see Fig. 3.8 (a)) [197, 198]. The plasma frequency is directly related to the superfluid density inside the superconductor $\Omega_J \propto \sqrt{\rho_s}$. The dielectric response

can be determined from the dispersion relation eq. 3.24 and can be written as [198],

$$\varepsilon_n(\omega) = \varepsilon_\infty \left(1 - \frac{\omega_{J,n}^2}{\omega^2} \right) + i\varepsilon_\infty \omega_{J,n}^2 \delta(\omega) + 4\pi i/\omega \sigma_{n,R}. \quad (3.27)$$

Here the finite conductivity $\sigma_{n,R}$ is due to quasiparticle scattering and corresponds to the shunted resistor in the RCSJ-model. Different to a dissipative plasmon, the imaginary part of the dielectric function ε_2 is a delta peak at zero frequency and the real part ε_1 diverges as $1/\omega^2$ plotted in Figure 3.8 (b). The delta peak is responsible for the zero dc-resistance of the superconductor. This becomes obvious when considering the case of a Lorentz oscillator at zero resonance frequency in the limit of zero damping ($\gamma \rightarrow 0$) (see Chapter 1). The Josephson plasmons, and longitudinal modes in general, are identified by a peak in the loss function ($Im(-1/\varepsilon)$), which is centered around the plasma frequency Ω_J drawn in Figure 3.8 (c). This simple oscillator model succeeds (for small φ) to describe the infrared optical properties of so-called single layer cuprates, like $La_{2-x}Ba_xCuO_4$, by fitting eq. 3.27 to a measured dielectric function [6, 199].

However, other cuprates (especially those with a T_c higher than $T_{N_2,liq.} = 77$ K) are composed of a stack of two ((Y-Ba-Cu-O compounds) [187] or more (Bi-Sr-Ca-Cu-O compounds) [200]) inequivalent Josephson junctions as sketched in Figure 3.9. This has important consequences for the optical properties and the dynamics of the Josephson plasma-polaritons. Like the description within the RCSJ-model these stacks can be considered as multiple inequivalent circuits in series like shown in Figure 3.9 (b) [198]. Thus, the optical conductivity ($\sigma(\omega) = -i\omega\varepsilon(\omega)/4\pi$) of such a stack is equal to the series conductivity of the individual junction $\sigma_n(\omega)$ weighted by a geometric factor $s_n = d_n/D$,

$$\sigma(\omega) = \left(\sum_n \frac{s_n}{\sigma_n(\omega)} \right)^{-1} \rightarrow \varepsilon(\omega) = \left(\sum_n \frac{s_n}{\varepsilon_n(\omega)} \right)^{-1}. \quad (3.28)$$

Here, $\varepsilon_n(\omega)$ is the dielectric response of an individual junction as in eq. 3.27. For the case of a bilayer cuprate (two CuO_2 layers per unit cell) the total dielectric function is

$$\frac{\varepsilon(\omega)}{\varepsilon_\infty} = \frac{(\omega^2 - \omega_{J,1}^2)(\omega^2 - \omega_{J,2}^2)}{\omega^2(\omega^2 - \omega_T^2)}, \quad (3.29)$$

where $\Omega_T^2 = (s_1\Omega_{J,2}^2 + s_2\Omega_{J,1}^2)/(s_1 + s_2)$ is the so-called transverse Josephson plasmons frequency. Interestingly, there are two plasma edges, corresponding to two longitudinal plasmons and a

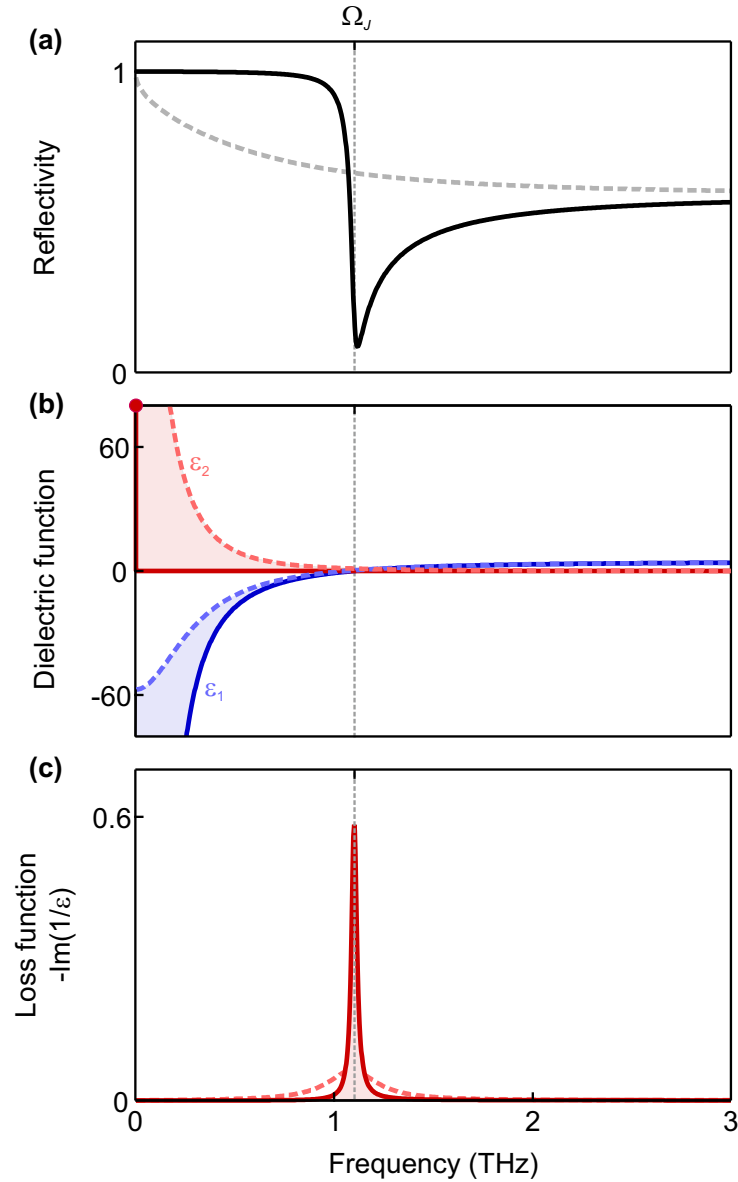


Figure 3.8: Optical properties of a single layer Cuprate. (a) Simulated THz-reflectivity of a Josephson plasma resonance. A Josephson plasma resonance appears as a sharp reflectivity edge at the Josephson plasma frequency Ω_J (black line). A normal electron plasma oscillation with the same plasma frequency produces a smooth reflectivity profile (dashed line). (b) Simulated dielectric function of a Josephson plasma resonance. The dielectric function of the Josephson plasma resonance is a delta peak at zero frequency (imaginary part, red) and a $1/\omega$ divergence of the real part (blue). The normal plasmon shows a Lorentzian centered around $\omega = 0$ due to the finite damping coefficient γ of dissipative transport (dashed red). Instead of a $1/\omega$ divergence, the real part of the dielectric functions saturates to a finite value (dashed blue). (c) Simulated loss function of a Josephson plasma resonance. Both, Josephson and normal plasmon, exhibit a characteristic peak in the loss function ($-\text{Im}(1/\epsilon)$).

pole in the real part of the dielectric function at ω_T which corresponds to a transverse optical plasma oscillation, with oscillator-strength $A_T = \varepsilon_\infty(1 - \Omega_{J,1}^2/\Omega_T^2)(1 - \Omega_{J,2}^2/\Omega_T^2)$ (see Fig. 3.9 (c)). The resulting frequency dependent reflectance is similar to two transverse excitations with $\Omega_{TO,1} = 0$ and $\Omega_{T=,2} = \Omega_T$ separated by a Reststrahlenband from their corresponding longitudinal frequencies at $\Omega_{LO,1} = \Omega_{J,1}$ and $\Omega_{LO,2} = \Omega_{J,2}$ (see Fig. 3.9 (a) and Chapter 1).

The transverse mode appears because the different junctions are connected in series, and the response functions is given by the sum of the individual impedances (see Fig. 3.5) instead of conductances (see Chapter 1). The two Josephson plasma modes represent the in-phase ($\Omega_{J,1}$) and out-off phase ($\Omega_{J,2}$) solutions of the differential equations, i.e., the lower frequency plasmon corresponds to in-phase tunneling currents across both junctions, whereas the higher frequency plasmon are out-off-phase currents in the two junctions [197, 201]. The current density of the higher frequency mode, due to their stronger coupling ($\propto 1/d$), is mostly concentrated in between the more closely spaced layers [202]. That is why this plasmon is commonly referred to as intra-bilayer and the low frequency plasmon as inter-bilayer mode. Their real space current patterns are sketched in Figure 3.9 (d) and (f). The two longitudinal modes are identified by peaks in the energy-loss function $Im(-1/\varepsilon)$, whereas the transverse mode creates a peak in the imaginary part of ε which is shown in Fig. 3.9 (c).

Figure 3.10 compares this model to the prototypical bilayer cuprate $\text{YBa}_2\text{Cu}_3\text{O}_{6.5}$ (Data taken from [30, 203, 204]). The two Josephson plasma resonances of the inter-bilayer junction at $\Omega_{J,1} = 29 \text{ cm}^{-1}$ and the bilayer junction at $\Omega_{J,2} = 475 \text{ cm}^{-1}$ have clear signatures in the loss function and the reflectivity. The transverse mode at $\Omega_T = 410 \text{ cm}^{-1}$ is visible as a peak in the imaginary part of the dielectric function. These optical features of the superconducting state are well reproduced by the model above and are superimposed on top of a background of infrared active lattice vibrations. An extension of this model to finite momentum, like presented for a single junction, involving the Josephson equations is presented in Ref. [205] and [202]. The main result are the dispersion relations for the two Josephson plasma modes,

$$\omega_i^2(q_{x,y}) = \frac{\Omega_{J,1}^2 + \Omega_{J,2}^2 + c^2 q_{x,y}^2/\varepsilon_\infty}{2} \pm \sqrt{\left(\frac{\Omega_{J,1}^2 + \Omega_{J,2}^2 + c^2 q_{x,y}^2/\varepsilon_\infty}{2}\right)^2 - \Omega_{J,1}^2 \Omega_{J,2}^2 - c^2 q_{x,y}^2/\varepsilon_\infty}, \quad (3.30)$$

in the transverse configuration. Similar, to Fig. 3.6 and the relation for a single junction the dispersion of the transverse modes scales as $q_{x,y}^2$, for small $q_{x,y}$. However, when $\Omega_{J,1}(q_{x,y})$

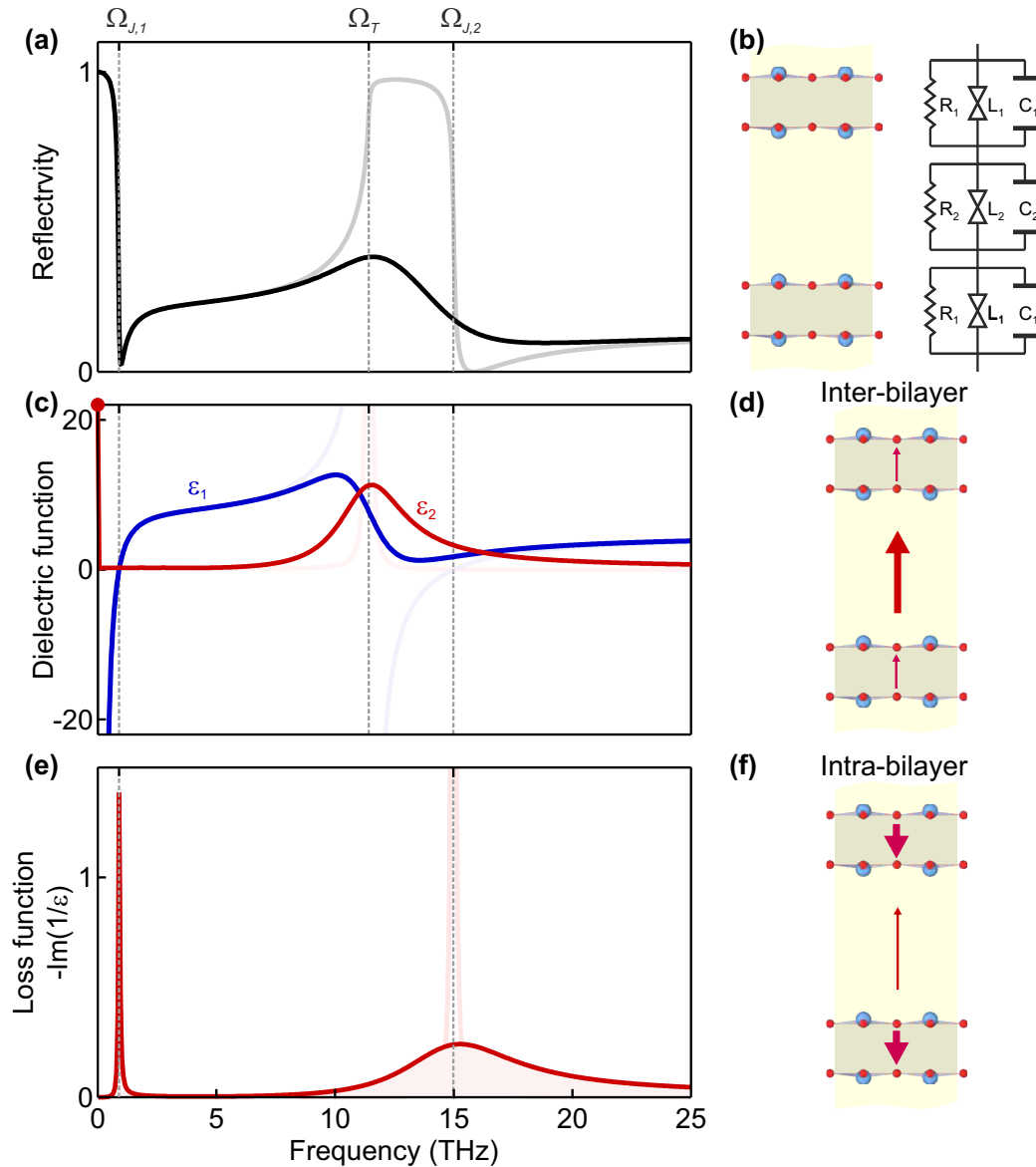


Figure 3.9: Optical properties of a bilayer cuprate. (a) Simulated reflectivity of a stack of in-equivalent Josephson junctions. A stack of in-equivalent Josephson junctions (depicted in panel (b)) creates multiple reflectivity edges at the Josephson plasma frequencies $\Omega_{J,i}$ (black curve). In between the two plasma edges a transverse resonance Ω_T appears, which is separated by a Reststrahlenband from $\Omega_{J,2}$. The grey line is a simulation result for low dissipation (grey line). (b) Schematic geometry of two in-equivalent intrinsic Josephson junctions and the corresponding equivalent circuit. (c) Simulated dielectric function of a stack of in-equivalent Josephson junctions. The dielectric function shows a $1/\omega$ divergence of the real part (blue) at low frequencies in addition to a dispersive feature at $\Omega_{J,2}$, and the imaginary part is a delta peak at zero frequency and a Lorentzian of finite width at Ω_T . The light red and blue lines are simulations for low dissipation. (e) Simulated loss function of a stack of inequivalent Josephson junctions. The two Josephson plasma modes become visible as peaks in the loss function and their current pattern mainly involves current in the inter-bilayer (shown in panel (d)) and intra-bilayer (shown in panel (f)) region.

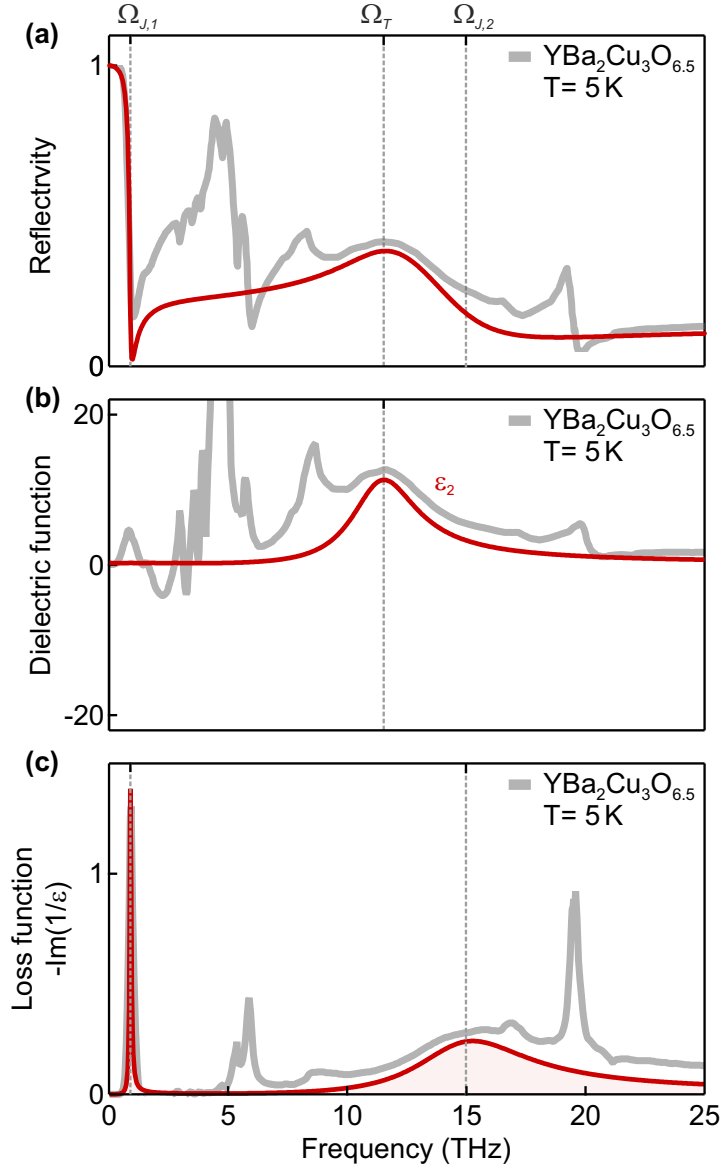


Figure 3.10: Optical properties of a bilayer $\text{YBa}_2\text{Cu}_3\text{O}_{6.5}$. (a) The optical properties of the bilayer Cuprate $\text{YBa}_2\text{Cu}_3\text{O}_{6.5}$ (grey) below the transition temperature $T_c = 52\text{ K}$ can accurately be described with the optical properties shown in Fig. 3.9 (red curves). It captures the two plasma edges at $\Omega_{J,1} = 29\text{ cm}^{-1}$ and $\Omega_{J,2} = 475\text{ cm}^{-1}$, as well as the transverse plasma resonance at $\Omega_T = 410\text{ cm}^{-1}$ (see panel (b)) and the peaks in the loss function at $\Omega_{J,1} = 29\text{ cm}^{-1}$ and $\Omega_{J,2} = 475\text{ cm}^{-1}$ (see panel (c)). The remaining features in the optical properties are due to infrared active lattice vibrations.

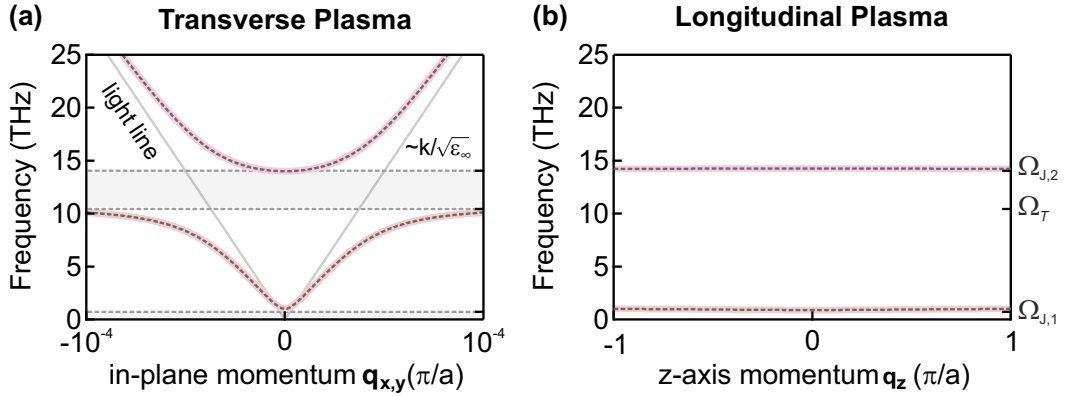


Figure 3.11: Dispersion relation of the Josephson plasma mode in a bilayer system. (a) Dispersion relation of the transverse Josephson plasma modes in a bilayer system. The dispersion of Josephson plasma modes in bilayer system shows two branches (black dashed lines), one for the inter-bilayer and one for the intra-bilayer mode. The dispersion of the transverse modes which propagates along the CuO_2 planes show a parabolic dispersion close to $q_{\text{Plas}} = 0$, which approach the linear dispersion of light $\nu = k/\sqrt{\epsilon_\infty}$. The high frequency plasmon at $\Omega_{J,2}$ monotonously disperses upwards, whereas the lower frequency plasmon at $\Omega_{J,1}$ shows an avoided crossing behavior when $\Omega_{J,1}(q_{x,y})$ approaches $\Omega_{J,2}(0)$ and $\Omega_{J,1}(q_{x,y}) \rightarrow \Omega_J$, for $q_{x,y} \rightarrow \infty$. This behavior is reminiscent of a phonon-polariton dispersion (see Chapter 1). (b) Dispersion relation of the longitudinal Josephson plasma modes in a bilayer system. The longitudinal plasma modes only show a weak dispersion up to the Brillouin zone boundary.

approaches $\Omega_{J,2}(0)$, the dispersions exhibits an avoided crossing behavior and $\Omega_{J,1}(q_{x,y})$ asymptotically approaches Ω_T as can be seen in Figure 3.11 (a). The high frequency plasmon $\Omega_{J,2}(q_{x,y})$ monotonously disperses upwards. The coupling between the two junctions in this configuration is dominated by an capacitive response leading to the strong (light like) dispersion of the transverse Josephson plasmons [202].

In the longitudinal configuration the phase-differences vary along the z-axis and the coupling is purely inductive [202][146]. As a result, the dispersion along the z-axis is very weak and featureless (see Fig. 3.11 (b)), but also shows two Josephson plasmon branches.

These optical fingerprints of the superconducting condensate in bi-layer cuprates are strongly temperature dependent as can be seen in Figure 3.12. The simple addition of $\epsilon_{\text{JPR}}(\omega)$ to $\epsilon_{\text{Phonon}}(\omega)$ to model the total infrared optical dielectric response however fails to explain this temperature dependence. As shown in Figure 3.12 (a), the emergence of the transverse mode is accompanied by a phonon reshaping in the spectral range of 200 cm^{-1} to 700 cm^{-1} , which is strongest for the Cu-O bending mode at 320 cm^{-1} [204]. The transverse Josephson plasma

mode gains spectral weight from this phonon. To explain this, Munzar et al. extended the original model by including local fields for the inter- and intra-bilayer region, which act on the ions of the infrared-active phonon modes [206, 207]. The phonon anomalies can be explained by changes in these local electric fields due to the transition in the superconducting state. To fit the temperature dependence it was only necessary to adjust the damping rate γ of the transverse plasma mode as shown in Figure 3.12 (b). Interestingly, the phonon reshaping due to the intra-bilayer plasmon persists up to 150 K, far above the transition temperature of $T_c \approx 59$ K and it has been proposed that this is a signature of a precursor state of superconductivity [208]. This precursor state is believed to involve pre-formed Cooper pairs in the CuO_2 planes far above T_c and Josephson coupling within the strongly coupled bilayers. While this process sets in above the transition temperature, large phase fluctuations prevent coherent tunneling between the superconducting condensates across the inter-bilayer junction [68, 192]. In fact, the low frequency Josephson plasma mode in $\text{YBa}_2\text{Cu}_3\text{O}_{6.5}$ shows the expected behavior with increasing temperature. Fig. 3.12 (c) shows the temperature dependence of the low frequency loss function peak of $\text{YBa}_2\text{Cu}_3\text{O}_{6.5}$. The spectral weight of the peak ($\sim \Omega_{J,1}^2$) as well as its position decrease with increasing temperature and vanish at T_c . Further, this mode usually lies below the energy range of the infrared active lattice vibration which allows the simple description of its dielectric response by $\varepsilon_1(\omega) = \varepsilon_\infty \left(1 - \omega_{J,1}^2/\omega^2\right)$, without any reshaping of the optical lattice vibrations. Indeed, the total phonon spectral weight in $\text{YBa}_2\text{Cu}_3\text{O}_{6.5}$ remains constant up to high temperatures and only shows a smooth transition at T_c as plotted in Fig. 3.12 (d) [206, 207, 212].

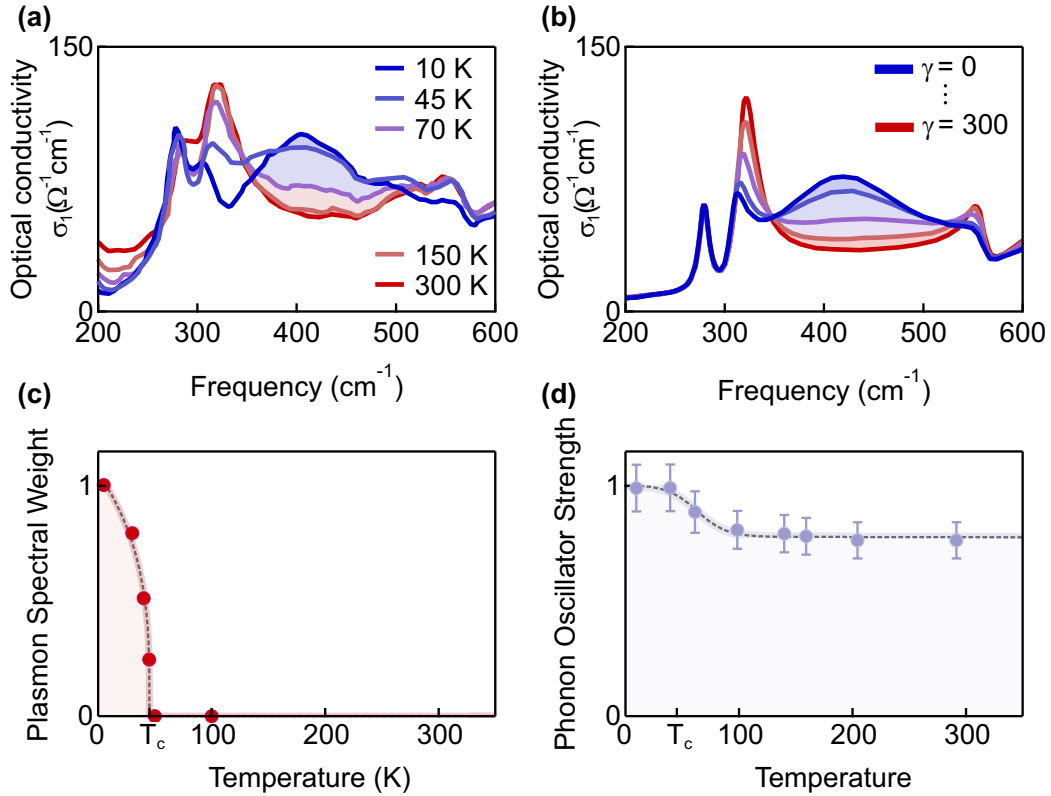


Figure 3.12: Temperature dependence of the optical properties of $\text{YBa}_2\text{Cu}_3\text{O}_{6.5}$. (a) Optical conductivity of $\text{YBa}_2\text{Cu}_3\text{O}_{6.5}$ for different temperatures. The optical conductivity of $\text{YBa}_2\text{Cu}_3\text{O}_{6.5}$ shows a spectral weight transfer from the $\Omega_{\text{IR}} = 320 \text{ cm}^{-1}$ phonon mode to the transverse plasma mode at $\Omega_{\text{T}} = 410 \text{ cm}^{-1}$ that sets in at 150 K. (b) Simulated optical conductivity of $\text{YBa}_2\text{Cu}_3\text{O}_{6.5}$ for different damping parameters of the intra-bilayer plasmon. The simulation involves introducing local fields in between the inter and intra-bilayer region according to the work of Munzar et al. [206, 207]. Only the damping rate γ of the transverse plasma mode is varied to reproduce the experimentally observed behavior accurately. (c) Temperature dependence of the spectral weight of the inter-bilayer Josephson plasmon. The low-frequency Josephson plasma edge of the inter-bilayer junction disappears at T_c . (d) Temperature dependence of the phonon oscillator strength. The spectral weight of the infrared phonons only shows a small anomaly at T_c and then stays constant up to room temperature. Part of the figure, caption and data are adapted from Ref. [209–212].

Chapter 4

Parametrically Amplified Phase-Incoherent Superconductivity in $\text{YBa}_2\text{Cu}_3\text{O}_{6+\delta}$

4.1 Introduction

Recent optical experiments using intense THz frequency excitations pulses demonstrated a plethora of nonlinear phenomena of the Josephson physics in cuprates, like the nonlinear propagation of Josephson plasmons in the form of solitons [74], as well as parametric amplification [75] and third harmonic generation [41] from a Josephson plasma resonance. Beyond, resonant large amplitude lattice excitation in the mid-infrared range revealed signatures of Josephson coupling of the stacked CuO_2 plane above the equilibrium transition [30–32]. These experiments showed that optical excitation can tip the competition between electronic/magnetic orders and superconductivity in favor of the latter and suggest that preformed, phase-incoherent, Cooper pairs exist throughout the pseudogap phase and which are being synchronized by the optical driving. These signs of a precursor state of superconductivity were also predicted by several other measurements of the equilibrium superconducting properties [208, 213–217].

Two of the out-of-equilibrium experiments on the THz- Josephson plasmon dynamics motivated the work presented in the following paragraphs. The first involves the resonant optical excitation of the apical oxygen vibrations in the underdoped bilayer cuprate $\text{YBa}_2\text{Cu}_3\text{O}_{6.5}$ [32]. Above the critical temperature, this vibrational excitation entails the appearance of a short-lived characteristic peak in the THz loss-function reminiscent of a transiently formed Josephson plasmon shown in Fig. 4.1 (a) as red symbols at a pump-probe time-delay of 0.8 ps. The grey curve (also in panel (b)) shows the equilibrium loss which is featureless. This finding was later

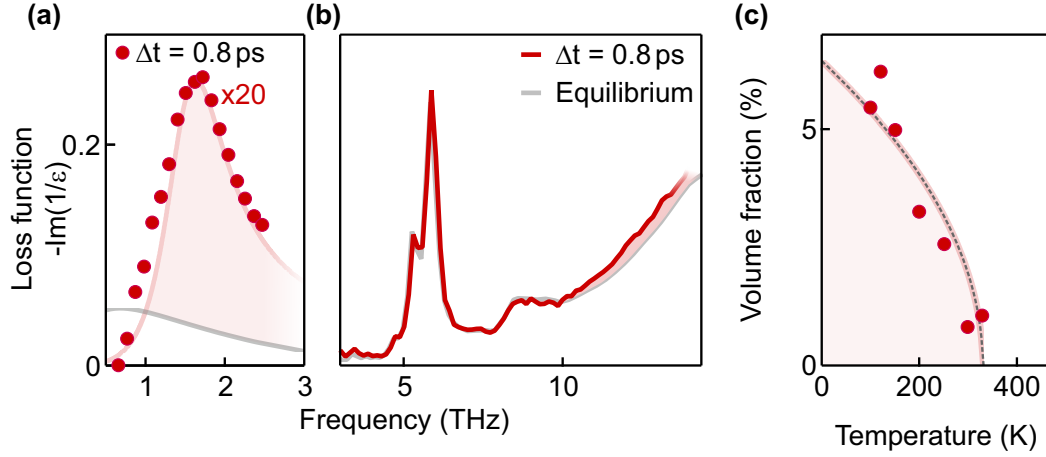


Figure 4.1: Light-induced superconductivity and competing orders. (a) Light induced loss function peak in $\text{YBa}_2\text{Cu}_3\text{O}_{6.5}$. After resonant lattice excitation of the apical oxygen vibration in $\text{YBa}_2\text{Cu}_3\text{O}_{6.5}$, above the equilibrium T_c , a peak in the loss function appears at 1.9 THz, which was attributed to the inter-bilayer plasma resonance. (b) Light induced red-shift of the loss function of the intra-bilayer Josephson plasmon in $\text{YBa}_2\text{Cu}_3\text{O}_{6.5}$. Together with the reappearance of the low frequency loss function peak, the loss function peak of the intra-bilayer junction shifts to lower frequencies (shaded in red). (c) The volume fraction of the transformed volume, which shows these optical fingerprints of a superconductors, vanishes only above 350 K. Part of the figure and caption are adapted from Ref. [30, 32].

corroborated by another time-resolved reflectivity measurement carried out in the mid-infrared spectral range [30], which allowed for the measurement of the intra-bilayer Josephson plasmon at $\Omega_{\text{intra}} = 14.2$ THz. It was found that in the transient state, drawn as a red line in Fig. 4.1 (b), the inter-bilayer (low frequency) Josephson plasmon acquires spectral weight at the expense of the intra-bilayer plasma mode, while the total spectral weight remained conserved. This can be seen in Fig. 4.1 (b) as a red-shift of the high-frequency intra-bilayer plasmon from its equilibrium position drawn in grey and the independent measurement at the low THz frequencies (shown in Fig. 4.1 (a)) [30]. The spectral weight of both plasmons is determined by the superfluid density and consequently their plasma frequencies $\omega_p^2 \propto \rho_s$. Thus, this type of excitation increases inter-bilayer coupling at the expense of the intra-bilayer coupling, which strengthens the superconducting state. Above T_c , the same behavior was observed up to the pseudogap temperature $T^* = 350$ K, creating a short-lived state with all THz-optical signatures of the superconducting state. The second set of experiments used strong-field THz nonlinear spectroscopy to reveal hidden states, which are invisible to linear spectroscopy. The responsible

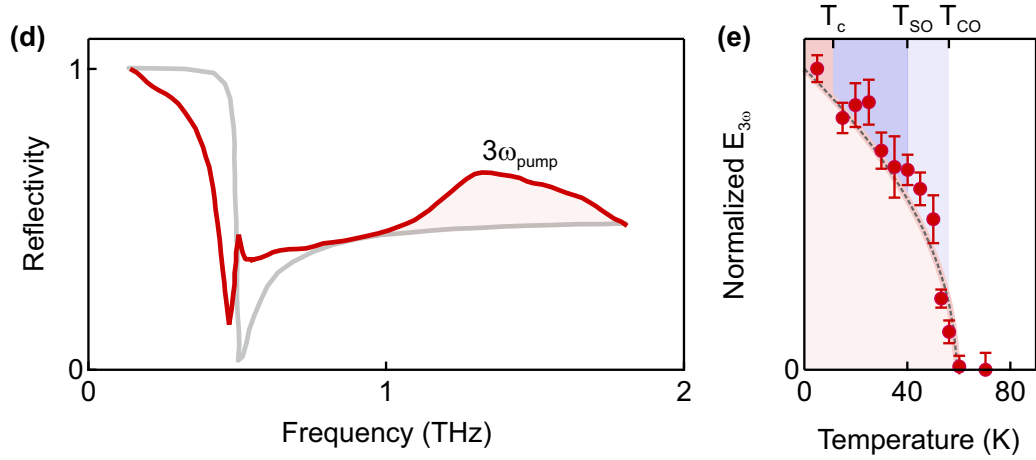


Figure 4.2: Third-harmonic generation in a cuprate superconductor (a) THz-reflectivity of $\text{La}_{1.885}\text{Ba}_{0.115}\text{CuO}_4$ for small and high THz-fields. The THz reflectivity of a single Josephson junction (grey) strongly reshapes and shows a third harmonic response (red and shaded red) when driven by strong THz light pulses. (b) The third harmonic response was taken as a hallmark of superconducting tunneling and could be observed up to the characteristic charge ordering temperature T_{CO} , far above T_c , in the single layer cuprate $\text{La}_{1.885}\text{Ba}_{0.115}\text{CuO}_4$. Part of the figure and caption are adapted from Ref. [41].

nonlinear four-wave mixing allowed to detect the optical third harmonic of a single-cycle THz-pulse generated from $\text{La}_{1.885}\text{Ba}_{0.115}\text{CuO}_4$ as a measure of the third-order optical nonlinearity $\chi^{(3)}$ induced by the superconducting state [41, 75]. Figure 4.2 (a) shows the THz reflectivity of $\text{La}_{1.885}\text{Ba}_{0.115}\text{CuO}_4$ for low fields (grey) and high fields (red). The low field response shows a reflectivity edge at the plasma frequency as predicted by the linear sine-Gordon equation. At larger electric field, this edge distorts due to parametric amplification, and a third harmonic peak appears at three times the center frequency of the THz light. This nonlinearity originates from the Josephson tunneling described by the sine-Gordon equation and expanding $\sin(\varphi)$ up to the second term

$$\nabla_{xy}^2 \varphi = \left(1 - \frac{\partial^2}{\partial z^2}\right) \left(\varphi - \frac{1}{6}\varphi^3 + \gamma \frac{\partial \varphi}{\partial t} + \frac{\partial^2 \varphi}{\partial t^2}\right) \quad (4.1)$$

Most importantly, the third harmonic could be detected even above the equilibrium transition temperature T_c , and up to a temperature T_{CO} as plotted in Fig. 4.2 (b). The red data points are the integrated spectral weight of the optical third-harmonic (shaded red in Fig. 4.1 (d)). Below T_{CO} the material develops a charge-ordered phase. This supports the presence of a pair density wave condensate, proposed earlier [43, 44, 71, 218, 219], in which nonlinear mixing of

optically silent tunneling modes drives large dipole-carrying supercurrents [41]. This type of optical nonlinearity has some analogy to the hyper-polarizability in hyper-Raman scattering. Both types of nonlinear interaction are sensitive to optically silent modes, which do not appear in the linear optical properties, measured by infrared or Raman spectroscopy.

The following paragraphs will show how ultra-fast second harmonic generation can be used to measure the coherent dynamics of Josephson plasma modes in $\text{YBa}_2\text{Cu}_3\text{O}_{6+\delta}$, impossible with conventional time-resolved THz-spectroscopy. They appear as coherent oscillations in the time-resolved second harmonic intensity after optical excitation. Similar to [41, 75] and the previous experiments on $\text{YBa}_2\text{Cu}_3\text{O}_{6+\delta}$ [30, 32], these results suggest residual pairing fluctuations above the equilibrium transition temperature. Beyond that, momentum-resolved measurements of the SH-intensity allow to identify the coherent oscillations as finite-momentum Josephson plasma modes. These results and the earlier ones involving THz time-domain spectroscopy [30, 32] can be explained by a new microscopical model, also outlined below. Parts of this chapter are taken from Ref. [166, 220].

4.2 Properties of $\text{YBa}_2\text{Cu}_3\text{O}_{6+\delta}$

The experiments presented in the next paragraphs were conducted on underdoped $\text{YBa}_2\text{Cu}_3\text{O}_{6+\delta}$ single crystals. The samples were grown by the top-seeded solution (flux) method in Y-stabilized zirconium crucibles [221, 222]. The compound $\text{YBa}_2\text{Cu}_3\text{O}_{6.5}$ crystallizes in a centrosymmetric orthorhombic unit cell with $Pmmm$ space group symmetry and comprises bilayers of buckled CuO_2 planes as depicted in Figure 4.3 (a) [223]. The two intrinsic Josephson junctions are sketched in Figure 4.3 (b) shaded in grey and beige. The more closely spaced intra-bilayer junction ($\Omega_{\text{P},2} = 14.2$ THz) is separated by an insulating layer of Yttrium atoms, whereas the weakly-coupled inter-bilayer junction ($\Omega_{\text{P},2} = 0.9$ THz) contains Cu-O chains along the b-axis that serve as charge reservoir and control the hole doping of the CuO_2 planes. With increasing oxygen content, the electrons in the CuO_2 -planes are progressively transferred to the Cu-O chains and the compound becomes hole-doped. Technically, this doping p is controlled through annealing in flowing O_2 -atmosphere and subsequent rapid quenching [224, 225]. $\text{YBa}_2\text{Cu}_3\text{O}_{6.5}$ contains both filled and empty chains in equal numbers and exhibits short-range Ortho-II ordering of the vacancies, in which adjacent chains are alternately filled or empty as shown in Figure

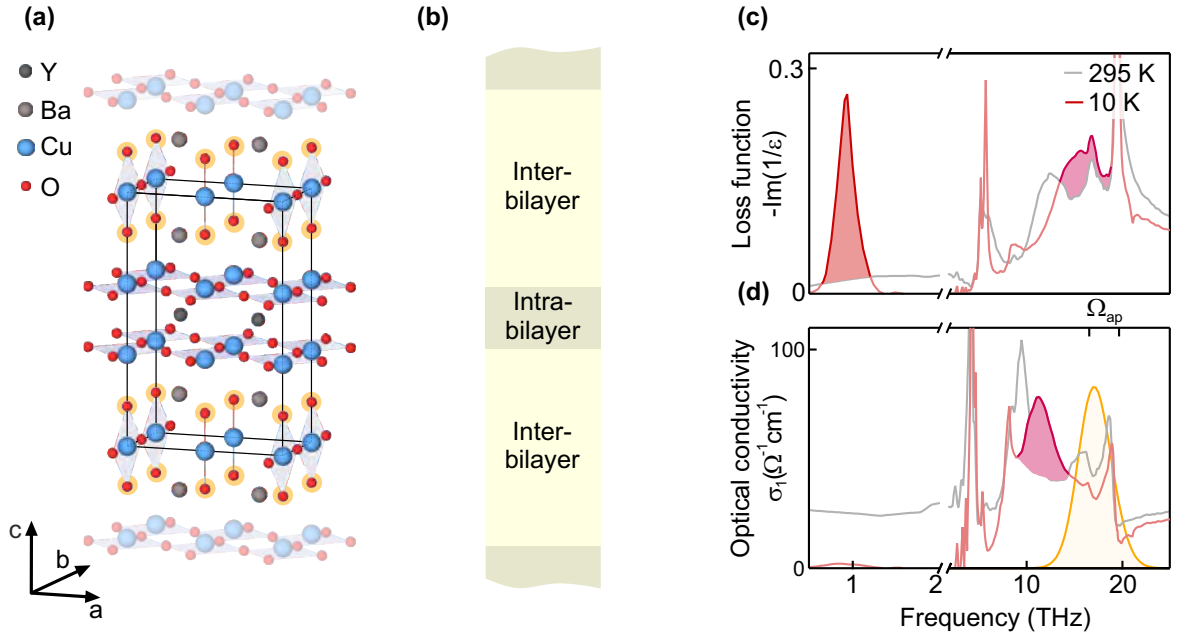


Figure 4.3: Structure and optical properties of $\text{YBa}_2\text{Cu}_3\text{O}_{6.5}$. (a) Crystal structure of $\text{YBa}_2\text{Cu}_3\text{O}_{6.5}$. $\text{YBa}_2\text{Cu}_3\text{O}_{6.5}$ crystallizes in a centrosymmetric orthorhombic unit cell with $Pmmm$ space group symmetry. The CuO_2 layer are separated by insulating layers containing Yttrium (intra-bilayer) and charge reservoir layers containing Barium atoms (inter-bilayer). The apical oxygen atoms in the inter-bilayer region are shaded in yellow. The doping of the Y-Ba-Cu-O compounds is controlled by the oxygen concentration of the inter-bilayer region in the so-called chains. (b) Schematic of the inter- and intra-bilayer junction. (c) The energy loss function and real part of the optical conductivity $\sigma_1(\omega)$ along the c-axis of $\text{YBa}_2\text{Cu}_3\text{O}_{6.5}$ for temperatures of 10 K (red lines) and 295 K (grey lines) identifies the Josephson plasma modes as red and magenta shaded peaks. The remaining resonances can be ascribed to infrared-active lattice vibrations. The apical oxygen vibrations at $\Omega_{\text{ap,YBCO7}} = 17.2$ THz and $\Omega_{\text{ap,YBCO6}} = 20.5$ THz, were excited by optical pump-pulses tuned to $\Omega_{\text{MIR}} = 18$ THz center frequency (spectrum shaded in orange).

4.3 (a) [223].

The oxygen atom connecting the chain-copper atoms and the plane-copper atoms, highlighted yellow in Fig. 4.3 (a), the apical oxygen, deserves special attention. This oxygen atom was found to be intimately related to the superconducting state as its distance from the CuO_2 changes with doping and is correlated with T_c [226–228]. The highest frequency lattice vibration in $\text{YBa}_2\text{Cu}_3\text{O}_{6+\delta}$ corresponds to a polar oscillation of this apical oxygen ion which splits into two inequivalent modes, due to the different chemical environment of the filled and empty chains [204]. The oscillations of the apical oxygen on a filled chain and empty chain site resonant at

$\Omega_{\text{YBCO7}} = 17.2$ THz and $\Omega_{\text{YBCO6}} = 20.5$ THz, respectively. They appear as dispersive peaks in the real part of the optical conductivity plotted in Fig. 4.3 (d), denoted with Ω_{ap} . Continuous filling of the chains, starting from the parent compound $\text{YBa}_2\text{Cu}_3\text{O}_6$ to near-optimally doped $\text{YBa}_2\text{Cu}_3\text{O}_7$, leads to a continuous shift of the spectral weight from the high frequency to the low-frequency mode [204].

4.2.1 Phase diagram of $\text{YBa}_2\text{Cu}_3\text{O}_{6+\delta}$ and Precursor Superconductivity

The phase diagram of $\text{YBa}_2\text{Cu}_3\text{O}_{6+\delta}$ is shown in Figure 4.4 and follows the generic cuprate phase-diagram which is sketched in 3.7 (c) [192]. The electronic properties of the $\text{YBa}_2\text{Cu}_3\text{O}_{6+\delta}$ compounds are dominated by the CuO_2 and the orbital order between the Cu^{2+} and O^{2-} ions. Fig. 4.4 (b) shows an on-top view of the orbital orientation of the CuO_2 -planes. The $p\sigma(x, y)$ orbitals (two lobes) of the oxygen ions hybridize with the $d(x^2 - y^2)$ orbitals (four lobes) of the copper ions. Super exchange interaction between the Cu^{2+} and O^{2-} ions within the layers leads to an antiferromagnetic ordering of the spins. As a result, the undoped parent compound $\text{YBa}_2\text{Cu}_3\text{O}_6$ is an antiferromagnetic insulator (AFI), shaded in green in Figure 4.4 (a), which only extends up to a moderate doping of $p = 0.02$. Increasing doping empties the $p\sigma$ -band closest to the Fermi energy which arises from the planar $d(x^2 - y^2)$ states of the Cu^{2+} and $p\sigma(x, y)$ states of O^{2-} [191, 229, 230] and superconducting dome (shaded in red) emerges which generally peaks at a doping level $p = 0.2$, corresponding to $\text{YBa}_2\text{Cu}_3\text{O}_{6.92}$. Weaker doping levels are generally referred to as *underdoped* and stronger doping as *overdoped*. A sketch of the Fermi surface along the in-plane momenta k_x and k_y is shown in Fig. 4.4 (c). Two regions of the Fermi surface are of special interest: the antinode at the Brillouin zone boundary and the nodal region which lies on a diagonal cut through the Brillouin zone. Since the superconducting condensate arises from the charge carriers closest to E_F also the superconducting gap will exhibit this $d(x^2 - y^2)$ symmetry which was confirmed by angle resolved photoemission measurements. These measurements reveal a gap of ~ 30 meV at optimal doping in the nodal region of the Fermi surface [69, 191, 231]. The gap size was observed to increase with decreasing hole doping levels [232].

In the underdoped region the superfluid density and with-it T_c increases linearly with progressive doping [234]. This linear correlation is not expected from the BCS theory and is a unique feature of the cuprate superconductors which relates the transition temperature to the phase stiffness,

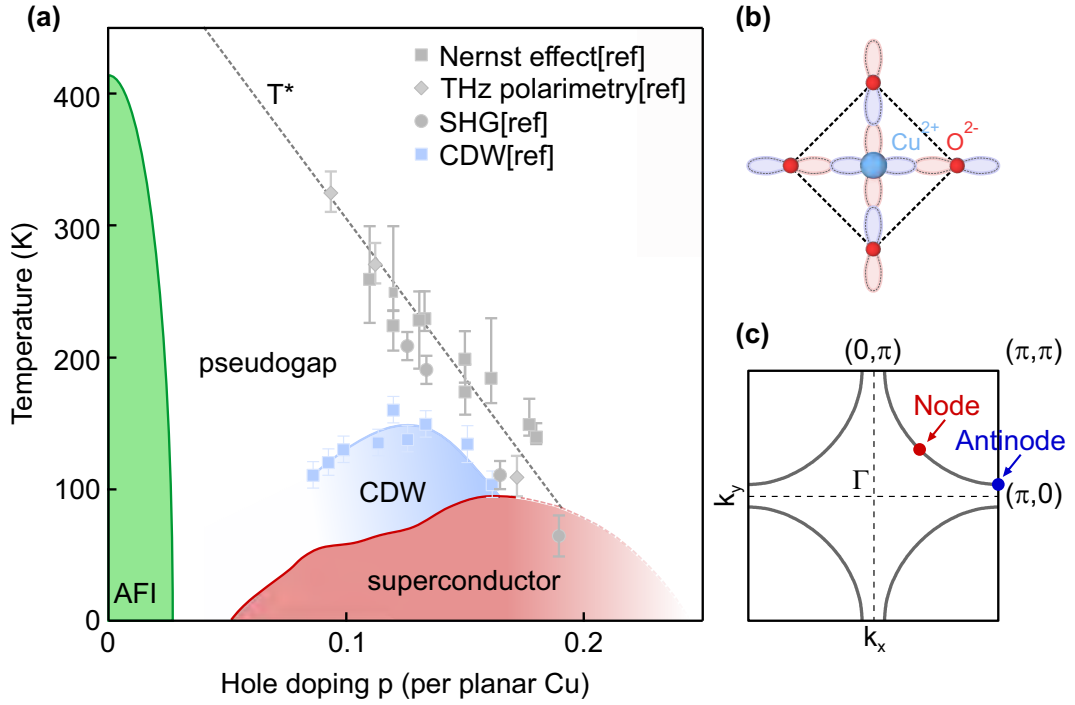


Figure 4.4: Temperature-doping phase diagram of $\text{YBa}_2\text{Cu}_3\text{O}_{6+\delta}$. (a) The phase diagram of the bilayer cuprate $\text{YBa}_2\text{Cu}_3\text{O}_{6+\delta}$ shows an antiferromagnetic insulator (AFI, green) near zero doping which extends up to high temperatures. With increasing doping of the parent compounds the AF-order is suppressed and at low temperatures a superconducting dome appears (shaded red), which peaks at a doping of 0.2 electrons per planar Cu ($\delta = 0.92$). Around a doping of 0.12 the superconducting dome is slightly suppressed by the emergence of a charge density wave (CDW, blue squares). At higher temperatures up to T^* , the material is in the so-called pseudogap phase, where the material breaks a number of symmetries as witnessed by different techniques (grey symbols). (b) Orbital arrangement of the plane Cu^{2+} and O^{2-} ions. The p -orbitals (two lobes) of the oxygen are aligned with the $d(x^2 - y^2)$ orbital of the copper (four lobes). (c) Schematic of the Fermi surface of the cuprates. In the Fermi surface (grey lines), the superconducting gap opens in the nodal-region (red dot), whereas a gap in the anti-nodal region already opens at T^* . Part of the figure and caption are adapted from Ref. [69, 233].

defined by ρ_s/m^* [196, 235]. Usually ρ_s/m^* identifies a temperature T_θ below which a phase coherent condensate can form. In conventional superconductors $T_\theta \gg T_c$; hence once Cooper pairs form at T_c they immediately condense. However in the cuprates, due to their anomalously small superfluid density [192, 196], T_θ and T_c are of the same order and the thermal fluctuations of the phase suppress the superconducting ground state [68].

The discrepancy between T_θ and T_c lead to the general debate whether Cooper pairs already

form at the so-called pseudogap temperature T^* , which is shown as a dashed line in Fig 4.4 (a). These pre-formed pairs then, at the far lower temperature T_c , phase lock to form the long-range ordered superconducting state. Some evidence of such a precursor state of superconductivity and pre-formed Cooper pairs was found in infrared spectroscopy [208], angle-resolved photoemission spectroscopy (ARPES) [213] and other techniques [44, 214–217].

The interpretation of the pseudogap region as precursor state of superconductivity exist between other exotic phases, which allow to explain the strange properties of the pseudogap region. These phases include a variety of orders which compete with superconductivity and involve ordering of the electrons into stripes as well as a possible spatially modulated superconducting state (pair density wave in $\text{Bi}_2\text{Sr}_2\text{CaCu}_2\text{O}_{8+x}$ or $\text{La}_{1.885}\text{Ba}_{0.115}\text{CuO}_4$) [43, 44, 71, 218, 219]. In the single layer cuprate $\text{La}_{2-x}\text{Ba}_x\text{CuO}_4$, competition with a charge ordered phase fully suppresses superconductivity at 1/8th doping [236]. Such a charge ordered phase also exists in $\text{YBa}_2\text{Cu}_3\text{O}_{6+\delta}$ in the underdoped regime around 1/8th doping shown as blue dots in Fig. 4.4 (a) [237–239]. Here, however the superconducting state is only slightly suppressed due to the more robust superconducting condensate in $\text{YBa}_2\text{Cu}_3\text{O}_{6+\delta}$ compared to $\text{La}_{2-x}\text{Ba}_x\text{CuO}_4$ [240].

One of the physical characteristics that distinguish the pseudogap region from the other non-superconducting phases of the cuprates is the partial opening of an electronic gap in the antinodal direction of the Brillouin zone (see Fig. 4.4 (c)). This gap was initially seen in *c*-axis polarized infrared conductivity measurements and is associated with an upturn in the *c*-axis resistivity [241]. Most strikingly, it was then also observed in angle-resolved photoemission spectroscopy in the antinodal direction of the Brillouin zone [242, 243] where it smoothly evolved into the *d*-wave superconducting gap below T_c , hinting at precursor pairing. Further measurement with other techniques revealed, that the opening of the gap is accompanied by a breaking of time-reversal [70, 244], rotational [215] and mirror [245] symmetries.

More recently, static SH-polarimetry revealed the point-group symmetry of $\text{YBa}_2\text{Cu}_3\text{O}_{6+\delta}$ compounds and found broken inversion symmetry as well as broken two-fold rotational symmetry below T^* [233]. Hence, the space-group symmetry of $\text{YBa}_2\text{Cu}_3\text{O}_{6+\delta}$ is not the inversion-symmetric $Pmmm$, as one would expect from the crystal structure, but rather $P2'/m$ or $Pm1'$. These findings suggest the existence of an odd-parity order that does not arise from competing Fermi surface instabilities, such as superconductivity and charge-order, and exhibits a quantum phase transition inside the superconducting dome [246]. So far, no consensus about the true nature of

the pseudogap phase could be achieved, but it is generally accepted to be a true phase transition [70].

4.3 Coherent Josephson Plasmon Dynamics in $\text{YBa}_2\text{Cu}_3\text{O}_{6+\delta}$

4.3.1 Time-Resolved Second Harmonic Detection Setup

The pump probe experiments presented in the following on $\text{YBa}_2\text{Cu}_3\text{O}_{6+\delta}$ combined the excitation of the apical oxygen vibrations at frequencies $\Omega_{\text{YBCO7}} = 17.2 \text{ THz}$ and $\Omega_{\text{YBCO6}} = 20.5 \text{ THz}$ with time resolved polarization-rotation and SH intensity measurements (see Fig. 4.5 (a)). The setup used in this experiment is similar to the one sketched in Figure 2.9. It was modified to collect both the SH light emitted from the sample and the linear polarization rotation of the 800-nm probe light, in reflection geometry. CEP stable mid-infrared pump 18-THz pulses (2 μJ to 3 μJ pulse energy), focused down to a 60 μm spot size, were used to excite the sample. They were 150 fs in duration and polarized along the *c*-axis. The pump spectrum is shown in Fig. 4.3 (d), shaded in yellow, clearly covering the frequencies of the two apical oxygen vibrations. The probe pulses were 30 fs in duration, centered at 800 nm wavelength and had an energy of 70 nJ focused to a spot size of 25 μm on the sample. A $\lambda/2$ -waveplate was used to rotate their linear polarization. The emitted second-harmonic beam and the reflected fundamental 800-nm beams are separated at a dichroic mirror. A Wollaston prism in the SH beam selects a specific polarization of the SH light to be detected at the highly sensitive photomultiplier tube (PMT). The polarization rotation of the reflected 800-nm light is analyzed by balancing the intensity of two cross-polarized components on two photodiodes, achieved by using a $\lambda/2$ -waveplate and a Wollaston prism. The time delay Δt dependent changes of the SH intensity and of the 800-nm polarization rotation after optical excitation are read-out by two independent lock-in amplifiers locked into the modulation frequency of a mechanical chopper that blocks the mid-infrared pump pulses at half the laser repetition rate of 1 kHz.

4.3.2 Time-Resolved Second Harmonic Measurements

First, the incoming probe pulses were polarized along the $\text{YBa}_2\text{Cu}_3\text{O}_{6+\delta}$ *c*-axis direction as depicted in Fig. 4.5 (a). The 30-fs duration of the optical probe allowed to resolve dynamics up to 30 THz in frequency and therefore covers all the low energy excitations of $\text{YBa}_2\text{Cu}_3\text{O}_{6+\delta}$

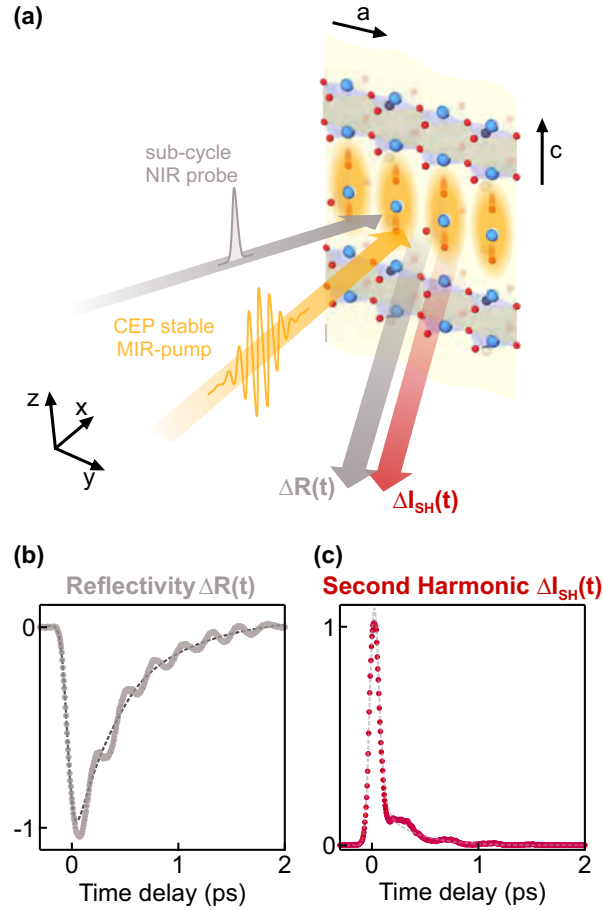


Figure 4.5: Schematic of the pump-probe experiment on $\text{YBa}_2\text{Cu}_3\text{O}_{6+\delta}$. (a) Schematic of the pump-probe geometry. In the experiment a CEP stable MIR pulse tuned to 17.5 THz resonantly excites vibrations of the apical oxygen (shaded in yellow). The dynamics are sampled by a time delayed NIR probe-pulse. Both light pulses are polarized along the crystals c -axis. The time-delay dependent measurement of the linear polarization rotation $\Delta R(t)$ of the NIR probe (grey) and the second harmonic intensity $I_{SH}(t)$ (red) revealed all symmetry even and symmetry odd dynamics in the material, respectively. (b) The time-resolved polarization rotation signal showed coherent oscillations on top of a slowly changing background. (c) The time-dependent second harmonic intensity showed a sharp response around time delay $\Delta t = 0$, followed by coherent oscillations on a smooth background. The experiment was carried out at a sample temperature of $T = 5$ K.

shown in Fig. 4.3 (c) and (d). Figures 4.5 (b) and (c) show the time-resolved SH intensity and polarization rotation (PR) signals for a mid-infrared excitation peak field strength of 7 MV/cm and a sample temperature of 5 K. The modulation in PR and in the SH intensity, in Figure 4.5 (b) and (c), are both characterized by a prompt change as pump and probe pulses overlapped in time and show coherent oscillations on top of a slowly varying background at later delays. Because of the centrosymmetric point group of $\text{YBa}_2\text{Cu}_3\text{O}_{6+\delta}$ compounds the two probes are either sensitive to symmetry-even (PR) or symmetry-odd modes (SH) [79, 116, 120]. The probe penetrated into the material up to a depth of 200 nm, much shorter than the extinction depth of the MIR pump pulses [247, 248]. This relation ensured a homogeneous excitation of the probed volume.

The coherent oscillations in the time-resolved PR signal in Fig. 4.5 (b) will be shown to descend from third-order nonlinear phononics in a later paragraph. The following discussion will focus on the time-resolved second harmonic intensity measurements.

The time-dependent second harmonic intensity $\Delta I_{\text{SH}(t)}$, plotted in Fig. 4.5 (c) exemplary for an experiment on $\text{YBa}_2\text{Cu}_3\text{O}_{6.48}$, detects all the coherently excited infrared-active and silent excitations. Those are symmetry-odd and hence modulate the second-order susceptibility $\Delta\chi^{(2)}(t)$ in time through a Hyper-Raman process (see Chapter 1). Fig. 4.6 (a), (c) and (e), report the coherent oscillations of the second harmonic signal after subtracting the slowly varying non-oscillatory contributions to the signal for three different excitation field strength, 300 kV/cm, 500 kV/cm and 7 MV/cm at a sample temperature of 5 K, well below the corresponding critical temperature $T_{c, 6.48} = 48$ K. The background can be attributed to nonlinear optical mixing of pump and probe pulses and therefore electric-field-induced second harmonic generation (EFISH) (see Chapter 1).

The data shown in Fig. 4.6 (a), for the lowest excitation strength 300 kV/cm, and the corresponding Fourier transform in Fig. 4.6 (b)(dashed black line), are representative of linear excitation of two modes at 17 and 20 THz, which were simultaneously driven by the broad spectrum of the ultrashort pump pulse. $\Delta I_{\text{SH}(t)}$ oscillated at the eigen-frequencies of these two modes and decayed within a few hundred femtoseconds after the excitation. The dashed line in panel (a) is a fit to the data (for details of the signal dissection see Appendix C.1) and the colored peaks in panel (b) are Fourier transforms of the individual oscillatory components of this fit. The real space motion of both modes is sketched in Fig. 4.8 (c).

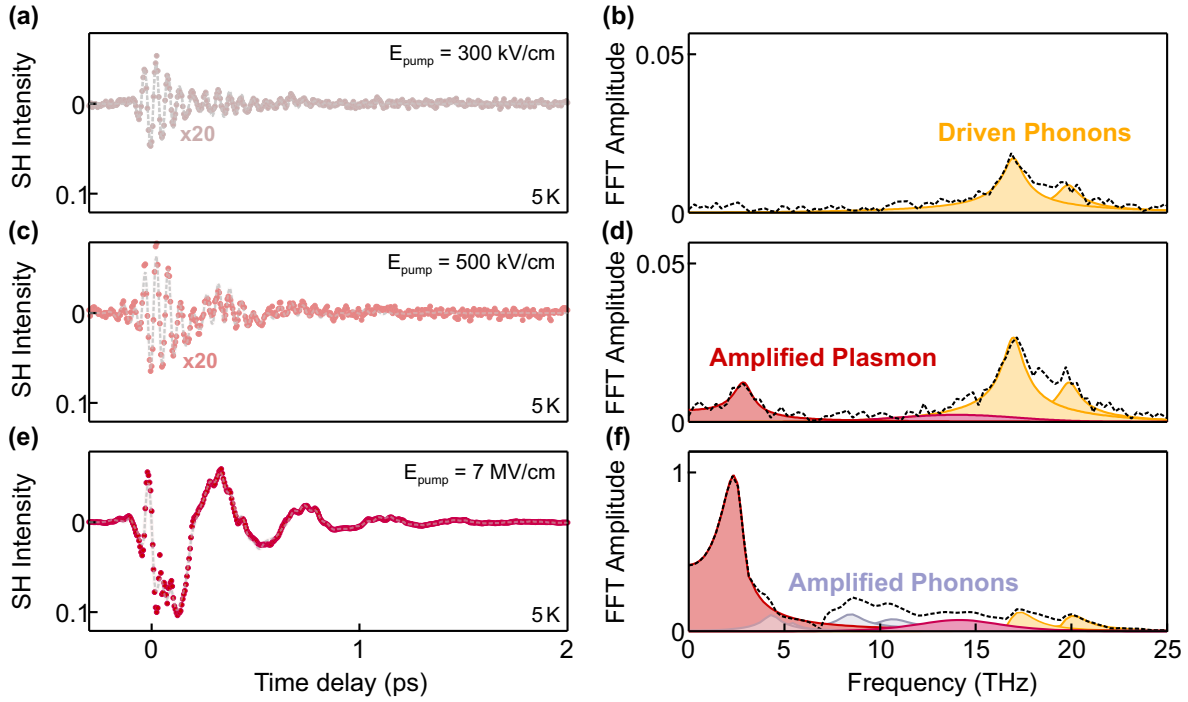


Figure 4.6: Coherent oscillations in the time-resolved second harmonic intensity. (a) and (b), Coherent oscillations of the SH signal at the lowest excitation field ($E = 0.3 \text{ MV/cm}$) and the corresponding Fourier amplitude spectrum (dashed line) at $T = 5 \text{ K}$, well below the critical temperature $T_c = 48 \text{ K}$. The high frequency oscillations at 17 and 19.5 THz (yellow peaks) are coherent symmetry breaking apical oxygen vibrations, resonantly driven by the excitation pulse. (c) and (d), Coherent SH response at higher excitations fields ($E = 0.5 \text{ MV/cm}$) at the same temperature. The peaks at $\nu_1 = 2.5 \text{ THz}$ and $\nu_2 = 14 \text{ THz}$ (red and magenta) are ascribed to coherent oscillations of Josephson plasma modes. (e) and (f), The coherent SH response at significantly stronger excitations ($E = 7 \text{ MV/cm}$) show the same coherences of panel (c) and (d), with additional modes drawn as grey peaks. These additional peaks are dominated by those at 8.6 and 10.5 THz and label additional phonons nonlinearly coupled to the resonantly driven lattice modes.

The higher field data reported in Fig. 4.6 (c), (d) (500 kV/cm) and (e), (f) (7 MV/cm) reflect a nonlinear response regime, where other nonlinearly coupled modes respond to the resonant excitation of the directly driven vibrations. One specific mode, shaded in red in panel (c), stands out already at the low fields of 500 kV/cm, oscillating at 2.5 THz frequency, for which no c -axis symmetry-odd vibration is expected as can be seen from the equilibrium optical properties of $\text{YBa}_2\text{Cu}_3\text{O}_{6.5}$ in Fig. 4.3 and Ref. [203, 204, 212] as well as DFT (see Appendix C.6). However, the THz-reflectometry measurements [30, 32] reported the emergence of a Josephson plasmon resonance close to these frequencies in similarly doped compounds. Therefore, we assign

these low-frequency coherent oscillations to coherent oscillations of the Josephson plasmon, an assignment that will be justified below. The real space current distributions of the equilibrium, zero momentum, Josephson plasma modes are sketched in Fig. 4.8 (a) and labelled with their respective eigenfrequencies. The amplitude of this mode increased nearly 100-fold as the pump field was increased from 500 kV/cm to 7 MV/cm (Fig. 4.6 (e), (f)), evidencing a regime of amplification that will be analyzed in the remainder of this chapter.

Other modes of the solid were also observed at the highest excitation fields including four phonon modes at 4, 6, 8.6 and 10.5 THz [203, 204] which are plotted as grey peaks in Fig. 4.6 (f) and their real space motion is shown in Fig. 4.8 (b). These correspond to well known infrared-active phonons at or near zero momentum [203, 204, 212], which are excited by a higher order, phononic four-wave mixing process. This will be discussed at the end of this chapter. Further, a broad feature centered around 14 THz, reminiscent of an intra-bilayer Josephson plasma mode, which appears as a peak in the equilibrium loss function around 14 THz to 15 THz (see Fig. 3.10 and 4.3 (c) and (d)) [206, 208].

The sum of all these coherent motions could be fitted with a set of oscillators whose frequencies were constrained to the phonon frequencies observed in equilibrium infrared spectroscopy, plus two oscillators for the low- and high-frequency Josephson plasma modes (see Appendix C.1). The Fourier transforms of the resulting coherent signals are shown as shaded peaks in Fig. 4.6 (b),(d) and (f). The total sum of all these oscillators is exemplary shown in Fig. 4.6 (a), (c) and (e) as dashed lines and shows perfect agreement with the experimental data.

4.3.3 Doping-dependence

We augmented these experiment on $\text{YBa}_2\text{Cu}_3\text{O}_{6.48}$ with measurements on two more dopings $\text{YBa}_2\text{Cu}_3\text{O}_{6.65}$ and $\text{YBa}_2\text{Cu}_3\text{O}_{6.92}$. A comparison of the coherent oscillations of the SHG signal for the three compounds is shown in Fig. 4.7. Here, the panels (a), (c) and (e) show the coherent component of the time-domain SH signal for $\text{YBa}_2\text{Cu}_3\text{O}_{6.48}$, $\text{YBa}_2\text{Cu}_3\text{O}_{6.65}$ and $\text{YBa}_2\text{Cu}_3\text{O}_{6.92}$, respectively. The corresponding Fourier transform amplitude spectra are shown in panels (b), (d) and (f). The temperature of 5 K, at which the data were taken, was well in the low temperature superconducting state ($T_{c, 6.48} = 48 \text{ K}$, $T_{c, 6.65} = 67 \text{ K}$, $T_{c, 6.92} = 92 \text{ K}$).

The coherent oscillations for the two lower dopings $\text{YBa}_2\text{Cu}_3\text{O}_{6.48}$ and $\text{YBa}_2\text{Cu}_3\text{O}_{6.65}$ show a dominant response at 2.5 THz and 2.8 THz, respectively (see Fig. 4.7 (b) and (d)). A simi-

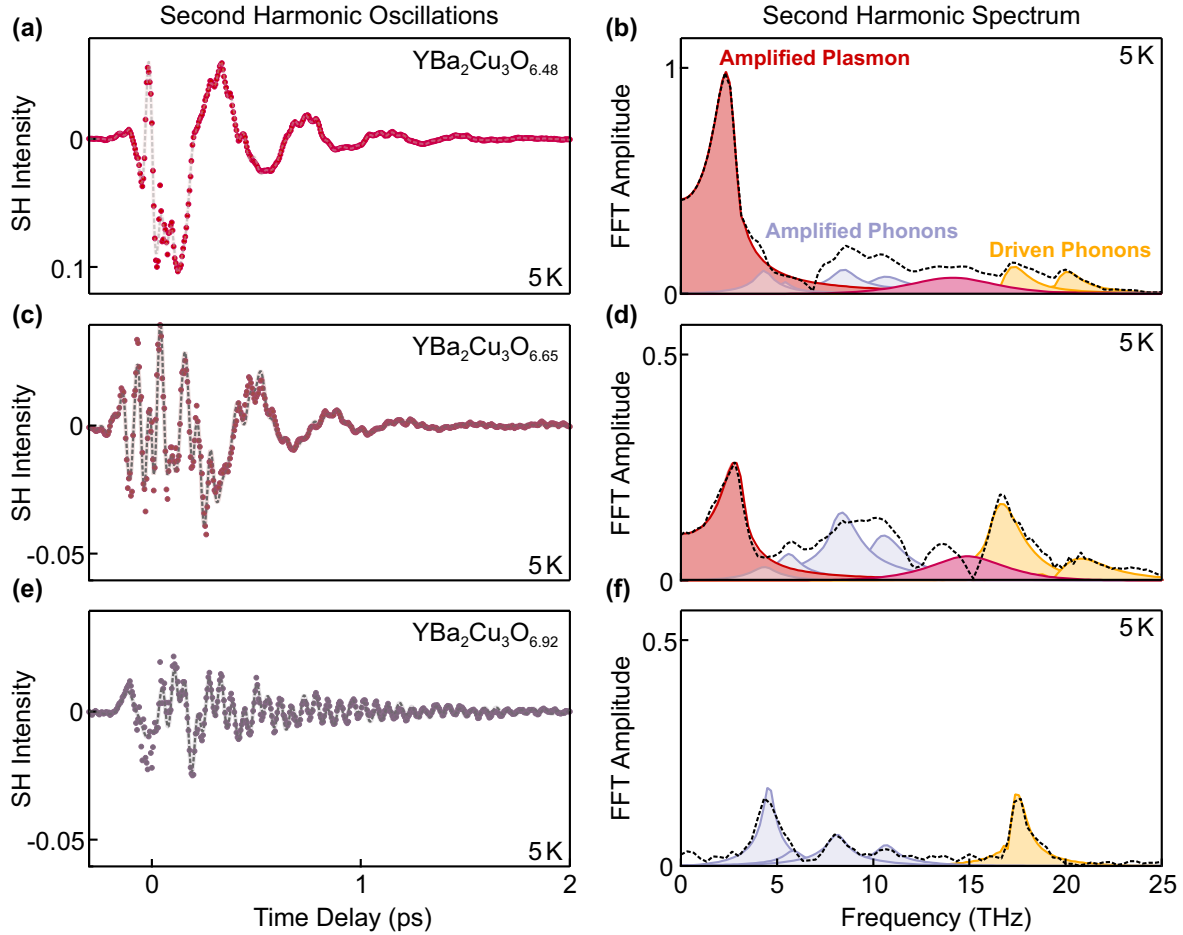


Figure 4.7: Doping dependence of the coherent oscillations of the time-resolved second harmonic intensity. (a),(c),(e) Coherent SH oscillations for three dopings. The time-resolved SH signal showed coherent oscillations for all three dopings $\text{YBa}_2\text{Cu}_3\text{O}_{6.48}$ (a), $\text{YBa}_2\text{Cu}_3\text{O}_{6.65}$ (c) and $\text{YBa}_2\text{Cu}_3\text{O}_{6.92}$ (e), at 5 K. The coherent oscillations of the $\text{YBa}_2\text{Cu}_3\text{O}_{6.48}$ and $\text{YBa}_2\text{Cu}_3\text{O}_{6.65}$ samples measured at 5 K show a dominant response at 2.5 THz and 2.8 THz, for $\text{YBa}_2\text{Cu}_3\text{O}_{6.48}$ ((b), red peak) and $\text{YBa}_2\text{Cu}_3\text{O}_{6.65}$ ((d), red peak), respectively. These oscillations are absent in $\text{YBa}_2\text{Cu}_3\text{O}_{6.92}$ (f). In addition to the low frequency oscillations a number of additional peaks (shaded in grey in panels (b),(d),(f)) appear at 4, 6, 8 and 10 THz, which correspond to known infrared-active phonons. The driven apical oxygen vibrations are shown as yellow peaks in the FFTs of the coherent signals. The dashed curves in panels (a),(c),(e) were obtained by a time-domain fit of the coherent signals. The individual oscillators contributing to this fit are shown as colored peaks in the FFTs in panels (b),(d),(f).

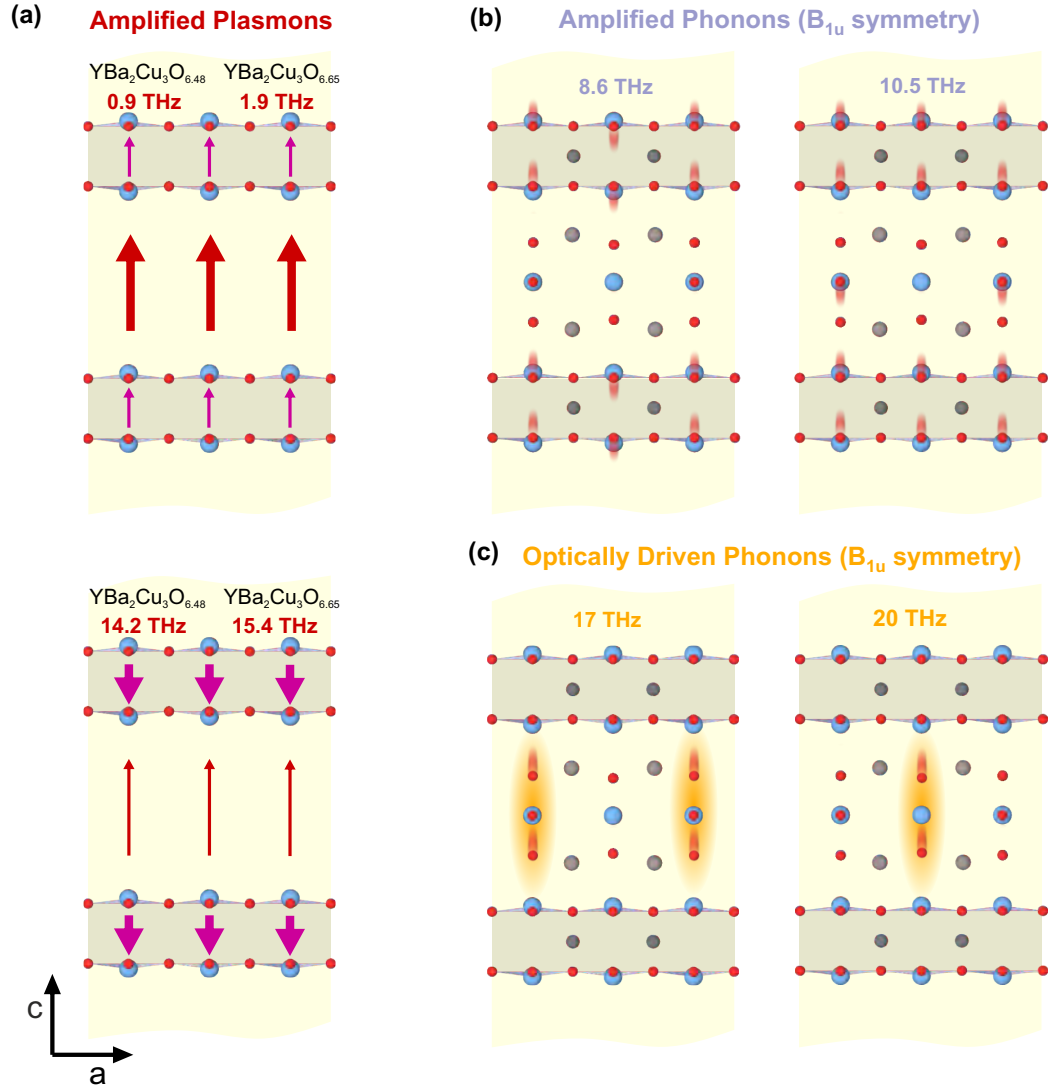


Figure 4.8: Real space currents and atomic vibrations of the coherent odd-symmetry modes. (a) Real-space current pattern of the Josephson plasma modes in $\text{YBa}_2\text{Cu}_3\text{O}_{6.5}$. The equilibrium real-space current pattern of the low frequency Josephson plasmon is located in the inter-bilayer region (red arrows) with a small in-phase current in the intra-bilayer region. The plasmons resonates at 0.9 and 1.9 THz in $\text{YBa}_2\text{Cu}_3\text{O}_{6.48}$ and $\text{YBa}_2\text{Cu}_3\text{O}_{6.65}$, respectively. The equilibrium current pattern of the high frequency Josephson plasmon on the other hand involves strong currents between the bilayers (violet) which are out-of-phase with a small inter-bilayer current (red). These currents resonate at 14.2 and 15.4 THz in $\text{YBa}_2\text{Cu}_3\text{O}_{6.48}$ and $\text{YBa}_2\text{Cu}_3\text{O}_{6.65}$, respectively. (b) Real-space motions of the amplified phonons. The amplified phonons at 8.6 and 10.5 THz resonance frequency mainly involve motions of the oxygen atom in the CuO_2 layers (shaded red). (c) Real-space motions of the optically driven phonons. The two apical oxygen vibrations oscillate at 17 and 20 THz and involve motions of the apical oxygen along the c -axis on the filled and unfilled chain site, respectively.

lar response is absent in the $\text{YBa}_2\text{Cu}_3\text{O}_{6.92}$ sample. All three dopings show the same set of nonlinearly coupled phonon modes, which are again plotted as grey peaks, which unlike the putative Josephson plasma mode show only minor shifts and appear at frequencies of known infrared-active lattice modes [203, 204]. Also, the amplitudes of the apical oxygen vibrations follow the expected doping dependence, where spectral weight is shifted from the high frequency ($\Omega_{\text{YBCO6}} = 20.5$ THz) to low frequency mode ($\Omega_{\text{YBCO7}} = 17.2$ THz) with progressive doping [203, 204].

4.3.4 Time-resolved SH-polarimetry

The point group symmetry of the observed polar excitations was assessed by SH polarimetry measurements in $\text{YBa}_2\text{Cu}_3\text{O}_{6.48}$. To this end, the polarization angle φ of the incoming 800 nm pulses was controlled with a $\lambda/2$ -waveplate and the polarization of the emitted 400-nm SH light was selected with a prism analyzer in front of the PMT, choosing either $E_{400} \parallel c$ or $E_{400} \parallel a, b$ (see Fig. 4.9 (a)). For each angle φ the time-resolved SH intensity changes were recorded and dissected as detailed in Appendix C.1. This procedure enables us to determine amplitude and phase for all the coherently oscillating signal components for each 800-nm polarization angle φ and therefore to assess the point group of their underlying excitation. The results for vertical polarization of the emitted SH light ($E_{400} \parallel c$) are shown in Fig. 4.9, Appendix C.3 presents data for the orthogonal direction ($E_{400} \parallel a, b$). The polarimetry signals of the driven and amplified phonons, that are oscillations at 17 and 20 THz and 4, 6, 8 and 10 THz frequencies, at a time-delay $\Delta t = 150$ fs are shown in Figures 4.9 (b) and (d). Both excitations show a similar shape of the polarimetry signal that exhibits two main lobes, when the probe polarization is aligned along the crystal c-axis, and two significantly smaller lobes when the polarization is aligned with the CuO_2 layers. To support the assignment of the infrared-active phonons (at 4, 6, 8, 10, 17 and 20 THz) we consider the point group symmetry which results from a B_{1u} symmetry operation on the equilibrium $Pmmm$ space-group of $\text{YBa}_2\text{Cu}_3\text{O}_{6+\delta}$. The eigenvectors of the polar lattice distortions can be determined from ab-initio calculations [143] and therefore their symmetry-breaking is known. The displacement of the crystal ions along the coordinates of the infrared-active B_{1u} modes, which breaks the mirror-symmetry normal to the c-axis, lowers the symmetry of the unit cell to $Pmm2$. The SHG tensor of the corresponding $mm2$ point group is

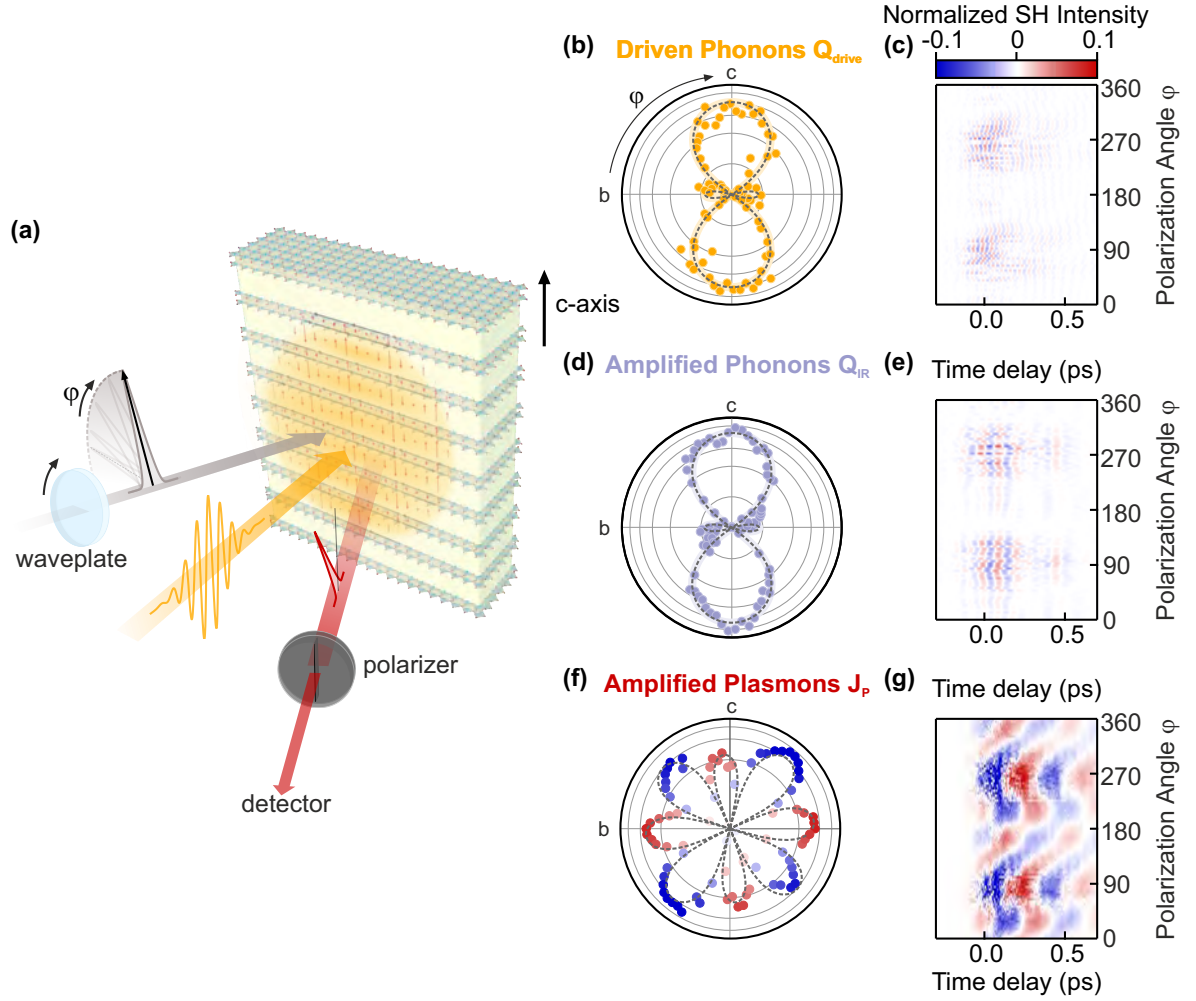


Figure 4.9: Time-resolved SH polarimetry. (a) Schematic of the SH polarimetry geometry. The polarization angle φ of 800-nm NIR probe pulses (grey) is controlled by rotating a $\lambda/2$ -waveplate. The reflected second harmonic light (red arrow) passes through an analyzer to measure the different polarization components individually. (b) The amplitude of the coherent oscillations of the driven apical modes as function polarization angle φ , rotated from the b-axis (0° , 180° , 360°) towards the c-axis (90° , 270°), shows two lobes in a polar plot, which are aligned along the c-axis (yellow). The amplitude is plotted on a logarithmic scale. The dashed line is a fit with a point-group symmetry of $mm2$. (c) The time-resolved polarimetry measurement reveals amplitude and phase of the coherent oscillations for all angles φ . (d) The amplitude of the amplified phonons (grey) shows the same polarimetry signal of $mm2$ symmetry as the driven phonons. (e) For the amplified phonons, the amplitude and phase resolved measurement reveals the same phase of the oscillations for all angles φ . (f) The polarimetry measurement of the coherent Josephson plasmon oscillations shows a more complex pattern compared to the phonons. Instead of two lobes, it shows a total of 8 lobes. The color-coding indicates the phase of the oscillation amplitude (red: 0, blue: π) for a certain polarization angle φ , extracted from time-resolved polarimetry measurement in panel (g).

$$\Delta\chi^{(2)} = \begin{pmatrix} 0 & 0 & 0 & 0 & d_{15} & 0 \\ 0 & 0 & 0 & d_{24} & 0 & 0 \\ d_{31} & d_{32} & d_{33} & 0 & 0 & 0 \end{pmatrix} \quad (4.2)$$

and has five non-zero elements. A fit to the polarimetry data, using this tensor, shows excellent agreement as evidenced by the dashed lines in Fig. 4.9 (b) and (d). Together with the frequency of these oscillations, these excitations can unambiguously be assigned to the c-axis polarized infrared-active phonons modes of $\text{YBa}_2\text{Cu}_3\text{O}_{6.48}$. The same analysis was repeated for all time delays between - 0.3 and + 0.7 ps, the resulting 2-D maps are shown in Fig. 4.9 (c) and (e) and report the time evolution of the polarimetry signal. It is noteworthy, that the coherent oscillations of the driven and amplified phonons have the same phase for every polarization angle φ .

The polarimetry signal of the putative Josephson plasma oscillations at 2.5 THz, shown in Fig. 4.9 (f) again for only one time-delay of $\Delta t = 150$ fs, suggests a fundamentally different symmetry. It differs in shape, which shows additional lobes at multiples of 45° , but also the phase of the oscillations changes as function of the probe polarization angle (see Fig. 4.9 (f)). This leads to a complex temporal evolution of the polarimetry signal as shown in Fig. 4.9 (g) and sets the polarimetry signal of the Josephson plasmon apart from the phonons¹. The color-coding in Fig. 4.9 (f), represents the phase of the coherent oscillation at a specific polarization angle φ , with red a phase of 0 and blue a phase of π .

Figure 4.8 (a) displays the current pattern of the zone center Josephson plasma modes, which will be evaluated here as a possible explanation of the symmetry pattern of the 2.5 THz excitation. The currents along the c-axis between the planes break both time-reversal and inversion symmetry, however their combined action, time-reversal and inversion, remains a symmetry operation. In total, the point group reduces to mmm' due to the remaining mirror symmetries on the a-c and b-c planes. The symmetry operation that connects the two point-groups mmm and mmm' is part of the irreducible representation $B_{1u'}$ [142]. Accordingly, the symmetry of the Josephson oscillation at the zone center is part of the same irreducible representation $B_{1u'}$ and the resulting polarimetry signal should be identical with that of the phonons. This, however, is not observed in the experiment!

Hence, the effective $\chi^{(2)}$ tensor needs to have a symmetry lower than $Pmm2$ or $Pmmm'$. This

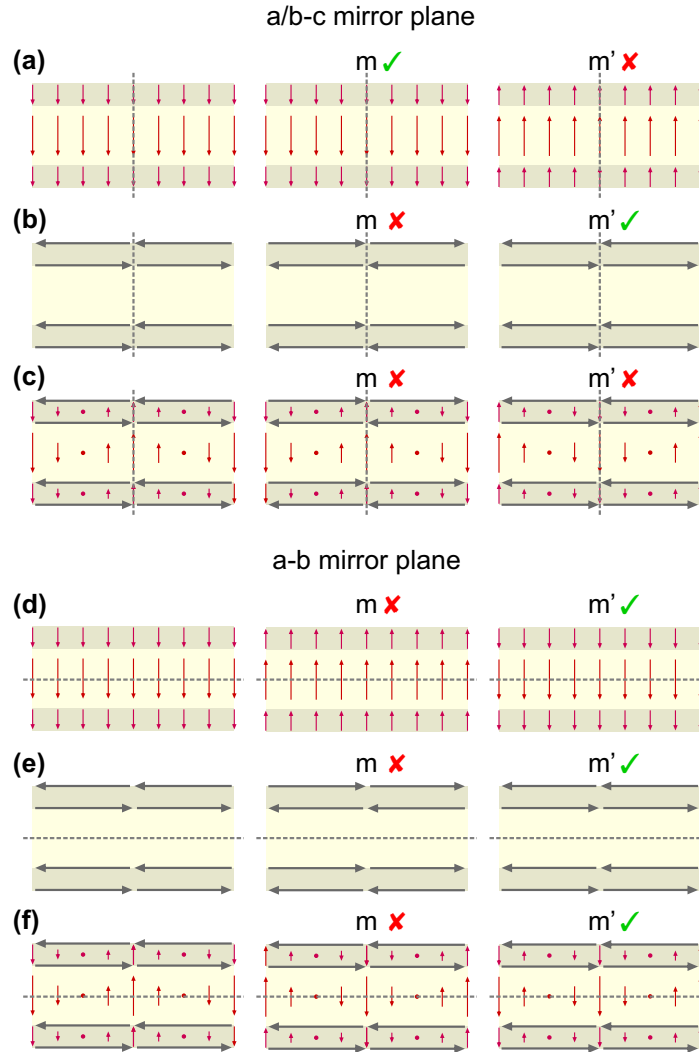


Figure 4.10: Symmetry-considerations of Josephson current patterns. (a) Mirror and time-reversal symmetry of a zero momentum Josephson mode. A zero-momentum Josephson current pattern (red arrows) along the c-axis will preserve the mirror with a/b-c mirror planes (m) but will break the mirror symmetry combined with a time-reversal (m'). (b) Mirror and time-reversal symmetry of in-plane supercurrents. An in-plane current (grey arrows) breaks the a/b-c mirror symmetry but preserves a/b-c mirror symmetry combined with a time-reversal (m'). (c) Mirror and time-reversal symmetry of combined finite-momentum Josephson currents and in-plane supercurrents. A combination of the two current patterns leads to finite momentum Josephson currents. The resulting currents break mirror and time-reversal symmetry and consequently lower the point group of $\text{YBa}_2\text{Cu}_3\text{O}_{6+\delta}$ from $Pmmm$ to Pm or even lower. (d),(e),(f) Similar consideration can be made for the a-b mirror plane. However, here the combined current pattern preserves the a-b mirror symmetry combined with a time-reversal.

requires additional symmetry breaking along the in-plane direction, i.e, along the a-b crystallographic axes, which is only possible when additional currents are also flowing along the CuO_2 planes in the a-b-plane. This implies a finite phase gradient ($I \propto \nabla\theta$) inside the CuO_2 layers because the super-current flow is proportional to the phase gradient $\nabla\theta$ (see Chapter 3.3). Therefore, two inequivalent or even antiparallel currents on adjacent CuO_2 would result in a spatially modulated phase difference $\Delta\theta$ across the inter-bilayer junction,

$$\nabla_{x,y}\Delta\theta(y) = \nabla_{x,y}\theta_1 - \nabla_{x,y}\theta_2. \quad (4.3)$$

Consequently, this leads to a spatial modulation of the c-axis tunnelling current, $I \propto \sin(\Delta\theta)$, which is equivalent to propagating Josephson plasma modes. The in-plane supercurrent together with the out-of-plane Josephson currents break time-reversal and mirror symmetry of the a-c and b-c plane and therefore lower the point group to Pm' . The symmetry operations are summarized in Figure 4.10. These considerations are supported by recent equilibrium SH polarimetry measurement, which reported similar point groups ($2'/m$ and $m1'$) in the superconducting and pseudogap phase of YBCO [233]. The SHG tensor of the m' point group has ten non-zero elements

$$\Delta\chi^{(2)} = \begin{pmatrix} d_{11} & d_{12} & d_{13} & 0 & d_{15} & 0 \\ 0 & 0 & 0 & d_{24} & 0 & d_{26} \\ d_{31} & d_{32} & d_{33} & 0 & d_{35} & 0 \end{pmatrix} \quad (4.4)$$

and allows us to describe the polarimetry signal of the Josephson plasma oscillation. This is shown by the dashed line in Fig. 4.9 (f), which is a fit to the data taking into account these tensor elements. This result further implies that the low frequency coherent oscillations are excitations of the Josephson plasma at finite momentum $q_{x,y}$, propagating along the in-plane direction.

4.3.5 Momentum-resolved SH measurement

The momentum of these excitations is analyzed in the following. To this end, the geometry of the experiment was changed, aligning the pump and probe beams collinear and detecting the spatial profile of the emitted SH light. This geometry is sketched in Fig. 4.11 (a). The

spatial filtering is achieved by moving a 200 μm slit perpendicularly across the reflected beam in a distance 10 cm away from the sample. A finite deflection δ of the SH light away from the specular reflection at $\delta = 0$ would then reveal an in-plane momentum transfer in the scattering process as was already discussed in Chapter 2.3.2. The resulting spatial profile of the SH light needs to be deconvolved from the divergence of the probe beam in order to obtain the intrinsic momentum transfer of the Josephson plasmon (see Appendix C.2). The deflection angle can be directly converted to the absolute momentum transfer, by

$$q = \sqrt{\varepsilon_\infty} \tan(\delta) k_{400}, \quad (4.5)$$

where k_{400} is the wavenumber of the SH light. The result of this experiment is shown in Fig. 4.11 (b) and shows two distinct peaks at $q_y = \pm 190 \text{ cm}^{-1}$, which is in perfect agreement with the dispersion relation of the inter-bilayer Josephson plasmon in $\text{YBa}_2\text{Cu}_3\text{O}_{6.48}$ (see Fig. 3.11 (a)). The dispersion-relation of $\text{YBa}_2\text{Cu}_3\text{O}_{6.48}$, which was calculated using eq. 3.30 and predicts an eigenfrequency of the Josephson plasma of 2.5 THz for an in-plane momentum of $\sim 200 \text{ cm}^{-1}$. The shaded grey areas denote the maximum accessible momentum of the experiment, which is limited by the spot size of the probe beam on the sample ($d = 25 \mu\text{m}$).

The excitation strength dependence of the low 2.5-THz oscillations can be evaluated by controlling the peak electric field of the mid-infrared pulses using a pair of wire grid polarizers and determining their amplitude. The dissection of the oscillatory signal (discussed above and in Appendix C.1), yields this amplitude J_{JP} as well as those of the other oscillatory contributions as a function of the amplitude of the apical oxygen vibrations Q_{drive} from a single time trace. As shown in Fig. 4.11 (c), J_{P} scales exponentially with Q_{drive} reminiscent of parametric amplification. This dependence can be fitted with an exponential function with a finite excitation threshold b , drawn as a dashed line.

4.4 Coherent Phonon Dynamics in $\text{YBa}_2\text{Cu}_3\text{O}_{6+\delta}$

To further underline the uniqueness of the 2.5-THz Josephson plasma mode we also analyzed the response of the directly driven Q_{drive} and the nonlinearly coupled, Q_{R} and $Q_{\text{amplified}}$, phonons. This is possible, because the infrared active modes (Q_{drive} and $Q_{\text{amplified}}$), appear in the same time-resolved SH traces as the Josephson plasma mode. The simultaneous detection of the linear

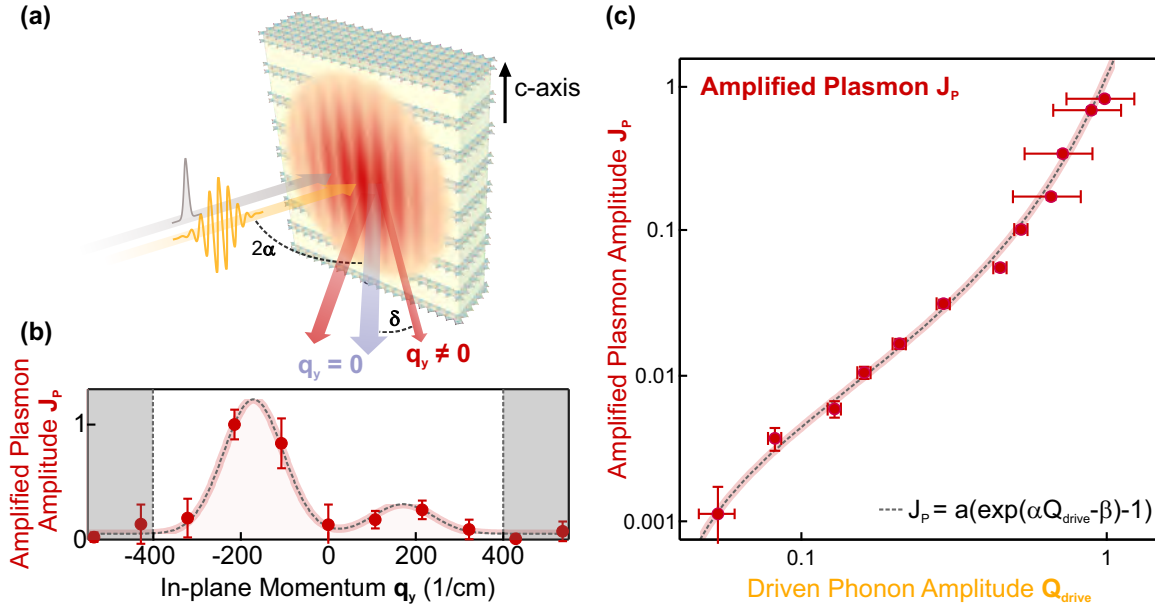


Figure 4.11: Momentum resolved measurement of the Josephson plasmon amplitude and excitation strength dependence. (a) Schematic of the SH collinear pump-probe geometry. To measure the spatial dependence of the emitted SH light and with it the transferred in-plane momentum, pump and probe must hit the sample in a collinear geometry. The interaction with finite-momentum excitations inside the material will lead to deflection δ of the SH light (red) away from the specular NIR-reflection (grey). (b) Experimental momentum dependence of the coherent Josephson plasma amplitude. The momentum distribution of the coherent Josephson plasmon oscillations shows two peaks at $q_y = \pm 190 \text{ cm}^{-1}$. The maximum experimental momentum resolution is denoted as grey shaded area. (c) Experimental excitation field dependence of the coherent Josephson plasmon amplitude. The amplitude of the Josephson plasma oscillation J_P shows exponential scaling with the amplitude of the apical oxygen vibration Q_{IR} (yellow). This excitation strength dependence can be described with an exponential function with an excitation threshold b (dash line).

polarization rotation of the 800-nm beam further allowed to detect the even-order Raman modes Q_{R} .

4.4.1 Characteristics of the Resonantly Driven Phonons

The momentum and excitation field dependence were also analyzed for the directly driven phonon modes at 17 and 20 THz and the results are shown in Figure 4.12. They are supposed to take their momentum from the mid-infrared electric field, hence their in-plane components are determined by the divergence of the focused excitation beam. The measured momentum distribution, shown in Fig. 4.12 (b), is centered around zero with a FWHM of 300 cm^{-1} , con-

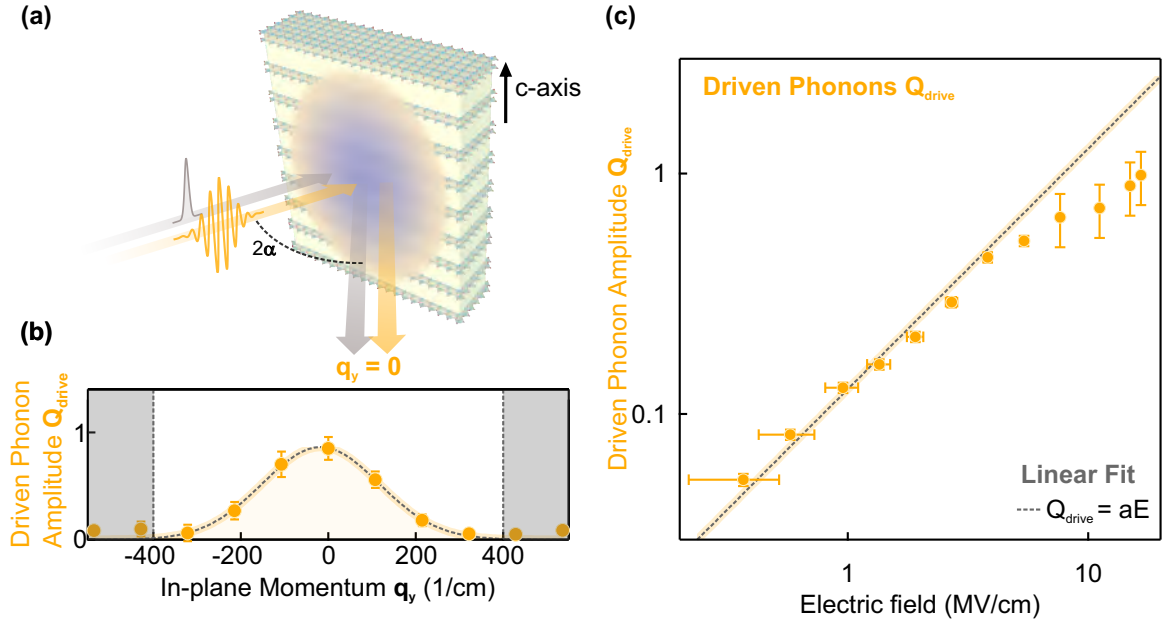


Figure 4.12: Momentum resolved measurement of the driven phonon amplitude and excitation strength dependence. (a) Schematic of the SH collinear pump-probe geometry. (b) Experimental momentum dependence of the optically driven phonon amplitude. The resulting momentum distribution of the driven phonons shows a distribution around $q_y = 0$. The maximum experimental momentum resolution is denoted as grey shaded area. (c) Experimental excitation field dependence of the optically driven phonon mode. The amplitude of the amplified phonons initially shows linear scaling with the amplitude of the electric field up to $E = 4 \text{ MV/cm}$ (yellow). Above $E = 5 \text{ MV/cm}$ the driven phonon amplitude saturates. This excitation strength dependence can be described with a linear function with $Q_{\text{drive}} = aE$ (dashed line). The data points were obtained through a numerical fit as explained in Appendix C.1

sistent with the value estimated from the divergence of the MIR beam, 280 cm^{-1} ($\theta = 14^\circ$). Importantly, this momentum distribution of the driven apical phonon mode is fundamentally different to one of the Josephson plasma modes (see Fig. 4.11).

Fig. 4.12 (c) shows the amplitude of the driven apical oxygen modes, extracted from amplitude spectra similar to Fig. 4.6, to increase linearly at small electric-field strength ($E < 4 \text{ MV/cm}$), confirmed by the dashed line which is a linear fit. At larger electric field strengths the amplitude Q_{drive} saturates. Here, the self-anharmonicities (further discussed in Chapter 2.2) of the driven-mode weaken energy transfer from the pump-pulses into the vibrational mode and coupling to the Josephson plasmon and other lattice modes (see next paragraph) draw energy from the apical vibrations.

4.4.2 Cubic-order Phonon Coupling

A second type of three-wave mixing like the phonon-Josephson-plasmon coupling discussed above is phonon coupling of the type $Q_{\text{R}}Q_{\text{drive}}^2$, between the driven mode and fully symmetric A_g Raman mode. These modes are detected in the linear reflection of polarization rotation of the NIR-probe. Fig. 4.13 (a) and (c), report the coherent oscillations, extracted from the time-dependent PR signal by subtraction of the slowly varying background, for three doping levels of $\text{YBa}_2\text{Cu}_3\text{O}_{6.48}$, $\text{YBa}_2\text{Cu}_3\text{O}_{6.65}$ and $\text{YBa}_2\text{Cu}_3\text{O}_{6.92}$. Again, all data were taken at 5 K. The corresponding Fourier transforms plotted in Fig. 4.13 (b), (d) and (f) show peaks at frequencies which can be associated with zone-center totally symmetric modes of A_g symmetry [53, 249]. The dominant response appears at 3.7 and 5 THz. Ab-initio theoretical methods reveal the real-space motions of these modes, which are depicted in Fig 4.14 (a). They involve mostly non-polar oscillations of the Cu atoms residing in the CuO_2 planes. The amplitudes of these oscillations Q_{R} as a function of the amplitude of the driven apical oxygen vibration Q_{drive} is shown in Fig. 4.14 (b) and scales quadratically with Q_{drive} . The data points were extracted by a time domain fit to the coherent oscillations which is drawn as dashed lines in Fig 4.13(a), (c) and (e). These Raman modes were already observed in a previous experiment published in Ref. [53]. They are coherently driven by nonlinear phononic coupling of the type $gQ_{\text{rive}}^2Q_{\text{R}}$. This is supported by the parabolic dependence of Q_{R} on Q_{drive} of the excitation strength dependence in Fig. 4.14 (b).

4.4.3 Quartic-order Phonon Coupling

The excitation of the lower-energy infrared-active lattice vibrations can be explained by a quartic coupling to the directly driven apical oxygen phonons, also leading to parametric amplification. In centrosymmetric materials, like $\text{YBa}_2\text{Cu}_3\text{O}_{6.48}$, coupling between infrared-active modes is only possible through these quartic nonlinearities. The two dominant amplified phonons oscillate at frequencies of 8.6 and 10.5 THz (see Fig. 4.7 (b), (d) and (e)) and involve polar vibrations of the oxygen atoms in the CuO_2 layers (see Fig. 4.8 (b)). To understand this dominant response at approximately half the frequency of the driven apical oxygen vibration ($\Omega_{\text{YBCO7}} = 17.2$ THz and $\Omega_{\text{YBCO}} = 20.5$ THz), one has to consider the fourth order coupling terms in the potential energy,

$$\Delta V(Q_{\text{drive}}, Q_{\text{P}}) = hQ_{\text{drive}}^2Q_{\text{P}}^2 + kQ_{\text{drive}}^3Q_{\text{P}} + lQ_{\text{drive}}Q_{\text{P}}^3. \quad (4.6)$$

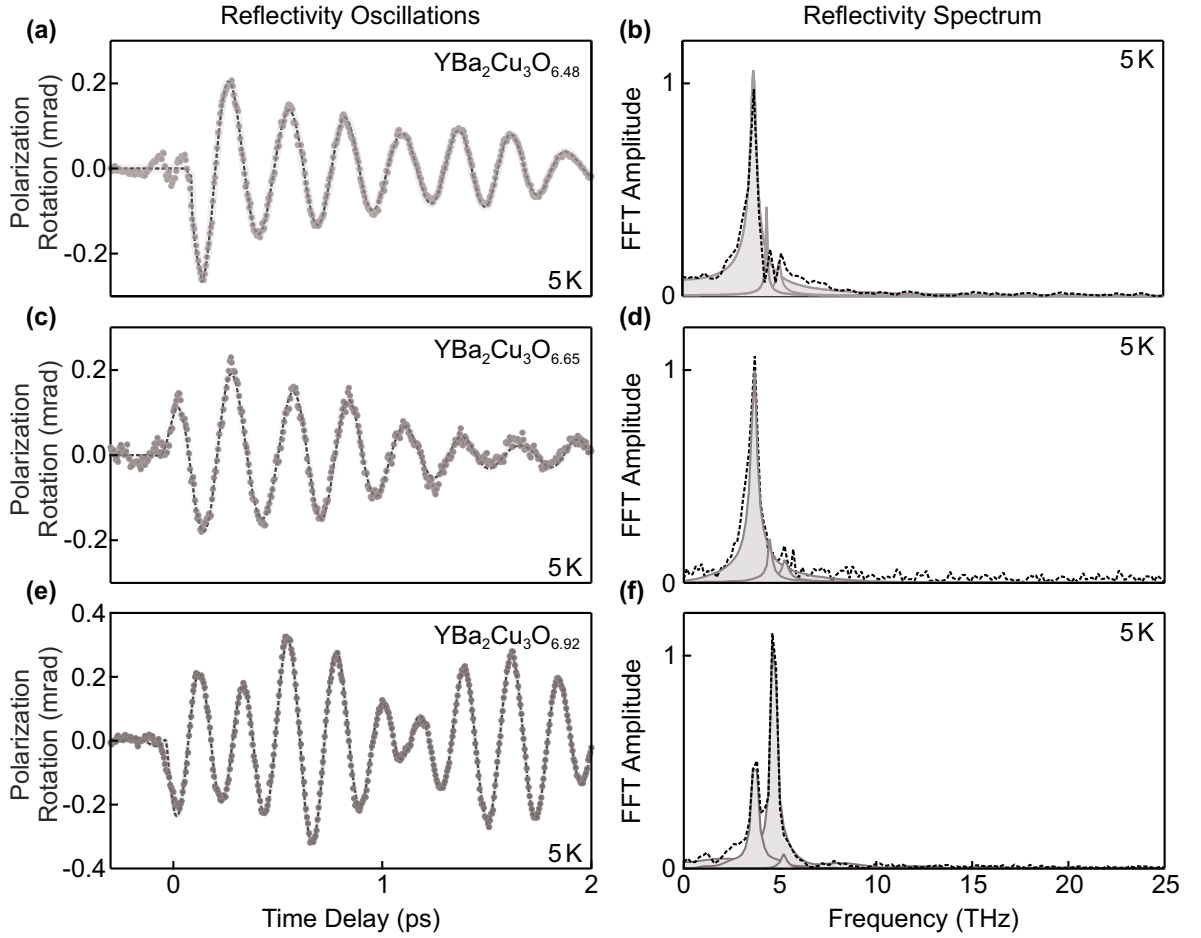


Figure 4.13: Coherent oscillations of the time-resolved polarization rotation. (a),(c),(e) The time-resolved polarization rotation signal showed coherent oscillations of Raman modes for all three dopings $\text{YBa}_2\text{Cu}_3\text{O}_{6.48}$ (a), $\text{YBa}_2\text{Cu}_3\text{O}_{6.65}$ (b) and $\text{YBa}_2\text{Cu}_3\text{O}_{6.92}$ (c), at 5 K. (b),(d),(f) FFT-amplitude spectra (dashed line) of the time-resolved polarization rotation signal show peaks at 3.7 and 4.6 THz which descend from Ionic-Raman scattering of the excited apical oxygen vibrations.

As discussed in Chapter 2, these terms lead to an impulsive force, through cubic-linear coupling ($kQ_{\text{drive}}^3 Q_{\text{P}}$), and subsequent parametric amplification, through bi-quadratic coupling ($hQ_{\text{drive}}^2 Q_{\text{P}}^2$), acting onto Q_{P} . This is described by the equations of motion,

$$\ddot{Q}_{\text{drive}} + 2\gamma_{\text{drive}}\dot{Q}_{\text{drive}} + (\Omega_{\text{drive}}^2 + \mathbf{h}Q_{\text{P}}^2 + 3\mathbf{k}Q_{\text{drive}}^2 Q_{\text{P}})Q_{\text{drive}} = Z_{\text{drive}}^* E(t) \quad (4.7)$$

$$\ddot{Q}_{\text{P}} + 2\gamma_{\text{P}}\dot{Q}_{\text{P}} + (\omega_{\text{P}}^2 + \mathbf{h}Q_{\text{drive}}^2)Q_{\text{P}} + \mathbf{h}Q_{\text{drive}}^3 = 0. \quad (4.8)$$

Solutions to the equations are shown in Fig. 4.15, for the driven apical oxygen modes in panels

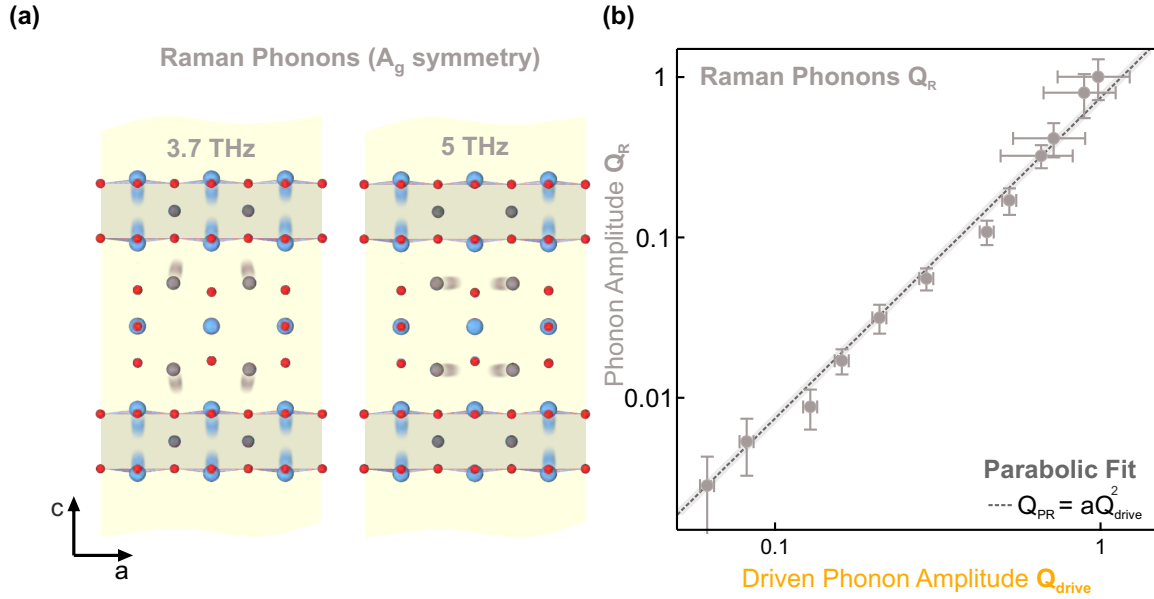


Figure 4.14: Real-space motions of the coherent Raman modes and excitation strength dependence. (a) The real-space motions of the coherent Raman modes observed with time-resolved polarization rotation (see Fig. 4.5), mostly involve oscillations of the plane Cu ions, which lead to a breathing (3.7 THz) and buckling (5 THz) of the CuO_2 planes along the crystals c -axis. (b) Excitation strength dependence of the coherent Raman modes. The amplitude Q_R of the coherent oscillations scales with the square of the amplitude of the driven apical oxygen vibration (Q_{drive} , yellow) as predicted by the theory of nonlinear phononics (see Chapter 2) and confirmed by a least squares fit (dashed line).

(a) and (b) and the amplified c -axis polar modes in panels (c) and (d). These simulations included the coupling between all 24 (13 B_{1u} and 11 A_g) relevant modes for probe and pump fields polarized along the crystals c -axis, and the coupling coefficients were determined by ab-initio methods described in Ref. [143] and Appendix C.6. These results were convolved with the experimental time resolution of 30 fs to allow close comparison to the experiment. The resulting time traces and amplitude spectra shown in Fig. 4.15 show qualitatively good agreement with the SH spectra shown in Fig. 4.7 and the dissected signal in Appendix C.1 and confirm excitation of the phonons predominantly around 8.6 and 10.5 THz.

Importantly, the bi-quadratic term responsible for the parametric amplification exhibits a resonant enhancement when $\Omega_{\text{drive}} = 2\Omega_P$, i.e., a *parametric resonance* [146, 250]. This is the case for the 8.6 and 10.5 THz phonons in $\text{YBa}_2\text{Cu}_3\text{O}_{6+\delta}$ and leads to an exponential increase of the amplitude Q_P with respect to Q_{drive} [146, 250]. The measured amplification is shown Fig. 4.17 (c), where the data points were obtained by integrating the spectral weight around of

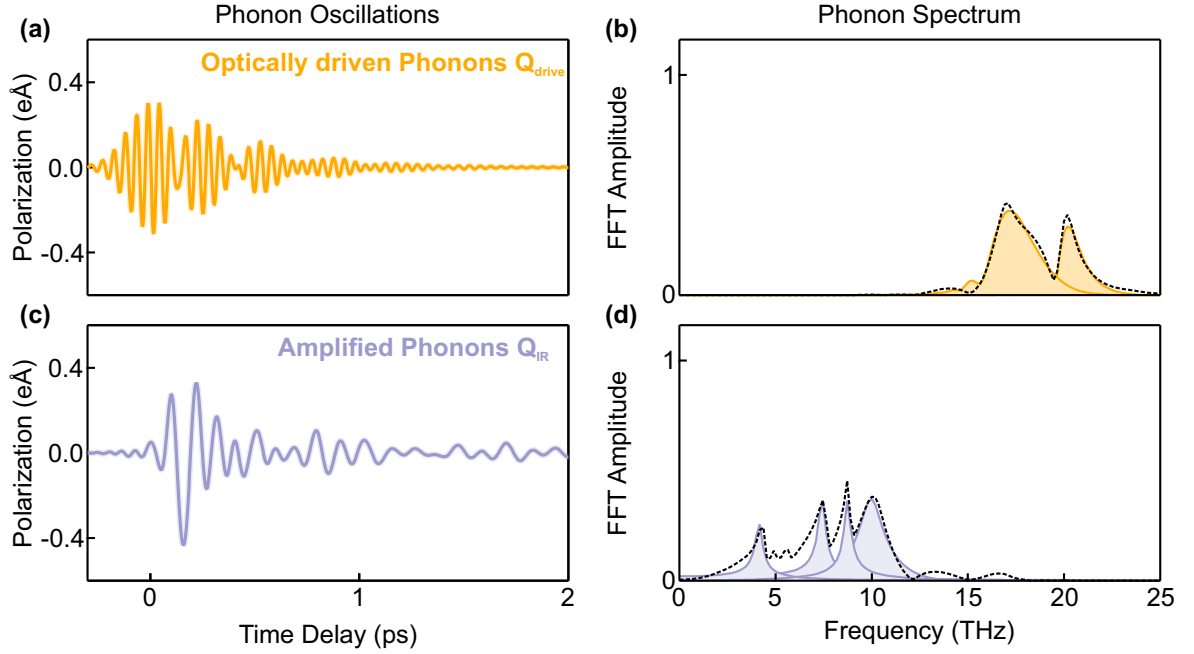


Figure 4.15: Theoretical model of fourth-order phonon-phonon coupling. (a) Simulated polarization of the optically driven phonon modes. Resonant driving of the apical oxygen vibrations Q_{drive} leads coherent oscillations of two modes which creates a beating-pattern (yellow). (b) The corresponding FFT spectrum shows two peaks at 17 and 20 THz (dashed line). The individual phonon responses are shown as yellow peaks. (c) Simulated polarization time-trace of the nonlinear coupling between the driven phonons and lower frequency phonons at 4, 6, 8 and 10 THz Q_{IR} (grey). (d) The FFT amplitude spectrum (dashed black) can be dissected into the response of the individual modes (grey peaks).

the amplitude spectra in the region 7 THz to 11 THz for every excitation strength and plotting against the driven phonon amplitude Q_{drive} . The resulting dependence can be fitted with an exponential function with a finite excitation threshold b , drawn as a dashed line. This exponential scaling of the experimental pump strength dependence (dots in Fig. 4.17 (c)) is confirmed by a similar exponential scaling of the simulated 8.6 and 10.5 THz phonons shown in Fig. 4.16 (c) as a dashed line, together with the experimental scaling (shaded dots). The parametric amplification leads to the creation of pairs of phonons with opposite wavevectors $\mathbf{q}_1 = -\mathbf{q}_2$ and therefore we expect a broad featureless momentum distribution. To confirm this, the momentum distribution of the phonons was measured in a collinear pump-probe geometry (see Fig. 4.17 (a)) and indeed shows a broad momentum distribution up to the highest momenta which can be resolved in the experiment (shaded in grey in Fig. 4.17 (b)). In the simulations, the momentum dependence was determined by choosing the resonance frequencies $\Omega_i(q_y)$ and the coupling coefficients $h(q_y) = \text{const.}$, $k(q_y) = \delta(q_y)$ to be momentum dependent. The response is

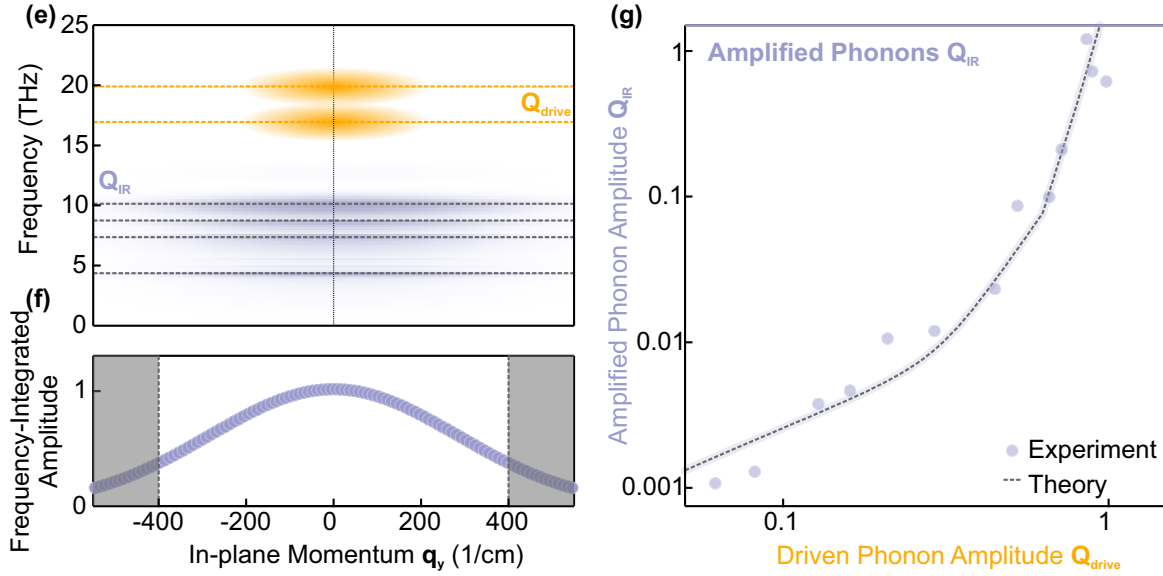


Figure 4.16: Theoretical model of fourth-order phonon-phonon coupling. (a) Dispersion of the infrared optical phonon along q_y . The in-plane momentum distribution of the driven modes (yellow) are centred around $q_y = 0$. The width is given by the divergence of the focused MIR-pump field (shaded yellow). The fourth-order nonlinear phonon coupling creates pairs of phonons at opposite momentum and therefore leads to broad momentum distribution around $q_y = 0$ (shaded in grey). (b) The frequency integrated response of panel (a) shows a broad peak around $q_y = 0$. (c) Simulated excitation strength dependence of the amplified phonon amplitude. The simulations reveal exponential scaling amplitude of the amplified phonon amplitude as a function of the driven phonon amplitude Q_{drive} (yellow). Here, the simulation results (dashed line) are overlaid with the experimental amplitude scaling (dots) from Fig. 4.17.

also convolved with the momentum resolution of the experiment and yields a broad momentum distribution of the amplified phonons similar to the experiment (see Fig. 4.16 (a) and (b)).

4.5 Temperature Dependence of Josephson Plasmons and Phonons

The equilibrium low frequency Josephson Plasma mode, which participates in the three-wave mixing process, disappears at T_c in the linear optical spectra of Figure 3.12 and 4.5. This could lead to the conclusion that the oscillations in second harmonic should disappear at the same temperature. However, when raising the temperature above T_c the coherent Josephson plasma oscillations show a smooth continuous transition and vanish only above $T = 400$ K. Fig. 4.18 (a) reports the full temperature dependence of the low frequency coherent Josephson plasma

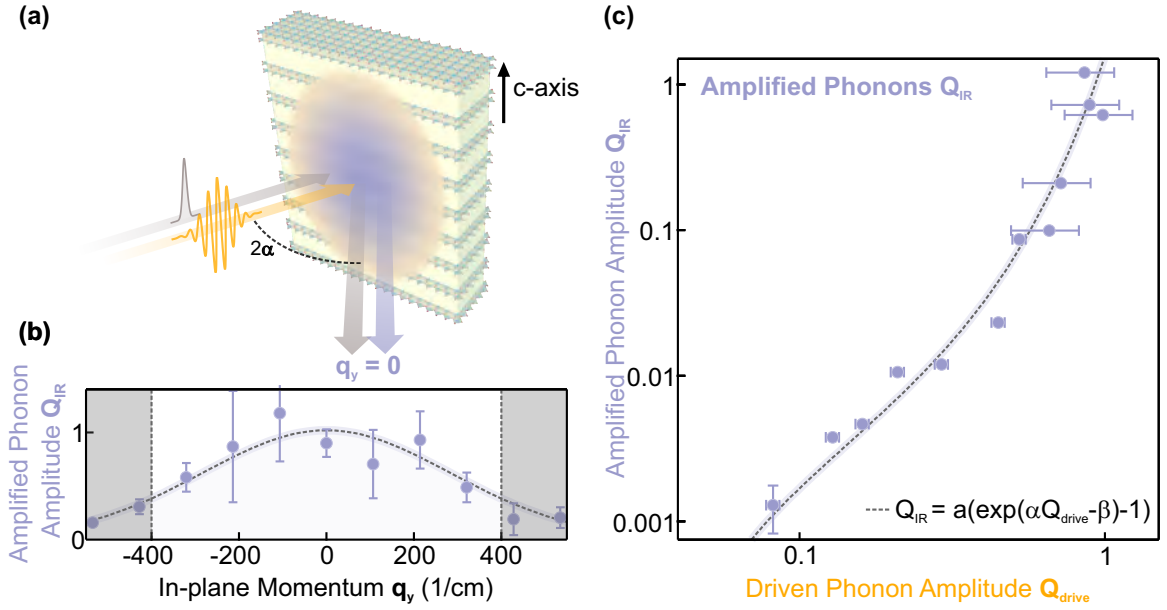


Figure 4.17: Momentum resolved measurement of the amplified phonon amplitude and excitation strength dependence. (a) Schematic of the SH collinear pump-probe geometry. (b) Experimental momentum dependence of the coherent amplified phonon amplitude. The resulting momentum distribution of the coherent amplified phonon amplitude shows a broad distribution around $q_y = 0$. The maximum experimental momentum resolution is denoted as grey shaded area. (c) Experimental excitation field dependence of the amplified phonon mode. The amplitude of the amplified phonons shows exponential scaling with the amplitude of the apical oxygen vibration (yellow). This excitation strength dependence can be described with an exponential function with excitation threshold β (dashed line).

mode amplitude in the range between 5 K and 475 K for $\text{YBa}_2\text{Cu}_3\text{O}_{6.48}$ and $\text{YBa}_2\text{Cu}_3\text{O}_{6.65}$. The amplitude of the coherent Josephson plasma oscillation smoothly decreases and vanishes at $T' = 280 \text{ K}$ and $T' = 390 \text{ K}$ for $\text{YBa}_2\text{Cu}_3\text{O}_{6.65}$ and $\text{YBa}_2\text{Cu}_3\text{O}_{6.48}$, respectively. Importantly, these temperatures coincide with the transition temperature of the pseudogap phase T^* in these two compounds, which is drawn as a dashed line in Fig. 4.18 (c) together with experimentally determined transition temperatures as red dots [215, 233, 245, 251, 252].

The amplified infrared phonons show a different temperature dependence, which exhibits only a small anomaly at T_c and a temperature independent amplitude in the normal state (see Fig. 4.18 (b)). This is similar to the equilibrium temperature dependence of the phonon's spectral weight (see Fig. 3.12). The anomalous temperature dependence of the coherent Josephson plasma modes was similarly observed in the transient THz reflectivity measurements. There the transformed volume fraction scaled in a similar way and vanished at T^* (see Fig. 4.1

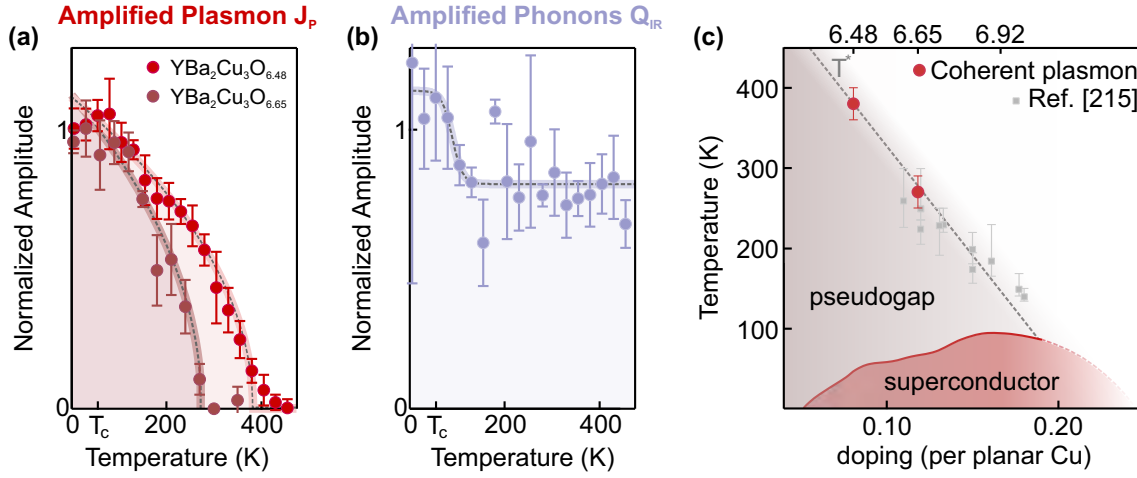


Figure 4.18: Temperature dependence of the coherent Josephson plasmon oscillations. (a) The temperature dependence of the Josephson plasma amplitudes of $\text{YBa}_2\text{Cu}_3\text{O}_{6.48}$ (red circles) and $\text{YBa}_2\text{Cu}_3\text{O}_{6.65}$ (dark red circles) smoothly decrease from low to high temperatures. The lines are fits to the data with a mean-field approach $\propto \sqrt{1 - T/T'}$, yielding $T' = 380$ K for $\text{YBa}_2\text{Cu}_3\text{O}_{6.48}$ and $T' = 280$ K for $\text{YBa}_2\text{Cu}_3\text{O}_{6.65}$. (b) Temperature dependence of the amplified phonon amplitude. The amplitude of the amplified phonons remains almost constant up to the highest temperatures and only shows a minor anomaly at T_c . (c) The phase-diagram of $\text{YBa}_2\text{Cu}_3\text{O}_{6+\delta}$ shows the regions of equilibrium superconductivity (red) and the pseudogap (grey). The temperatures T' , above which the coherent Josephson plasmon oscillations are shown as red circles. They agree well with the pseudogap temperature T^* extrapolated from Nernst effect measurements [215] (grey line).

(b)) [30]. The next section will present a theory that links both observations, the coherent Josephson plasma oscillations in the SH intensity and the Josephson plasma edge in transient THz reflectivity, to the same microscopic mechanism.

4.6 Theoretical Model of Phonon-Josephson Plasmon Coupling

The experimental findings presented above enabled us to develop a microscopic theory which not only explains the experimental evidence above but also the previous THz-reflectometry experiments [30, 32]. In this model, the excitation of the apical oxygen vibration is described as a spatially homogenous excitation at the center of the Brillouin zone ($q_x = 0$, $q_y = 0$). The phonon coordinate $Q_{\text{drive}}(t)$ follows the equation of motion of a linear damped harmonic oscillator driven by the laser field:

$$\ddot{Q}_{\text{drive}} + 2\gamma_{\text{drive}}\dot{Q}_{\text{drive}} + \Omega_{\text{drive}}^2 Q_{\text{drive}} = Z^* E(t). \quad (4.9)$$

To derive the equations of motion for the Josephson plasma modes when these are coupled to the driven lattice vibrations, one has to consider the kinetic energies of the in-plane superflow,

$$E_{J_{\text{plane}}} = \frac{1}{2\rho_s} \mathbf{J}_p^2 = \frac{1}{2}\rho_s \left(\nabla\theta_n(x, y, t) - \frac{2e}{c}A \right)^2. \quad (4.10)$$

Here, $\theta_n(x, y, t)$ is the order parameter within each layer n , ρ_s denotes the local superfluid density and A is the vector potential. This equation can be derived from the expression for the current density eq. 3.5. The apical oxygen lattice vibration excited by the pump are infrared-active and hence symmetry odd, and modify the local superfluid densities in a bilayer structure in a way that is antisymmetric with respect to the two layers, $\delta\rho_{s1,2} \propto \pm Q_{\text{drive}}$. This modulation of the superfluid density on the adjacent layers is sketched in Figure 4.19 (a) as a red shade on top of the CuO_2 layers. This modulation of the superfluid density is an exclusive feature to the apical oxygen vibrations [220, 227]. The effect of these vibrations on the in-plane superflow is to increase and decrease the kinetic energy $E_{J_{\text{plane}}}$ in neighbouring planes in an oscillatory fashion, and can be written as (see Appendix C.5):

$$\delta E_{J_{\text{plane}}} = \delta\rho_{s1}v_{s1}^2 + \delta\rho_{s2}v_{s2}^2 \propto Q_{\text{drive}}(t)(v_{s1} - v_{s2})(v_{s1} + v_{s2}) \propto Q_{\text{drive}}J_1J_2. \quad (4.11)$$

Importantly, the modulation of the in-plane kinetic energy leads to an in-plane current which propagates along the x-y direction and in opposite direction on two adjacent layers sketched as grey arrows in Fig. 4.19 (a). The resulting phase gradients on the CuO_2 layers effectively drives the Josephson tunneling currents because the gradient leads to spatial modulation of the

c-axis tunnelling ($I \propto \sin(\Delta\theta)$). Therefore two types of finite-momentum tunnelling modes are excited with $J_1 \sim v_{s1} - v_{s2}$ (inter-bilayer) and $J_2 \sim v_{s1} + v_{s2}$ (intra-bilayer) (see Appendix C.5 for more details). The equations of motion for the plasmons are then

$$\ddot{J}_1 + 2\gamma_{J_1}\dot{J}_1 + \Omega_{J_1}^2(q_{x1}, q_{y1})J_1 = -aq^2Q_{\text{drive}}(t)J_2 \quad (4.12)$$

$$\ddot{J}_2 + 2\gamma_{J_2}\dot{J}_2 + \Omega_{J_2}^2(q_{x2}, q_{y2})J_2 = -aq^2Q_{\text{drive}}(t)J_1 \quad (4.13)$$

where $\Omega_{J_i}(q_{xi}, q_{yi})$ describe the in-plane equilibrium dispersion of the Josephson plasma modes. These equations predict three-wave mixing between the apical oxygen phonons and the upper and lower Josephson plasmons, leading to the excitation of damped harmonic oscillations for J_1 and J_2 at finite momenta along the dispersion. The driving term depends on the momentum of the Josephson plasma mode as q^2 , and it is zero for long wavelengths ($q = 0$) but naturally couples to supercurrents at finite in-plane wavevectors. The two equations of motion predict that the phonon excites pairs of Josephson plasma polaritons with frequencies that satisfy $\Omega_1(q) + \Omega_2(-q) = \Omega_{\text{drive}}$ driven at opposite in-plane momenta ($q_{x1} = -q_{x2}$ or $q_{y1} = -q_{y2}$).

A numerical solution of these equations of motion is shown in Figure 4.19 (b) as color-coded dispersion. There, the three-wave mixing process is shown to couple preferentially the driven phonon to plasma modes at in plane momenta $q_y \sim 200 \text{ cm}^{-1}$ ($\lambda \sim 50 \mu\text{m}$) where momenta and energies match. This scattering process is depicted by the two red (blue) arrows in Figure 4.19 (b). This results in the excitation of pairs of high (intra-bilayer) and low (inter-bilayer) frequency Josephson plasma modes, which propagate along the optical surface $J_1(\Omega_1, +q_y)$ and $J_2(\Omega_2, -q_y)$, or $J_1(\Omega_1, -q_y)$ and $J_2(\Omega_2, +q_y)$. Because the pump optical field is screened in the propagation direction (perpendicular to the optical surface) over a skin depth of $\sim 1.5 \mu\text{m}$, phase matching is inefficient along the x-direction. Cuts along the y-direction through the dispersion and simulations results are shown in Fig. 4.20 (c). Here, the zero-momentum phonon excitation is shaded in yellow and the amplification process is again depicted by red and blue arrows. Fig. 4.20 (d) displays the frequency integrated response and predicts two broad peaks centered around $\pm \sim 200 \text{ cm}^{-1}$, consistent with our experimental findings shown in Fig. 4.11 (b).

To achieve a non-zero amplitude response of J_1 and J_2 requires a finite amplitude before time zero $J_i(t < 0) \neq 0$. To this end, the set of coupled equations for the Josephson plasmon dynamics were solved by utilizing a stochastic approach, where Langevin noise on Josephson

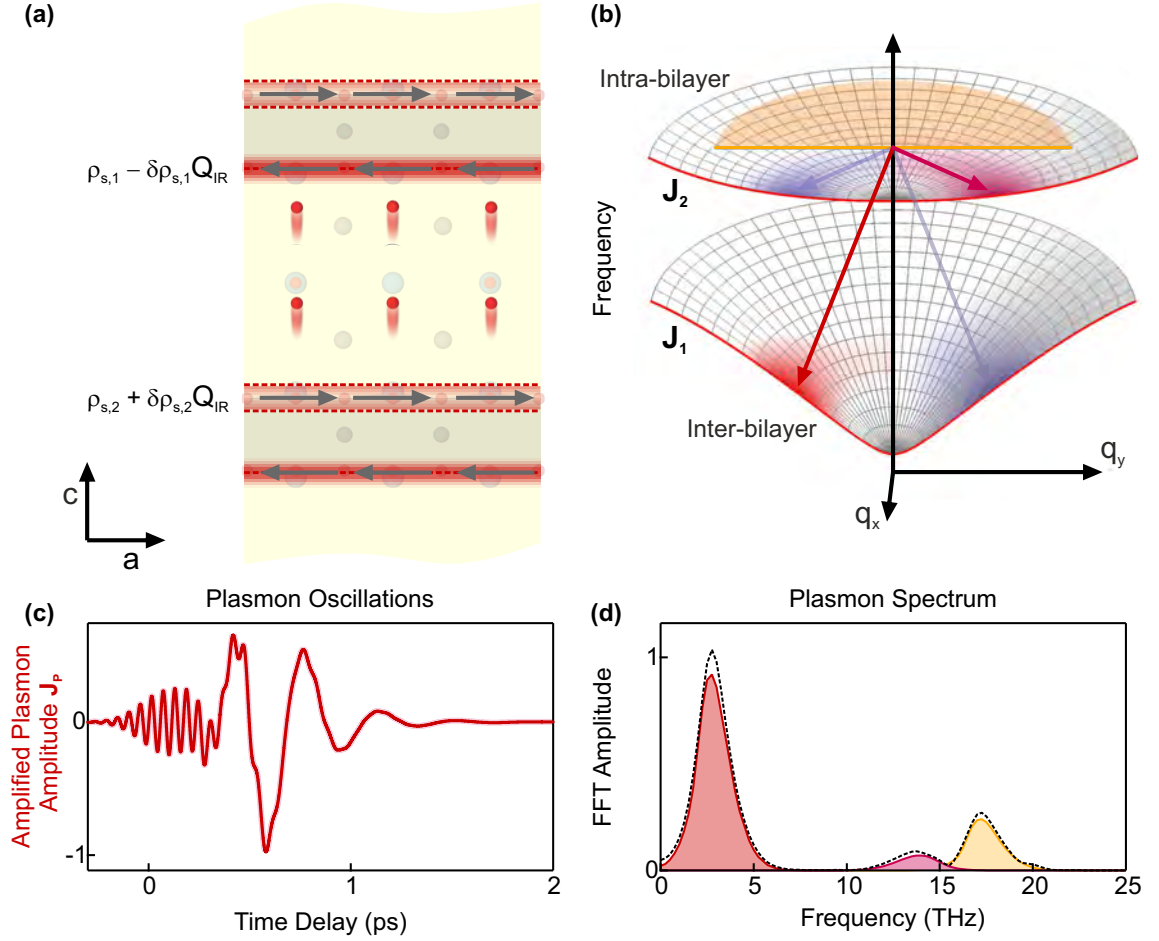


Figure 4.19: Theoretical model of nonlinear phonon-Josephson plasmon coupling. (a) Schematic of the superfluid density modulations and in-plane currents driven by the apical oxygen vibration. The superfluid density $\rho_{s,i}$ on the two CuO_2 is modulated with opposite sign. This leads to counterpropagating in-plane currents (grey arrows), which in turn drive out-of-plane tunneling currents. (b) Dispersion of the inter (J_1) and intra-bilayer (J_2) Josephson plasma modes along the in-plane momenta q_x and q_y in $\text{YBa}_2\text{Cu}_3\text{O}_{6.5}$. The red lines are a cut through the $q_x = 0$ plane. The apical oxygen phonon mode at 17 THz (yellow) does not disperse along either direction. The three-wave scattering process is sketched as red and blue arrows and results from a numerical simulation in response to the resonant drive of the apical oxygen phonon at $q = 0$ are shaded in the same colors. The response vanishes along q_x , parallel to the light propagation direction. (c) The time-dependent momentum-integrated response of panel (b) shows coherent oscillations of the Plasma modes. (d) The corresponding Fourier amplitude spectrum shows peaks at $\Omega_{J,1} = 2.3$ THz (red) and $\Omega_{J,2} = 14$ THz (magenta), which are plotted together with the Fourier spectrum of the driven phonon at 17 THz (yellow).

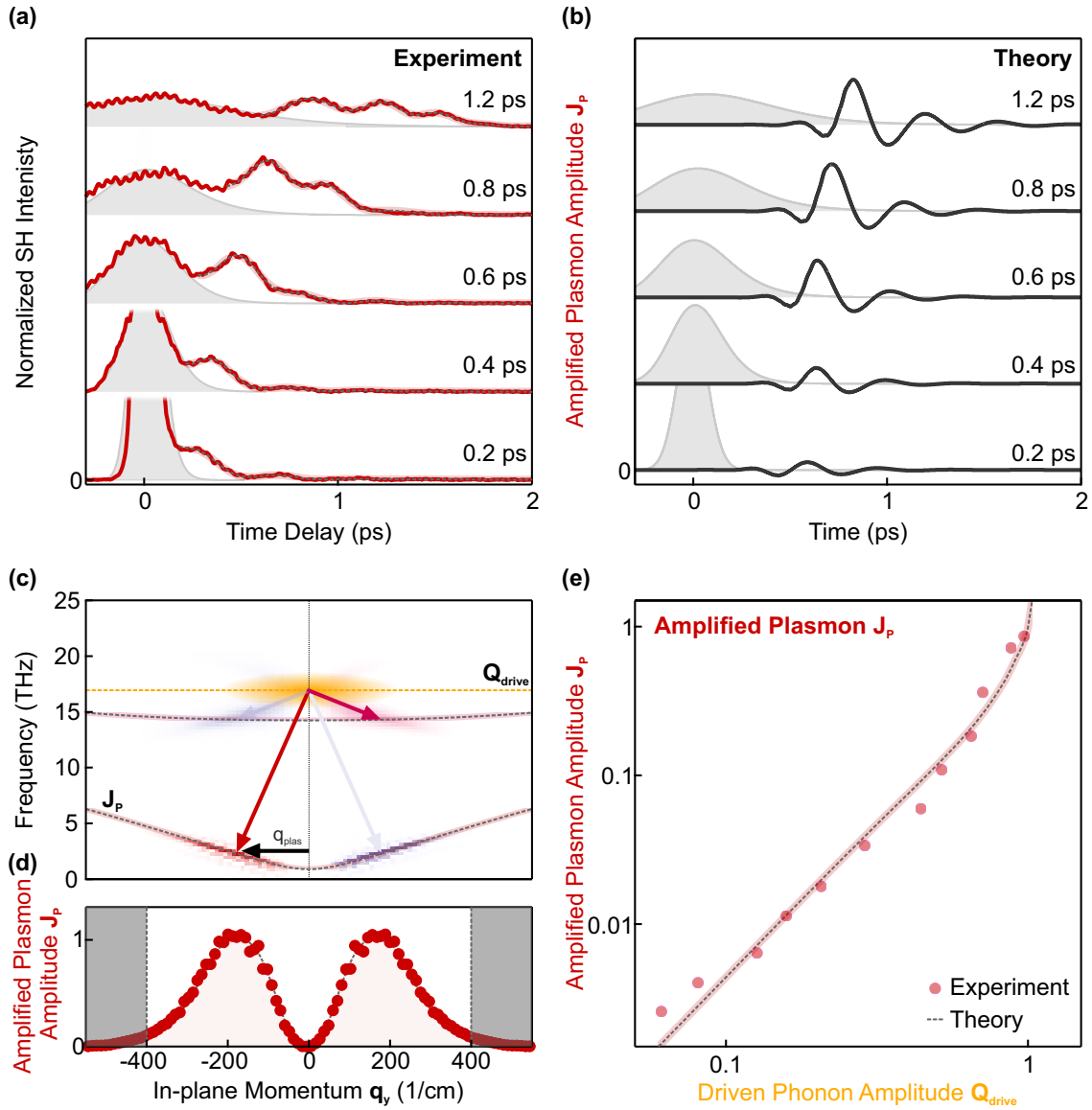


Figure 4.20: Pump-pulse duration dependence, in-plane momentum distribution and excitation strength dependence. (a) Experimental pump-duration dependence. The pump-pulse duration, with pulse durations from 0.2 to 1.2 ps, reveals a delayed onset of the Josephson plasma oscillations for longer excitation pulses. The envelope of the respective mid-infrared pump pulses are shaded in grey. (b) Simulated pump-duration dependence. The same delayed response is observed in time-domain simulations of the three-wave mixing model. (c) Detailed insight into the simulation results along q_y (for $q_x = 0$). The driven phonon with zero momentum excites a pair of Josephson plasmon polaritons, J_1 and J_2 , with opposite wavevectors q_y and frequencies that add up to the phonon frequency. The two processes for mirrored momentum transfer are shown as red and blue arrows, respectively. (d) The frequency integrated response of panel (c) shows two response peaks at $q_y = \pm 200 \text{ cm}^{-1}$. (e) Simulated excitation-strength dependence of the coherent Josephson mode. The simulations reveal exponential scaling amplitude of the Josephson plasma oscillation as a function of the amplitude of the driven apical oxygen vibration Q_{drive} (yellow). Here, the simulation results (dashed line) is overlaid with the experimental amplitude scaling (dots) from Fig. 4.11.

plasma amplitude was used to create an incoherent initial state, otherwise the amplitude of J_1 and J_2 would remain zero for all times. The final trajectory shown in Fig. 4.19 (c) was then computed by solving the equations of motion one million times with an algorithm based on the Euler-Maruyama method and integrating over all momenta. Thus, this type of three-wave mixing requires finite amplitude fluctuations which are amplified and synchronized by the optical drive.

The corresponding responses in time and frequency (see Fig. 4.19 (c) and (d)) shows the combined response of the three fields involved J_1 , J_2 and Q_{drive} , which resonate at 2.5 THz (red), 14.5 THz (magenta) and 17 THz (yellow). The simulated time-response in Fig. 4.19 (c), further shows a delayed reaction of the Josephson plasmon to the optical drive; the plasma oscillations start after the excitation pulse is gone. This also becomes obvious experimentally when placing a transparent dispersive medium in the beam path to stretch the excitation pulse in time while retaining the stable carrier envelope phase. Fig 4.20 (a) shows the time-resolved SH intensity changes for pump-pulse durations from 0.2 ps (unstretched) to 1.2 ps (5 mm ZnSe). The square of the respective pulse envelope is shown in grey. The increase of the excitation pulse duration leads to a linear shift of the Josephson plasma oscillations in time. The same shift can be reproduced mathematically by solving the equations of motion for the stretched excitation pulse profile, which are plotted in Fig. 4.20 (b). Finally, Fig. 4.20 (e) compares the excitation strength dependence of experiment (dots, also shown above in Fig. 4.11) and theory (dashed line). Here, the amplitude of the simulated Josephson plasmon J_{JP} is plotted as a function of the simulated driven phonon amplitude Q_{drive} . For an excitation strength comparable to the experiment we find a similar exponential scaling, which is characteristic of parametric three-wave mixing.

Overall, the presented model agrees in its key aspects, the excitation of finite-momentum Josephson plasmons ($q_y \sim 200 \text{ cm}^{-1}$), symmetry considerations (in-plane and out-of-plane currents) and the excitation field dependence with the experiments. Beyond that, we confirmed that the amplified Josephson plasmon amplitude scales with the resonant enhancement of the driven apical oxygen phonon amplitude Q_{drive} when excited by MIR pulses tuned in resonance with Ω_{drive} (see Appendix C.4). This excludes a scenario, where the incident light field couples directly to the Josephson plasmon polariton and supports the proposed theoretical model. It further predicts the appearance of a coherent signal from the high-frequency intra-bilayer plasmon as

abroad peak at 14 THz. This is also confirmed by the experiment, where a broad feature appears between the low frequency (4, 6, 8 and 10 THz) and the high frequency (17 and 20 THz) phonons (see Fig. 4.6). The absence of all these features in the optimally doped compound $\text{YBa}_2\text{Cu}_3\text{O}_{6.92}$ is because there the relation $\Omega_1(q_y) + \Omega_2(-q_y) = \omega_{\text{drive}}$ can not be fulfilled for any pair of plasmons. This is due to the high frequency of both the inter-bilayer (7 THz) and intra-bilayer (32 THz) plasmon in this compound [201].

Note that also other mechanisms can couple the driven phonon to Josephson plasma polaritons, such as those that descend from the modification of the interlayer Josephson coupling strength, e.g., by modifying the dielectric constant between the bilayers. However, symmetry requires that this coupling scales with Q_{drive}^2 and is to be thought of as a four-wave mixing process between two phonons and two Josephson plasma polaritons, which is weaker, not frequency resonant and hence not taken into account. More details of this type of phonon-Josephson-plasmon coupling can be found in Appendix C.5 and Ref. [220].

4.6.1 THz-optical Response of Parametrically Amplified Josephson Plasmons

Importantly, the coherent oscillations of the condensates order parameter also explain the observation of the light induced coherent transport above T_c in time-resolved THz reflectometry measurements [30, 32, 143]. The full theoretical work in Ref. [220] of the model outlined above, predicts that the nonlinearly excited finite momentum Josephson plasma oscillations lead to a parametric instability at Ω_J and re-radiation of incident THz fields at $q = 0$ close to this frequency. In this process, two counter propagating Josephson plasmons with opposite momentum $\pm q_{\text{JP}}$ interfere and produce a standing wave pattern of the superconducting phase θ along the crystals y direction,

$$\theta(y, t) = \theta_0 \cos(q_{\text{JP}}y) \sin(\Omega_{\text{JP}}t). \quad (4.14)$$

This is sketched in Figure 4.21 (a), where the two counter propagating plasmons are drawn as blue and red sinusoidal waves. In turn, these dynamics modulate the superfluid density $\rho_s(y, t)$ at $q_y = 0$ through [75]

$$\rho_s(y, t) = \rho_{s,0} \cos(\theta(y, t)). \quad (4.15)$$

For small excursions of the condensate phase $\theta(y, t)$, this relation predicts a time-independent spatial modulation of the superfluid density at $2q_{\text{JP}}$ as well as a temporal modulation at $q_y = 0$,

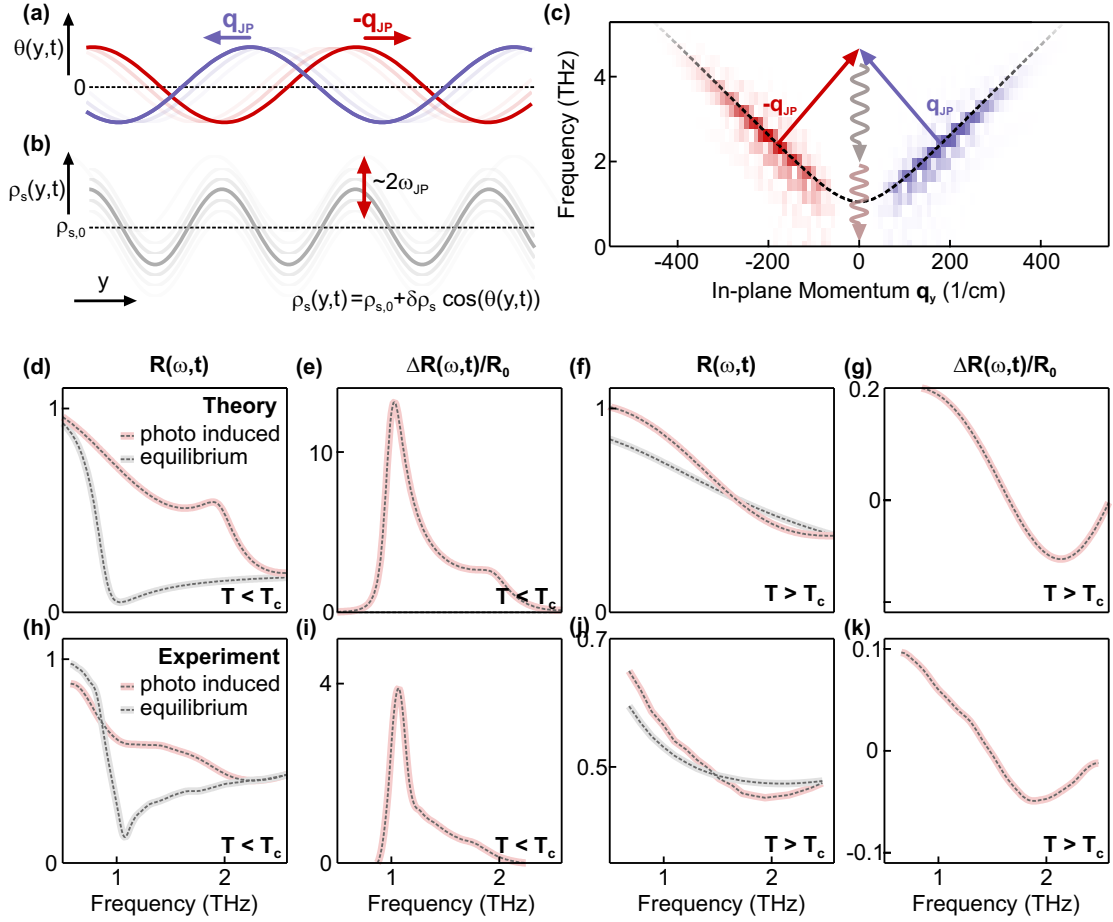


Figure 4.21: Time-resolved THz response of amplified finite-momentum Josephson plasma oscillations. (a) Two counterpropagating Josephson plasmons with opposite momentum $\pm q_{JP}$ (red and blue) interfere and form a standing wave pattern of the superconducting phase θ along the y direction. (b) Resulting spatial and temporal (shaded grey) modulation of the superfluid density $\rho_s(y,t)$ around its equilibrium value $\rho_{s,0}$. The zero-momentum temporal modulation proceeds at twice the Josephson plasma frequency $2\Omega(q_{JP})$ (grey lines). (c) Frequency-momentum diagram of the parametric amplification that drives the THz emission. The two counter-propagating plasmons (red and blue arrows) enter into a virtual zero-momentum state, from which two THz photons are emitted. (d) and (e) Calculated photo-induced (red) and equilibrium (grey) THz reflectivity below T_c and the normalized reflectivity changes $\Delta R(\omega,t)/R_0$, respectively. The finite-momentum Josephson plasmon polariton induces a second plasma edge at a frequency close to $2\Omega(q_{JP})$ and overall enhancement of the reflectivity above the equilibrium plasma edge. (f) and (g) Calculated photo-induced (red) and equilibrium (grey) THz reflectivity above T_c and the normalized reflectivity changes $\Delta R(\omega,t)/R_0$, respectively. Excitation of the apical oxygen vibration leads to the appearance of a plasma edge at a frequency close to $2\Omega(q_{JP})$, which is clearly visible in the normalized reflectivity changes $\Delta R(\omega,t)/R_0$. (h),(i),(j) and (k), show the same features, observed experimentally in time-resolved THz-reflectivity measurements after resonant excitation of apical oxygen oscillations at the peak of the signal at $\Delta t = 0.8$ ps. Experimental data taken from Ref. [30, 32].

$$\rho_s(y, t) \approx \rho_{s,0} \left[1 - \left\{ \theta_0^2 + \theta_0^2 \cos(2q_{\text{JP}}y) - \theta_0^2 \cos(2\Omega_{\text{JP}}t) - \theta_0^4 \cos(2\Omega_{\text{JP}}t) \cos(2q_{\text{JP}}y) \right\} / 4 \right]. \quad (4.16)$$

This is drawn in Figure 4.21 (b) where the grey line denotes the superfluid density, which is modulated around its equilibrium value $\rho_{s,0}$. The zero-momentum temporal modulation at twice the plasmon frequency $2\Omega_{\text{JP}}(q_{\text{JP}})$ is drawn as shaded lines, which do not depend on the spatial coordinate y . This zero-momentum, $2\Omega_{\text{JP}}(q_{\text{JP}})$ modulation of the superfluid density ρ_s leads to parametric amplification of a zero-momentum plasma wave at Ω_{JP} , which can be summarized in an frequency-momentum diagram. The two Josephson plasmons with opposite momentum $\pm q_{\text{JP}}$ (red and blue arrows) scatter into a virtual state at zero momentum and twice the plasmon frequency, $2\omega_{\text{JP}}(q_{\text{JP}})$. This virtual state relaxes by emitting two photons at signal ν_s (grey arrow) and idler ν_i (light red arrow) frequencies with zero in-plane momentum.

The simulated THz reflectivity below T_c , plotted in Fig. 4.21 (d), shows the appearance of a light induced plasma edge at a frequency $\Omega_{\text{JP}} \sim 2$ THz, well above the equilibrium Josephson plasma edge at ~ 1 THz (Fig. 4.21 d, grey line) [222]. The resulting normalized reflectivity changes $\Delta R/R$ in Fig. 4.21 (e) show a strongly enhanced reflectivity between the equilibrium plasma edge and the light induced edge.

Above T_c , the simulated equilibrium THz reflectivity is featureless, as evidence by the grey line in Fig. 4.21 (f). Therefore, in the temperature range $T_c < T$, Josephson plasmons can be described as overdamped modes which do not produce a plasma edge [220]. However, for strong driving of the apical oxygen phonon, the plasma edge is seen to re-emerge at $\Omega_{\text{JP}0} \sim 2$ THz, again blue shifted with respect to the below- T_c equilibrium resonance (red line in Fig. 4.21 (f)). At this frequency parametric driving compensates dissipation most efficiently and revives the features of the dissipation less state, i.e., the plasma edge at $2\Omega_{\text{JP}}(q_{\text{JP}})$. The edge feature becomes even clearer in the normalized reflectivity changes $\Delta R/R$ in Fig. 4.21 (g). Figures 4.21 (h),(i),(j),(k) compare these calculations to experimental data reported in Kaiser et al. for a $\text{YBa}_2\text{Cu}_3\text{O}_{6.48}$ sample [32], and find qualitative agreement below and above T_c . This suggests that the finite momentum coherent Josephson plasma oscillations reported above and the fingerprints of light-induced coherent transport in transient THz-reflectivity originate from the same microscopic mechanism.

4.7 Discussion

The presented results provide useful perspective for the physics of high- T_c cuprates. The finite momentum ($q_y = \pm 190 \text{ cm}^{-1}$) interlayer coherent Josephson modes, unlike the zero momentum excitation detected in linear equilibrium measurements, were not observed to disappear at T_c (see Fig. 3.12) but extended smoothly into the pseudogap phase and above room temperature. The fact that these fluctuations are connected smoothly across T_c points to a similarity between the superconducting mode below T_c and the charge oscillations above it. Furthermore, the observation of normal state coherent interlayer tunneling is difficult to reconcile with the incoherent charge dynamics characteristic of the pseudogap phase of cuprates [201, 253–255] and experimentally demonstrated no other symmetry-odd mode (like phonons) could explain these oscillations.

The results suggest that the coherent Josephson modes observed in the normal state are more convincingly explained by hypothesizing the existence of high temperature superconducting fluctuations at THz frequencies and correlation lengths of several microns [68], possibly connected to condensation at finite momentum [41, 71, 256, 257]. These finite momentum pairing fluctuations act as a seed to the three-wave mixing and are amplified and synchronized to coherent tunneling currents. These are then detected as coherent oscillations in the SH intensity and as a Josephson plasma edge in transient THz reflectivity. These putative fluctuations would lie at frequencies and wavevectors inaccessible to established equilibrium THz reflectivity measurements, and hence have remained undetected to date. On this note, the higher frequency intra-bilayer fluctuations near 12 THz lie at the edge of the light cone, which may explain why these are observed in linear optical spectroscopy at temperatures above T_c , while the lower energy inter-bilayer modes are not (see Fig. 3.11) [203, 206, 207].

4.8 Summary

Nonlinear phonon-Josephson plasmon coupling could be experimentally demonstrated by exciting the polar apical oxygen vibration in $\text{YBa}_2\text{Cu}_3\text{O}_{6.48}$. After strong-field mid-infrared excitation, time-resolved second harmonic generation revealed coherent oscillations at 2.5 THz which do not coincide with any equilibrium lattice excitation of the material. SH polarimetry measurements confirmed a different point group symmetry of this polar excitation from the driven

phonons and identified the coherent 2.5 THz oscillations as Josephson plasma tunneling modes which lower the point group symmetry of the crystal from mmm to m' . Spatially resolved measurements of the emitted SH light by spatial filtering through a slit further confirmed this symmetry assignment by revealing a finite in-plane momentum ($q_y = \pm 190 \text{ cm}^{-1}$) of the coherent Josephson plasma mode. Finally, a pump intensity dependence reveals an exponential amplification of this coherent Josephson mode with increasing amplitude of the driven apical oxygen phonon.

These results enabled the development of a microscopic theory, that involves three-wave mixing between the driven apical phonon and the inter and intra-bilayer Josephson plasma modes. This type of coupling leads to the creation of two Josephson plasmons with opposite momentum and at frequencies which obey the conservation of energy $\Omega_{J,1} + \Omega_{J,2} = \Omega_{\text{drive}}$. For this type of coupling to work, it requires a finite amplitude of the individual waves prior to the resonant phonon excitation, i.e., it requires an (incoherent) seed. The increase of the excitation strength lead to parametric amplification and exponential increase of the Josephson plasma mode amplitude, consistent with the experimental finding. The theory further predicts that in-plane currents drive the out-of-plane tunneling current consistent with the symmetry considerations of the SH polarimetry measurements.

Ultimately, the experimental temperature dependence revealed a smooth connection of the coherent Josephson plasmon's amplitude across T_c and therefore points to a similarity between the superconducting mode below T_c and the charged oscillations above it. These results suggest that the coherent Josephson modes observed in the normal state could be explained by hypothesizing the existence of high temperature superconducting fluctuations. Besides the observation of coherent Josephson plasma modes, the SH experiments also revealed parametric amplification of infrared active lattice vibrations through fourth-order phonon coupling. The excitation of the 17 and 20 THz apical phonon vibrations lead to a parametric resonance at 8.5 and 10 THz and a dominant vibrational response and exponential gain at these frequencies. Ultimately, the presented experiments can open new perspectives of frequency resonant wave mixing as a new means to study cooperative phenomena in quantum materials.

Conclusion and Outlook

In the past decades, optical techniques have been extended to allow for the ultrafast control of materials, revealing hidden states of matter inaccessible by other means. These non-equilibrium states include insulator-metal transitions, melting of magnetic order and even transient superconducting behavior [30–38], which were seen to follow the resonant excitation of the crystal lattice. The latter could be achieved through the recent development of intense sources at THz frequencies. All these previous experiments relied on measuring the linear optical properties and their corresponding response functions, thus limiting the understanding of the microscopic mechanisms which drive these transitions.

The aim of this work was then to extend the well-established nonlinear optical techniques from equilibrium to non-equilibrium measurements. This approach can reveal dynamics which are inaccessible by linear optical probes due to symmetry constraints. To this end, we developed a setup which detects the second harmonic (SH) light generated inside the investigated material by ultra-short laser pulses of 800-nm wavelength through the second-order nonlinear susceptibility $\chi^{(2)}$. To access non-equilibrium states of matter, this nonlinear probe was combined with intense MV/cm mid-infrared laser pulses which resonantly excite infrared active lattice vibrations.

The first set of experiments reported in this thesis (Chapter 2) involves the resonant excitation of an infrared active lattice vibration to large amplitudes and the reconstruction of its energy potential. As a model system we chose the ferroelectric material LiNbO_3 , which, due to its large optical nonlinearities, proved to be an ideal candidate to assess the capabilities of probing second harmonic light generation. In this experiment, we excited the highest frequency optical phonon in LiNbO_3 with strong mid-infrared fields at 17.5 THz. The measurement of the time-delay dependent SH intensity revealed not only coherent oscillations of the driven lattice vibration at its fundamental eigenfrequency but also several harmonics, signifying the anharmonic atomic motion. The time-resolved SHG experiment could be reproduced by finite-difference time-domain

(FDTD) simulations taking into account the full anharmonic lattice potential determined by DFT calculations. The key result of this experiment was the reconstruction of the shape of the potential energy of the driven mode directly from the time-resolved signal. This not only permitted the benchmarking of the first-principles calculations but also the direct measurement of the lattice potential energy of the driven mode and the underlying interatomic forces. This work established time-resolved SHG as a sensitive probe of out-of-equilibrium dynamics.

In a second time-resolved SHG experiment on LiNbO_3 , the nonlinear coupling between the same driven high frequency lattice vibration and the ferroelectric distortion was investigated. This coupling was predicted by DFT calculations and would allow the ultrafast reversal of the ferroelectric polarization. Since this polarization cannot be probed by linear optical methods, time-resolved second harmonic generation is again an ideal tool for this study. Beyond, the phase-sensitive detection of this SH light revealed a transiently reversed polarization. This could only be observed when the frequency of the excitation field was tuned in resonance with the highest frequency lattice vibration and at field strengths exceeding 20 MV/cm. Overall, this experiment has paved a way towards ultrafast ferroelectric switching, which is of technological interest for ultrafast data storage.

The second set of experiments shifted the focus towards the study of non-equilibrium dynamics in cuprate high-temperature superconductors. In the past, the resonant excitation of an apical oxygen vibration in these compounds disclosed the appearance of optical features commonly associated with non-equilibrium superconducting behavior even above the equilibrium transition temperature. THz reflectivity and second harmonic generation share the same selection rules, hence transient features in the THz reflectivity should also appear in time-resolved SHG. We used the same resonant lattice excitation in $\text{YBa}_2\text{Cu}_3\text{O}_{6+\delta}$ (YBCO), which was shown to create a transient superconducting-like state and probed the ensuing dynamics with this nonlinear technique.

We observed coherent oscillations at a frequency of 2.5 THz, close to that of the light-induced Josephson plasmon reflectivity edge. These oscillations exhibit an exponential scaling with the amplitude of the driven phonon mode, anomalous momentum distribution and distinct symmetry in SH polarimetry, which identified them as finite-momentum Josephson plasma oscillations. Strikingly, they were observed to have a finite amplitude above T_c and up to the pseudogap temperature T^* .

On the basis of these observations, a microscopic theory was developed which describes the phonon-plasmon coupling in terms of a three-wave mixing process. This can be understood as a coherent process driven by the apical phonon mode which amplifies a high-frequency and a low-frequency Josephson plasmons under energy and momentum conservation. The theory considers the existence of superconducting pairing fluctuations at THz frequencies and at finite momentum above T_c [41, 71, 256, 257], which act as a seed in the three-wave mixing process and are amplified and synchronized to form coherent Josephson currents between CuO_2 layers. This theory not only succeeds in capturing the most essential findings of the SHG measurements, but also explains the appearance of the Josephson plasma edge in the transient THz reflectivity. This work helped to render a refined picture of the nature of light induced superconductivity and additionally shed light on the nature of the pseudogap phase and the microscopic mechanism of high temperature superconductivity.

Besides the observation of coherent Josephson plasmon dynamics, the intense excitation of the crystal lattice in $\text{YBa}_2\text{Cu}_3\text{O}_{6+\delta}$ also involved nonlinear phononic coupling to amplify low energy phonons. In contrast to phonon-plasmon coupling, this phonon-phonon coupling involves four waves and displays a fundamentally different momentum distribution, temperature dependence and symmetry. This type of phonon amplification in a centrosymmetric material was hypothesized by DFT but had not been observed experimentally yet. It offers a novel approach to transiently break symmetries in solids and thus engineer new material properties arising from such a broken-symmetry state.

Another important result of the experiments presented here is the excellent agreement between the ab-initio DFT calculations and the time-resolved measurements. The predictive power of these computational methods was demonstrated by the perfect agreement between the experimentally determined phonon mode potential and the one calculated by DFT. A combination of these theoretical tools and the increasingly sensitive pump probe experiments will help boost our understanding of the microscopic origins of the macroscopic properties of correlated materials. In total, the work presented in this thesis establishes time-resolved SHG experiments as a powerful tool to investigate lattice as well as electronic dynamics. This type of nonlinear probe is complementary to time-resolved linear techniques and is capable of revealing microscopic dynamics which remain hidden otherwise.

Naturally, this non-linear probe technique can be extended in many directions. The experiments

on LiNbO_3 pave the way towards ultrafast ferroelectric switching via direct lattice control. Leading on from this, one can envision the ultrafast functional control of thin film materials and superlattices grown on top of ferroelectric substrate materials. Direct excitation of the substrate, as previously demonstrated [258], could induce new functionalities in the film as well as couple existing functionalities to the polarization state of the substrate, possibly creating multiferroic order. This would represent a powerful tool set for the realization of functional meta-material control for ultrafast applications. Besides these practical implications, the comprehensive measurement of the lattice dynamics with ultrafast x-ray diffraction during the ultrafast reversal of the ferroelectric polarization would deepen our understanding of these types of ferroic transitions. This research is urgently needed, because even today the nature of these transitions, either displacive or order-disorder type, is still not fully understood. The prospect of measuring the full lattice potential, made possible by the recent development of a novel tunable narrowband THz light source [143], will help to resolve this dichotomy.

The time-domain SH experiments on $\text{YBa}_2\text{Cu}_3\text{O}_{6+\delta}$ ultimately helped to establish a microscopic theory which helps to explain the nature of light induced superconductivity in bilayer cuprates. They open up new perspectives of frequency resonant wave mixing as a new tool to study cooperative phenomena in quantum materials. The insights gathered from the experiments described here can be further corroborated by more comprehensive methods such as resonant inelastic x-ray scattering [72, 259] and high-resolution electron energy loss probes [260].

A next systematic step can be to extend this work to single-layer cuprates, which exhibit similar signs of enhanced coherence above T_c [31]. These seemingly simpler compounds display a more direct competition between superconductivity and other types of order, such as pair-density waves, which are optically silent modulations of the Cooper pair density. These can be revealed by SH Hyper-Raman scattering and would allow to gain more insight into the direct competition of charge order and superconductivity in cuprates. The employed SH Hyper-Raman scattering techniques are not limited to non-equilibrium pump-probe experiments but can also be used as an equilibrium probe to reveal these optically silent states and help improve the understanding of the electronic ground state of cuprate superconductors. To this end, short NIR-pulses can be combined with scanning probe techniques to achieve the relevant fs-temporal and nm-spatial resolution to optically reveal these short range fluctuating orders in cuprates [43, 44, 71, 261].

Author Contributions

In the following, my contributions to the experiments presented in this thesis are summarized and the corresponding publications cited.

Chapter 1

The theoretical framework of the nonlinear optical effects and how they can be applied to measure coherent excitations in solids as presented in this thesis is the result of discussions with all colleagues of my group and external collaborators. I especially want to thank Roman Mankowsky, Michael Först, Michael Fechner, Roberto Merlin and Andrea Cavalleri for stimulating discussions.

Chapter 2

The theory of Nonlinear Phononics presented in this thesis has been discussed with all colleagues of my group and external collaborators. I especially want to thank Roman Mankowsky, Michael Först, Michael Fechner, Roberto Merlin and Andrea Cavalleri for stimulating discussions. The experimental work of Chapter 2 has been done in the laser lab in Hamburg. The samples were commercially available crystals for which I designed a suitable sampleholder. The measurements were taken together with Roman Mankowsky, with whom I also designed the SHG detection setup. The analysis of the strong field Nonlinear Phononics measurements and the reconstruction of the lattice potential was done by me as well as the FDTD simulations. The DFT calculations were performed by Michael Fechner. This part of Chapter 2 was published in Ref. [65]. Alaska Subedi developed the theory that lead to the experimental demonstration of the ultra-fast reversal of the ferroelectric polarization in LiNbO_3 [63, 64]. The SH experiments and the phasing measurements were performed and analyzed by Roman Mankowsky and me. The results are published in [64].

Chapter 3

Chapter 3 is an introduction to Chapter 4 which reports the time-resolved SH experiments of Josephson dynamics in YBCO and summarizes work performed by others.

Chapter 4

The time-resolved SH measurements of the coherent Josephson dynamics in YBCO following resonant lattice excitation were performed in the laser lab in Hamburg. The samples were provided by J. Porras and B. Keimer [166] and ahead of the experiments polished I polished them to optical grade. I took all the measurements, with assistance of Niloofar Hosseinabadi, analyzed the data and contributed to discussion about the microscopic theory which was developed Marios Michael and Eugene Demler [220]. This theory proved to be fundamental for the interpretation of the work and I want to thank Marios Michael and Eugene Demler for their work. The time-domain simulation of the Josephson plasmon and phonon were performed by Michael Fechner, who also performed the DFT calculations. I especially also want to thank Michael Först for stimulating discussions. The results were published in [166]

List of Publications

The results presented in this thesis are based on the following publications:

- (1) **A. von Hoegen**, R. Mankowsky, M. Fechner, M. Först, A. Cavalleri, Probing the interatomic potential of solids with strong-field nonlinear phononics, *Nature*, 555, 79-82 (2018)
- (2) R. Mankowsky, **A. von Hoegen**, M. Först, A. Cavalleri, Ultrafast Reversal of the Ferroelectric Polarization, *Phys. Rev. Lett.*, **118**, 247601 (2017)
- (3) **A. von Hoegen**, M. Fechner, M. Först, J. Porras, B. Keimer, M. Michael, E. Demler, A. Cavalleri, Probing coherent charge fluctuations in $\text{YBa}_2\text{Cu}_3\text{O}_{6+x}$ at wavevectors outside the light cone, arXiv:1911.08284 (2020)
- (4) M. H. Michael, **A. von Hoegen**, M. Fechner, M. Först, A. Cavalleri, E. Demler, Parametric resonance of Josephson plasma waves: A theory for optically amplified interlayer superconductivity in $\text{YBa}_2\text{Cu}_3\text{O}_{6+x}$, arXiv:2004.13049 (2020)
- (5) R. Mankowsky, M. Fechner, M. Först, **A. von Hoegen**, J. Porras, T. Loew, G.L. Dakovski, M. Seaberg, S. Möller, G. Coslovich, B. Keimer, S.S. Dhesi, and A. Cavalleri, Optically-induced lattice deformations, electronic structure changes and enhanced superconductivity in $\text{YBa}_2\text{Cu}_3\text{O}_{6.48}$, *Structural Dynamics*, **4**, 044007 (2017)

Appendix A

Nonlinear Optics and Pump-Probe Experiments

A.1 Basics of Pump probe Experiments and Experimental Practice

Pump-probe spectroscopy measures the physical properties after the excitation of a materials into a non-equilibrium excited state and the subsequent relaxation back to equilibrium. Typically, a laser pulse is split into a strong pump-pulse and a weak probe-pulse. The pump is used to drive the sample into an excited state and the probe is used to monitor a certain property of the sample, usually its reflectivity. The time evolution of this property is then be mapped out by varying the relative arrival time between pump and probe at the sample position. (see Fig. 1.1). Nonlinear light conversion, for example with an optical parametric amplifier (see A.4), allows one to choose different wavelengths of both pump and probe pulses, which can span several orders of magnitude from the far-infrared to excite and probe low energy excitations of the material up to hard x-rays to probe its structural properties. Lab-based laser systems usually operate either at MHz repetition rate (oscillator based systems) with low pulse energies or at kHz repetition rate (amplifier based systems), which provide laser pulses of higher energy. The later was made possible by chirped pulse amplification, where the ultra-short seed pulse from an oscillator is stretched prior to the amplification to impede damage to the laser active medium, Ti:sapphire. In all experiments presented in this thesis, we used laser pulses to resonantly excite infrared active lattice vibrations. Typical energies of these excitation are in the range of 300 meV to 350 meV. This made it necessary to down convert the 800-nm (1.5 eV) wavelength photons of the Ti:sapphire amplifier, which still is a highly inefficient process (see A.4). Therefore, we used a KMLabs Dragon™ multipass amplifier, which provides high pulse

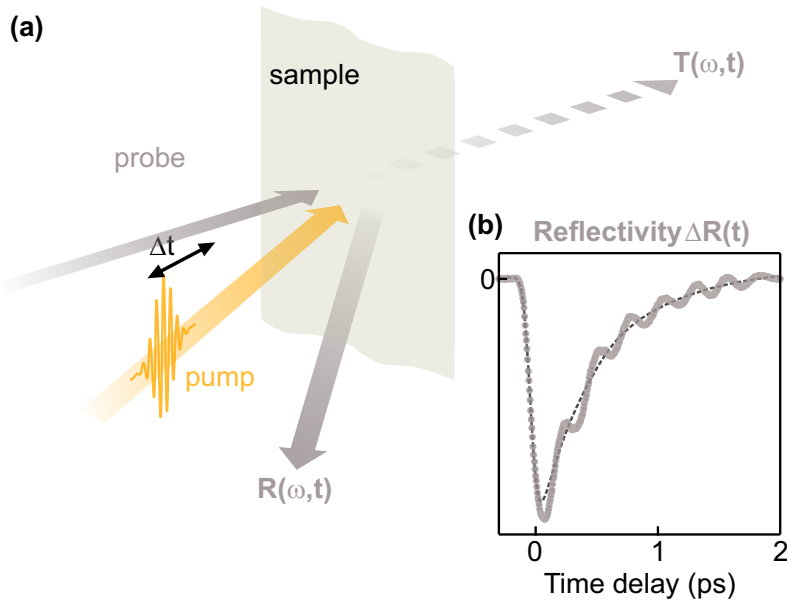


Figure 1.1: Schematic of pump-probe geometry. (a) In a typical pump probe experiment two pulses hit the sample, the probe pulse (grey) and the pump pulse (yellow). To measure the time evolution of the optical properties of the sample material the time delay Δt between pump and probe pulse is varied in steps. The reflected or transmitted (dashed grey) probe pulse are then measured by an optical detector. (b) Shows an example curve of a pump probe trace, where the optical reflectivity in the NIR spectra was measured.

energies of 2 mJ (35-fs duration, p-polarized), as basis to generate the pump pulses, limiting the repetition rate of the experiments to 1 kHz. The pump pulses are usually chopped and the intensity of the probe pulses are measured by photodiodes or a photomultiplier tube (depending on the detected wavelength). In order to increase the limited signal to noise ratio due to the low 1 kHz repetition rate, the electrical output of these optical sensors is then measured with a lock-in amplifier, which locks into the modulation frequency of the mechanical chopper, significantly increasing the signal-to-noise ratio. Typical integration times of the lock-in amplifiers are 300 ms. The samples are usually kept at 1×10^{-6} mbar pressure in an Oxford MicrostatHe-RTM cryostat and the beams pass through a 300 μm thick diamond window, transparent for all important wavelength. This allowed us to control the sample temperature in a range from 4 K to 500 K and protect it from degradation due to humidity. The Y-Ba-Cu-O samples used in our experiments have been synthesized and characterized by Prof. B. Keimer and J. Porras in the Max-Planck Institute for solid state research in Stuttgart (Germany). The samples are single crystal of typical dimensions $1 \times 1 \times 0.5$ mm characterized X-ray diffraction and SQUID

magnetometry measurements. These samples are very susceptible to degradation due to decomposition by H₂O and were stored in an evacuated storage cabinet. The sample surface was polished down to a grit size of 100 nm to optical grade, to obtain a single specular reflection. The LiNbO₃ samples are commercially available and were bought from the company SurfaceNet in Rheine. They are x-cut mono-domain congruently grown LiNbO₃ crystals of 5 × 5 × 5 mm dimension. We validated this by SHG polarimetry.

A.2 Optical Parametric Amplification

Optical parametric amplification is used to down convert the frequency of a high intensity input field, which normally is called pump E_{ω_p} . To achieve this the pump field is overlapped with a significantly weaker signal field E_{ω_s} in a crystal which shows a second order nonlinearity $\chi^{(2)}$. The interaction of the two fields through the $\chi^{(2)}$ nonlinearity, described by the equations introduced in 1, transfers energy from the pump to the signal. Therefore, the frequency of the signal field (seed) has to be chosen to coincide with the desired target frequency. Further to conserve energy a third field E_{ω_i} is generated, commonly dubbed idler. The process can be summarized as shown in Figure 1.2, a pump photon excites the system to a virtual state which then emits two photons with energies $\hbar\omega_s$ and $\hbar\omega_i$. Following the discussion above the rate equations capturing this process are given by

$$\frac{dE_{\omega_s}}{dz} = 2i \frac{\chi^{(2)} \omega_s^2}{c^2 k_{\omega_s}} E_{\omega_p} E_{\omega_i}^* e^{i\Delta k x} \quad (\text{A.1})$$

$$\frac{dE_{\omega_i}}{dz} = 2i \frac{\chi^{(2)} \omega_i^2}{c^2 k_{\omega_i}} E_{\omega_p} E_{\omega_s}^* e^{i\Delta k x} \quad (\text{A.2})$$

considering an undepleted pump $dE_{\omega_s}/dz = 0$. In typical applications $\Delta k = 0$ is achieved by choosing an appropriate geometry (see below) of the interacting light fields. Differentiating eq. A.1 and inserting eq. A.2 finally yields the spatial evolution of $E_{\omega_{s/i}}$ as

$$\frac{d^2 E_{\omega_{s/i}}}{dz^2} = \kappa_{s/i}^2 E_{\omega_{s/i}} \quad (\text{A.3})$$

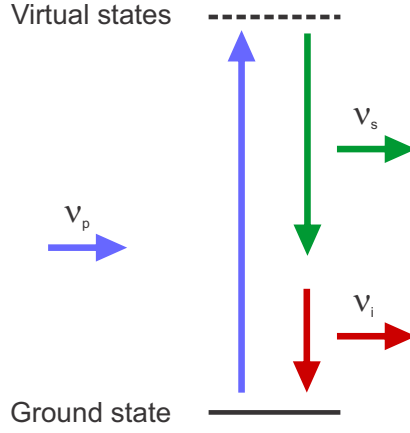


Figure 1.2: Energy diagram of optical parametric amplification. An incident laser field with frequency ν_p , called pump, promotes the system into a virtual electronic state. When it relaxes back the system emits two electric fields with frequencies ν_s and ν_i , called signal and idler, respectively. Due to conservation of energy $\nu_p = \nu_s + \nu_i$.

where $\kappa_{s/i} = 2i\chi^{(2)}\omega_{s/i}^2/c^2k_{\omega_{s/i}}E_{\omega_p}$. This equation has a general solution when perfect phase matching is assumed,

$$E_{\omega_{s/i}}(z) = a \sinh(\kappa_{s/i}z) + b \cosh(\kappa_{s/i}z) \quad (\text{A.4})$$

The boundary conditions ($E_{\omega_s}(0) = 0, E_{\omega_s}(0) = \text{const.}$ [78]) then yield,

$$E_{\omega_s}(z) = E_{\omega_s}(0) \cosh(\kappa_s z) \quad (\text{A.5})$$

$$E_{\omega_i}(z) = i \frac{E_{\omega_p} E_{\omega_s}^*(0)}{|E_{\omega_p}|} \left(\frac{n_{\omega_s} \omega_i}{n_{\omega_i} \omega_s} \right)^{1/2} \sinh(\kappa_i z) \quad (\text{A.6})$$

which for $\kappa z \gg 1$ can be approximated as $e^{(\kappa z)}$. Thus, the two fields E_{ω_i} and E_{ω_s} will experience exponential growth at the expense of E_{ω_p} , signifying parametric amplification. It is worth noting that the signal field E_{ω_s} retains its initial phase given by the seed $E_{\omega_s}(0)$ [78].

A.3 Difference Frequency Generation

Like optical parametric amplification, also difference frequency generation (DFG) involves the interaction of three distinct light fields. However, different to OPA in applications two of these light fields (pump and signal) are supplied in equal strength and similar frequency ($\omega_p - \omega_s <$

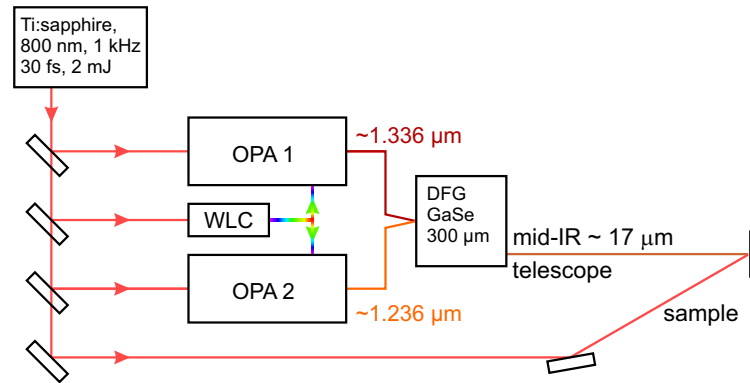


Figure 1.3: Schematic representation of the experimental setup. 30-fs pulses from a Ti:sapphire amplifier are used to pump two optical parametric amplifiers (OPA), which are seeded by the same white light continuum (WLC). Carrier envelope phase stable 3- μ J 150-fs pulses at 17 μ m wavelength are obtained by difference frequency generation of the two signal beams from the OPAs. The mid-infrared light (yellow) is focused to a spotsize of approximately 65 μ m using a telescope and overlapped with the 800-nm probe beam (red).

30 THz) to obtain an idler beam at mid-infrared frequencies. Their interaction is again given by equations A.2, A.1 and their solution takes a similar form as eq. A.6. Importantly, the phase of the idler beam can be precisely controlled by the difference of the phases of the input beams [78]. Thus, by supplying two laser beams, pump and signal, with a constant phase offset allows the generation of phase stable pulses in the MIR spectral region.

A.4 Generation of Broadband Mid-Infrared Radiation

The setup used to generate the mid-infrared pulses is shown in Figure A.1.3. The 800-nm wavelength 35 fs laser pulses from the Ti:Sapphire amplifier is split to pump two optical parametric amplifier (OPA). A small portion of the pump is used to generate a white light continuum through self-phase modulation in a 500 μ m thick sapphire plate. This white light continuum is used as a seed in the two symmetrical arms of the OPAs. These consist of two stages: The first stages use the white light as a seed to amplify a single frequency from the continuum, selected by phase matching in a Beta Barium Borate (β -BBO) crystal. The second stage then amplifies the output of the first stage.

The two OPAs are pumped with 35 fs pulses with 1.5 mJ at 1 kHz, which are split by a 50/50 beam splitter for the two paths. The pump pulses are s-polarized and the signal wavelengths of 1236 nm and 1336 nm are amplified from the continuum. The two first stages are pumped

with 110 μJ pulses focused to peak intensities of 55 GW/cm^2 , which yields signals with energies of around 8 μJ (1236 nm) and 11 μJ (1336 nm) respectively. These two beams are then amplified by 630 μJ pump pulses (peak intensities of 55 GW/cm^2) in the second stages to 140 μJ (1336 nm) and 200 μJ at 1236 nm (see figure A.1.3). The two second stage outputs are loosely focused and non-collinearly (0.5°) overlapped in a 330 μm thick GaSe crystal oriented for type-II difference frequency generation of 17 μm radiation. The carrier envelope phase (CEP) of mid-infrared pulses is passively stabilized since both OPAs are seed by the same white light continuum and hence the same phase offset. The whole process yields 2 μJ to 3 μJ pulse energy at 17- μm wavelength and 150-fs duration, an overall conversion efficiency of approximately 0.2% (see Fig. 1.3).

A.5 Time-Resolved Detection of Strong Mid-Infrared Fields

The spectral and temporal shape of the ultra-short mid-infrared pulses is determined by electrooptic sampling (EOS). For an EOS, a mid-infrared beam is focused into a detection crystal, typically GaSe, GaP or ZnTe. The focused beam is then overlapped with a so-called gate pulse, which samples the beam by exploiting the Pockels effect. The pulse duration of this gate pulse has to be shorter than a full period of the mid-infrared field. The mid-infrared and the short gating pulse co-propagate in a nonlinear detection crystal with a variable delay. The detection efficiency is optimized through phase-matching of the propagating gate and mid-infrared pulse. The mid-infrared field (quasi-DC) induces a transient birefringence in the nonlinear detection crystal that rotates the gating pulse polarization. The polarization rotation is directly proportional to the instantaneous mid-infrared field. After passing through the detection crystal this polarization rotation is measured by balanced detection setup (see Fig. 1.4). The gating pulse is linearly polarized (either s- or p-) and after interacting with the mid-infrared field in the detection crystal, the polarization remains linear but is rotated with respect to the incident polarization. The two orthogonal polarization components are separated by a $\lambda/2$ waveplate and a Wollaston prism. The two resulting beams are detected with two photodiodes which measure their intensities I_1 and I_2 . The instantaneous mid-infrared field can be extracted from the intensity difference signal $E_{\text{MIR}} \propto I_1 - I_2$.

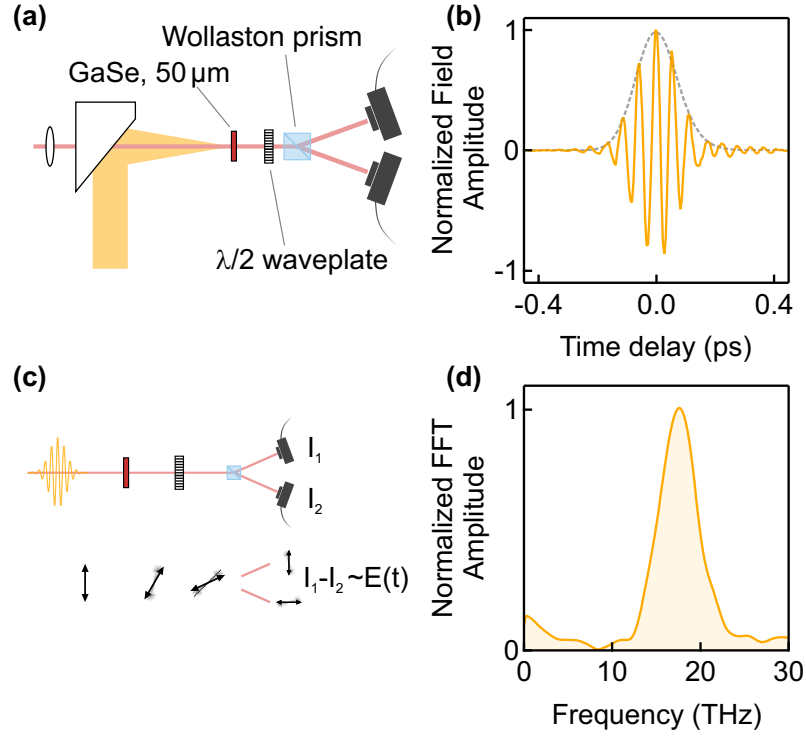


Figure 1.4: Schematic representation of the EOS setup. (a) The mid-infrared light (yellow) is focused into an electro optic medium (GaSe) and overlapped with a short gate pulse (red). The gate pulse is then detected by balancing two photo diodes with a half-waveplate and a Wollaston prism. (b) The difference signal of the two photo diodes is directly proportional to the electric field of the mid-infrared pulse, which is shown in panel (c). The envelope of the pulse is shown as a dashed line. (d) The mid-infrared pulses used for the experiments in this thesis were typically tuned to center wavelength of 16 THz to 22 THz with nearly 25% bandwidth. The yellow peak is the FFT of the waveform in panel (c).

A.6 Phase-Matching Type-I and Type-II

Phase-matching in a nonlinear medium is often difficult to achieve because usually the refractive index increases monotonically as a function of frequency. As a result, the condition for perfect phase matching,

$$\frac{n(\omega_1)\omega_1}{c} + \frac{n(\omega_2)\omega_2}{c} = \frac{n(\omega_3)\omega_3}{c}, \quad (\text{A.7})$$

with $\omega_3 = \omega_1 + \omega_2$, cannot be achieved. However, phase matching can be achieved by making use of the birefringence displayed by many nonlinear crystals. Birefringence is the dependence of the refractive index on the direction of polarization of the optical radiation [2 chap1]. In order to

achieve phase matching by using the birefringence, the highest-frequency wave $\omega_3 = \omega_1 + \omega_2$ is polarized in the direction that gives it the lower of the two possible refractive indices. Here, the refractive index along the optical axis is n_e , for the extraordinary beam, and for light polarized perpendicular to the optical axis it is n_o , the ordinary beam. Usually, n_e is smaller than n_o so the highest frequency light should be polarized along the optical axis. However, there are two choices for the polarizations of the lower-frequency waves., which define the two most common types of phase-matching:

Type I: The two lower-frequency waves have the same polarization.

Type II: The two lower-frequency waves have orthogonal polarization.

Usually, type-I phase matching is easier to achieve than type-II [78]. Careful control of crystalline axis of the birefringent material is required to achieve the phase-matching condition ($\Delta k = 0$). In a uniaxial crystal the phase matching for second harmonic generation condition becomes,

$$\frac{\sin^2(\theta)}{n_e (2\omega_1)^2} + \frac{\cos^2(\theta)}{n_o (2\omega_1)^2} = \frac{1}{n(\omega_1)^2}. \quad (\text{A.8})$$

In this equation θ denotes the angle between the propagation direction and the optical axis [78].

Appendix B

Time-resolved SH experiments on LiNbO_3

B.1 Scaling the Reconstructed Potential

This paragraph describes the steps how the experimentally determined lattice potential of Chapter 2 was rescaled to absolute physical units following the description in the supplementary information of Ref. [65]. The unknown proportionality factor B , which connects the measured SH signal to the vibrational velocity via $I_{\text{SH}}(\tau) = B \dot{Q}(\tau)$, leaves a single scaling factor to the reconstruction. The kinetic energy becomes $E_{\text{kin}}(\tau) = 1/2(I_{\text{SH}}(\tau))^2/B^2$ and the vibrational amplitude $Q(\tau) = \int I_{\text{SH}}(\tau)/B d\tau$. Hence, the y-axis of the reconstruction will be scaled with B^2 and the x-axis with B to the correct absolute values. This constant B can most effectively be derived by fitting the function $f(Q) = 1/B^2 U(BQ)$ to the experimental data, where $U(Q)$ is the potential obtained by DFT. Once B is retrieved, the experimental x and y axis can be rescaled to the absolute phonon amplitude in terms of $\text{\AA}\sqrt{\text{amu}}$ and the potential energy in eV, respectively. The maximum displacement of the oxygen atoms involved in the A_1 vibrational mode was calculated with the knowledge of the phonon eigenvectors, which we obtained from DFT calculations (see Appendix B.10). We find a maximum displacement of the oxygen atoms of approximately 14 pm, which amounts to 7% of the Nb-O and 5% of the O-O nearest neighbour distance at the corresponding potential energy (0.7 eV), which agrees with the estimated energy deposited per unit cell (0.6 eV at 3 μJ pulse energy).

B.2 Phase-matching between the Probe Light and the Phonon-Polariton

The amplitude spectra shown in 2.12 are well understood by considering the phase-matching between the probe light and the phonon-polariton propagating into the crystal. The phonon-polariton dispersion of LiNbO₃ (black line) is plotted as $\nu_p = c_0 q \sqrt{\varepsilon(\nu)}$, where c_0 is the vacuum speed of light and $\varepsilon(\nu)$ the dielectric function. The light lines $\nu = v_g q$ of the 800 nm (red, $v_{g,800} = c_0/2.3$) and the 400 nm ($v_{g,400} = c_0/3.03$) probe fields are also shown, where v_g and q denote the group velocity and wave number, respectively. Phase-matching occurs at those frequencies for which the light lines intersect the phonon-polariton dispersion curve [92, 137], i.e. at 14.6 THz (PR), 15.4 THz (SH) and 19 THz (both PR and SH) (see Fig. 2.1).

B.3 Effect of Inter-Phonon Coupling of the Type $g_j Q_{\text{IR}}^2 Q_j$

This paragraph discusses the influence of non-linear mode coupling on the resonance frequency of the driven mode in the LiNbO₃ experiments of Chapter 2 following the description in the supplementary information of Ref. [65].

Besides the nonlinearities of the driven lattice mode, the full lattice potential also comprises coupling to other phonon modes of the form $g_j Q_{\text{IR}}^2 Q_j$:

$$U(Q_{\text{IR}}, Q_j) = \frac{1}{2} \omega_{\text{TO}}^2 Q_{\text{IR}}^2 + \frac{1}{3} a_3 Q_{\text{IR}}^3 + \frac{1}{4} a_4 Q_{\text{IR}}^4 + \frac{1}{5} a_5 Q_{\text{IR}}^5 + \sum_j \frac{1}{2} \omega_j^2 Q_j^2 + \sum_j g_j Q_{\text{IR}}^2 Q_j. \quad (\text{B.1})$$

Here, the Q_j denote the amplitude of coupled lattice modes and Ω_j their resonance frequency [58, 64]. For strongly driven Q_{IR} the nonlinear interaction leads to a directional force on the coupled mode Q_j , which can be used to control materials functionality [64]. In addition, the finite amplitude Q_j renormalizes the fundamental frequency of Q_{IR} , as can be seen in the equations of motion

$$\ddot{Q}_{\text{IR}} + 2\gamma \dot{Q}_{\text{IR}} + (\omega_{\text{TO}}^2 - 2g Q_j Q_{\text{IR}}) = Z^* E(t) \quad (\text{B.2})$$

$$\ddot{Q}_j + 2\gamma_j \dot{Q}_j + \omega_j^2 Q_j = g_j Q_{\text{IR}}^2 \quad (\text{B.3})$$

This frequency renormalization $\omega'_{\text{TO}} = \sqrt{(\omega_{\text{TO}}^2 - 2g Q_j)}$ was observed in our experiment with a

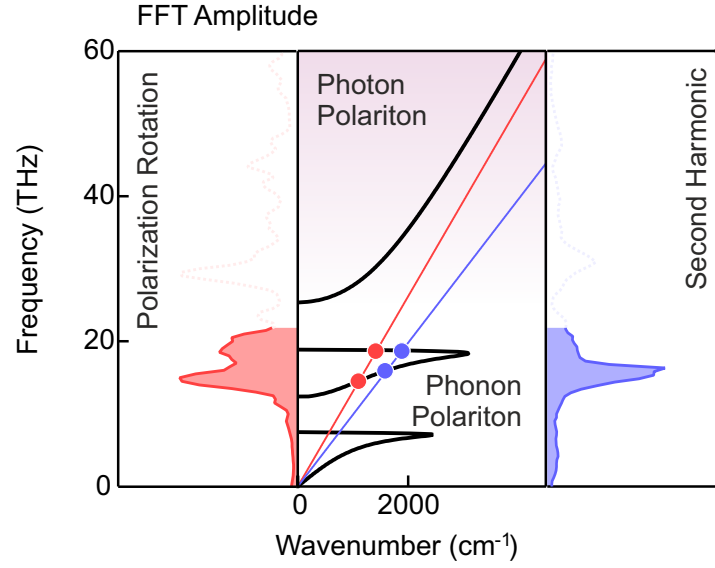


Figure 2.1: Phonon-polariton dispersion. The phonon-polariton dispersion of the two dominant lattice modes in LiNbO₃ (black curve) intersects the two light lines $\nu = v_{gq}$ for 800 nm (red) and 400 nm (blue) wavelengths at 14.6 THz and 15.4 THz, respectively. The dots mark the points of intersection with the dispersion relation, which correspond to the observed fundamental frequencies of the driven mode (left and right panel).

maximum change of 3.5% at the highest driving field (see Fig 2.2).

B.4 Nonlinear Eigenfrequency Renormalization

At large amplitudes a nonlinear oscillator experiences a frequency renormalization due to its anharmonic potential energy

$$U(Q_{\text{IR}}) = \frac{1}{2}\omega_{\text{TO}}^2 Q_{\text{IR}}^2 + \frac{1}{3}a_3 Q_{\text{IR}}^3 + \frac{1}{4}a_4 Q_{\text{IR}}^4 + \frac{1}{5}a_5 Q_{\text{IR}}^5 + \dots \quad (\text{B.4})$$

This becomes obvious by rewriting the equation of motion of the oscillator which includes the cubic order nonlinear term of the potential energy,

$$\ddot{Q}_{\text{IR}} + 2\gamma\dot{Q}_{\text{IR}} + (\omega_{\text{TO}}^2 + a_3 Q_{\text{IR}} + a_4 \dots)Q_{\text{IR}} = Z^* E(t) \quad (\text{B.5})$$

the instantaneous frequency is thus

$$\omega(Q_{\text{IR}}) = \sqrt{\omega_{\text{TO}}^2 + a_3 Q_{\text{IR}}}. \quad (\text{B.6})$$

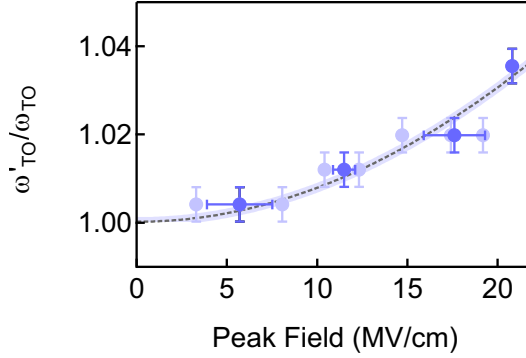


Figure 2.2: Frequency renormalization of the driven through nonlinear phonon coupling. The normalized frequency of the driven mode in LiNbO₃ increases quadratically with the peak field of the pump pulse. The light blue points are directly extracted from the FFT of the pump probe signal. Due to the limited frequency resolution the data points were binned (dark blue). The dashed line is a fit of the type $\Omega(E)/\Omega_0 = \sqrt{1 + aE^2}$.

For this we can find an analytical solution which predicts an on-average lower resonance frequency of the strongly driven oscillator

$$\omega(Q_{\text{IR}}) = \omega_{\text{TO}} - \frac{5}{12} \frac{a_3^2}{\omega_{\text{TO}}^3} Q_{\text{IR}}^2. \quad (\text{B.7})$$

Since the higher harmonics appear only appear at the highest amplitudes of the oscillatory motion they will be strongly influenced by the renormalized frequency. As derived above, they will experience an on average lower frequency compared to the fundamental oscillation and are therefore shifted to lower frequencies compared to the integer multiples of the fundamental frequency (see Fig. 2.3). The situation is slightly different when the potential energy only contains even order terms. Then the lowest order of the anharmonic expansion is the quartic term

$$U(Q_{\text{IR}}) = \frac{1}{2} \omega_{\text{TO}}^2 Q_{\text{IR}}^2 + \frac{1}{4} a_4 Q_{\text{IR}}^4 + \dots, \quad (\text{B.8})$$

which leads to an instantaneous frequency given by

$$\omega(Q_{\text{IR}}) = \sqrt{\omega_{\text{TO}}^2 + a_4 Q_{\text{IR}}^2}. \quad (\text{B.9})$$

The additional term leads to a unidirectional increase or decrease of the frequency depending on the sign of the coefficient a_4 (see Fig. 2.3). Similar to the reasoning above, this change of

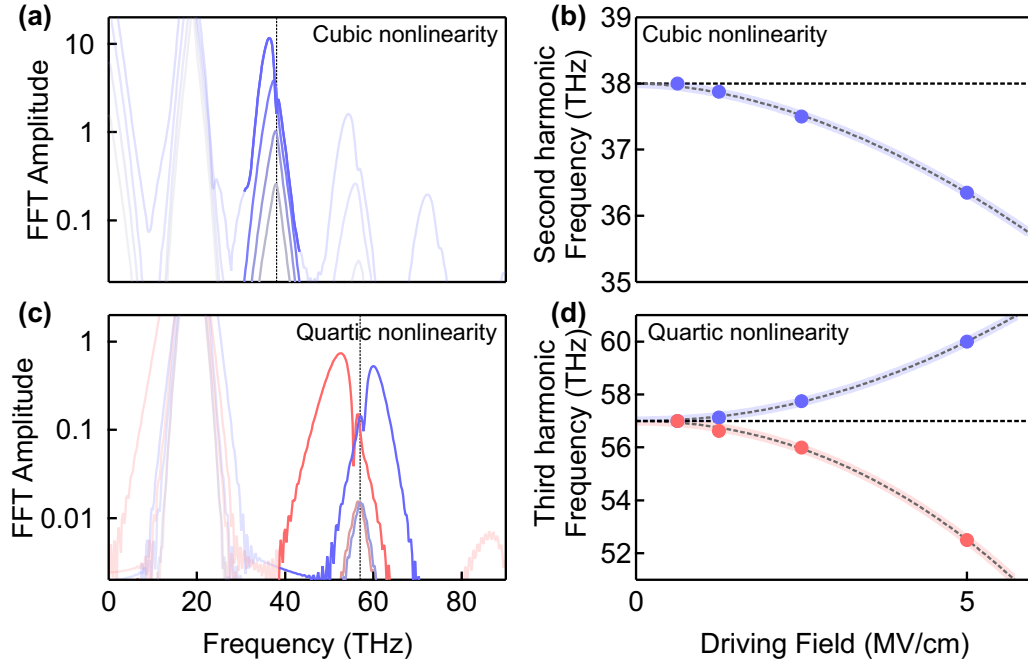


Figure 2.3: Frequency renormalization due to the self-anharmonicity. (a) For a cubic lattice nonlinearity, the peaks of the second (highlighted in full color) and higher harmonics (faded color), always shift to lower frequencies as a function of the excitation field (increasing from grey to blue.) (b) The peak maximum position to lower frequencies and can be fitted by eq. B.7 (dashed line). (c) For a quartic nonlinearity in the lattice potential the shift of the higher harmonics can be either positive (blue peaks) or negative (red peaks), depending on the sign of the coefficient. (d) For the same magnitude, a negative nonlinear coefficient leads to a larger frequency shift for a given fluence (compare blue and red dots). The dashed line is a fit with equation eq. B.10.

the instantaneous frequency at the highest amplitudes will shift the higher harmonics to lower or higher frequencies depending on the sign of a_4 ,

$$\omega(Q_{\text{IR}}) = \omega_{\text{TO}} + \frac{3}{8} \frac{a_4}{\omega_{\text{TO}}} Q_{\text{IR}}^2. \quad (\text{B.10})$$

B.5 Solution of Mathieu Equation and Exponential Scaling

An oscillator with time-dependent parameters, i.e., frequency and damping coefficient, is called a parametric oscillator. In the special case, when the frequency of the oscillator is periodically

modulated the equation of motion will be

$$\ddot{Q} + \omega_0^2(1 + \alpha \sin(\Omega t))Q = 0, \quad (\text{B.11})$$

and is commonly known as *Mathieu equation* [146]. With basic consideration of Floquet theory, for example the periodicity of the solutions ($Q(t) = Q(t + 1/\Omega)$), one finds that $Q(t)$ is periodic within a constant scale factor $e^{\mu/\Omega}$,

$$Q(t + 1/\Omega) = e^{\mu/\Omega}Q(t). \quad (\text{B.12})$$

If now this is expressed with the periodic function $P(t) = P(t+T)$ one can see

$$Q(t) = e^{\mu t}P(t), \quad (\text{B.13})$$

$$Q(t + 1/\Omega) = e^{\mu(t+1/\Omega)}P(t + 1/\Omega) = e^{\mu/\Omega}e^{\mu t}P(t) = e^{\mu/\Omega}Q(t). \quad (\text{B.14})$$

Therefore, for a positive sign of μ one acquires an exponential increase of the vibrational amplitude with time [146].

B.6 Interaction Length in LiNbO₃ SH Experiments

Part of this paragraph are adapted from the supplementary information of Ref. [64]. The time-resolved second harmonic signal in the LiNbO₃ experiments is due to the homogenous solution to the wave equation, which results from the discontinuity of the optical properties at the boundary of the crystal [97, 98]. The generation occurs in a layer below the surface with thickness given by the SH coherence length of $l_{\text{coh}} = 1.27 \mu\text{m}$. The coherence length determines over which depth in the bulk material the dipole emission builds up constructively [99]:

$$l_{\text{coh}} = \frac{\lambda}{4 |n_{2\omega} - 2n_{\omega}|}. \quad (\text{B.15})$$

The homogeneous solution is thus sensitive to polarization and phonon dynamics in the pumped volume and it propagates with a group velocity determined by the linear optical properties and

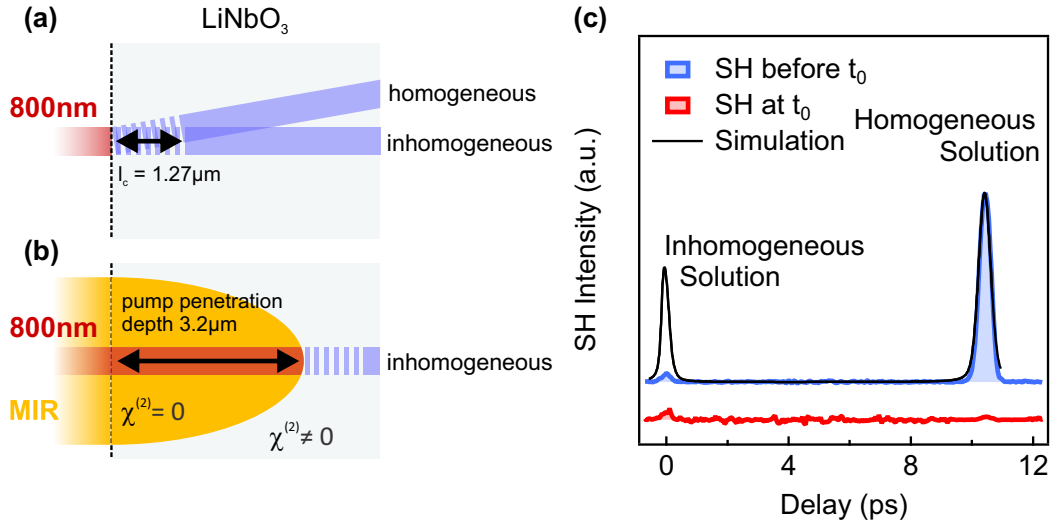


Figure 2.4: Homogeneous and inhomogeneous solution of SHG in a pump probe experiment. (a) In an unpumped LiNbO₃ crystal, the homogeneous SH solution (blue) is generated in the coherence length l_c (dashed blue) behind the crystal surface by the 800-nm wavelength probe pulses. After propagation in the crystal the homogeneous and inhomogeneous solution separate temporally and spatially. (b) If the MIR pump now depletes $\chi^{(2)}$ up to a depth larger than l_c , no homogeneous solution will be generated. The inhomogeneous solution on the other hand will be generated in the bulk behind the volume of depleted $\chi^{(2)}$ (blue). (c) A cross-correlation measurement of the SH light emitted from an unpumped (blue line) and a pumped (red line) LiNbO₃ crystal, show that indeed the homogeneous solution vanishes when the crystal is pumped with mid-infrared light. The black line is a simulation of the SH process with the software package SNLO [130]. Part of the figure and caption are taken from Ref. [64].

dispersion of the crystal at 2ω . In addition to this predominantly surface sensitive SH signal, a second pulse with wave vector $2k_\omega$ is constantly generated by the fundamental beam (800 nm) as it propagates through the crystal. This second pulse is inhomogeneous solution to the wave equation, and it co-propagates both in time and space with the fundamental pulse. Thus, it shows an apparent group velocity determined by the dispersion at ω . Therefore, the two second harmonic pulses will separate, both spatially and temporally, when propagating through the crystal [100]. Importantly, the intensity of the inhomogeneous solution is thus not affected by changes in the excited volume close to the surface (see Fig. 2.4 (b)). The two pulses can be detected by cross-correlating the total second harmonic radiation emitted from the 5 mm thick LiNbO₃ crystal, with a synchronized time delayed 800-nm pulse in a β -BBO crystal. Figure 2.4 (c) shows intensity of the sum frequency generation of this process together with a simulation

using the SNLO software package (black curve) [130]. The two solutions are separated in time by 10.5 ps, in good agreement with the simulations. The difference intensities of the homogeneous and inhomogeneous solutions are due to the slightly different propagation direction of the two beams leading to a spatial separation on the detection crystal. The red curve in Figure 2.4 (c) shows the cross correlation at the maximum of the SH intensity depletion of the experiments presented in Chapter 2. While the inhomogeneous solution is unaffected by the MIR pump pulses, due to the limited MIR penetration depth, the homogeneous solution vanishes due to a complete suppression of the optical nonlinearity $\chi^{(2)}$ in the excited volume close to the surface. Hence, changes in the excited surface region can be followed by measuring the SH pulses of the homogeneous solution in transmission through the bulk sample.

B.7 Finite-Differences Time Domain Simulations

The phonon-polariton propagation dynamics in LiNbO₃ have been calculated by solving Maxwell's equations in space and time. To this end we used finite-difference time domain (FDTD) in one spatial dimension [262–264], cartella. FDTD simulations are commonly used to numerically solve Maxwell's equations in space and time. This method approximates the commonly appearing space and time derivatives in Maxwells equations with finite differences as difference quotients,

$$\left. \frac{df(x)}{dx} \right|_{x=x_0} \approx \frac{f\left(x_0 + \frac{\delta}{2}\right) - f\left(x_0 - \frac{\delta}{2}\right)}{\delta} \quad (\text{B.16})$$

Here x is either a spatial or temporal variable and the difference quotient in eq. B.16 becomes exact in the limit of $\delta \rightarrow 0$. The approximation becomes increasingly inaccurate for large δ . Therefore, when dealing with electromagnetic waves, the discretization d has to be done in steps which are small compared to the full temporal periods and wavelengths of the electromagnetic field involved. Additionally, the time discretization has to obey the Courant-Friedrichs-Lewy stability criterion [265] which states that the time steps Δt have to be smaller than the time it takes for a wave packet to propagate from one spatial point in the grid to the next Δz :

$$\Delta t \leq n\Delta zc. \quad (\text{B.17})$$

These conditions can very quickly lead to simulations which are computationally very expensive

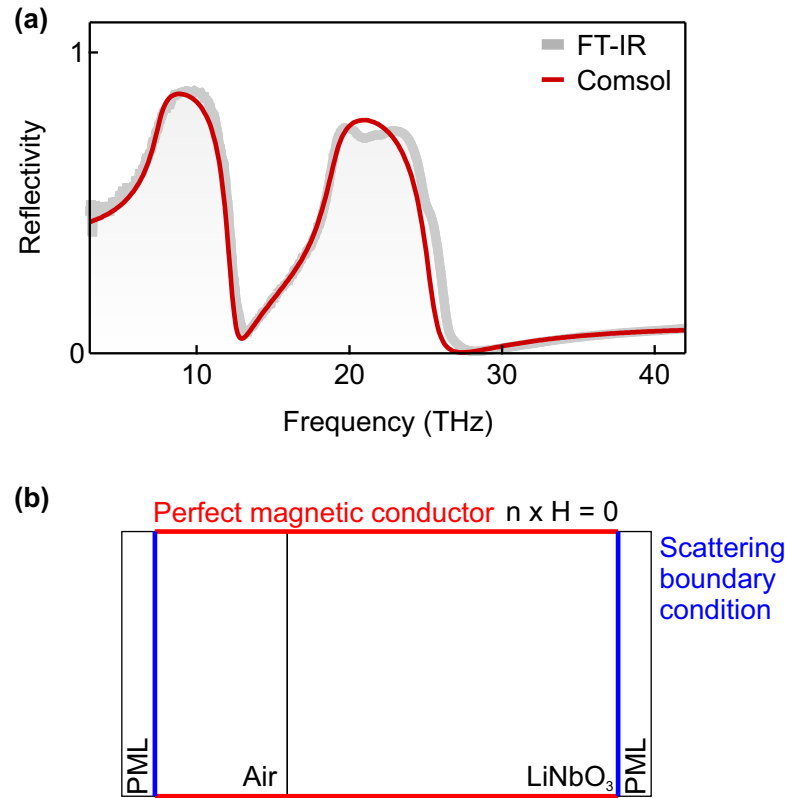


Figure 2.5: Simulated reflectivity. (a) The simulated reflectivity (red), where only the two strongest c-axis optical phonons in LiNbO₃ were considered, still describes the measured c-axis reflectivity (grey) reasonably well. (b) To reduce the computational afford, the simulation were reduced to a single dimension, by introducing perfectly magnetic layer boundary conditions on the x-boundaries (red). The light field was launched via scattering boundary condition on the inlet (left, blue) as a plane wave. A scattering boundary condition together with a perfectly matched layer (PML) were used on the right boundary to impede back reflection into the simulated volume.

and require large RAM when the dimensions of the simulated volume are significantly larger than the wavelength of the electromagnetic wave. The equations calculated in the FDTD simulations are discretized Maxwell's equation. In a one dimensional space, with the electromagnetic waves propagating along the x direction the fields are uniform along y and z , and therefore the partial derivatives $\partial/\partial y$ and $\partial/\partial z$ in the curl operators vanish. This reduces Maxwell's equations to two independent set of equations describing propagating electric E and magnetic field H . This one-dimensional simulation is equivalent to a light field which is incident onto a bulk material and linearly polarized along a major axis the crystal. If the electric field is now considered to be polarized along the z -direction Maxwell's equations simplify to

$$\frac{\partial E_z}{\partial x} = \mu \frac{\partial H_y}{\partial t} \quad (\text{B.18})$$

$$\frac{\partial H_y}{\partial x} = \epsilon \frac{\partial E_z}{\partial t} \quad (\text{B.19})$$

The partial derivatives of eq. B.18 and B.19 are replaced with finite differences as noted in eq. B.16 above. These finite differences will be calculated for every finite grid point and if the fields are known at all grid points at a certain time point, it is possible to use the above equations to one step in the future. This is achieved with a self-consistent loop over the whole grid which updates the fields. This procedure is repeated for every discrete point in time to simulate the whole propagation. This is how the propagation of electromagnetic fields in a linear dielectric medium without resonances on a discrete grid can be calculated. The full practical implementation is very involved and discussed in detail in Ref. [264]. The FTDT simulations in this thesis on the other side were computed using the commercially available software package ComsolTM, which is optimized for large volume simulations.

B.8 Modelling Resonant Phonon Excitation

The above description of FDTD simulations only considers a linear, non-resonant material. However, to model the resonant mid-infrared pump experiments the infrared active phonon modes have to be added to simulation as well. As discussed in Chapter 1 this can be done by considering the auxiliary dielectric displacement field D ,

$$D = \epsilon_0 E + P = \epsilon_0 \epsilon_r(\omega) E \quad (\text{B.20})$$

where P denotes the polarization generated by the motion of the infrared active phonon,

$$P = \omega_{TO} \sqrt{\epsilon_0 - \epsilon_\infty} \sqrt{\epsilon_0 n} Q_{\text{IR}} \quad (\text{B.21})$$

with n the oscillator density, ϵ_0 the vacuum permittivity, Q_{IR} the phonon amplitude and ϵ_0 and ϵ_∞ the low and high frequency limits of the dielectric function, respectively. The prefactor in front of the phonon amplitude Q_{IR} is the effective charge density of the individual phonon an is usually abbreviated with Z^*n . We modeled the linear response of the material using the

Oscillator #	Frequency (cm ⁻¹)	Oscillator strength (cm ⁻¹)	Damping (cm ⁻¹)
1	249.3	922.8	27.7
2	271.6	384.1	20
3	632	955.9	33.5
4	696.7	352.5	76.2
ϵ_∞	4.4054		

Table B.1: Values obtained from a fit of four Lorentzian oscillators to the reflectivity spectrum of our LiNbO₃ sample.

parameters of the two dominant optical phonons obtained from fitting the FT-IR measurement (see Table B.1). For each mode, the equation of motion is given by

$$\ddot{Q}_{\text{IR}} + 2\gamma\dot{Q}_{\text{IR}} + \omega_{\text{IR}}^2 Q_{\text{IR}} = Z_{\text{IR}}^* E \quad (\text{B.22})$$

Here, γ is the damping constant, ω_{IR} the phonon angular frequency and Z_{IR}^* the mode effective charge, which can be expressed as

$$\omega_{\text{IR}} \sqrt{\epsilon_0 - \epsilon_\infty} \sqrt{\frac{\epsilon_0}{n}}. \quad (\text{B.23})$$

The oscillator density n was approximated as one oscillator per unit cell. For each mode, ϵ_0 and ϵ_∞ were derived from the generalized Lydanne-Sachs-Teller relation [266]. The above equation was solved at every discrete point of the grid in space and time using the values of the electric field calculated from Maxwell's equation. Fig. 2.5 (a) shows that by only considering the two strongest phonons the linear optical properties of LiNbO₃ can be largely reproduced in the spectral range interesting for the SHG experiment. Nonlinear phonon dynamics were introduced by considering the anharmonic lattice potential of the driven A₁ mode into the above equation of motion:

$$\ddot{Q}_{\text{IR}} + 2\gamma\dot{Q}_{\text{IR}} + \omega_{\text{IR}}^2 Q_{\text{IR}} + a_3 Q_{\text{IR}}^2 + a_4 Q_{\text{IR}}^3 + a_5 Q_{\text{IR}}^4 = Z_{\text{IR}}^* E \quad (\text{B.24})$$

The anharmonic coefficients a_3 , a_4 and a_5 are taken from ab-initio Density Functional Theory calculations as described below ($a_3 = 1567.65 \text{ meV amu}^{-3/2} \text{ \AA}^{-3}$, $a_4 = 900.8 \text{ meV amu}^{-2} \text{ \AA}^{-4}$, $a_5 = 7.1 \text{ meV amu}^{-5/2} \text{ \AA}^{-5}$). In the simulations the mid-infrared pump pulse was set to a peak field strength of 30 MV/cm, carrier frequency 17.5 THz and 180 fs duration, comparable to the experiment. We evaluated the equations in time steps of 0.5 fs and with a spatial grid of 0.5 μm . Perfectly matched boundary conditions were implemented to impede back reflection. Fig. 2.5

(b) shows the implementation in the software package ComsolTM, and the boundary conditions used at the limits of the simulated volume.

B.9 Interference Signal LiNbO₃

To determine the sign of the polarization, the phase of the emitted SH electric field from the sample was interfered with the SH light generated in a second LiNbO₃ crystal at all time delays. A sketch of the experimental geometry is shown in Figure 2.17. The beams were overlapped on the screen of a CCD-camera which visualized the interference pattern. The intensity of the interference fringe at time delay Δt between pump and probe pulses is given by

$$I_{\text{total,SH}}(\varphi(\Delta t)) = |E_{\text{SH}}(\Delta t)|^2 + |E_{\text{SH,ref}}|^2 + 2 |E_{\text{SH,ref}}| |E_{\text{SH}}(\Delta t)| \cos(\varphi(\Delta t) - \varphi_{\text{ref}}), \quad (\text{B.25})$$

where $E_{\text{SH,ref}}$ denotes the amplitude of the SH electric field from the reference LiNbO₃ crystal and $E_{\text{SH}}(\Delta t)e^{i\varphi(\Delta t)}$ the time-delay dependent amplitude and phase of the SH field from the sample. The interference pattern can be extracted by subtracting the contribution from the terms $|E_{\text{SH}}(\Delta t)|^2 + |E_{\text{SH,ref}}|^2$, which appear as a Gaussian background along the x and y direction of the CCD. A sine-fit to the residual yields $\varphi(t)$ as shown in Figure 2.6.

B.10 DFT Calculations LiNbO₃

The DFT calculations used in this thesis are based on the approach presented in the supplementary information of Ref. [65] and were carried out by Michael Fechner, one of the authors of that study. The following summary of these calculations are adapted from the supplementary information from Ref. [65]. The first-principle computations to determine the full anharmonic lattice potential of LiNbO₃ were carried out within the framework of density functional theory (DFT). All our computations were carried out using DFT as implemented in the Quantum Espresso code³⁶. We used ultrasoft pseudopotentials, which contain as valence states the 2p 2s for Lithium, 4s²4p⁶4d⁴5s¹ for Niobium and 2s²2p⁴ for Oxygen. As numerical parameters, we applied a cut-off energy for the plane wave expansion of 80 Rydberg and five times this value for the charge density. For all computations, we sampled the Brillouin zone by a 17 x 17 x 17 k-point mesh generated with the Monkhorst and Pack scheme [267] and reiterated total energy

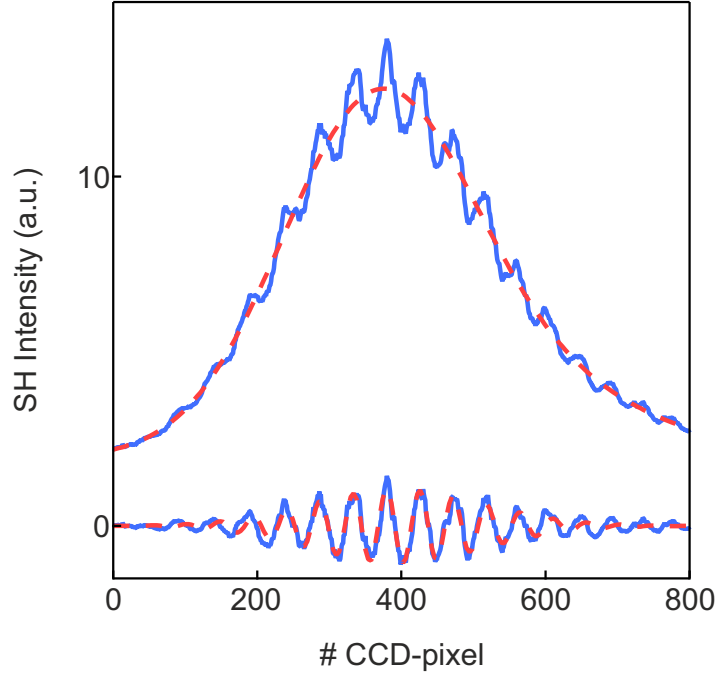


Figure 2.6: SH interference pattern. (a) The interference of the SH beam from the excited LiNbO₃ with a reference beam on a CCD camera leads to interference fringes on top of a gaussian background (dashed red line). (b) Subtraction of this background reveals the interference pattern which can be fitted by sine-function convolved with an envelope (dashed red line).

calculations until the total energy became less than 10-10 Rydberg. Before calculating phonon-modes we fully structural relaxed the unit-cell regarding forces and pressure below the threshold of $5 \mu\text{Ry}/a_0$. We finally performed density functional perturbation theory [268] calculations to obtain phonon modes eigenvectors and frequencies. Finally, the anharmonic phonon potential was computed by calculating the total energy for structures, which have been modulated with the phonon eigenvector. Least mean square fits of this total energy landscape reveal the anharmonic coefficients of Chapter 2 and the phonon mode eigenvector as shown in Figure 2.10.

Appendix C

Time-resolved SH experiments on $\text{YBa}_2\text{Cu}_3\text{O}_{6+\delta}$

C.1 Signal Dissection of the Time-Resolved SH Signal from $\text{YBa}_2\text{Cu}_3\text{O}_{6+\delta}$

The measured time-resolved second harmonic intensity $\Delta I_{\text{SH}}(t)$ (see for example Fig. 4.5 of the Chapter 4) was fitted by the product of (i) a Gaussian envelope to map the nonlinear optical mixing of pump and probe electric fields at time delay zero (electric field induced second harmonic generation, EFISH) and (ii) a step function of finite width, multiplied by a decaying exponential, i.e. $A(\tau) = A(1 + \text{erf}((\tau - \tau_0)/\sigma))\exp(-\gamma(\tau - \tau_0))$, to describe the exponentially decaying background signal. Subtraction of this slowly varying background revealed the coherent oscillations shown in Figures 4.6 of the Chapter 4 for different excitation strengths. The oscillatory signals can be divided into sets of three exponentially decaying oscillators: the driven polar phonons Q_{drive} , the amplified phonons $Q_{\text{amplified}}$, and the nonlinearly coupled Josephson Plasmon Polaritons J_1 and J_2 (see Fig. 3.1). These were fitted as $A(\tau) = A(1 + \text{erf}((\tau - \tau_0)/\sigma))\exp(-\gamma(\tau - \tau_0))\sin(2\pi\Omega\tau + \phi_0)$. For the phonons, their frequencies Ω_{phonon} were constrained to values measured by linear infrared spectroscopy [204].

C.2 Momentum-Resolved Detection of the Josephson Plasmon Polariton

In the SH measurement, the 400-nm wavelength light is generated in a thin layer l of about 100 nm below the sample surface. The finite in-plane momentum q_y of the amplified Josephson

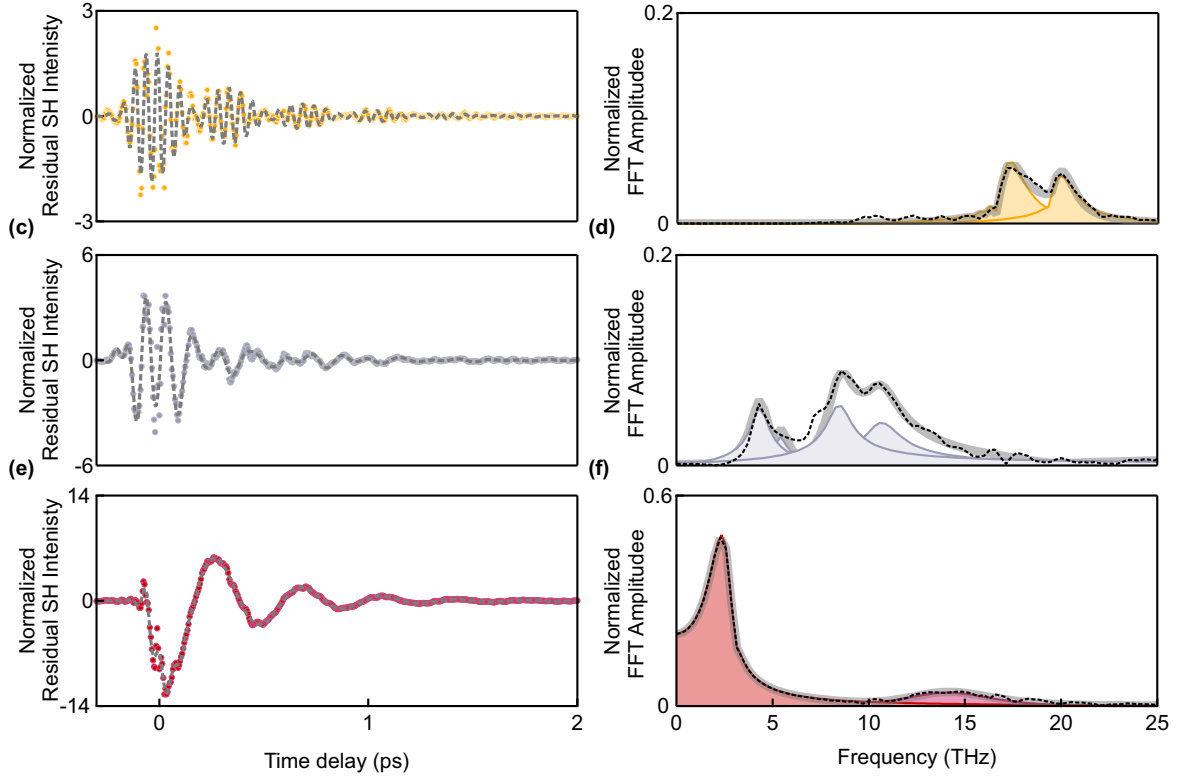


Figure 3.1: Dissection of the coherent SH oscillations. (a) The dissection of the coherent oscillations of the SH signal is done by a comprehensive time-domain fit, exemplary on the data set from $\text{YBa}_2\text{Cu}_3\text{O}_{6.48}$ for 7 MV/cm excitation at 5 K. The contributions from known infrared vibrations were constrained by their equilibrium frequency. By doing so, the contributions from the driven apical oxygen vibrations (yellow, in panel (a) and (b)), the amplified phonons (grey, in panel (c) and (d)) could be separated from the coherent signal of the Josephson plasma oscillations (red, in panel (e) and (f)).

Plasmon Polariton leads to a deflection of the second harmonic light with respect to the specular reflection. The spatial distribution of the emitted radiation was determined by taking second harmonic intensity measurements $\Delta I_{\text{SH}(t)}$ at different positions of a 200- μm slit, which was scanned across the re-collimated reflected beam. The amplitudes of the frequency-filtered 2.5-THz JPP and the amplified phonon contributions are plotted as a function of the slit position in Figure 3.2 (c), together with the EFISH amplitude at time zero shown in Figure 3.2 (a). The momentum transfer was calculated from the deflection angle $\Delta\theta$ by

$$q_y = \sqrt{\epsilon_\infty} \tan(\Delta\theta) k_{400}, \quad (\text{C.1})$$

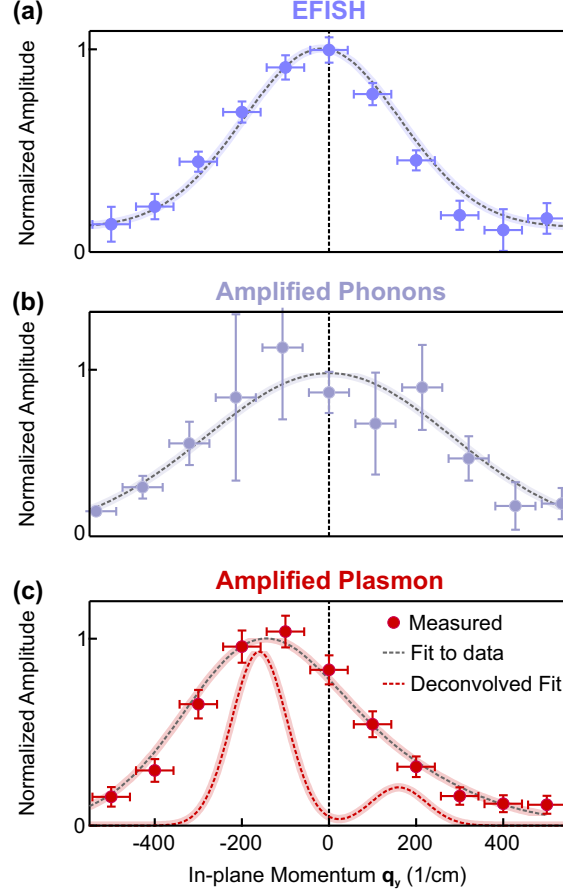


Figure 3.2: Deconvolution of the spatial-resolved measurements. (a) In-plane momentum distribution of the EFISH-component, (b) amplitude of the amplified phonon oscillations and (c) coherent Josephson Plasmon Polariton oscillations, as measured in the experiment sketched in Figure 4.11 (a) of the main text. Data points are shown as blue, grey and red symbols. The Gaussian fit to the EFISH data, shown as a dashed grey line in a, reveals the divergence of the second harmonic beam. In panel (c), the fit to the raw data and of the Josephson Plasmon Polariton amplitude and its $\omega_{IR} = \omega_{J1}(q_{plas}) + \omega_{J2}(-q_{plas})$ deconvolution are plotted as dashed grey and red lines, respectively. Error bars represent the standard deviation σ of the amplitudes extracted by numerical fits. Horizontal error bars represent the standard deviation σ due to the finite width of the measurement slit.

where k_{400} is the vacuum wavenumber of the 400-nm light. While both the EFISH and amplified phonon contributions are symmetric and peak at zero in-plane momentum transfer q_y , the plasmon response is asymmetric and peaks at a finite momentum $q_y = 190 \text{ cm}^{-1}$.

The momentum distribution of the Josephson Plasmon Polariton, shown in Figure 4.11 (c) of the main text, was then obtained by deconvolving the measured JPP profile (see Fig. 3.2 (c)) from the divergence of the probe beam. To this end, consistent with our theoretical model, two

constrained Gaussian profiles, with equal but opposite abscissa offsets and same widths, were fitted to the data. The best fit was deconvolved with the Gaussian profile of the undeflected second harmonic beam, which is accessible from the momentum dependent EFISH signal due to the collinearity between the incident mid-IR excitation and 800-nm probe beams in these measurements. The error-bars of the deconvoluted data points are determined by the deviation of the least squares fit to the data points. Note that while the deconvolution result is not unique, the 190 cm^{-1} momentum shift is already clearly visible in the raw data (Figure S8c).

C.3 SH-Polarimetry Measurements for p-Analyzer

The results of the SH polarimetry measurements with the analyzer oriented along the $\text{YBa}_2\text{Cu}_3\text{O}_{6.48}$ c axis (s-analyzer) are shown in Figure 4.9 of the main text. The measurements taken with the analyzer oriented along the b axis (p-analyzer, see the optical setup in Figure S7a) are discussed here. Figure 3.3 (b) shows the corresponding measurement as a function of incoming 800-nm polarization angle φ and pump probe time delay. The frequency-filtered SH polarimetry signals for one representative time delay ($t = 500\text{ fs}$) are shown in Figures 3.3 (c),(d),(e). Again, the directly driven phonons (yellow) and the amplified phonons (grey) can be fitted by the χ^2 tensor of the $mm2$ point group (dashed lines), as expected for the B_{1u} -symmetry lattice distortions. Also, the sign of the phonon amplitudes at this delay, and hence their phases, are independent of the polarization angle φ . In contrast, the φ angular dependence of the 2.5-THz Josephson plasmon mode, shown in Figure 3.3 (e), requires a fit by the χ^2 tensor of a lower-symmetry point group (m or lower). In addition, the amplitude of this mode changes sign as a function of incoming polarization angle φ . Both results agree with the symmetry analysis presented in the main text for the s-analyzer configuration.

C.4 Excitation Frequency Dependence of the Josephson Plasmon Amplification

Our theory predicts the amplification of the Josephson Plasmon Polariton by three-wave mixing with the c-axis apical oxygen phonon mode. Hence, we expect the amplification to be enhanced when the mid-infrared excitation pulses are frequency-tuned into resonance with this phonon,

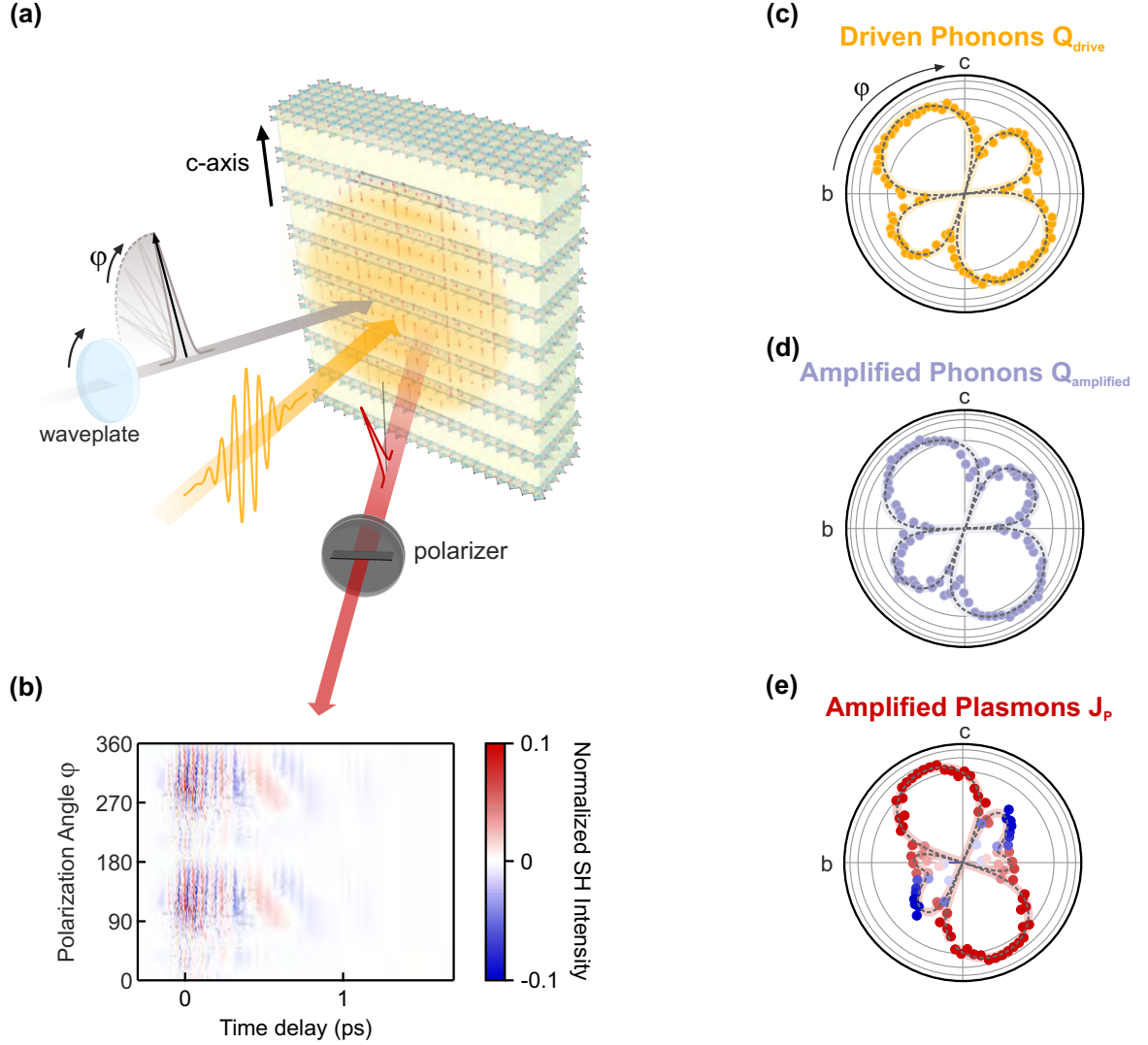


Figure 3.3: Time-resolved SH polarimetry for p-analyzer. (c), (d) and (e), Normalized polarimetry signal of the driven phonons (yellow dots), amplified phonons (grey dots) and amplified Josephson Plasmon Polariton (red and blue dots) for an analyzer oriented along the crystal b-axis, at one time-delay $t = 500$ fs. The polarimetry signal of the two sets of phonons can be reproduced by a fit to a $mm2$ point group symmetry (dashed line) and the phase of the oscillations is polarization angle φ independent. The polarimetry signal of the amplified Josephson plasmon agrees with a fit to point group m (dashed line). The phase of the polarimetry signal is indicated by the red and blue color-coding.

where the latter is driven to largest amplitudes.

We tested this prediction by recording the amplitude of the 2.5 THz mode in $YBa_2Cu_3O_{6.48}$ for different center frequencies of the mid-infrared pulses, keeping the peak electric field constant at ~ 7 MV/cm. In Figure 3.4, we plot this dependence together with the real part of the

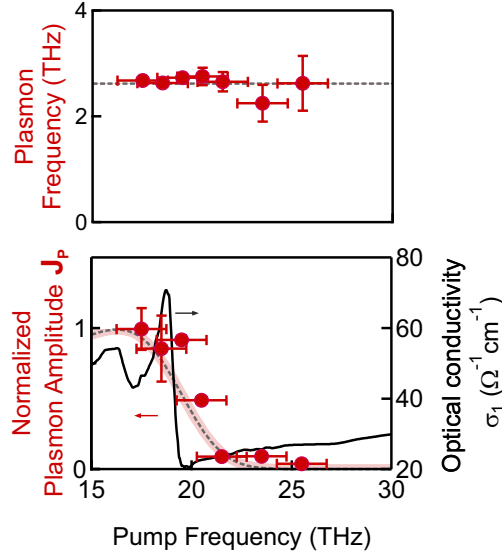


Figure 3.4: Excitation frequency dependence of the Josephson plasma mode.

Amplitude and frequency of the low-frequency Josephson Plasmon Polariton in $\text{YBa}_2\text{Cu}_3\text{O}_{6.48}$ at different mid-infrared frequencies, shown as red points, for a fixed peak electric field of $\sim 7 \text{ MV/cm}$. The amplitude increases towards the resonance of the apical oxygen infrared vibration. The real part of the optical conductivity is drawn as solid black line, and as a dashed line when convolved with the bandwidth of the excitation pulses. Error bars represent the standard deviation σ of the JPP amplitudes extracted by numerical fits. Horizontal error bars represent the standard deviation σ of the center wavelength determined by electro-optic sampling.

optical conductivity. Clearly, the Josephson Plasmon Polariton amplitude increases when the mid-infrared pulses are tuned into the phonon resonance, supporting the proposed three-wave phonon-plasmon mixing.

Furthermore, Figure 3.4 shows that the frequency of the amplified Josephson Plasmon Polariton does not change as function of the mid-infrared center frequency. Given the JPP dispersion, this implies that in the three-wave mixing process, with resonance condition $\omega_{\text{IR}} = \omega_{\text{J1}}(q_{\text{plas}}) + \omega_{\text{J2}}(-q_{\text{plas}})$, the frequency ω_{IR} always takes the same value. Hence, this has to be the eigenfrequency ω_{drive} of the phonon and not the tunable frequency of the excitation pulses. Together, these two observations show that the amplified JPP amplitude scales with the resonant enhancement of the driven apical oxygen phonon amplitude Q_{drive} and exclude a scenario, where the incident light field couples directly to the Josephson Plasmon Polariton.

C.5 Theoretical Analysis of the Josephson Plasmons and Plasmon-Phonon coupling

C.5.1 Analysis of the Collective Modes

The plasmon dispersion in a layered superconductor can be obtained by combining linearized dynamical equations for superflow currents and charges with Maxwell equations for electromagnetic fields [198, 202, 269–272]. The fundamental degrees of freedom are density fluctuations of the condensate $\delta\rho_{\lambda,i}(\vec{x})$, the phase of the superconducting order parameter $\phi_{\lambda,i}(\vec{x})$, and the 4-component vector potential $(V_{\lambda,i}(\vec{x}), A_{\lambda,i,z}(\vec{x}), \vec{A}_{\lambda,i,\vec{x}}(\vec{x}))$. Here i corresponds to the index of the unit cell along the c -axis, $\lambda = 1, 2$ labels the number of the layer inside the unit cell, and \vec{x} is the in-plane coordinate, which we will omit in the equations below for brevity. While the in-plane components of the vector potential $\vec{A}_{\lambda,i,\vec{x}}(\vec{x})$ are defined within the corresponding layers, $A_{\lambda,i,z}(\vec{x})$ is defined to be on the links between layers starting on layer λ, i as shown in Fig. 3.5. In linearized hydrodynamics, superflow currents are given by

$$j_{\lambda,i,\vec{x}} = \Lambda_s (\partial_{\vec{x}}\phi_{\lambda,i} - e^* A_{\lambda,i,\vec{x}}), \quad (\text{C.2})$$

$$j_{\lambda,i,z} = j_{c\lambda} (\Delta_z\phi_{\lambda,i} - e^* A_{\lambda,i,z}). \quad (\text{C.3})$$

Here \vec{x} denotes the in-plane x, y components and z denotes the c -axis coordinate of the crystal. Coupling to the vector potential is given by the Cooper pair charge, $e^* = 2e$, and we work in units where $\hbar = 1$ for the rest of this section. The in-plane components of the superfluid current are defined within individual layers and have continuous gradients. The z component of the current is defined as the Josephson current between adjacent layers and has a lattice gradient which corresponds to the phase difference between adjacent layers,

$$\Delta_z\phi_{\lambda,i} = \begin{cases} (\phi_{2,i} - \phi_{1,i})/d_1, & \text{for } \lambda = 1, \\ (\phi_{1,i+1} - \phi_{2,i})/d_2, & \text{for } \lambda = 2 \end{cases} \quad (\text{C.4})$$

The coefficient Λ_s is related to the in-plane London penetration length as $\Lambda_s = \frac{\epsilon c^2}{\lambda_L^2 (e^*)^2}$, where $\epsilon = \epsilon_r \epsilon_0$. Physically, it corresponds to the intra-layer superfluid stiffness and is proportional to

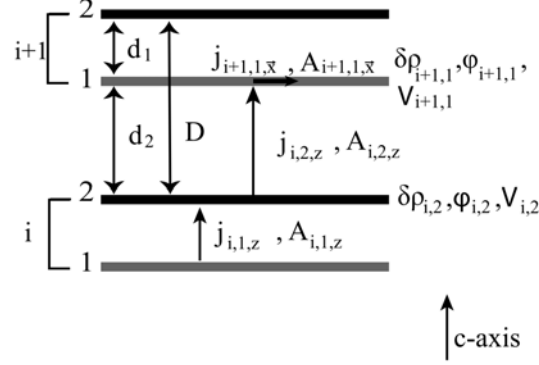


Figure 3.5: Schematic drawing of a bilayer superconductor. Variables $\delta\rho_{i,\lambda}$, $\phi_{i,\lambda}$, $j_{i,\lambda,\vec{x}}$, and $A_{i,\lambda,\vec{x}}$ are defined within layer λ in unit cell i and describe condensate density fluctuations, phase of the order parameter, parallel component of the superfluid current, electrostatic potential, and in-plane vector potential respectively. Variables $j_{i,\lambda,z}$, and $A_{i,\lambda,z}$ are defined between the layers and correspond to interlayer Josephson current and out of plane component of the vector potential, respectively. Part of the figure and caption are taken from [220].

the condensate density, $\Lambda_{s\lambda} \propto \rho_\lambda$. In linear analysis of the collective modes we can set $\Lambda_{s\lambda}$ to be equal to their equilibrium values since they multiply superfluid velocities, $\vec{v}_{\lambda,i} = \partial_{\vec{x}}\phi_{\lambda,i} - e^*A_{\lambda,i,\vec{x}}$, which are already first order in fluctuations. This is why we omitted the layer index for Λ_s in equation (1). Coefficients $j_{c,\lambda}$ correspond to interlayer Josephson tunneling couplings and obey $j_{c,\lambda} \propto \sqrt{\rho_1\rho_2}$. In linearized hydrodynamics we take $j_{c,\lambda}$ to be equal to their equilibrium value and neglect corrections due to $\delta\rho_\lambda$. Both ρ_λ and $j_{c,\lambda}$ can be modified by exciting apical oxygen phonons, which results in phonon-plasmon coupling that will be discussed below. We introduce an effective Hamiltonian that describes plasmon degrees of freedom and show that its equations of motion give the correct equations for light and matter fields.

$$H = H_{pot.} + H_{kin.} + H_{EM}. \quad (\text{C.5})$$

The first term in eq. C.5 describes the finite compressibility of Cooper pairs and their coupling to electrostatic potential

$$H_{pot.} = \int d^2x \sum_{i,\lambda} \left\{ \frac{\gamma}{2} \delta\rho_{\lambda,i}^2 + e^* \delta\rho_{\lambda,i} V_{\lambda,i} \right\}. \quad (\text{C.6})$$

Compressibility γ can be related to the Thomas-Fermi length, λ_{TF} , as $\gamma = \frac{\lambda_{\text{TF}}^2 (e^*)^2}{\epsilon}$. The

superflow kinetic energy is given by

$$H_{\text{kin.}} = \int d^2x \sum_{i,\lambda} \left\{ \frac{1}{2\Lambda_s} j_{\lambda,i,\vec{x}}^2 + \frac{1}{2j_{c,\lambda}} j_{\lambda,i,z}^2 \right\}. \quad (\text{C.7})$$

For electromagnetic fields we adopt the Lorenz gauge condition

$$\frac{1}{c^2} \partial_t V_{\lambda,i} + \partial_{\vec{x}} A_{\lambda,i,\vec{x}} + \Delta_z A_{\lambda,i,z} = 0 \quad (\text{C.8})$$

then the Hamiltonian for electromagnetic fields is given by

$$\begin{aligned} H_{EM} = \int d^2x \left\{ \sum_{i,\lambda} \frac{c^2}{2\epsilon} P_{V,\lambda,i}^2 + \frac{\epsilon}{2} \left((\partial_{\vec{x}} V_{\lambda,i})^2 + (\Delta_z V_{\lambda,i})^2 \right) \right. \\ \left. + \frac{1}{2\epsilon} P_{A_{\vec{x},\lambda,i}}^2 + \frac{\epsilon c^2}{2} \left((\partial_{\vec{x}} A_{\lambda,i,\vec{x}})^2 + (\Delta_z A_{\lambda,i,\vec{x}})^2 \right) \right. \\ \left. + \frac{1}{2\epsilon} P_{A_{z,\lambda,i}}^2 + \frac{\epsilon c^2}{2} \left((\partial_{\vec{x}} A_{\lambda,i,z})^2 + (\Delta_z A_{\lambda,i,z})^2 \right) \right\} \end{aligned} \quad (\text{C.9})$$

Variables $P_{V,\lambda,i}, P_{A_{\vec{x},\lambda,i}}, P_{A_{z,\lambda,i}}$ correspond to the conjugate momenta of the scalar and vector potentials, and magnetic permeability $\mu = \mu_r \mu_0$ is included in the speed of light $c^2 = 1/\mu\epsilon$. In eq. C.9 gradients in the z direction are taken in the lattice form so, for example,

$$\Delta_z A_{\lambda,i,z} = \begin{cases} \frac{A_{1,i,z}}{d_1} - \frac{A_{2,i-1,z}}{d_2}, & \text{for } \lambda = 1, \\ \frac{A_{2,i,z}}{d_2} - \frac{A_{1,i,z}}{d_1}, & \text{for } \lambda = 2 \end{cases} \quad (\text{C.10})$$

We use Heisenberg equations of motion (EOM) for the operators, $\partial_t \hat{O} = i[H, \hat{O}]$, to study dynamics of the fields. In deriving equations of motion we use canonical commutation relations between ρ and ϕ , V and P_V , \vec{A} and $P_{\vec{A}}$, i.e. $[\rho_i(\vec{x}), \phi_j(\vec{x}')] = i\delta^2(\vec{x} - \vec{x}')\delta_{i,j}$, etc. EOM for the density and phase operators give the continuity equation and Josephson relation

$$\partial_t \delta \rho_{\lambda,i} + \partial_{\vec{x}} j_{\lambda,i,\vec{x}} + \Delta_z j_{\lambda,i,z} = 0 \quad (\text{C.11})$$

$$\partial_t \phi_{\lambda,i} = -\gamma \delta \rho_{\lambda,i} - e^* V_{\lambda,i}. \quad (\text{C.12})$$

By combining EOM for the electromagnetic fields ϕ, \vec{A} and their conjugate momenta we obtain

Maxwell's equations:

$$\begin{aligned}
 \left(\frac{1}{c^2}\partial_t^2 - \partial_{\vec{x}}^2 - \Delta_z^2\right) V_{\lambda,i} &= \frac{e^*}{\epsilon} \delta\rho_{\lambda,i}, \\
 \left(\frac{1}{c^2}\partial_t^2 - \partial_{\vec{x}}^2 - \Delta_z^2\right) A_{\lambda,i,\vec{x}} &= \frac{1}{c^2} \frac{e^*}{\epsilon} j_{\lambda,i,\vec{x}}, \\
 \left(\frac{1}{c^2}\partial_t^2 - \partial_{\vec{x}}^2 - \Delta_z^2\right) A_{\lambda,i,z} &= \frac{1}{c^2} \frac{e^*}{\epsilon} j_{\lambda,i,z}
 \end{aligned} \tag{C.13}$$

To find collective modes we look for the solutions of equations C.11, C.12, C.13 in the form of plane waves, $\delta\rho_{\lambda,l}(x, t) = \delta\rho_{\lambda}(q_{\vec{x}}, q_z, \omega) e^{i(q_x x + q_y y + q_z D l - \omega t)}$, with similar expressions for other variables. It is convenient not to combine EOM for electromagnetic fields and their conjugate variables, so that we have first order linear differential equations of the form $\partial_t \vec{v} = \underline{\mathbf{M}} \vec{v}$. Matrix $\underline{\mathbf{M}}$ contains gradient operators which leads to implicit dependence on momentum \vec{q} . We define the characteristic polynomial for $\underline{\mathbf{M}}$ as $\chi(\omega) = \det[i\omega + \underline{\mathbf{M}}]$. Due to the Lorenz gauge used in our analysis the characteristic polynomial contains non-physical degrees of freedom. However, gauge constraint C.8 guarantees that they do not couple to matter fields and the characteristic polynomial factorizes into physical and non-physical contributions, $\chi(\omega) = \chi_{phys}(\omega) \chi_{unphys}(\omega)$. Collective modes of the system can be found by solving the secular equation $\chi_{phys}(\omega) = 0$. The two lowest energy modes correspond to the Josephson plasmons and their dispersion is shown in Fig 3.6. To express physical quantities in terms of the amplitudes of the plasmon modes we can use eigenvectors $v_{1,2,q}^l$ of the secular equation, where components l correspond to $\delta\rho_{\lambda}$, ϕ_{λ} , V , \vec{A} , etc. Shown in a matrix form:

$$\begin{pmatrix} \rho_{\lambda}(q) \\ \vdots \\ \phi_{\lambda}(q) \\ \vdots \end{pmatrix} = \begin{pmatrix} v_{1,q}^{\delta\rho_{\lambda}} & \dots & (v_{1,q}^{\delta\rho_{\lambda}})^* & \dots \\ \vdots & & \vdots & \\ v_{1,q}^{\phi_{\lambda}} & & (v_{1,q}^{\phi_{\lambda}})^* & \\ \vdots & & \vdots & \end{pmatrix} \cdot \begin{pmatrix} b_1 \\ \vdots \\ b_1^* \\ \vdots \end{pmatrix} \tag{C.14}$$

where b_1 and b_2 are amplitudes of the two plasmon modes oscillating at frequencies corresponding to their dispersion relations. The eigenvectors, $v_{1,2,q}^l$, are defined through the EOM up to a normalization constant. Normalization is fixed through the commutation relations of canonically conjugate pairs, such as $[\rho_{\lambda}(q), \phi_{\lambda'}(q')] = i\delta_{q,q'}\delta_{\lambda,\lambda'}$ and commutation relations of the plasmon fields, which should correspond to bosonic creation/annihilation operators $[b_i, b_j^{\dagger}] = \delta_{i,j}$.

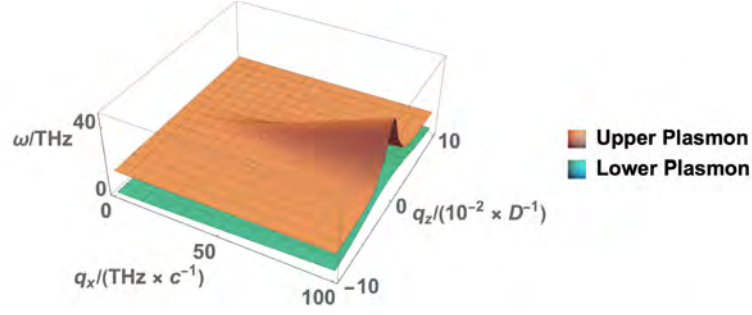


Figure 3.6: Dispersion relation of the Josephson plasma modes. Dispersion relation of the Josephson plasma modes two lowest energy modes of equations C.11-C.13 in the $\{q_x, q_z\}$ -plane. At $q_z = 0$, the upper plasmon is strongly hybridized with the original photon mode. This results in the energy of the mode increasing rapidly along the q_x axis with the slope approaching the speed of light. Away from $q_z = 0$ strong mixing with the photon is absent and the frequency of the mode decreases with increasing q_x . Part of the figure and caption are taken from Ref. [220].

C.5.2 Phonon-Plasmon Interaction

The apical oxygen phonon is expected to modify the in-plane superfluid stiffness either by changing the in-plane density of carriers or by modifying their hopping. Symmetry of this mode requires that these changes are antisymmetric with respect to the two layers inside one unit cell, so that $\delta\Lambda_{s,1,2}^{phon}(t) = \pm\xi Q_{IR}(t)\Lambda_s$, where coefficient ξ characterizes the coupling strength. Changes of the interlayer Josephson currents arise from changes in the superfluid density $\delta\rho_{1,2}^{phon} = \pm\tilde{\xi}Q_{IR}(t)\rho$, which results in $\delta j_{c,\lambda}(t) = -\left(\tilde{\xi}Q_{IR}\right)^2 \frac{j_{c,\lambda}}{2\rho}$. The last equation shows that interlayer Josephson currents couple quadratically to the apical oxygen phonon and lead to four-wave phonon/plasmon mixing. Resonant three wave mixing considered in the main text comes from phonons modifying $\Lambda_{s,1,2}$ and coupling to the in-plane current. To derive plasmon dynamics in the presence of an excited phonon mode we need to modify equation C.7 to include $\delta\Lambda_{s\lambda}^{phon}$ arising due to phonons. We find

$$\delta H_{\text{kin.}} = -\xi \sum_i \int d^2x \left\{ \frac{Q_{IR}(t)}{2\Lambda_s} (j_{1,i,\vec{x}}^2 - j_{2,i,\vec{x}}^2) \right\} \quad (\text{C.15})$$

The phonon mode causes a zero momentum three wave parametric process that excites pairs of plasmons at opposite momenta. Resonant processes that satisfy energy matching condition $\omega_{\text{ph}} = \omega_1(q) + \omega_2(-q)$ lead to exponential instability discussed in the main text. After projecting

the modified EOM to the two the lowest eigenmodes we find equations for parametrically coupled oscillators

$$\partial_t^2 J_1(q) + 2\gamma_1 \partial_t J_1(q) + \omega_1^2(\vec{q}) J_1(q) = -q_x^2 f(\vec{q}) Q_{\text{IR}}(t) J_2(q), \quad (\text{C.16})$$

$$\partial_t^2 J_2(q) + 2\gamma_2 \partial_t J_2(q) + \omega_2^2(\vec{q}) J_2(q) = -q_x^2 f(\vec{q}) Q_{\text{IR}}(t) J_1(q) \quad (\text{C.17})$$

In writing equations C.16 and C.17 we added phenomenological damping constants γ_i to describe dissipation due to quasiparticles. Factors of q_x^2 in equations C.16 and C.17 originate from the fact that phonons couple to plasmons through the in-plane superflow kinetic energy. There is also an implicit weaker q dependence in $f(\vec{q})$ arising from projecting the interaction to the plasmon subspace, which can be derived using the $v_{1,2,q}^{j,\vec{x}}$ components of the eigenvectors of the secular equation. We also note that inversion symmetry forbids three-mode coupling between the phonon and Josephson plasmons in the same band. The equation of motion for the polar phonon reads

$$\ddot{Q}_{\text{IR}} + 2\gamma_{\text{IR}} \dot{Q}_{\text{IR}} + \omega_{\text{IR}}^2 Q_{\text{IR}} = Z^* E(t) - q_y^2 J_1 J_2, \quad (\text{C.18})$$

where Z^* is the coupling to the optical drive field and γ_{IR} accounts for the finite lifetime of the vibrational mode. We solved the set of coupled equations for the phonon and plasmon dynamics by utilizing a stochastic approach, where we introduced Langevin noise on both, the Josephson plasma and phonon coordinates, to create an incoherent initial state. The final trajectories shown in the manuscript (see Figure 2e) were then computed by solving the equations of motion one million times with an algorithm based on the Euler-Maruyama method. In addition to the harmonic terms that describe the resonant driving of the polar phonon mode, we also considered higher-order (quartic) phonon anharmonicities.

C.6 DFT Calculations $\text{YBa}_2\text{Cu}_3\text{O}_{6.5}$

The DFT calculations used in this thesis are based on the approach presented in Ref. [143] and were carried out by Michael Fechner, one of the authors of that study. The following summary of these calculations are based on Ref. [143] and Ref. [166].

First-principles total energy calculations in the framework of the density functional theory (DFT) were used to compute all harmonic and anharmonic terms included in the nonlinear equations

element	Wykoff position	x	z	element	Wykoff position	X	z
Y	l	0.251	0.500	O1	e	0.000	0.000
Ba	x	0.244	0.187	O2	w	0.250	0.378
Cu1	a	0.000	0.000	O3	r	0.000	0.378
Cu2	b	0.500	0.000	O4	t	0.500	0.378
Cu3	q	0.000	0.356	O5	q	0.000	0.161
Cu4	s	0.500	0.355	O6	s	0.500	0.153

Table C.1: DFT minimized structural configuration of the $\text{YBa}_2\text{Cu}_3\text{O}_{6.5}$ ortho-II cell with $a = 7.55 \text{ \AA}$, $b = 3.81 \text{ \AA}$, and $c = 11.50 \text{ \AA}$. The data was taken from Ref. [143].

mentioned in Chapter 4. Specifically, we used the implementation of DFT, applying the linearized augmented-plane wave method (LAPW) within the ELK-code [273] and the local density approximation to determine the exchange-correlation functional. All relevant numerical parameters entering the computation underwent a careful test. A result was well-converged when the truncation corresponded to $l_{\text{max}} = 10$ of the angular expansion of wave functions and potential within the muffin-tin radii (2.6, 2.8, 1.85 and 1.4 a.u. for Y, Ba, Cu, and O, respectively). A $|G|_{\text{max}} = 20 \text{ a.u.}^{-1}$ limited the potential and density expansion within the interstitial region and $R_{\text{MT}} \times k_{\text{max}} = 8.0$ for truncating the plane-wave wavefunction expansion. The computations were carried out on a $11 \times 19 \times 5$ k-point mesh. This configuration was already previously in Ref. [274] and, within this setting, the forces (most relevant for phonons and anharmonic terms) were made to converge by less than 0.1 meV/\AA . Before computing the coefficients of the anharmonic potential, the unit cell of $\text{YBa}_2\text{Cu}_3\text{O}_{6.5}$ was structurally relaxed, considering the ortho-II structure, following previous studies and the experimental setting [58]. As lowest energy state, we obtained the atomic configuration given in Table C.1. Finally, the phonon eigensystem was computed by frozen-phonon calculation using symmetry-adapted distortions generated with the Phonopy package [275]. All modes at the zone center are listed in Table C.2. To calculate the anharmonic the third order constants the prescription in Ref. [276] was applied together with the approach in Ref. [277] for the quartic order terms. The mode-effective charges were calculated by using the nominal averaged ionic charges of each atom as Born charges. Explicitly, we have for Yttrium 3+, Barium 2+, Copper 2+ and Oxygen 2-.

Label	f (THz)						
A_g	3.1	B_{1u}	7.4	B_{2u}	17.0	B_{3u}	8.1
A_g	3.5	B_{1u}	7.6	B_{2u}	17.4	B_{3u}	8.4
A_g	4.2	B_{1u}	8.8	B_{2g}	1.8	B_{3u}	10.3
A_g	5.1	B_{1u}	10.2	B_{2g}	2.6	B_{3u}	10.5
A_g	6.3	B_{1u}	15.0	B_{2g}	4.1	B_{3u}	11.8
A_g	10.5	B_{1u}	16.5	B_{2g}	4.2	B_{3u}	13.4
A_g	10.9	B_{1u}	20.5	B_{2g}	6.5	B_{3u}	18.3
A_g	12.6	B_{1g}	2.9	B_{2g}	7.4	B_{3g}	2.0
A_g	14.1	B_{1g}	3.8	B_{2g}	8.7	B_{3g}	4.1
A_g	15.3	B_{1g}	9.7	B_{2g}	10.0	B_{3g}	5.4
A_g	18.0	B_{2u}	2.4	B_{2g}	11.3	B_{3g}	6.5
A_u	2.8	B_{2u}	3.6	B_{2g}	11.4	B_{3g}	10.3
A_u	10.8	B_{2u}	4.7	B_{2g}	18.1	B_{3g}	11.1
B_{1u}	2.5	B_{2u}	5.2	B_{3u}	2.5	B_{3g}	16.6
B_{1u}	3.4	B_{2u}	5.6	B_{3u}	2.9	B_{3g}	17.2
B_{1u}	3.9	B_{2u}	8.0	B_{3u}	3.7		
B_{1u}	4.4	B_{2u}	10.3	B_{3u}	3.8		
B_{1u}	5.0	B_{2u}	11.5	B_{3u}	4.7		
B_{1u}	5.6	B_{2u}	16.6	B_{3u}	5.4		

Table C.2: Computed DFT eigenfrequencies of the phonon modes at the center of the Brillouin zone for the $\text{YBa}_2\text{Cu}_3\text{O}_{6.5}$ ortho-II structure. The data was taken from Ref. [143].

Bibliography

- [1] E. Morosan, D. Natelson, A. H. Nevidomskyy and Q. Si. Strongly Correlated Materials. *Advanced Materials* **24**(36), 4896–4923 (2012).
- [2] P. Lacorre, J. Torrance, J. Pannetier, A. Nazzal, P. Wang and T. Huang. Synthesis, crystal structure, and properties of metallic PrNiO₃: Comparison with metallic NdNiO₃ and semiconducting SmNiO₃. *Journal of Solid State Chemistry* **91**(2), 225–237 (1991).
- [3] J. Torrance, P. Lacorre, A. Nazzal, E. Ansaldo and C. Niedermayer. Systematic study of insulator-metal transitions in perovskites RNiO₃ (R = Pr, Nd, Sm, Eu) due to closing of charge-transfer gap. *Physical Review B* **45**(14), 8209–8212 (1992).
- [4] J. V. Santen and G. Jonker. Electrical conductivity of ferromagnetic compounds of manganese with perovskite structure. *Physica* **16**(7-8), 599–600 (1950).
- [5] J. Volger. Further experimental investigations on some ferromagnetic oxidic compounds of manganese with perovskite structure. *Physica* **20**(1-6), 49–66 (1954).
- [6] J. G. Bednorz and K. A. Möller. Possible high T_c superconductivity in the Ba-La-Cu-O system. *Zeitschrift für Physik B Condensed Matter* **64**(2), 189–193 (1986).
- [7] J. G. Bednorz, K. A. Müller and M. Takashige. Superconductivity in Alkaline Earth-Substituted La₂CuO_{4-y}. *Science* **236**(4797), 73–75 (1987).
- [8] A. Cavalleri, C. Tóth, C. W. Siders, J. A. Squier, F. Ráksi, P. Forget and J. C. Kieffer. Femtosecond Structural Dynamics in VO₂ during an Ultrafast Solid-Solid Phase Transition. *Physical Review Letters* **87**(23) (2001).
- [9] D. N. Basov, R. D. Averitt, D. van der Marel, M. Dressel and K. Haule. Electrodynamics of correlated electron materials. *Reviews of Modern Physics* **83**(2), 471–541 (2011).

Bibliography

- [10] J. Jeong, N. Aetukuri, T. Graf, T. D. Schladt, M. G. Samant and S. S. P. Parkin. Suppression of Metal-Insulator Transition in VO₂ by Electric Field-Induced Oxygen Vacancy Formation. *Science* **339**(6126), 1402–1405 (2013).
- [11] E. Dagotto. Complexity in Strongly Correlated Electronic Systems. *Science* **309**(5732), 257–262 (2005).
- [12] S. N. Mott. Metal–insulator transitions. *Physics Today* **31**(11), 42–47 (1978).
- [13] H. Y. Hwang, T. T. M. Palstra, S.-W. Cheong and B. Batlogg. Pressure effects on the magnetoresistance in doped manganese perovskites. *Physical Review B* **52**(21), 15046–15049 (1995).
- [14] J. Fowlie. Electronic and Structural Properties of LaNiO₃-Based Heterostructures. Springer International Publishing (2019).
- [15] A. L. Cavalieri, N. Müller, T. Uphues, V. S. Yakovlev, A. Baltuška, B. Horvath, B. Schmidt, L. Blümel, R. Holzwarth, S. Hendel, M. Drescher, U. Kleineberg, P. M. Echenique, R. Kienberger, F. Krausz and U. Heinzmann. Attosecond spectroscopy in condensed matter. *Nature* **449**(7165), 1029–1032 (2007).
- [16] D. Strickland and G. Mourou. Compression of amplified chirped optical pulses. *Optics Communications* **55**(6), 447–449 (1985).
- [17] A. Cavalleri, T. Dekorsy, H. H. W. Chong, J. C. Kieffer and R. W. Schoenlein. Evidence for a structurally-driven insulator-to-metal transition in VO₂: A view from the ultrafast timescale. *Physical Review B* **70**(16) (2004).
- [18] R. D. Averitt, G. Rodriguez, A. I. Lobad, J. L. W. Siders, S. A. Trugman and A. J. Taylor. Nonequilibrium superconductivity and quasiparticle dynamics in YBa₂Cu₃O_{7- δ} . *Physical Review B* **63**(14) (2001).
- [19] R. Matsunaga and R. Shimano. Nonequilibrium BCS State Dynamics Induced by Intense Terahertz Pulses in a Superconducting NbN Film. *Physical Review Letters* **109**(18) (2012).
- [20] C. W. Siders, A. Cavalleri, K. Sokolowski-Tinten, C. Toth, T. Guo, M. Kammler, M. H. von Hoegen, K. R. Wilson, D. von der Linde and C. P. J. Barty. Detection of Nonthermal Melting by Ultrafast X-ray Diffraction. *Science* **286**(5443), 1340–1342 (1999).

-
- [21] K. Sokolowski-Tinten, C. Blome, C. Dietrich, A. Tarasevitch, M. H. von Hoegen, D. von der Linde, A. Cavalleri, J. Squier and M. Kammler. Femtosecond X-Ray Measurement of Ultrafast Melting and Large Acoustic Transients. *Physical Review Letters* **87**(22) (2001).
- [22] K. Sokolowski-Tinten, C. Blome, J. Blums, A. Cavalleri, C. Dietrich, A. Tarasevitch, I. Uschmann, E. Förster, M. Kammler, M. H. von Hoegen and D. von der Linde. Femtosecond X-ray measurement of coherent lattice vibrations near the Lindemann stability limit. *Nature* **422**(6929), 287–289 (2003).
- [23] L. Stojchevska, I. Vaskivskiy, T. Mertelj, P. Kusar, D. Svetin, S. Brazovskii and D. Mihailovic. Ultrafast Switching to a Stable Hidden Quantum State in an Electronic Crystal. *Science* **344**(6180), 177–180 (2014).
- [24] M. Matsubara, Y. Okimoto, T. Ogasawara, Y. Tomioka, H. Okamoto and Y. Tokura. Ultrafast Photoinduced Insulator-Ferromagnet Transition in the Perovskite Manganite $\text{Gd}_{0.55}\text{Sr}_{0.45}\text{MnO}_3$. *Physical Review Letters* **99**(20) (2007).
- [25] T. Li, A. Patz, L. Mouchliadis, J. Yan, T. A. Lograsso, I. E. Perakis and J. Wang. Femtosecond switching of magnetism via strongly correlated spin–charge quantum excitations. *Nature* **496**(7443), 69–73 (2013).
- [26] M. Gao, C. Lu, H. Jean-Ruel, L. C. Liu, A. Marx, K. Onda, S. ya Koshihara, Y. Nakano, X. Shao, T. Hiramatsu, G. Saito, H. Yamochi, R. R. Cooney, G. Moriena, G. Sciaini and R. J. D. Miller. Mapping molecular motions leading to charge delocalization with ultrabright electrons. *Nature* **496**(7445), 343–346 (2013).
- [27] Y. Tokura. Photoinduced Phase Transition: A Tool for Generating a Hidden State of Matter. *Journal of the Physical Society of Japan* **75**(1), 011001 (2006).
- [28] M. Fiebig, T. Lottermoser, D. Fröhlich, A. V. Goltsev and R. V. Pisarev. Observation of coupled magnetic and electric domains. *Nature* **419**(6909), 818–820 (2002).
- [29] A. Sell, A. Leitenstorfer and R. Huber. Phase-locked generation and field-resolved detection of widely tunable terahertz pulses with amplitudes exceeding 100 MV/cm. *Optics Letters* **33**(23), 2767 (2008).

- [30] W. Hu, S. Kaiser, D. Nicoletti, C. R. Hunt, I. Gierz, M. C. Hoffmann, M. L. Tacon, T. Loew, B. Keimer and A. Cavalleri. Optically enhanced coherent transport in $\text{YBa}_2\text{Cu}_3\text{O}_{6.5}$ by ultrafast redistribution of interlayer coupling. *Nature Materials* **13**(7), 705–711 (2014).
- [31] D. Fausti, R. I. Tobey, N. Dean, S. Kaiser, A. Dienst, M. C. Hoffmann, S. Pyon, T. Takayama, H. Takagi and A. Cavalleri. Light-Induced Superconductivity in a Stripe-Ordered Cuprate. *Science* **331**(6014), 189–191 (2011).
- [32] S. Kaiser, C. R. Hunt, D. Nicoletti, W. Hu, I. Gierz, H. Y. Liu, M. L. Tacon, T. Loew, D. Haug, B. Keimer and A. Cavalleri. Optically induced coherent transport far above T_c in underdoped $\text{YBa}_2\text{Cu}_3\text{O}_{6+x}$. *Physical Review B* **89**(18) (2014).
- [33] M. Rini, R. Tobey, N. Dean, J. Itatani, Y. Tomioka, Y. Tokura, R. W. Schoenlein and A. Cavalleri. Control of the electronic phase of a manganite by mode-selective vibrational excitation. *Nature* **449**(7158), 72–74 (2007).
- [34] A. D. Caviglia, R. Scherwitzl, P. Popovich, W. Hu, H. Bromberger, R. Singla, M. Mitrano, M. C. Hoffmann, S. Kaiser, P. Zubko, S. Gariglio, J.-M. Triscone, M. Först and A. Cavalleri. Ultrafast Strain Engineering in Complex Oxide Heterostructures. *Physical Review Letters* **108**(13) (2012).
- [35] M. Först, R. I. Tobey, S. Wall, H. Bromberger, V. Khanna, A. L. Cavalieri, Y.-D. Chuang, W. S. Lee, R. Moore, W. F. Schlotter, J. J. Turner, O. Krupin, M. Trigo, H. Zheng, J. F. Mitchell, S. S. Dhesi, J. P. Hill and A. Cavalleri. Driving magnetic order in a manganite by ultrafast lattice excitation. *Physical Review B* **84**(24) (2011).
- [36] M. Först, A. D. Caviglia, R. Scherwitzl, R. Mankowsky, P. Zubko, V. Khanna, H. Bromberger, S. B. Wilkins, Y.-D. Chuang, W. S. Lee, W. F. Schlotter, J. J. Turner, G. L. Dakovski, M. P. Minitti, J. Robinson, S. R. Clark, D. Jaksch, J.-M. Triscone, J. P. Hill, S. S. Dhesi and A. Cavalleri. Spatially resolved ultrafast magnetic dynamics initiated at a complex oxide heterointerface. *Nature Materials* **14**(9), 883–888 (2015).
- [37] T. F. Nova, A. S. Disa, M. Fechner and A. Cavalleri. Metastable ferroelectricity in optically strained SrTiO_3 . *Science* **364**(6445), 1075–1079 (2019).

-
- [38] X. Li, T. Qiu, J. Zhang, E. Baldini, J. Lu, A. M. Rappe and K. A. Nelson. Terahertz field-induced ferroelectricity in quantum paraelectric SrTiO₃. *Science* **364**(6445), 1079–1082 (2019).
- [39] S. A. Denev, T. T. A. Lummen, E. Barnes, A. Kumar and V. Gopalan. Probing Ferroelectrics Using Optical Second Harmonic Generation. *Journal of the American Ceramic Society* **94**(9), 2699–2727 (2011).
- [40] J. Itatani, J. Levesque, D. Zeidler, H. Niikura, H. Pépin, J. C. Kieffer, P. B. Corkum and D. M. Villeneuve. Tomographic imaging of molecular orbitals. *Nature* **432**(7019), 867–871 (2004).
- [41] S. Rajasekaran, J. Okamoto, L. Mathey, M. Fechner, V. Thampy, G. D. Gu and A. Cavalleri. Probing optically silent superfluid stripes in cuprates. *Science* **359**(6375), 575–579 (2018).
- [42] R. Matsunaga, N. Tsuji, H. Fujita, A. Sugioka, K. Makise, Y. Uzawa, H. Terai, Z. Wang, H. Aoki and R. Shimano. Light-induced collective pseudospin precession resonating with Higgs mode in a superconductor. *Science* **345**(6201), 1145–1149 (2014).
- [43] M. H. Hamidian, S. D. Edkins, S. H. Joo, A. Kostin, H. Eisaki, S. Uchida, M. J. Lawler, E.-A. Kim, A. P. Mackenzie, K. Fujita, J. Lee and J. C. S. Davis. Detection of a Cooper-pair density wave in Bi₂Sr₂CaCu₂O_{8+x}. *Nature* **532**(7599), 343–347 (2016).
- [44] H.-D. Chen, O. Vafek, A. Yazdani and S.-C. Zhang. Pair Density Wave in the Pseudogap State of High Temperature Superconductors. *Physical Review Letters* **93**(18) (2004).
- [45] M. Fiebig, D. Fröhlich, S. Leute and R. Pisarev. Topography of antiferromagnetic domains using second harmonic generation with an external reference. *Applied Physics B: Lasers and Optics* **66**(3), 265–270 (1998).
- [46] J. M. Choi. U.S. Patent No. 6,044,008 (2000).
- [47] R. Landauer. Electrostatic Considerations in BaTiO₃ Domain Formation during Polarization Reversal. *Journal of Applied Physics* **28**(2), 227–234 (1957).

- [48] J. Li, B. Nagaraj, H. Liang, W. Cao, C. H. Lee and R. Ramesh. Ultrafast polarization switching in thin-film ferroelectrics. *Applied Physics Letters* **84**(7), 1174–1176 (2004).
- [49] T. Qi, Y.-H. Shin, K.-L. Yeh, K. A. Nelson and A. M. Rappe. Collective Coherent Control: Synchronization of Polarization in Ferroelectric PbTiO₃ by Shaped THz Fields. *Physical Review Letters* **102**(24) (2009).
- [50] S. Grübel, J. A. Johnson, P. Beaud, C. Dornes, A. Ferrer, V. Haborets, L. Huber, T. Huber, A. Kohutych, T. Kubacka, M. Kubli, S. O. Mariager, J. Rittmann, J. I. Saari, Y. Vysochanskii, G. Ingold and S. L. Johnson. Ultrafast x-ray diffraction of a ferroelectric soft mode driven by broadband terahertz pulses. *arXiv* (2020).
- [51] F. Chen, Y. Zhu, S. Liu, Y. Qi, H. Y. Hwang, N. C. Brandt, J. Lu, F. Quirin, H. Enquist, P. Zalden, T. Hu, J. Goodfellow, M.-J. Sher, M. C. Hoffmann, D. Zhu, H. Lemke, J. Glowia, M. Chollet, A. R. Damodaran, J. Park, Z. Cai, I. W. Jung, M. J. Highland, D. A. Walko, J. W. Freeland, P. G. Evans, A. Vailionis, J. Larsson, K. A. Nelson, A. M. Rappe, K. Sokolowski-Tinten, L. W. Martin, H. Wen and A. M. Lindenberg. Ultrafast terahertz-field-driven ionic response in ferroelectric BaTiO₃. *Physical Review B* **94**(18) (2016).
- [52] M. Först, C. Manzoni, S. Kaiser, Y. Tomioka, Y. Tokura, R. Merlin and A. Cavalleri. Nonlinear phononics as an ultrafast route to lattice control. *Nature Physics* **7**(11), 854–856 (2011).
- [53] R. Mankowsky, M. Först, T. Loew, J. Porras, B. Keimer and A. Cavalleri. Coherent modulation of the YBa₂Cu₃O_{6+x} atomic structure by displacive stimulated ionic Raman scattering. *Physical Review B* **91**(9) (2015).
- [54] M. Först, R. Mankowsky, H. Bromberger, D. Fritz, H. Lemke, D. Zhu, M. Chollet, Y. Tomioka, Y. Tokura, R. Merlin, J. Hill, S. Johnson and A. Cavalleri. Displacive lattice excitation through nonlinear phononics viewed by femtosecond X-ray diffraction. *Solid State Communications* **169**, 24–27 (2013).
- [55] T. P. Martin and L. Genzel. Ionic Raman Scattering and Ionic Frequency Mixing. *physica status solidi (b)* **61**(2), 493–502 (1974).

-
- [56] R. F. Wallis and A. A. Maradudin. Ionic Raman Effect. II. The First-Order Ionic Raman Effect. *Physical Review B* **3**(6), 2063–2075 (1971).
- [57] D. L. Mills. Ionic contributions to the Raman tensor of insulators. *Physical Review B* **35**(17), 9278–9283 (1987).
- [58] R. Mankowsky, A. Subedi, M. Först, S. O. Mariager, M. Chollet, H. T. Lemke, J. S. Robinson, J. M. Glowia, M. P. Minitti, A. Frano, M. Fechner, N. A. Spaldin, T. Loew, B. Keimer, A. Georges and A. Cavalleri. Nonlinear lattice dynamics as a basis for enhanced superconductivity in $\text{YBa}_2\text{Cu}_3\text{O}_{6.5}$. *Nature* **516**(7529), 71–73 (2014).
- [59] S. R. White and A. E. Feiguin. Real-Time Evolution Using the Density Matrix Renormalization Group. *Physical Review Letters* **93**(7) (2004).
- [60] J. K. Freericks, V. M. Turkowski and V. Zlatić. Nonequilibrium Dynamical Mean-Field Theory. *Physical Review Letters* **97**(26) (2006).
- [61] H. Aoki, N. Tsuji, M. Eckstein, M. Kollar, T. Oka and P. Werner. Nonequilibrium dynamical mean-field theory and its applications. *Reviews of Modern Physics* **86**(2), 779–837 (2014).
- [62] A. Subedi, A. Cavalleri and A. Georges. Theory of nonlinear phononics for coherent light control of solids. *Physical Review B* **89**(22) (2014).
- [63] A. Subedi. Proposal for ultrafast switching of ferroelectrics using midinfrared pulses. *Physical Review B* **92**(21) (2015).
- [64] R. Mankowsky, A. von Hoegen, M. Först and A. Cavalleri. Ultrafast Reversal of the Ferroelectric Polarization. *Physical Review Letters* **118**(19) (2017).
- [65] A. von Hoegen, R. Mankowsky, M. Fechner, M. Först and A. Cavalleri. Probing the interatomic potential of solids with strong-field nonlinear phononics. *Nature* **555**(7694), 79–82 (2018).
- [66] H. K. Onnes. The discovery of superconductivity. *Commun. Phys. Lab.* **12**, 120 (1911).
- [67] J. Bardeen, L. N. Cooper and J. R. Schrieffer. Microscopic Theory of Superconductivity. *Physical Review* **106**(1), 162–164 (1957).

- [68] V. J. Emery and S. A. Kivelson. Importance of phase fluctuations in superconductors with small superfluid density. *Nature* **374**(6521), 434–437 (1995).
- [69] M. Hashimoto, I. M. Vishik, R.-H. He, T. P. Devereaux and Z.-X. Shen. Energy gaps in high-transition-temperature cuprate superconductors. *Nature Physics* **10**(7), 483–495 (2014).
- [70] A. Kaminski, S. Rosenkranz, H. M. Fretwell, J. C. Campuzano, Z. Li, H. Raffy, W. G. Cullen, H. You, C. G. Olson, C. M. Varma and H. Höchst. Spontaneous breaking of time-reversal symmetry in the pseudogap state of a high-T_c superconductor. *Nature* **416**(6881), 610–613 (2002).
- [71] S. D. Edkins, A. Kostin, K. Fujita, A. P. Mackenzie, H. Eisaki, S. Uchida, S. Sachdev, M. J. Lawler, E.-A. Kim, J. C. S. Davis and M. H. Hamidian. Magnetic field-induced pair density wave state in the cuprate vortex halo. *Science* **364**(6444), 976–980 (2019).
- [72] W. S. Lee, I. M. Vishik, K. Tanaka, D. H. Lu, T. Sasagawa, N. Nagaosa, T. P. Devereaux, Z. Hussain and Z.-X. Shen. Abrupt onset of a second energy gap at the superconducting transition of underdoped Bi2212. *Nature* **450**(7166), 81–84 (2007).
- [73] A. Dienst, M. C. Hoffmann, D. Fausti, J. C. Petersen, S. Pyon, T. Takayama, H. Takagi and A. Cavalleri. Bi-directional ultrafast electric-field gating of interlayer charge transport in a cuprate superconductor. *Nature Photonics* **5**(8), 485–488 (2011).
- [74] A. Dienst, E. Casandruc, D. Fausti, L. Zhang, M. Eckstein, M. Hoffmann, V. Khanna, N. Dean, M. Gensch, S. Winnerl, W. Seidel, S. Pyon, T. Takayama, H. Takagi and A. Cavalleri. Optical excitation of Josephson plasma solitons in a cuprate superconductor. *Nature Materials* **12**(6), 535–541 (2013).
- [75] S. Rajasekaran, E. Casandruc, Y. Laplace, D. Nicoletti, G. D. Gu, S. R. Clark, D. Jaksch and A. Cavalleri. Parametric amplification of a superconducting plasma wave. *Nature Physics* **12**(11), 1012–1016 (2016).
- [76] D. Nicoletti and A. Cavalleri. Nonlinear light-matter interaction at terahertz frequencies. *Advances in Optics and Photonics* **8**(3), 401 (2016).

-
- [77] J. D. Jackson. *Classical Electrodynamics* Third Edition. Wiley (1998).
- [78] R. W. Boyd. *Nonlinear Optics*. Academic Press (2008).
- [79] J. X. Cheng and X. S. Xie. *Coherent Raman scattering microscopy*. CRC Press, Taylor & Francis Group, Boca Raton (2013).
- [80] V. Denisov, B. Mavrin and V. Podobedov. Hyper-Raman scattering by vibrational excitations in crystals, glasses and liquids. *Physics Reports* **151**(1), 1–92 (1987).
- [81] A. Cartella, T. F. Nova, M. Fechner, R. Merlin and A. Cavalleri. Parametric amplification of optical phonons. *Proceedings of the National Academy of Sciences* **115**(48), 12148–12151 (2018).
- [82] A. Cartella. Amplification of optically driven phonons. Ph.D. thesis, Universität Hamburg (2018).
- [83] K. Kao. *Dielectric Phenomena in Solids*. Elsevier, Burlington (2004).
- [84] R. Prasankumar and A. J. Taylor. *Optical techniques for solid-state materials characterization*. CRC Press, Boca Raton (2012).
- [85] P. Griffiths. Fourier transform infrared spectrometry. *Science* **222**(4621), 297–302 (1983).
- [86] M. S. Dresselhaus. *Group Theory: Application to the Physics of Condensed Matter*. Springer (2008).
- [87] J. P. Elliott and P. G. Dawber. *Symmetry in physics*. Oxford University Press, New York (1979).
- [88] G. Eckold. Phonons, pp. 266–293. Springer Netherlands, Dordrecht (2003).
- [89] M. I. Aroyo, A. Kirov, C. Capillas, J. M. Perez-Mato and H. Wondratschek. Bilbao Crystallographic Server. II. Representations of crystallographic point groups and space groups. *Acta Crystallographica Section A Foundations of Crystallography* **62**(2), 115–128 (2006).
- [90] L. Tonks and I. Langmuir. Oscillations in Ionized Gases. *Physical Review* **33**(2), 195–210 (1929).

Bibliography

- [91] J. Goldshteyn. Frequency-Resolved Ultrafast Dynamics of Phonon Polariton Wavepackets in the Ferroelectric Crystals LiNbO_3 and LiTaO_3 . Ph.D. thesis, Universität Potsdam (2014).
- [92] R. Claus. Light scattering by optical phonons and polaritons in perfect crystals. *Physica Status Solidi (b)* **50**(1), 11–32 (1972).
- [93] R. Merlin. Generating coherent THz phonons with light pulses. *Solid State Communications* **102**(2-3), 207–220 (1997).
- [94] D. A. Long. The Raman Effect - A Unified Treatment of the Theory of Raman Scattering by Molecules. Wiley, New York (2002).
- [95] M. V. Hobden. Phase-Matched Second-Harmonic Generation in Biaxial Crystals. *Journal of Applied Physics* **38**(11), 4365–4372 (1967).
- [96] P. D. Maker, R. W. Terhune, M. Nisenoff and C. M. Savage. Effects of Dispersion and Focusing on the Production of Optical Harmonics. *Physical Review Letters* **8**(1), 21–22 (1962).
- [97] M. Mlejnek, E. M. Wright, J. V. Moloney and N. Bloembergen. Second Harmonic Generation of Femtosecond Pulses at the Boundary of a Nonlinear Dielectric. *Physical Review Letters* **83**(15), 2934–2937 (1999).
- [98] V. Roppo, M. Centini, C. Sibilìa, M. Bertolotti, D. de Ceglia, M. Scalora, N. Akozbek, M. J. Bloemer, J. W. Haus, O. G. Kosareva and V. P. Kandidov. Role of phase matching in pulsed second-harmonic generation: Walk-off and phase-locked twin pulses in negative-index media. *Physical Review A* **76**(3) (2007).
- [99] N. Bloembergen and P. S. Pershan. Light Waves at the Boundary of Nonlinear Media. *Physical Review* **128**(2), 606–622 (1962).
- [100] E. Fazio, F. Pettazzi, M. Centini, M. Chauvet, A. Belardini, M. Alonzo, C. Sibilìa, M. Bertolotti and M. Scalora. Complete spatial and temporal locking in phase-mismatched second-harmonic generation. *Optics Express* **17**(5), 3141 (2009).

-
- [101] M. Centini, V. Roppo, E. Fazio, F. Pettazzi, C. Sibilia, J. W. Haus, J. V. Foreman, N. Akozbek, M. J. Bloemer and M. Scalora. Inhibition of Linear Absorption in Opaque Materials Using Phase-Locked Harmonic Generation. *Physical Review Letters* **101**(11) (2008).
- [102] J. F. McGilp. A review of optical second-harmonic and sum-frequency generation at surfaces and interfaces. *Journal of Physics D: Applied Physics* **29**(7), 1812–1821 (1996).
- [103] Y. R. Shen. Surface studies by optical second harmonic generation: An overview. *Journal of Vacuum Science & Technology B: Microelectronics and Nanometer Structures* **3**(5), 1464 (1985).
- [104] J. McGilp, D. Weaire and C. Patterson. *Epioptics : linear and nonlinear optical spectroscopy of surfaces and interfaces*. Springer, Berlin New York (1995).
- [105] P. N. Butcher. *Nonlinear optical phenomena*. Ohio State University (1965).
- [106] H. Rabin. *Quantum electronics a treatise*. Academic Press, New York (1975).
- [107] D. A. Kleinman. Nonlinear Dielectric Polarization in Optical Media. *Physical Review* **126**(6), 1977–1979 (1962).
- [108] M. Fiebig, V. V. Pavlov and R. V. Pisarev. Second-harmonic generation as a tool for studying electronic and magnetic structures of crystals: review. *Journal of the Optical Society of America B* **22**(1), 96 (2005).
- [109] M. Fiebig, T. Lottermoser, V. V. Pavlov and R. V. Pisarev. Magnetic second harmonic generation in centrosymmetric CoO, NiO, and KNiF₃. *Journal of Applied Physics* **93**(10), 6900–6902 (2003).
- [110] M. Fiebig, D. Fröhlich, K. Kohn, S. Leute, T. Lottermoser, V. V. Pavlov and R. V. Pisarev. Determination of the Magnetic Symmetry of Hexagonal Manganites by Second Harmonic Generation. *Physical Review Letters* **84**(24), 5620–5623 (2000).
- [111] C. C. Neacsu, B. B. van Aken, M. Fiebig and M. B. Raschke. Second-harmonic near-field imaging of ferroelectric domain structure of YMnO₃. *Physical Review B* **79**(10) (2009).

Bibliography

- [112] M. Trassin, G. D. Luca, S. Manz and M. Fiebig. Probing Ferroelectric Domain Engineering in BiFeO₃ Thin Films by Second Harmonic Generation. *Advanced Materials* **27**(33), 4871–4876 (2015).
- [113] R. C. Miller and A. Savage. Temperature Dependence of the Optical Properties of Ferroelectric LiNbO₃ and LiTaO₃. *Applied Physics Letters* **9**(4), 169–171 (1966).
- [114] B. A. Ruzicka, L. K. Werake, G. Xu, J. B. Khurgin, E. Y. Sherman, J. Z. Wu and H. Zhao. Second-Harmonic Generation Induced by Electric Currents in GaAs. *Physical Review Letters* **108**(7) (2012).
- [115] R. W. Terhune, P. D. Maker and C. M. Savage. Measurements of Nonlinear Light Scattering. *Physical Review Letters* **14**(17), 681–684 (1965).
- [116] H. Vogt. Coherent and hyper-raman techniques. *Topics in Applied Physics*, pp. 207–244. Springer Berlin Heidelberg (1982).
- [117] K. Inoue, N. Asai and T. Sameshima. Experimental Study of the Hyper-Raman Scattering Due to Raman Inactive Lattice Vibration in SrTiO₃. *Journal of the Physical Society of Japan* **50**(4), 1291–1300 (1981).
- [118] H. Vogt, J. A. Sanjurjo and G. Rossbroich. Soft-mode spectroscopy in cubic BaTiO₃ by hyper-Raman scattering. *Physical Review B* **26**(10), 5904–5910 (1982).
- [119] H. Vogt and G. Neumann. Observation of infrared active and silent modes in cubic crystals by hyper-Raman scattering. *Physica Status Solidi (b)* **92**(1), 57–63 (1979).
- [120] V. Denisov, B. Mavrin and V. Podobedov. Hyper-Raman scattering by vibrational excitations in crystals, glasses and liquids. *Physics Reports* **151**(1), 1–92 (1987).
- [121] J. Kerr. XL. A new relation between electricity and light: Dielectrified media birefringent. *The London, Edinburgh, and Dublin Philosophical Magazine and Journal of Science* **50**(332), 337–348 (1875).
- [122] P. A. Franken, A. E. Hill, C. W. Peters and G. Weinreich. Generation of Optical Harmonics. *Physical Review Letters* **7**(4), 118–119 (1961).
- [123] *Ultrashort Laser Pulse Phenomena*. Elsevier (2006).

-
- [124] E. Treacy. Optical pulse compression with diffraction gratings. *IEEE Journal of Quantum Electronics* **5**(9), 454–458 (1969).
- [125] J. A. Armstrong. MEASUREMENT OF PICOSECOND LASER PULSE WIDTHS. *Applied Physics Letters* **10**(1), 16–18 (1967).
- [126] D. J. Kane and R. Trebino. Single-shot measurement of the intensity and phase of an arbitrary ultrashort pulse by using frequency-resolved optical gating. *Optics Letters* **18**(10), 823 (1993).
- [127] J. Valdmanis, G. Mourou and C. Gobel. Subpicosecond electrical sampling. *IEEE Journal of Quantum Electronics* **19**(4), 664–667 (1983).
- [128] R. Thomson, C. Leburn and D. Reid, eds. *Ultrafast Nonlinear Optics*. Springer International Publishing (2013).
- [129] G. Cerullo and S. D. Silvestri. Ultrafast optical parametric amplifiers. *Review of Scientific Instruments* **74**(1), 1–18 (2003).
- [130] A. V. Smith. SNLO nonlinear optics code, AS-Photonics, Albuquerque, NM .
- [131] M. Hugenschmidt. *Lasermesstechnik*. Springer Berlin Heidelberg (2007).
- [132] Y.-X. Yan, E. B. Gamble and K. A. Nelson. Impulsive stimulated scattering: General importance in femtosecond laser pulse interactions with matter, and spectroscopic applications. *The Journal of Chemical Physics* **83**(11), 5391–5399 (1985).
- [133] V. M. Agranovich and V. Ginzburg. *Crystal Optics with Spatial Dispersion, and Excitons*. Springer Berlin Heidelberg (1984).
- [134] J. K. Wahlstrand, R. Merlin, X. Li, S. T. Cundiff and O. E. Martinez. Impulsive stimulated Raman scattering: comparison between phase-sensitive and spectrally filtered techniques. *Optics Letters* **30**(8), 926 (2005).
- [135] H. Nyquist. Certain Topics in Telegraph Transmission Theory. *Transactions of the American Institute of Electrical Engineers* **47**(2), 617–644 (1928).

Bibliography

- [136] S. Keiber, S. Sederberg, A. Schwarz, M. Trubetskov, V. Pervak, F. Krausz and N. Karpowicz. Electro-optic sampling of near-infrared waveforms. *Nature Photonics* **10**(3), 159–162 (2016).
- [137] T. E. Stevens. Cherenkov Radiation at Speeds Below the Light Threshold: Phonon-Assisted Phase Matching. *Science* **291**(5504), 627–630 (2001).
- [138] Y. Ikegaya, H. Sakaibara, Y. Minami, I. Katayama and J. Takeda. Real-time observation of phonon-polariton dynamics in ferroelectric LiNbO₃ in time-frequency space. *Applied Physics Letters* **107**(6), 062901 (2015).
- [139] D. C. Wallace. Thermal Expansion and Other Anharmonic Properties of Crystals. *Physical Review* **139**(3A), A877–A888 (1965).
- [140] R. Peierls. Zur Theorie der elektrischen und thermischen Leitfähigkeit von Metallen. *Annalen der Physik* **396**(2), 121–148 (1930).
- [141] N. M. Neil W. Ashcroft. Solid State Physics. Cengage Learning (1976).
- [142] M. I. Aroyo, A. Kirov, C. Capillas, J. M. Perez-Mato and H. Wondratschek. Bilbao Crystallographic Server. II. Representations of crystallographic point groups and space groups. *Acta Crystallographica Section A Foundations of Crystallography* **62**(2), 115–128 (2006).
- [143] B. Liu, M. Först, M. Fechner, D. Nicoletti, J. Porras, T. Loew, B. Keimer and A. Cavalleri. Pump Frequency Resonances for Light-Induced Incipient Superconductivity in YBa₂Cu₃O_{6.5}. *Physical Review X* **10**(1) (2020).
- [144] T. Dekorsy, V. A. Yakovlev, W. Seidel, M. Helm and F. Keilmann. Infrared-Phonon Polariton Resonance of the Nonlinear Susceptibility in GaAs. *Physical Review Letters* **90**(5) (2003).
- [145] Hamel. Georg Duffing, Ingenieur: Erzwungene Schwingungen bei veränderlicher Eigenfrequenz und ihre technische Bedeutung. Sammlung Vieweg. Heft 41/42, Braunschweig 1918. *ZAMM - Journal of Applied Mathematics and Mechanics Zeitschrift für Angewandte Mathematik und Mechanik* **1**(1), 72–73 (1921).

-
- [146] S. Strogatz. Nonlinear dynamics and chaos with applications to physics, biology, chemistry, and engineering. Westview Press, Cambridge, MA (2000).
- [147] P. G. Radaelli. Lecture 9 - Anharmonic effects in crystals (2013).
- [148] M. Kozina, M. Fechner, P. Marsik, T. van Driel, J. M. Glowina, C. Bernhard, M. Radovic, D. Zhu, S. Bonetti, U. Staub and M. C. Hoffmann. Terahertz-driven phonon upconversion in SrTiO₃. *Nature Physics* **15**(4), 387–392 (2019).
- [149] A. Cartella, T. F. Nova, M. Fechner, R. Merlin and A. Cavalleri. Parametric amplification of optical phonons. *Proceedings of the National Academy of Sciences* **115**(48), 12148–12151 (2018).
- [150] R. C. Miller. Optical Harmonic Generation in Single Crystal BaTiO₃. *Physical Review* **134**(5A), A1313–A1319 (1964).
- [151] A. S. Barker and R. Loudon. Dielectric Properties and Optical Phonons in LiNbO₃. *Physical Review* **158**(2), 433–445 (1967).
- [152] R. F. Schaufele and M. J. Weber. Raman Scattering by Lithium Niobate. *Physical Review* **152**(2), 705–708 (1966).
- [153] M. Porer, J.-M. Ménard and R. Huber. Shot noise reduced terahertz detection via spectrally postfiltered electro-optic sampling. *Optics Letters* **39**(8), 2435 (2014).
- [154] S. Kojima, K. Kanehara, T. Hoshina and T. Tsurumi. Optical phonons and polariton dispersions of congruent LiNbO₃ studied by far-infrared spectroscopic ellipsometry and Raman scattering. *Japanese Journal of Applied Physics* **55**(10S), 10TC02 (2016).
- [155] B. S. Dastrup, J. R. Hall and J. A. Johnson. Experimental determination of the interatomic potential in LiNbO₃ via ultrafast lattice control. *Applied Physics Letters* **110**(16), 162901 (2017).
- [156] F. A. Lindemann. The calculation of molecular vibration frequencies. *Physikalische Zeitung* p. 609 (1910).
- [157] J. Bardeen and W. H. Brattain. The Transistor, A Semi-Conductor Triode. *Physical Review* **74**(2), 230–231 (1948).

Bibliography

- [158] P. H. Siegel. Terahertz Pioneer: David H. Auston. *IEEE Transactions on Terahertz Science and Technology* **1**(1), 6–8 (2011).
- [159] I. S. Osborne. Ultrafast plasmonic modulation. *Science* **358**(6363), 604.2–604 (2017).
- [160] M. Ayata, Y. Fedoryshyn, W. Heni, B. Baeuerle, A. Josten, M. Zahner, U. Koch, Y. Salamin, C. Hoessbacher, C. Haffner, D. L. Elder, L. R. Dalton and J. Leuthold. High-speed plasmonic modulator in a single metal layer. *Science* **358**(6363), 630–632 (2017).
- [161] M. Henstridge, C. Pfeiffer, D. Wang, A. Boltasseva, V. M. Shalaev, A. Grbic and R. Merlin. Synchrotron radiation from an accelerating light pulse. *Science* **362**(6413), 439–442 (2018).
- [162] P. Muhlschlegel. Resonant Optical Antennas. *Science* **308**(5728), 1607–1609 (2005).
- [163] K. B. Crozier, A. Sundaramurthy, G. S. Kino and C. F. Quate. Optical antennas: Resonators for local field enhancement. *Journal of Applied Physics* **94**(7), 4632–4642 (2003).
- [164] B. Josephson. Possible new effects in superconductive tunnelling. *Physics Letters* **1**(7), 251–253 (1962).
- [165] J. R. Schrieffer and J. S. Brooks, eds. Handbook of High-Temperature Superconductivity. Springer New York (2007).
- [166] A. von Hoegen, M. Fechner, M. Först, J. Porras, B. Keimer, M. Michael, E. Demler and A. Cavalleri. Probing coherent charge fluctuations in $\text{YBa}_2\text{Cu}_3\text{O}_{6+x}$ at wavevectors outside the light cone. *arXiv* (2020).
- [167] L. N. Cooper. Bound Electron Pairs in a Degenerate Fermi Gas. *Physical Review* **104**(4), 1189–1190 (1956).
- [168] J. Annett. Superconductivity, superfluids, and condensates. Oxford University Press, Oxford New York (2004).
- [169] I. Giaever and K. Megerle. Study of Superconductors by Electron Tunneling. *Physical Review* **122**(4), 1101–1111 (1961).
- [170] R. Kleiner and W. Buckel. Superconductivity : an introduction. Wiley-VCH Verlag GmbH & Co. KGaA, Weinheim, Germany (2016).

-
- [171] M. Tinkham. Introduction to superconductivity. Dover Publications, Mineola, N.Y (2004).
- [172] F. London. Superfluids. Dover Publications, New York (1961).
- [173] R. Gross and A. Marx. Festkörperphysik. De Gruyter, Berlin Germany Boston Massachusetts (2014).
- [174] B. T. Matthias, T. H. Geballe and V. B. Compton. Superconductivity. *Reviews of Modern Physics* **35**(1), 1–22 (1963).
- [175] K. Gavroglu and Y. Goudaroulis. Understanding macroscopic quantum phenomena: The history of superfluidity 1941–1955. *Annals of Science* **45**(4), 367–385 (1988).
- [176] F. London and H. London. The electromagnetic equations of the supraconductor. *Proceedings of the Royal Society of London. Series A - Mathematical and Physical Sciences* **149**(866), 71–88 (1935).
- [177] B. D. Josephson. Coupled Superconductors. *Reviews of Modern Physics* **36**(1), 216–220 (1964).
- [178] B. Josephson. Supercurrents through barriers. *Advances in Physics* **14**(56), 419–451 (1965).
- [179] J. M. Rowell, P. W. Anderson and D. E. Thomas. Image of the Phonon Spectrum in the Tunneling Characteristic Between Superconductors. *Physical Review Letters* **10**(8), 334–336 (1963).
- [180] W. C. Stewart. Curren-Voltage Characteristics of Josephson Junctions. *Applied Physics Letters* **12**(8), 277–280 (1968).
- [181] D. E. McCumber. Effect of ac Impedance on dc Voltage-Current Characteristics of Superconductor Weak-Link Junctions. *Journal of Applied Physics* **39**(7), 3113–3118 (1968).
- [182] S. Savel'ev, V. A. Yampol'skii, A. L. Rakhmanov and F. Nori. Terahertz Josephson plasma waves in layered superconductors: spectrum, generation, nonlinear and quantum phenomena. *Reports on Progress in Physics* **73**(2), 026501 (2010).

Bibliography

- [183] X. Hu and S.-Z. Lin. Phase dynamics in a stack of inductively coupled intrinsic Josephson junctions and terahertz electromagnetic radiation. *Superconductor Science and Technology* **23**(5), 053001 (2010).
- [184] L. N. Bulaevskii, D. Domínguez, M. P. Maley, A. R. Bishop and B. I. Ivlev. Collective mode and the *c*-axis critical current of a Josephson-coupled superconductor at high parallel magnetic fields. *Physical Review B* **53**(21), 14601–14610 (1996).
- [185] D. Rybicki, M. Jurkutat, S. Reichardt, C. Kapusta and J. Haase. Perspective on the phase diagram of cuprate high-temperature superconductors. *Nature Communications* **7**(1) (2016).
- [186] R. Kleiner and P. Müller. Intrinsic Josephson effects in high-*T_c* superconductors. *Physical Review B* **49**(2), 1327–1341 (1994).
- [187] M. K. Wu, J. R. Ashburn, C. J. Torng, P. H. Hor, R. L. Meng, L. Gao, Z. J. Huang, Y. Q. Wang and C. W. Chu. Superconductivity at 93 K in a new mixed-phase Y-Ba-Cu-O compound system at ambient pressure. *Physical Review Letters* **58**(9), 908–910 (1987).
- [188] R. Baquero. Manifestations of the Electron-Phonon Interaction (1994).
- [189] R. J. Cava. Oxide Superconductors. *Journal of the American Ceramic Society* **83**(1), 5–28 (2000).
- [190] Y. Tokura and T. Arima. New Classification Method for Layered Copper Oxide Compounds and Its Application to Design of New High-*T_c* Superconductors. *Japanese Journal of Applied Physics* **29**(Part 1, No. 11), 2388–2402 (1990).
- [191] A. Damascelli, Z. Hussain and Z.-X. Shen. Angle-resolved photoemission studies of the cuprate superconductors. *Reviews of Modern Physics* **75**(2), 473–541 (2003).
- [192] B. Keimer, S. A. Kivelson, M. R. Norman, S. Uchida and J. Zaanen. From quantum matter to high-temperature superconductivity in copper oxides. *Nature* **518**(7538), 179–186 (2015).
- [193] N. P. Armitage, P. Fournier and R. L. Greene. Progress and perspectives on electron-doped cuprates. *Reviews of Modern Physics* **82**(3), 2421–2487 (2010).

-
- [194] W. E. Lawrence and S. Doniach. Theory of Layer-Structure Superconductors (1971).
- [195] C. E. Gough, M. S. Colclough, E. M. Forgan, R. G. Jordan, M. Keene, C. M. Muirhead, A. I. M. Rae, N. Thomas, J. S. Abell and S. Sutton. Flux quantization in a high-Tc superconductor. *Nature* **326**(6116), 855–855 (1987).
- [196] Y. J. Uemura, G. M. Luke, B. J. Sternlieb, J. H. Brewer, J. F. Carolan, W. N. Hardy, R. Kadono, J. R. Kempton, R. F. Kiefl, S. R. Kreitzman, P. Mulhern, T. M. Riseman, D. L. Williams, B. X. Yang, S. Uchida, H. Takagi, J. Gopalakrishnan, A. W. Sleight, M. A. Subramanian, C. L. Chien, M. Z. Cieplak, G. Xiao, V. Y. Lee, B. W. Statt, C. E. Stronach, W. J. Kossler and X. H. Yu. Universal Correlations between Tc and $n s m^*$ (Carrier Density over Effective Mass) in High-Tc Cuprate Superconductors. *Physical Review Letters* **62**(19), 2317–2320 (1989).
- [197] D. van der Marel and A. A. Tsvetkov. Transverse-optical Josephson plasmons: Equations of motion. *Physical Review B* **64**(2) (2001).
- [198] D. van der Marel and A. Tsvetkov. Transverse optical plasmons in layered superconductors. *Czechoslovak Journal of Physics* **46**(S6), 3165–3168 (1996).
- [199] D. Nicoletti, D. Fu, O. Mehio, S. Moore, A. Disa, G. Gu and A. Cavalleri. Magnetic-Field Tuning of Light-Induced Superconductivity in Striped $\text{La}_{2-x}\text{Ba}_x\text{CuO}_4$. *Physical Review Letters* **121**(26) (2018).
- [200] E. J. Singley, M. Abo-Bakr, D. N. Basov, J. Feikes, P. Guptasarma, K. Holldack, H. W. Hübers, P. Kuske, M. C. Martin, W. B. Peatman, U. Schade and G. Wüstefeld. Measuring the Josephson plasma resonance in $\text{Bi}_2\text{Sr}_2\text{CaCu}_2\text{O}_8$ using intense coherent THz synchrotron radiation. *Physical Review B* **69**(9) (2004).
- [201] M. Grüninger, D. van der Marel, A. A. Tsvetkov and A. Erb. Observation of Out-of-Phase Bilayer Plasmons in $\text{YBa}_2\text{Cu}_3\text{O}_{7-\delta}$. *Physical Review Letters* **84**(7), 1575–1578 (2000).
- [202] T. Koyama. Josephson Plasma Resonances and Optical Properties in High-Tc Superconductors with Alternating Junction Parameters. *Journal of the Physical Society of Japan* **71**(12), 2986–2993 (2002).

Bibliography

- [203] C. Homes, T. Timusk, D. Bonn, R. Liang and W. Hardy. Optical properties along the c-axis of $\text{YBa}_2\text{Cu}_3\text{O}_{6+x}$, for $x = 0.50 \rightarrow 0.95$ evolution of the pseudogap. *Physica C: Superconductivity* **254**(3-4), 265–280 (1995).
- [204] C. C. Homes, T. Timusk, D. A. Bonn, R. Liang and W. N. Hardy. Optical phonons polarized along the c axis of $\text{YBa}_2\text{Cu}_3\text{O}_{6+x}$, for $x = 0.5 \rightarrow 0.95$. *Canadian Journal of Physics* **73**(11-12), 663–675 (1995).
- [205] T. Koyama. Quantum Charge Dynamics in an Array of Intrinsic Josephson Junctions. *Journal of the Physical Society of Japan* **70**(7), 2114–2123 (2001).
- [206] D. Munzar, C. Bernhard, A. Golnik, J. Humlíček and M. Cardona. A New Interpretation of the Phonon Anomalies in the Far-Infrared c-Axis Conductivity of Underdoped $\text{YBa}_2\text{Cu}_3\text{O}_y$. *physica status solidi (b)* **215**(1), 557–561 (1999).
- [207] D. Munzar, C. Bernhard, A. Golnik, J. Humlíček and M. Cardona. Phonon anomalies in the far-infrared c-axis conductivity of underdoped $\text{YBa}_2\text{Cu}_3\text{O}_y$ as Evidence for the intra-bilayer Josephson effect. *Journal of Low Temperature Physics* **117**(5/6), 1049–1053 (1999).
- [208] A. Dubroka, M. Rössle, K. W. Kim, V. K. Malik, D. Munzar, D. N. Basov, A. A. Schafgans, S. J. Moon, C. T. Lin, D. Haug, V. Hinkov, B. Keimer, T. Wolf, J. G. Storey, J. L. Tallon and C. Bernhard. Evidence of a Precursor Superconducting Phase at Temperatures as High as 180 K in $\text{RBa}_2\text{Cu}_3\text{O}_{7-\delta}$ (R=Y, Gd, Eu) Superconducting Crystals from Infrared Spectroscopy. *Physical Review Letters* **106**(4) (2011).
- [209] R. Mankowsky. Nonlinear phononics and structural control of strongly correlated materials. Ph.D. thesis, Universität Hamburg (2015).
- [210] T. Timusk. The mysterious pseudogap in high temperature superconductors: an infrared view. *Solid State Communications* **127**(5), 337–348 (2003).
- [211] T. Timusk and C. Homes. The role of magnetism in forming the c-axis spectral peak at 400cm^{-1} in high temperature superconductors. *Solid State Communications* **126**(1-2), 63–69 (2003).

-
- [212] J. Schützmann, S. Tajima, S. Miyamoto, Y. Sato and R. Hauff. Doping and temperature dependence of *c*-axis optical phonons in $\text{YBa}_2\text{Cu}_3\text{O}_y$ single crystals. *Physical Review B* **52**(18), 13665–13673 (1995).
- [213] A. Kanigel, U. Chatterjee, M. Randeria, M. R. Norman, G. Koren, K. Kadowaki and J. C. Campuzano. Evidence for Pairing above the Transition Temperature of Cuprate Superconductors from the Electronic Dispersion in the Pseudogap Phase. *Physical Review Letters* **101**(13) (2008).
- [214] G. Yu, D.-D. Xia, D. Pelc, R.-H. He, N.-H. Kaneko, T. Sasagawa, Y. Li, X. Zhao, N. Barišić, A. Shekhter and M. Greven. Universal precursor of superconductivity in the cuprates. *Physical Review B* **99**(21) (2019).
- [215] R. Daou, J. Chang, D. LeBoeuf, O. Cyr-Choinière, F. Laliberté, N. Doiron-Leyraud, B. J. Ramshaw, R. Liang, D. A. Bonn, W. N. Hardy and L. Taillefer. Broken rotational symmetry in the pseudogap phase of a high- T_c superconductor. *Nature* **463**(7280), 519–522 (2010).
- [216] Z. A. Xu, N. P. Ong, Y. Wang, T. Kakeshita and S. Uchida. Vortex-like excitations and the onset of superconducting phase fluctuation in underdoped $\text{La}_{2-x}\text{Sr}_x\text{CuO}_4$. *Nature* **406**(6795), 486–488 (2000).
- [217] Y. Wang, L. Li and N. P. Ong. Nernst effect in high- T_c superconductors. *Physical Review B* **73**(2) (2006).
- [218] D. F. Agterberg, J. S. Davis, S. D. Edkins, E. Fradkin, D. J. V. Harlingen, S. A. Kivelson, P. A. Lee, L. Radzihovsky, J. M. Tranquada and Y. Wang. The Physics of Pair-Density Waves: Cuprate Superconductors and Beyond. *Annual Review of Condensed Matter Physics* **11**(1), 231–270 (2020).
- [219] E. Fradkin, S. A. Kivelson and J. M. Tranquada. Colloquium: Theory of intertwined orders in high temperature superconductors. *Reviews of Modern Physics* **87**(2), 457–482 (2015).
- [220] M. H. Michael, A. von Hoegen, M. Fechner, M. Först, A. Cavalleri and E. Demler. Para-

Bibliography

- metric resonance of Josephson plasma waves: A theory for optically amplified interlayer superconductivity in $\text{YBa}_2\text{Cu}_2\text{O}_{6+x}$. *arXiv* (2020).
- [221] C. Lin, B. Liang and H. Chen. Top-seeded solution growth of Ca-doped YBCO single crystals. *Journal of Crystal Growth* **237-239**, 778–782 (2002).
- [222] C. Lin, W. Zhou, W. Liang, E. Schönherr and H. Bender. Growth of large and untwinned single crystals of YBCO. *Physica C: Superconductivity* **195**(3-4), 291–300 (1992).
- [223] A. Simon, K. Trübenbach and H. Borrmann. Single Crystal X-Ray Structure Analysis of $\text{YBa}_2\text{Cu}_3\text{O}_{6.5}$. *Journal of Solid State Chemistry* **106**(1), 128–133 (1993).
- [224] R. J. Cava, B. Batlogg, C. H. Chen, E. A. Rietman, S. M. Zahurak and D. Werder. Single-phase 60-K bulk superconductor in annealed $\text{Ba}_2\text{YCu}_3\text{O}_{7-\delta}$. *Physical Review B* **36**(10), 5719–5722 (1987).
- [225] J. D. Jorgensen, B. W. Veal, A. P. Paulikas, L. J. Nowicki, G. W. Crabtree, H. Claus and W. K. Kwok. Structural properties of oxygen-deficient $\text{YBa}_2\text{Cu}_3\text{O}_{7-\delta}$. *Physical Review B* **41**(4), 1863–1877 (1990).
- [226] E. Pavarini, I. Dasgupta, T. Saha-Dasgupta, O. Jepsen and O. K. Andersen. Band-Structure Trend in Hole-Doped Cuprates and Correlation with T_c max. *Physical Review Letters* **87**(4) (2001).
- [227] Y. Y. Peng, G. Dellea, M. Minola, M. Conni, A. Amorese, D. D. Castro, G. M. D. Luca, K. Kummer, M. Salluzzo, X. Sun, X. J. Zhou, G. Balestrino, M. L. Tacon, B. Keimer, L. Braicovich, N. B. Brookes and G. Ghiringhelli. Influence of apical oxygen on the extent of in-plane exchange interaction in cuprate superconductors. *Nature Physics* **13**(12), 1201–1206 (2017).
- [228] S. Johnston, F. Vernay, B. Moritz, Z.-X. Shen, N. Nagaosa, J. Zaanen and T. P. Devereaux. Systematic study of electron-phonon coupling to oxygen modes across the cuprates. *Physical Review B* **82**(6) (2010).
- [229] N. Plakida. High-Temperature Cuprate Superconductors. Springer Berlin Heidelberg (2010).

-
- [230] L. F. Mattheiss. Electronic band properties and superconductivity in $\text{La}_{2-y}\text{X}_y\text{CuO}_4$. *Physical Review Letters* **58**(10), 1028–1030 (1987).
- [231] D. H. Lu, D. L. Feng, N. P. Armitage, K. M. Shen, A. Damascelli, C. Kim, F. Ronning, Z.-X. Shen, D. A. Bonn, R. Liang, W. N. Hardy, A. I. Rykov and S. Tajima. Superconducting Gap and Strong In-Plane Anisotropy in Untwinned $\text{YBa}_2\text{Cu}_3\text{O}_{7-\delta}$. *Physical Review Letters* **86**(19), 4370–4373 (2001).
- [232] K. Nakayama, T. Sato, K. Terashima, T. Arakane, T. Takahashi, M. Kubota, K. Ono, T. Nishizaki, Y. Takahashi and N. Kobayashi. Doping dependence of the gap anisotropy of the high-temperature $\text{YBa}_2\text{Cu}_3\text{O}_{7-\delta}$ superconductor. *Physical Review B* **79**(14) (2009).
- [233] L. Zhao, C. A. Belvin, R. Liang, D. A. Bonn, W. N. Hardy, N. P. Armitage and D. Hsieh. A global inversion-symmetry-broken phase inside the pseudogap region of $\text{YBa}_2\text{Cu}_3\text{O}_y$. *Nature Physics* **13**(3), 250–254 (2016).
- [234] Y. S. Lee, K. Segawa, Z. Q. Li, W. J. Padilla, M. Dumm, S. V. Dordevic, C. C. Homes, Y. Ando and D. N. Basov. Electrodynamics of the nodal metal state in weakly doped high-Tc cuprates. *Physical Review B* **72**(5) (2005).
- [235] C. Timm, D. Manske and K. H. Bennemann. Phase diagram of underdoped cuprate superconductors: Effects of Cooper-pair phase fluctuations. *Physical Review B* **66**(9) (2002).
- [236] M. Fujita, H. Goka, K. Yamada, J. M. Tranquada and L. P. Regnault. Stripe order, depinning, and fluctuations in $\text{La}_{1.875}\text{Ba}_{0.125}\text{CuO}_4$ and $\text{La}_{1.875}\text{Ba}_{0.075}\text{Sr}_{0.050}\text{CuO}_4$. *Physical Review B* **70**(10) (2004).
- [237] T. Wu, H. Mayaffre, S. Krämer, M. Horvatić, C. Berthier, W. N. Hardy, R. Liang, D. A. Bonn and M.-H. Julien. Magnetic-field-induced charge-stripe order in the high-temperature superconductor $\text{YBa}_2\text{Cu}_3\text{O}_y$. *Nature* **477**(7363), 191–194 (2011).
- [238] G. Ghiringhelli, M. L. Tacon, M. Minola, S. Blanco-Canosa, C. Mazzoli, N. B. Brookes, G. M. D. Luca, A. Frano, D. G. Hawthorn, F. He, T. Loew, M. M. Sala, D. C. Peets, M. Salluzzo, E. Schierle, R. Sutarto, G. A. Sawatzky, E. Weschke, B. Keimer and

Bibliography

- L. Braicovich. Long-Range Incommensurate Charge Fluctuations in $(Y, Nd)Ba_2Cu_3O_{6+x}$. *Science* **337**(6096), 821–825 (2012).
- [239] E. Blackburn, J. Chang, M. Hücker, A. T. Holmes, N. B. Christensen, R. Liang, D. A. Bonn, W. N. Hardy, U. Rütt, O. Gutowski, M. v. Zimmermann, E. M. Forgan and S. M. Hayden. X-Ray Diffraction Observations of a Charge-Density-Wave Order in Superconducting Ortho-II $YBa_2Cu_3O_{6.54}$ Single Crystals in Zero Magnetic Field. *Physical Review Letters* **110**(13) (2013).
- [240] J. Chang, E. Blackburn, A. T. Holmes, N. B. Christensen, J. Larsen, J. Mesot, R. Liang, D. A. Bonn, W. N. Hardy, A. Watenphul, M. v. Zimmermann, E. M. Forgan and S. M. Hayden. Direct observation of competition between superconductivity and charge density wave order in $YBa_2Cu_3O_{6.67}$. *Nature Physics* **8**(12), 871–876 (2012).
- [241] C. C. Homes, T. Timusk, R. Liang, D. A. Bonn and W. N. Hardy. Optical conductivity of c axis oriented $YBa_2Cu_3O_{6.70}$: Evidence for a pseudogap. *Physical Review Letters* **71**(10), 1645–1648 (1993).
- [242] M. R. Norman, H. Ding, M. Randeria, J. C. Campuzano, T. Yokoya, T. Takeuchi, T. Takahashi, T. Mochiku, K. Kadowaki, P. Guptasarma and D. G. Hinks. Destruction of the Fermi surface in underdoped high- T_c superconductors. *Nature* **392**(6672), 157–160 (1998).
- [243] H. Ding, T. Yokoya, J. C. Campuzano, T. Takahashi, M. Randeria, M. R. Norman, T. Mochiku, K. Kadowaki and J. Giapintzakis. Spectroscopic Evidence for a Pseudogap in the Normal State of Underdoped High- T_c Superconductors. Peking University-World Scientific Advanced Physics Series, pp. 57–66. WORLD SCIENTIFIC (2018).
- [244] M. E. Simon and C. M. Varma. Symmetry considerations for the detection of second-harmonic generation in cuprates in the pseudogap phase. *Physical Review B* **67**(5) (2003).
- [245] Y. Lubashevsky, L. Pan, T. Kirzhner, G. Koren and N. Armitage. Optical Birefringence and Dichroism of Cuprate Superconductors in the THz Regime. *Physical Review Letters* **112**(14) (2014).
- [246] C. Proust and L. Taillefer. The Remarkable Underlying Ground States of Cuprate Superconductors. *Annual Review of Condensed Matter Physics* **10**(1), 409–429 (2019).

-
- [247] B. Koch, H. Geserich and T. Wolf. Anisotropy of the reflectance spectrum and of the dielectric function of $\text{YBa}_2\text{Cu}_3\text{O}_7$ within the (001) plane. *Solid State Communications* **71**(6), 495–499 (1989).
- [248] E. Uykur. Pseudogap and precursor superconductivity study of $\text{YBa}_2(\text{Cu}_{1-x}\text{Zn}_x)\text{O}_y$: c-axis optical study from underdoped to overdoped region (2013).
- [249] M. N. Iliev, V. G. Hadjiev, S. Jandl, D. L. Boeuf, V. N. Popov, D. Bonn, R. Liang and W. N. Hardy. Raman study of twin-free ortho-II $\text{YBa}_2\text{Cu}_3\text{O}_{6.5}$ single crystals. *Physical Review B* **77**(17) (2008).
- [250] L. Landau and E. Lifschitz. *Mechanik*. Akad.-Verl, Berlin (1987).
- [251] B. Fauqué, Y. Sidis, V. Hinkov, S. Pailhès, C. T. Lin, X. Chaud and P. Bourges. Magnetic Order in the Pseudogap Phase of High-Tc Superconductors. *Physical Review Letters* **96**(19) (2006).
- [252] H. A. Mook, Y. Sidis, B. Fauqué, V. Balédent and P. Bourges. Observation of magnetic order in a superconducting $\text{YBa}_2\text{Cu}_3\text{O}_{6.6}$ single crystal using polarized neutron scattering. *Physical Review B* **78**(2) (2008).
- [253] D. M. Ginsberg. *Physical Properties of High Temperature Superconductors V*. WORLD SCIENTIFIC (1996).
- [254] M. Turlakov and A. J. Leggett. Interlayer-c-axis transport in the normal state of cuprates. *Physical Review B* **63**(6) (2001).
- [255] B. Vignolle, B. J. Ramshaw, J. Day, D. LeBoeuf, S. Lepault, R. Liang, W. N. Hardy, D. A. Bonn, L. Taillefer and C. Proust. Coherent c-axis transport in the underdoped cuprate superconductor $\text{YBa}_2\text{Cu}_3\text{O}_y$. *Physical Review B* **85**(22) (2012).
- [256] E. Berg, E. Fradkin, E.-A. Kim, S. A. Kivelson, V. Oganesyan, J. M. Tranquada and S. C. Zhang. Dynamical Layer Decoupling in a Stripe-Ordered High-Tc Superconductor. *Physical Review Letters* **99**(12) (2007).
- [257] P. A. Lee. Amperean Pairing and the Pseudogap Phase of Cuprate Superconductors. *Physical Review X* **4**(3) (2014).

Bibliography

- [258] A. D. Caviglia, R. Scherwitzl, P. Popovich, W. Hu, H. Bromberger, R. Singla, M. Mitrano, M. C. Hoffmann, S. Kaiser, P. Zubko, S. Gariglio, J.-M. Triscone, M. Först and A. Cavalleri. Ultrafast Strain Engineering in Complex Oxide Heterostructures. *Physical Review Letters* **108**(13) (2012).
- [259] M. Hepting, L. Chaix, E. W. Huang, R. Fumagalli, Y. Y. Peng, B. Moritz, K. Kummer, N. B. Brookes, W. C. Lee, M. Hashimoto, T. Sarkar, J.-F. He, C. R. Rotundu, Y. S. Lee, R. L. Greene, L. Braicovich, G. Ghiringhelli, Z. X. Shen, T. P. Devereaux and W. S. Lee. Three-dimensional collective charge excitations in electron-doped copper oxide superconductors. *Nature* **563**(7731), 374–378 (2018).
- [260] M. Mitrano, A. A. Husain, S. Vig, A. Kogar, M. S. Rak, S. I. Rubeck, J. Schmalian, B. Uchoa, J. Schneeloch, R. Zhong, G. D. Gu and P. Abbamonte. Anomalous density fluctuations in a strange metal. *Proceedings of the National Academy of Sciences* **115**(21), 5392–5396 (2018).
- [261] M. Vershinin, S. Misra, S. Ono, Y. Abe, Y. Ando and A. Yazdani. Local Ordering in the Pseudogap State of the High-Tc Superconductor $\text{Bi}_2\text{Sr}_2\text{CaCu}_2\text{O}_{8+x}$. *Science* **303**(5666), 1995–1998 (2004).
- [262] B. Archambeault, O. M. Ramahi and C. Brench. The Finite-Difference Time-Domain Method. *EMI/EMC Computational Modeling Handbook*, pp. 35–67. Springer US (1998).
- [263] A. Taflove. *Computational electrodynamics : the finite-difference time-domain method*. Artech House, Boston (2005).
- [264] A. Cartella. Amplification of optically driven phonons. Ph.D. thesis, Universität Hamburg (2017).
- [265] R. Courant, K. Friedrichs and H. Lewy. Über die partiellen Differenzgleichungen der mathematischen Physik. *Mathematische Annalen* **100**(1), 32–74 (1928).
- [266] A. Chaves and S. Porto. Generalized Lyddane-Sachs-Teller relation. *Solid State Communications* **13**(7), 865–868 (1973).
- [267] H. J. Monkhorst and J. D. Pack. Special points for Brillouin-zone integrations. *Physical Review B* **13**(12), 5188–5192 (1976).

-
- [268] S. Baroni, S. de Gironcoli, A. D. Corso and P. Giannozzi. Phonons and related crystal properties from density-functional perturbation theory. *Reviews of Modern Physics* **73**(2), 515–562 (2001).
- [269] L. N. Bulaevskii, M. Zamora, D. Baeriswyl, H. Beck and J. R. Clem. Time-dependent equations for phase differences and a collective mode in Josephson-coupled layered superconductors. *Physical Review B* **50**(17), 12831–12834 (1994).
- [270] T. Koyama and M. Tachiki. I-V characteristics of Josephson-coupled layered superconductors with longitudinal plasma excitations. *Physical Review B* **54**(22), 16183–16191 (1996).
- [271] J. ichi Okamoto, A. Cavalleri and L. Mathey. Theory of Enhanced Interlayer Tunneling in Optically Driven High-Tc Superconductors. *Physical Review Letters* **117**(22) (2016).
- [272] J. ichi Okamoto, W. Hu, A. Cavalleri and L. Mathey. Transiently enhanced interlayer tunneling in optically driven high-Tc superconductors. *Physical Review B* **96**(14) (2017).
- [273] n. <http://elk.sourceforge.net> .
- [274] R. Mankowsky, M. Fechner, M. Först, A. von Hoegen, J. Porras, T. Loew, G. L. Dakovski, M. Seaberg, S. Möller, G. Coslovich, B. Keimer, S. S. Dhesi and A. Cavalleri. Optically induced lattice deformations, electronic structure changes, and enhanced superconductivity in $\text{YBa}_2\text{Cu}_3\text{O}_{6.48}$. *Structural Dynamics* **4**(4), 044007 (2017).
- [275] A. Togo and I. Tanaka. First principles phonon calculations in materials science. *Scripta Materialia* **108**, 1–5 (2015).
- [276] G. Khalsa and N. A. Benedek. Ultrafast optically induced ferromagnetic/antiferromagnetic phase transition in GdTiO_3 from first principles. *npj Quantum Materials* **3**(1) (2018).
- [277] M. Fechner and N. A. Spaldin. Effects of intense optical phonon pumping on the structure and electronic properties of yttrium barium copper oxide. *Physical Review B* **94**(13) (2016).